LEVEL

Report AFRPL-TR-77-47

2

A-B PLANE PG THROAT INSERTS

Philip A. Tomlinson James W. Murray

Atlantic Research Corporation 5390 Cherokee Avenue Alexandria, Virginia 22314 DDC PERTURIE AUG 24 1978 E

78 08 21 039

AD No.....

JUNE 1978

Interim Report December 1974 - November 1975

Approved for Public Release; Distribution Unlimited.

Prepared for
AIR FORCE ROCKET PROPULSION LABORATORY
Director of Science and Technology
Air Force Systems Command
Edwards AFB, CA 93523

NOTICES

When U.S. Government drawings, specifications, or other data are used for any purpose other than a definitely related government procurement operation, the Government thereby incurs no responsibility nor any obligation whatsoever, and the fact that the Government may have formulated, furnished, or in any way supplied the said drawings, specifications or other data, is not to be regarded by implication or otherwise, or in any manner licensing the holder or any other person or corporation, or conveying any rights or permission to manufacture, use or sell any patented invention that may in any way be related thereto.

FOREWORD

This report was submitted by Atlantic Research Corporation, 5390 Cherokee Avenue, Alexandria, Virginia 22314 under Contract F04611-75-C-0008, JON-672400HG, with the Air Force Rocket Propulsion Laboratory, Edwards AFB, CA 93523. Mr. James Murray was the Project Engineer and Mr. Philip Tomlinson was the Program Manager. The Pfizer Corporation of Easton, PA was a major subcontractor. Dr. Robert Froberg was the Principal Investigator and Program Manager for Pfizer.

This report has been reviewed by the Information Office/XOJ and is releasable to the National Technical Information Service (NTIS). At NTIS it will be available to the general public. This technical report has been reviewed and is approved for publication; it is unclassified and suitable for general public release.

LESTER TEPE Project Manager

FOR THE COMMANDER

CHARLES BY COOKE

Director, Solid Rocket Division

W.W. Wells

WILBUR W. WELLS Acting Chief, Ballistic Missile & Space Propulsion Branch

UNCLASSIFIED	
SECURITY CLASSIFICATION OF THIS PAGE (When Date Ente	ered)
REPORT MENTATION PA	GE READ INSTRUCTIONS
	GOVT ACCESSION NO. 3. RECIPIENT'S CATALOG NUMBER
AFRPLITR-77-47	Ne estados por emellores estrectores non o de-
A TITLE (and Subtitle)	TARE OF REPORT & TENIOR SOVERED
	Interim Pepti
A-B PLANE PG THROAT INSERTS	December 74 to November
=======================================	NDR-5649-4-76
7. AUTHOR(s)	CONTRACT OF GRANT NUMBER(s)
Philip A. Tomlinson, James W. Murray James O. Bird	5 Fp4611-75-C-0008
PERFORMING ORGANIZATION NAME AND ADDRESS	10. PROGRAM ELEMENT, PROJECT, TASK
Atlantic Research Corporation	ARE (WORK UNIT NUMBER
5390 Cherokee Avenue	JON 572ADOHG (11) 06
Alexandria, Virginia 22314	
CONTROLLING OFFICE NAME AND ADDRESS	REPORT DATE
Air Force Rocket Propulsion Laboratory/MI Edwards AFB, CA 93523	CC Jun 78
Edwards Al B, CA 95325	470
4. MONITORING AGENCY NAME & ADDRESS(If different fro	om Controlling Office) 15. SECURITY CLASS. (of this report)
(IA) II.HIL	UNCLASSIFIED
(12) TIT P /	15a. DECLASSIFICATION/DOWNGRADING
	SCHEDULE N/A
6. DISTRIBUTION STATEMENT (of this Report)	
Assessed for sublications. Distribution	
Approved for public release: Distribution un	nlimited.
63305A	
17. DISTRIBUTION STATEMENT (of the abstract entered in E	Block 20, if different from Report)
8. SUPPLEMENTARY NOTES	
9. KEY WORDS (Continue on reverse side if necessary and id	lentify by block number)
9. KEY WORDS (Continue on reverse side if necessary and id Rocket Nozzles	Thermostructural Analysis
Materials	Stress Analysis
Carbon	Failure Criteria
Pyrolytic Graphite	
Nozzle Coatings	

20. ABSTRACT (Continue on reverse side if necessary and identify by block number)

An exploratory program was conducted to design and develop free standing a-b plane pyrolytic graphite throat inserts for rocket nozzles. Thermal analysis and structural analysis were conducted to define and establish design concepts for nozzle inserts. Free standing a-b plane continuously nucleated pyrolytic graphite cylinders were fabricated and characterized to determine the thermal and mechanical properties over range of temperatures from 70°F to 5000°F. Failure criteria were investigated and the predictions were compared with the results of pyrolytic graphite throat inserts which fractured during (over)

DD 1 JAN 73 1473 A EDITION OF 1 NOV 65 IS OBSOLETE

UNCLASSIFIED

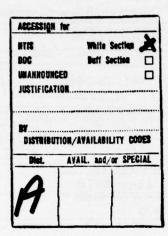
SECURITY CLASSIFICATION OF THIS PAGE (When Data Entered)

045 550

UNCLASSIFIED

SECURITY CLASSIFICATION OF THIS PAGE(When Date Entered)

cooldown. The throat insert configuration was defined and thirteen deposition runs were made to produce the throat inserts. All inserts fabricated were unacceptable for nozzle testing due to cracks and/or delaminations which occurred during cooldown.



UNCLASSIFIED

SECURITY CLASSIFICATION OF THIS PAGE(When Data Entered)

TABLE OF CONTENTS

INTRO	DUCTION	
PROGI	AM OBJECTIVES	
SUMM	RY	
DESIG	CONCEPTS	
4.1	ntroduction	
4.2	Design Concept Candidates	
4.3	Assessment of Past Programs	
	.3.1 Atlantic Research Corporation 7.0-inch PG Program	
	.3.2 Marquardt Free-Standing Chamber Programs	
	.3.3 Pfizer Bulk PG Program	
PYRO	TIC GRAPHITE PROPERTIES	
5.1	Available Property Data	
5.2	esting Program	٠
	.2.1 Data Required for Analysis	
	.2.2 Testing Accomplished	
	.2.3 Summary of Test Data	
	.2.4 Assessment of Test Results and Comparison with Literature Data	
DESIG	ANALYSIS	
6.1	ntroduction	
6.2	Thermal — Erosion Studies	
	.2.1 Analysis Techniques	
	2.2 Thermal Properties	
	.2.3 Boundary Conditions	
	2.4 Flow Field and Boundary Layer Analysis	
	.2.5 Thermal Analysis Results	
6.3	Thermostructural Studies	
	3.1 Analytical Techniques	
	.3.2 Failure Criteria	
	3.3 Residual Stresses	
	.3.4 Firing Stresses	

TABLE OF CONTENTS (Continued)

																					Page
7.0	AB PI	LANE PO	G FAB	RICA	TION																287
	7.1	Introd	uction						 												287
	7.2	Result	s .																		287
	7.3	Conclu	usions																		287
	7.4	Develo	pmen	tal Ru	ns .							٠.									290
		7.4.1		m Che																	290
		7.4.2		ostruct					 	 -											290
		7.4.3	Prod	uction	Runs																302
8.0	CONC	LUSIO	NS AN	D REC	СОММ	ENE	ATI	ONS								 					316
	8.1	Conclu										100							-		316
	8.2	Recom	ımena	ations						 •			•				•				318
9.0	REFE	RENCE	s																		320
10.0	LIST O	F SYMB	OLS													 					322
	ENDIX A										10				es						

LIST OF ILLUSTRATIONS

Figure		Page
1	Structure of the Technical Effort for the "a-b" Plane Pyrolytic Graphite Throat Insert Program	4
2	Single Layer PG Insert Configuration - Preliminary Concept	8
3	Dual Layer PG Insert Configuration - Preliminary Concept	9
4	Multilayered Pressure-bleed PG Insert Concept - Preliminary Concept	10
5	Tensile Modulus for Pyrolytic Graphite, a-b Plane	24
6	Tensile Strength for Pyrolytic Graphite, a-b Plane	26
7	Compressive Modulus for Pyrolytic Graphite, a-b Plane	27
8	Compressive Strength for Pyrolytic Graphite, a-b Plane	28
9	Unit Thermal Expansion for Pyrolytic Graphite, a-b Plane	30
10	Unit Thermal Expansion for Pyrolytic Graphite, C-direction	31
11	Interlaminar Shear Strength Test Specimen for Pyrolytic Graphite, 0.5 Inch Gage Section	32
12	Interlaminar Shear Strength Test Specimen for Pyrolytic Graphite, 0.25 Inch Gage Section	33
13	Test Results for Interlaminar Shear Strength of Pyrolytic Graphite	34
14	Finite Element Mesh for Shear Strength Test Specimen	36
15	Stress Distribution in Shear Strength Test Specimen	37
16	Preliminary A-B Plane Nozzle Insert Configuration	41
17	Thermal/Erosion Analysis Flow Chart	44
18	C-Direction Thermal Conductivity for PG/SiC	46
19	A-B Direction Thermal Conductivity for PG/SiC	47
20	With-Grain Thermal Conductivity for ATJ Graphite	48
21	Across-Grain Thermal Conductivity for ATJ Graphite	49

F	igure		Page
	22	Specific Heat for ATJ Graphite	50
	23	Thermal Boundary Condition Model Geometries	52
	24	Nozzle Geometry Used for Thermal Analysis	53
	25	Nondimensionalized Erosion Versus Temperature Using Bulk Graphite Kinetic Constants	55
	26	Nodimensionalized Erosion Versus Temperature Used Edge PG Kinetic Constants	56
	27	Nondimensionalized Erosion Versus Temperature Using A-B Plane PG Kinetic Constants	57
	28	Heat Transfer Coefficient Versus Nozzle Area Ratio	59
	29	Predicted Erosion Profiles for ATJ Graphite Entrance Cap, and Exit Ring	60
	30	Predicted Erosion Profiles for PG/SiC Entrance Cap and Exit Ring	61
	31	Predicted Erosion Profiles for 1.9 g/cc Carbon/Carbon Entrance Cap and Exit Ring	62
	32	Predicted Erosion for a-b Plane PG Insert	63
	33	Integral PG Insert/Nose Cap Design	65
	34	PG Insert with Separate PG Nose Cap	66
	35	PG Insert with PG/SiC Nose Cap	67
	36	PG Insert with PG Washer and PG/SiC Nose Cap	68
	37	PG Insert with PG Washer and Carbon/Carbon Nose Cap	69
	38	Effects of 35% Change in Heat Transfer Coefficient on Temperature Profile	70
	39	Effect of Increase of Heat Transfer Coefficient on Temperatures Near the Insert OD	73
	40	Five Second Isotherms in PG Insert Using the IO and NA Thermal Models	74

Figure		Page
41	Fifteen Second Isotherms in PG Insert Using IO and NA Models	75
42	Effects of Axial Conduction on Five and Fifteen Second Temperature Distributions	76
43	Five Second Isotherms in PG Insert Using Nafe Thermal Model	77
44	Fifteen Second Isotherms in the PG Insert Using the Nafe Thermal Model	78
45	Model Used for Thermal Analysis of PG Insert	79
46	Temperature Distributions in Column 2 for First Layer of PG and with ATJ Entrance Cap	80
47	Temperature Distributions in Column 3 for First Layer of PG with ATJ Entrance Cap	81
48	Temperature Distributions in Column 4 for First Layer of PG with ATJ Entrance Cap	82
49	Temperature Distributions in Column 5 for First Layer of PG with ATJ Entrance Cap	83
50	Temperature Distributions in Column 6 for First Layer of PG with ATJ Entrance Cap	84
51	Temperature Distributions in Column 7 for First Layer of PG with ATJ Entrance Cap	85
52	Temperature Distributions in Column 8 for First Layer of PG with ATJ Entrance Cap	86
53	Temperature Distributions in Column 9 for First Layer of PG with ATJ Entrance Cap	87
54	Temperature Distributions in Column 10 for First Layer of PG with ATJ Entrance Cap	88
55	One Second Isotherms in First Layer of the PG Insert	89
56	Five Second Isotherms in First Layer of PG Insert	90
57	Fifteen Second Isotherms in the First Layer of the PG Insert	91
58	Temperature Distributions in Column 1 for the First Layer of PG Insert with PG/SiC Entrance Cap	93

Figure		Page
59	Temperature Distributions in Column 2 for the First Layer of PG Insert with PG/SiC Entrance Cap	94
60	Temperature Distributions in Column 3 for the First Layer of PG Insert with PG/SiC Entrance Cap	95
61	Temperature Distributions in Column 4 for the First Layer of PG Insert with PG/SiC Entrance Cap	96
62	Temperature Distributions in Column 5 for the First Layer of PG Insert with PG/SiC Entrance Cap	97
63	Temperature Distributions in Column 6 for the First Layer of PG Insert with PG/SiC Entrance Cap	98
64	Temperature Distributions in Column 7 for the First Layer of PG Insert with PG/SiC Entrance Cap	99
65	Temperature Distributions in Column 8 for the First Layer of PG Insert with PG/SiC Entrance Cap	100
66	Temperature Distributions in Column 9 for the First Layer of PG Insert with PG/SiC Entrance Cap	101
67	Temperature Distributions in Column 10 for the First Layer of PG Insert with PG/SiC Entrance Cap	102
68	Fifteen Second Isotherms in the First Layer of the PG Insert	103
69	Thirty Second Isotherms in the First Layer of the PG Insert	104
70	Sixty Second Isotherms in the First Layer of the PG Insert	105
71	Comparison of the Temperature Distributions for a Single-Layer Insert and a Dual-Layer Insert	106
72	Comparisons of the Temperature Distributions in Column 1 for Single- and Dual-Layer PG Insert	107
73	Comparisons of the Temperature Distributions in Column 2 for Single- and Dual-Layer PG Insert	108
74	Comparisons of the Temperature Distributions in Column 3 for Single- and Dual-Layer PG Insert	109

Figure		Page
75	Comparisons of the Ten-perature Distributions in Column 4 for Single- and Dual-Layer PG Insert	110
76	Comparisons of the Temperature Distributions in Column 5 for Single- and Dual-Layer PG Insert	111
77	Comparisons of the Temperature Distributions in Column 6 for Single- and Dual-Layer PG Insert	112
78	Comparisons of the Temperature Distributions in Column 7 for Single- and Dual-Layer PG Insert	113
79	Comparisons of the Temperature Distributions in Column 8 for Single- and Dual-Layer PG Insert	114
80	Comparisons of the Temperature Distributions in Column 9 for Single- and Dual-Layer PG Insert	115
81	Comparisons of the Temperature Distributions in Column 10 for Single- and Dual-Layer PG Insert	116
82	Fifteen Second Isotherms for the Single-Layer PG Insert	117
83	Thirty Second Isotherms for the Single-Layer PG Insert	118
84	Sixty Second Isotherms for the Single-Layer PG Insert	119
85	Typical Finite Element Mesh Used for the Stress Analysis of the PG Insert	126
86	Axial and Hoop Stress Along the Inner Surface of the Insert for CN PG	129
87	Radial and Shear Stress Along the Insert Near the Middle Surface for CN PG	130
88	Axial and Hoop Stress Along the Outer Surface of the Insert for CN PG	131
89	Axial and Hoop Stress Along the Inner Surface of the Insert for SN PG	132
90	Radial and Shear Stress Along the Insert Near the Middle Surface for SN PG	133
91	Axial and Hoop Stress Along the Outer Surface of the Insert for SN PG	134
92	Safety Factors Along Inner Surface for 0.150 Inch Thick CN PG	135
93	Safety Factors Along Inner Surface for 0.300 Inch Thick CN PG	136

Figure		Page
94	Safety Factors Along Inner Surface for 0.45 Inch Thick CN PG	137
95	Safety Factors Along Outer Surface for 0.15 Inch Thick CN PG	138
96	Safety Factors Along Outer Surface for 0.30 Inch Thick CN PG	139
97	Safety Factors Along Outer Surface for 0.45 Inch Thick CN PG	140
98	Safety Factors Along the Inner Surface for 0.15 Inch Thick SN PG	141
99	Safety Factors Along the Inner Surface for 0.300 Inch Thick SN PG	142
100	Safety Factors Along Inner Surface of 0.45 Inch Thick SN PG	143
101	Safety Factors Along Outer Surface of 0.15 Inch Thick SN PG	144
102	Safety Factors Along Outer Surface of 0.30 Inch Thick SN PG	145
103	Safety Factors Along Outer Surface of 0.45 Inch Thick SN PG	146
104	Safety Factors Along Inner Surface of CN PG Using Average Properties	147
105	Safety Factors Along Outer Surface of CN PG Using Average Properties	148
106	Safety Factors Along Inner Surface of SN PG Using Averages Properties	149
107	Safety Factors Along Outer Surface of SN PG using Averages Properties	150
108	Minimum Factors versus Thickness for SN PG	151
109	Minimum Factors versus Thickness for CN PG	152
110	Safety Factors Along Length of CN PG Insert Using Measured Properties	153
111	Safety Factors Along Length of SN PG Insert Using Measured Properties	154
112	Residual Stress Test Ring Specimen Configuration	157
113	Strain Relief versus Material Removal in Residual Stress Test	158
114	Axial and Hoop Stress Along the Inner Surface of the Insert at 5 Seconds for CN PG	162
115	Axial and Hoop Strain Along the Inner Surface of the Insert at 5 Seconds for CN PG	163

Figure		Page
116	Safety Factors Along the Inner Surface of the Insert at 5 Seconds for CN PG	164
117	Shear Stress and Radial Stress at the Entrance End of the Insert at 5 Seconds in CN PG	165
118	Axial and Hoop Stress at the Entrance End of the Insert at 5 Seconds in CN PG	166
119	Safety Factors at the Entrance End of the Insert at 5 Seconds in CN PG	167
120	Axial and Hoop Stress and Exit End of the Insert at 5 Seconds in CN PG	168
121	Shear and Radial Stress at Exit End of the Insert at 2 Seconds for CN PG	169
122	Safety Factors at Exit End of the Insert at 5 Seconds in CN PG	170
123	Axial and Hoop Stress Along Outer Surface of the Insert at 5 Seconds in CN PG	171
124	Safety Factors Along Outer Surface of the Insert at 5 Seconds in CN PG	172
125	Axial and Hoop Stress Along the Inner Surface of the Insert at 15 Seconds for CN PG	173
126	Axial and Hoop Strain Along the Inner Surface of the Insert at 15 Seconds for CN PG	174
127	Safety Factors Along the Inner Surface of the Insert at 15 Seconds for CN PG	175
128	Shear Stress and Radial Stress at the Entrance End of the Insert at 15 Seconds in CN PG	176
129	Axial and Hoop Stress at the Entrance End of the Insert at 15 Seconds in CN PG	177
130	Safety Factors at the Entrance End of the Insert at 15 Seconds in CN PG	178
131	Axial and Hoop Stress and the Exit End of the Insert at 15 Seconds in CN PG	179
132	Shear and Radial Stress at Exit End of the Insert at 15 Seconds for CN PG	180
133	Safety Factors at Exit End of the Insert at 15 Seconds in CN PG	181
134	Axial and Hoop Stress Along Outer Surface of the Insert at 15 Seconds in CN PG	182
135	Safety Factors Along Outer Surface of the Insert at 15 Seconds in CN PG	183

Figure		Page
136	Axial and Hoop Stress Along the Inner Surface of the Insert at 60 Seconds for CN PG	184
137	Axial and Hoop Strain Along the Inner Surface of the Insert at 60 Seconds for CN PG	185
138	Axial and Hoop Stress at the Entrance End of the Insert at 60 Seconds in CN PG	186
139	Shear Stress and Radial Stress at the Entrance End of the Insert at 60 Seconds in CN PG	187
140	Safety Factors at the Entrance End of the Insert at 60 Seconds in CN PG	188
141	Shear and Radial Stress at Exit End of the Insert at 60 Seconds for CN PG	189
142	Axial and Hoop Stress and the Exit End of the Insert at 60 Seconds in CN PG	190
143	Safety Factors at Exit End of the Insert at 60 Seconds in CN PG	191
144	Axial and Hoop Stress Along Outer Surface of the Insert at 60 Seconds in CN PG	192
145	Safety Factors Along Outer Surface of the Insert at 60 Seconds in CN PG	193
146	Axial and Hoop Stress Along the Inner Surface of the Insert at 15 Seconds for SN PG	197
147	Axial and Hoop Strain Along the Inner Surface of the Insert at 15 Seconds for SN PG	198
148	Safety Factors Along the Inner Surface of the Insert at 15 Seconds for SN PG	199
149	Axial and Hoop Stress and the Exit End of the Insert at 15 Seconds in SN PG	200
150	Shear and Radial Stress at Exit End of the Insert at 15 Seconds for SN PG	201
151	Safety Factors at Exit End of the Insert at 15 Seconds in SN PG	202
152	Shear and Radial Stress at Entrance End of the Insert at 15 Seconds for SN PG	203
153	Axial and Hoop Stress and the Entrance End of the Insert at 15 Seconds in SN PG	204
154	Safety Factors at Entrance End of the Insert at 15 Seconds in SN PG	205

Figure		Page
155	Axial and Hoop Stress Along Outer Surface of the Insert at 15 Seconds in SN PG	206
156	Safety Factors Along Outer Surface of the Insert at 15 Seconds in SN PG	207
157	Axial and Hoop Stress Along the Inner Surface of the Insert at 60 Seconds for SN PG	208
158	Axial and Hoop Strain Along the Inner Surface of the Insert at 60 Seconds for SN PG	209
159	Axial and Hoop Stress and the Exit End of the Insert at 60 Seconds in SN PG	210
160	Shear and Radial Stress at Exit End of the Insert at 60 Seconds for SN PG	211
161	Axial and Hoop Stress at the Entrance End of the Insert at 60 Seconds in SN PG	212
162	Shear Stress and Radial Stress at the Entrance End of the Insert at 60 Seconds in SN PG	213
163	Safety Factors at the Entrance End of the Insert at 60 Seconds in SN PG	214
164	Axial and Hoop Stress Along Outer Surface of the Insert at 60 Seconds in SN PG	215
165	Safety Factors Along Outer Surface of the Insert at 60 Seconds in SN PG	216
166	Comparison of Hoop Stress Distributions for Single- and Dual-Layer Designs	218
167	Comparison of Hoop Strain Distributions for Single- and Dual-Layer Designs	219
168	Comparison of Shear Stress Distributions for Single- and Dual-Layer Designs	220
169	Comparison of Factors for Safety for Single- and Dual-Layer Designs	221
170	Axial and Hoop Stress Along the Inner Surface at 2 Seconds for a Single-Layer CN PG Insert	223
171	Hoop and Axial Strain Along the Inner Surface at 2 Seconds for a Single-Layer CN PG Insert	224
172	Safety Factors Along the Inner Surface at 2 Seconds for a Single-Layer CN PG Insert	225
173	Hoop and Axial Stress at Entrance End of the Insert at 2 Seconds for a Single-Layer CN PG	226

Figure		Page
174	Shear and Radial Stress at Entrance End of the Insert at 2 Seconds for a Single-Layer CN PG	227
175	Safety Factor at Entrance End of the Insert at 2 Seconds for a Single-Layer CN PG	228
176	Shear and Radial Stress at Exit End of the Insert at 2 Seconds for a Single-Layer CN PG	229
177	Axial and Hoop Stress at Exit End of the Insert at 2 Seconds for a Single-Layer CN PG	230
178	Safety Factors at the Exit End of the Insert at 2 Seconds for a Single-Layer CN PG	231
179	Axial and Hoop Stress Along the Outer Surface of the Insert at 2 Seconds for a Single-Layer CN PG	232
180	Safety Factors Along the Outer Surface of the Insert at 2 Seconds for a Single-Layer CN PG	233
181	Axial and Hoop Stress Along the Inner Surface of the Insert at 15 Seconds for a Single-Layer CN PG	234
182	Axial and Hoop Strain Along the Inner Surface of the Insert at 15 Seconds for a Single-Layer CN PG	235
183	Radial and Shear Stress at the Exit End of the Insert at 15 Seconds for a Single-Layer CN PG	236
184	Axial and Hoop Stress at Exit End of the Insert at 15 Seconds for a Single-Layer CN PG	237
185	Safety Factors at Exit End of the Insert at 15 Seconds for a Single-Layer CN PG	238
186	Axial and Hoop Stress at the Entrance End of the Insert at 15 Seconds for a Single-Layer CN PG	239
187	Radial and Shear Stress at the Entrance End of the Insert at 15 Seconds for a Single-Layer CN PG	240
188	Safety Factors at the Entrance End of the Insert at 15 Seconds for a	241

Figure		Page
189	Axial and Hoop Stress Along Outer Surface of the Insert at 15 Seconds for a Single-Layer CN PG	242
190	Axial and Hoop Stress Along the Inner Surface of the Insert at 60 Seconds for a Single-Layer CN PG	243
191	Axial and Hoop Strain Along the Inner Surface of the Insert at 60 Seconds for a Single-Layer CN PG	244
192	Radial and Shear Stress at the Exit End of the Insert at 60 Seconds for a Single-Layer CN PG	245
193	Axial and Hoop Stress at the Exit End of the Insert at 60 Seconds for a Single-Layer CN PG	246
194	Safety Factors at the Exit End of the Insert at 60 Seconds for a Single-Layer CN PG	247
195	Radial and Shear Stress at the Entrance End of the Insert at 60 Seconds for a Single-Layer CN PG	248
196	Axial and Hoop Stress at the Entrance End of the Insert at 60 Seconds for a Single-Layer CN PG	249
197	Safety Factors at the Entrance End of the Insert at 60 Seconds for a Single-Layer CN PG	250
198	Axial and Hoop Stress Along the Outer Surface of the Insert at 60 Seconds for a Single-Layer CN PG	251
199	Safety Factors Along the Outer Surface of the Insert at 60 Seconds for a Single-Layer CN PG	252
200	Critical Buckling Pressure versus Thickness Radios Ratio	259
201	Mode Shape for Buckling Due to External Pressure for $t/r_0 = 0.1$ and $n = 10$	260
202	Critical Buckling Pressure versus Thickness	261
203	Critical Buckling Pressure and Insert Stress versus Thickness at 60 Seconds for the Entrance End	262
204	Critical Buckling Pressure and Insert Stress versus Thickness at 60 Seconds for the Throat Plane	263

Figure		Page
205	Critical Buckling Pressure and Insert Stress versus Thickness at 60 Seconds for the Exit End	264
206	ATJ Graphite Entrance Cap and Exit Ring for the 15 Second Nozzle Design	266
207	Axial and Hoop Stress Along the Inner Surface of the Entrance Cap at 5 Seconds	267
208	Radial and Shear Stress Along the Inner Surface of the Entrance Cap at 5 Seconds	268
209	Axial and Hoop Strain Along the Inner Surface of the Entrance Cap at 5 Seconds	
		269
210	Radial and Shear Strain Along the Inner Surface of the Entrance Cap at 5 Seconds	270
211	Safety Factors Along the Inner Surface of the Entrance Cap at 5 Seconds	271
212	Safety Factors Along the Inner Surface of the Entrance Cap at 15 Seconds	273
213	Axial and Hoop Stress Along Inner Surface of the Exit Ring at 2 Seconds	274
214	Axial and Hoop Strain Along the Inner Surface of the Exit Ring at 2 Seconds	275
215	Axial and Hoop Stress Along Outer Surface of the Exit Ring at 2 Seconds	276
216	Axial and Hoop Strain Along Outer Surface of the Exit Ring at 2 Seconds	277
217	Axial and Hoop Stress Along the Inner Surface of the Exit Ring at 5 Seconds	278
218	Axial and Hoop Strain Along the Inner Surface of the Exit Ring at 5 Seconds	279
219	Axial and Hoop Stress Along the Outer Surface of the Exit Ring at 5 Seconds	280
220	Axial and Hoop Strain Along Outer Surface of the Exit Ring at 5 Seconds	281
221	Axial and Hoop Stress Along the Inner Surface of the Exit Ring at 15 Seconds	282
222	Axial and Hoop Strain Along the Inner Surface of the Exit Ring at 15 Seconds	283
223	Axial and Hoop Stress Along the Outer Surface of the Exit Ring at 15 Seconds	284
224	Axial and Hoop Strain Along the Outer Surface of the Exit Ring at 15 Seconds	285
225	Safety Factors Along the Inner Surface of the Exit Ring at 5 Seconds	286
226	Specified Deposition Shape	288

Figure		Page
227	Typical Deposit Assembly	289
228	Throat Insert Fabricated During Run M-211	291
229	Throat Insert Fabricated During Run M-212	292
230	Throat Insert Fabricated During Run M-213	293
231	Throat Insert Fabricated During Run M-214	294
232	Microstructure of Throat Insert Fabricated During Run M-213.50X	295
233	Microstructure of Throat Insert Fabricated During Run M-214.50X	296
234	Throat Insert Fabricated During Run M-216. Downstream End Removed	298
235	Throat Insert Fabricated During Run M-218	299
236	Microstructure of Throat Insert Fabricated During Run M-218.50X	301
237	Both Sections of Specimen Characterization Tube Fabricated During Run M-215	303
238	Partial Section of Specimen Characterization Tube Fabricated During Run M-217	304
239	Throat Insert Fabricated During Run M-219 Showing Separation Due to Extended Process Interruption	305
240	Throat Insert Fabricated During Run M-220. Upstream End View	306
241	Throat Insert Fabricated During Run M-220 Side View	307
242	Throat Insert Fabricated During Run M-221	309
243	Throat Insert Fabricated During Run M-222	310
244	Throat Insert Fabricated During Run M-223	311
245	Throat Insert Fabricated During Run M-224	312
246	Throat Insert Fabricated During Run M-225	313
247	Microstructure of Throat Insert Fabricated During Run M-224.50X	314
248	Coating Thickness Profile of Run M-224	315

Table		Page
1	Material Properties Pyrolytic Graphite	16
2	Thermal Properties	18
3	Substrate Nucleated PG	19
4	Continuously Nucleated PG	20
5	Pre-Test PG Cylinder Evaluation Matrix	23
6	Actual PG Cylinder Evaluation Matrix	23
7	Results of Torsion and Shear Modulus Plate Evaluations	29
8	Comparison of Test Results with Literature Data	39
9	Gasket Run Matrix	54
10	Structural Cooldown Results	127
11	Summary of Safety Factors Dual Layer Design - CN Material	195
12	Summary of Safety Factors Dual Layer - SN Material	217
13	Atlantic Research Corporation 0.300" Wall PG Shape	300

1.0 INTRODUCTION

Performance improvement for the propulsion systems of future strategic missile systems demand investigation and utilization of new nozzle materials, which provide for performance beyond the capability of materials currently used in nozzle designs. These new materials must be superior from a standpoint of their ablation, thermal, and structural performance. At the same time both weight and cost are very important aspects to be considered.

This program was undertaken by Atlantic Research Corporation for the U.S. Air Force under Contract F04611-75-C-0008 as one of several programs investigating PG coatings for solid propellant rocket nozzle throat inserts. Other programs, parallel to this program, investigated a particular approach to the utilization of a-b plane oriented PG for nozzle throat application.

This report describes the efforts of the work done at Atlantic Research Corporation to conceive, develop, and demonstrate designs for the use of commercially available a-b plane PG inserts in solid propellant rocket nozzles. As discussed later in this report, considerable difficulties were encountered in the fabrication of the throat inserts. It became apparent that the state of the art of PG deposition was not sufficiently advanced to fabricate throat inserts meeting the requirements as established during the course of the program. Continuation of the program as conceived would have required that resources be devoted to advance the state of the art of PG deposition. This was beyond the scope of the program and not consistent with the objectives of using commercially available materials in the development of nozzles for the high temperature, high performance solid motor booster applications of advanced ICBM propulsion systems.

2.0 PROGRAM OBJECTIVES

The objectives of the program were: (1) to develop and demonstrate the use of commercially available a-b plane pyrolytic graphite throat inserts in solid propellant rocket nozzles, and (2) to identify an a-b plane pyrolytic graphite throat insert approach for future MX Advanced Development Program demonstration efforts.

The approach taken to meet the above objectives consisted of an initial evaluation of current state of the art of a-b plane pyrolytic graphite throat insert technology based upon available materials. This was followed with a definition of the thermal and mechanical properties and the failure criteria necessary to perform the level of design analysis required to select and fabricate candidate throat inserts. To be included also was an identification of deficiencies in the analysis techniques and the failure criteria selection. With this a design and analysis methodology was established for the application of a-b plane pyrolytic graphite throat inserts for large diameter propulsion systems. This was then to be followed by a demonstration, through rocket nozzle testing, of the thermostructural integrity and erosion rates of the throat insert designs in solid propellant environments typical of ICBM propulsion systems.

3.0 SUMMARY

As originally structured, the program was organized within a framework consisting of five categories of technical effort. Figure 1 presents division of effort by phases. Because of the wide variation in types of pyrolytic graphite (PG) material which can be produced, the initial activities were concerned with the identification of the specific type of PG considered to offer the greatest potential for achieving the program objectives. Considered here were the microstructural categories of PG such as substrate nucleated and continuously nucleated material. Differences in physical, thermal, and mechanical properties were evaluated in an attempt to determine the desirability of one type of PG over the other relative to design applicability. Fabricability of the PG components necessarily was a major point of interest in this initial survey of PG materials.

A considerable amount of literature exists which deals with pyrolytic graphite. Early activities concentrated on the evaluation of literature and data regarding past and present programs which have direct bearing on the a-b plane pyrolytic graphite throat insert program objectives. Particular attention was given to existing literature which deals with specific differences in PG microstructure as related to the mechanical properties, fabricability, and the thickness-to-radius ratio for closed shapes. Additionally, emphasis was placed upon characteristics such as material structure changes or transformations resulting from exposure to the 5000°F and above temperatures of the nozzle environment.

The comparison of various design concepts and the selection of one or two of the more favorable approaches was addressed early in the program. Among the items considered in this comparison and selection were the elimination of potential failure modes, highest potential margins of safety, scalability, simplicity, insensitivity to structural restraints, cost, and fabricability.

Based upon the results of these efforts, the analysis and design of a-b plane pyrolytic graphite throat inserts was performed. Included in this were detailed analytical studies which addressed the assessment of failure criteria and predictions of margins of safety, thermal response, structural response, and the prediction of erosion for a-b plane PG throat inserts.

Within the framework of the insert analysis and design efforts, PG material representative of that selected for throat inserts was characterized with respect to the thermal and mechanical properties to obtain design analysis data.

Concurrent with the design and analysis of the throat inserts, the fabrication of PG components was performed. This activity was accomplished in three basic steps. The first being the deposition studies to establish process conditions to produce PG having a microstructure which was considered to be representative of the material selected for nozzle inserts. The second step was the fabrication of a cylinder of PG to be used to obtain key thermal and mechanical properties. The third step was the fabrication of actual throat inserts in the required shapes as determined by the insert analysis and design studies.

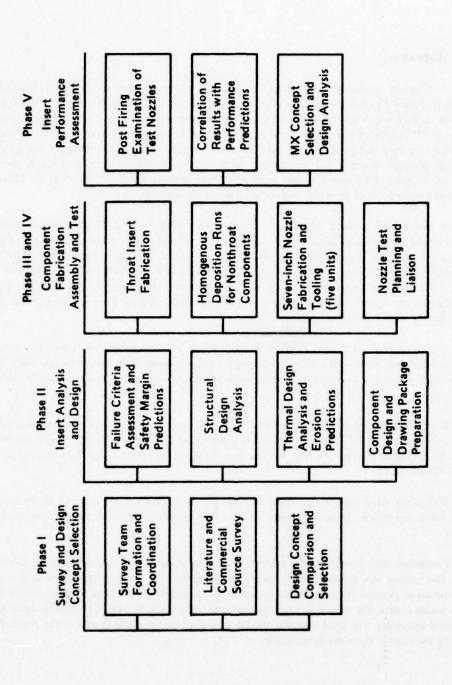


Figure 1. Structure of the Technical Effort for the "a-b" Plane Pyrolytic Graphite Throat Insert Program.

The first two of these were successfully accomplished. The third one, the fabrication of actual throat inserts, was not accomplished successfully. No throat inserts were fabricated which were defect free and had the desired thickness.

The program was then redirected to investigate the use of carbon/carbon materials as throat inserts for advanced strategic missile systems.

4.0 DESIGN CONCEPTS

4.1 Introduction

In the initial phase of the program, a number of a-b plane PG throat insert design concepts were identified which offered the possibility of meeting the stated design requirements of the program. The concepts considered included free-standing shapes composed of one or more layers of PG. PG deposited on several different kinds of substrates were also considered.

In considering the various concepts, active, on-going programs as well as previous work which offered reasonable relevance was reviewed. The specific objective being to identify concepts already addressed and to determine problems, failure modes, and degree of past success. The following programs were considered:

- 1. TRW AFML Carbon/Carbon Substrate Program[1]*
- 2. Hercules Design Studies [2]
- 3. ARC 7.0-inch Nozzle Program [3]
- 4. Aerotherm Analysis Study of ARC Program [4]
- 5. ARC 7.0-inch Scaleup Program (Codeposit)[5]
- 6. Royal Propulsion Establishment Efforts [6]
- 7. Pyrogenies (PFIZER) AFRPL Pyroid Program [7]
- 8. Marquardt Free-Standing Combustion Chamber Programs [8,9,10,11,12]
- 9. Lockheed Missile & Space Company PG Studies [13]

The bulk of the efforts relative to the deposition of PG coatings on substrates have been performed by the Atlantic Research Corporation and the British Royal Propulsion Establishment. Most of this work has been concentrated on depositing thin (0.050 - 0.100 inch) PG coatings on polycrystalline graphite substrates. The only publication of specific application is the final report of the ARC Large Nozzle Development Program. [3]

The in-progress AFML Carbon/Carbon Substrate Program^[1] at the time of this present activity had not addressed the problem of PG coating the substrate materials. Thus, it offered no results for consideration in this program relative to PG coatings.

The most significant work on PG deposition of free-standing shapes performed prior to this program was that done by the Marquardt Corporation on free-standing liquid rocket combustion chambers [8,9,10,11,12] and by Pfizer on free-standing PG nozzle components.^[7]

^{*}Numbers in square brackets refer to references listed in Section 9.0.

4.2 Design Concept Candidates

Based on the findings of the review and evaluation of programs listed previously, candidate concepts were established. These candidates are identified and discussed in the following paragraphs.

Shown in Figure 2 is the single layer, free-standing PG insert design concept. The concept as established identified a 0.30-inch-thick PG insert backed up by polycrystalline graphite or other material as determined to be appropriate from subsequent detail analysis. Among the early concerns with this concept was the problem of insert retention because of the relatively thin section of PG.

Added structural integrity of thicker sections was considered to be desirable. An approach to obtaining a thicker insert is shown in Figure 3. It includes a dual-layered pyrolytic graphite insert. Each layer of pyrolytic graphite is approximately 0.30-inch thick. The outer layer is first deposited in a "free-standing" state. The deposition process is then interrupted and the inner layer is then deposited. A deliberate weak interface is thus provided and the structural integrity of each layer is maintained during deposition.

The deposition of the two layers together ensures that at the deposition temperature the interfaces are matched. The two layers result in a total thickness of 0.60 inch. This provides adequate thickness to maintain axial retention as the downstream nozzle component erodes during the firing. The low conductivity of the pyrolytic graphite in the c direction maintains backside temperatures at low values. The insert backup could be either carbon phenolic or ATJ graphite.

Variations on this basic concept are shown in Figure 4. This concept shows three layers of pyrolytic graphite. Although this concept increases the complexity of the design, it results in more design variables which could aid in increasing margins of safety.

In conjunction with the three-layered design shown in Figure 4, a pressure bleed boundary condition is shown. The bleeding of pressure to the backside of the insert resulted in a successful test for a 3.5-inch throat diameter nozzle. A seal such as Grafoil is shown on the downstream face of the coating. Although three layers are shown, either one or two layers could be used for the pressure bleed concept. Some of the difficulties in the past efforts to successfully fire an a-b plane PG insert have been attributed to the lack of control and knowledge of the boundary conditions of the back side of the insert. The pressure bleed concept offers an opportunity for improvement in this regard. The major advantage of this system is that the insert can move outwardly under thermal growth and the backside boundary condition is well defined.

Other design concepts were considered. For the most part they involved PG coatings and thus the tailoring or developing of a substrate which would provide a suitable backup for the PG insert. In each case, the concepts were considered to require developmental efforts outside the scope of the present program.

The candidates which were selected for additional study and detailed analysis were of the free-standing concept. The details of these analyses are contained in Sections 5.0 and 6.0.

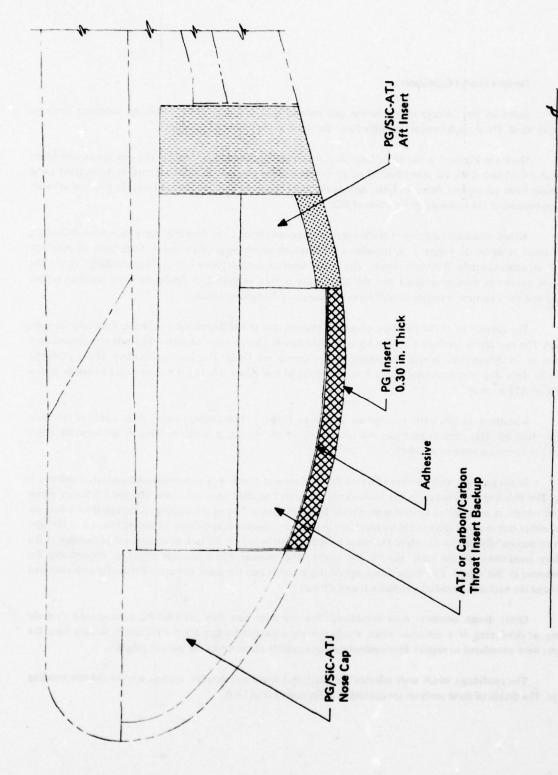


Figure 2. Single Layer PG Insert Configuration - Preliminary Concept.

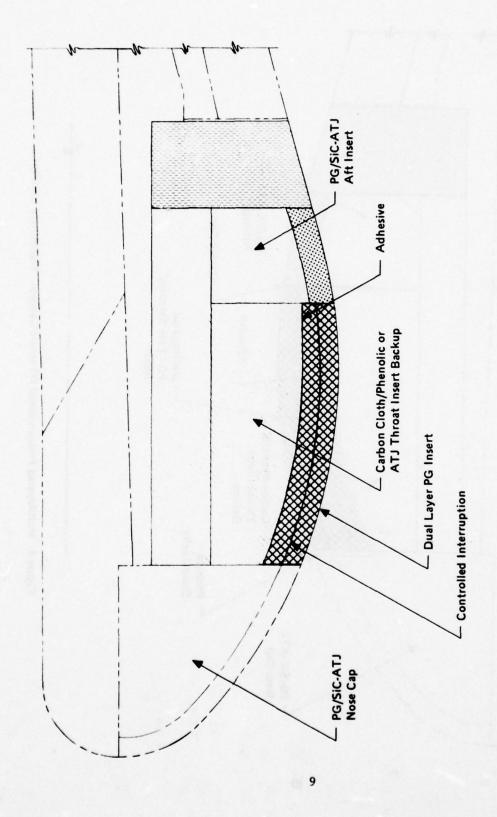


Figure 3. Dual Layer PG Insert Configuration - Preliminary Concept.

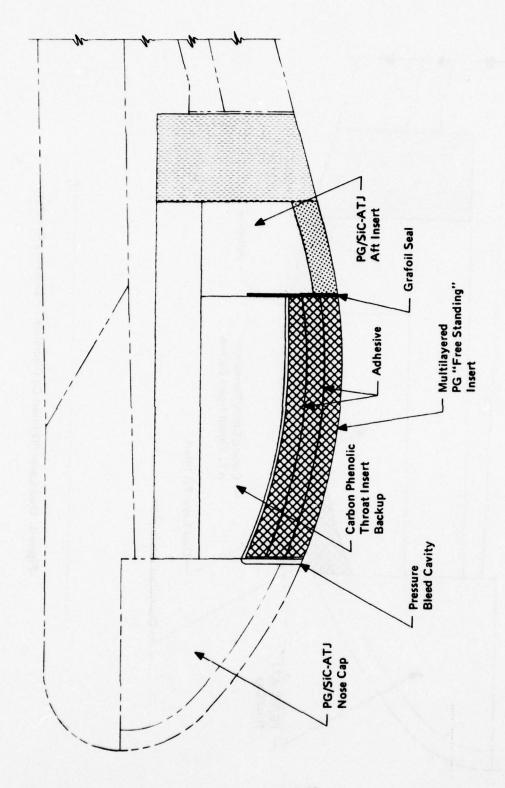


Figure 4. Multilayered Pressure-bleed PG Insert Concept - Preliminary Concept.

4.3 Assessment of Past Programs

Before presenting the details of the analyses of the selected design concepts, it is of interest to review briefly relevant past programs. In an effort to avoid the mistakes of the past, an assessment was made of previous a-b plane PG nozzle activities. In this, special attention was paid to the results and information available from the ARC 7.0-inch PG Program, [3] the Pfizer Bulk PG Program, [7] and the Marquardt Free-Standing Combustion Chamber Programs. [8,9,10,11,12]

This review then served as a guideline for an improved approach to the design and analysis of a-b plane PG throat inserts.

4.3.1 Atlantic Research Corporation 7.0-inch PG Program

During the course of the ARC 7.0-inch PG Program, [3] five nozzle firings were conducted. In each nozzle a throat insert comprised of an a-b plane PG coating on an AGSR graphite substrate was used. In each of the firings some failure of the PG coating occurred.

A thermostructural analysis of the PG/AGSR throat section was performed in the initial phase of that program. The analysis utilized the design methodology and material properties that were available at that time. In reviewing the analysis in reference to todays technology, several areas for improvements in the design approach and assumptions were identified. These are summarized below.

Pyrolytic Graphite Properties

The previous analysis used as property input an average set of Elastic Moduli and coefficients of linear expansion data obtained from test results with plate material. No attempt was made to distinguish data from CN and SN pyrolytic graphite. Strength data, except for a-b plane strengths, were based on very limited data. Tensile moduli were used throughout although the PG material is basically in a state of compressive stress during firing.

In the present program, the data available in the literature together with test data from SoRI was used to establish the significant properties required for a thermostructural analysis.

AGSR Properties

The properties of AGSR used in the analysis were based on very limited room temperature values. Strength data was almost nonexistent. Again tensile modulus was used. Subsequent testing of AGSR indicated a vastly different material behavior when loaded in compression instead of tension. This probably had a significant impact on the analysis results.

In the present program, the "free-standing" shell was taken as the primary design approach and no substrate is required, thus eliminating the questions relative to the properties of a substrate.

Analysis Technique

An elastic solution was used for determining the stresses and strains in the previous program. That resulted in an overestimation of the stresses in the problem and made failure predictions difficult since most calculated stress values were above the allowable properties published in the literature. For the case of PG coatings, the stresses imposed by mechanical loads are not insignificant by comparison with the thermal loads, making an assessment of failure on the basis of failure strains questionable as well. Therefore, the interpretation of the analysis results were made on a comparative basis with successful firings of nozzles having smaller throat diameters.

In the present program, the analyses were performed, taking the material nonlinearities into account using computer codes such as SAAS III. $^{[14]}$

Thermal Analysis

The previous analysis did not consider the affects of erosion or axial conduction into the substrate due to upstream and downstream components. Only radial conduction through the coating was considered and the local heating effects, which increase the substrate temperature, were not included in the structural analysis. In the present approach, both of these effects were accounted for. The details of the thermal analyses and the techniques used are presented in Section 6.2.

Cooldown Analysis

Throughout the previous program the deflection of the substrate at the OD due to residual stresses was underestimated by 50 percent. This was due to inaccurate material properties and probably due to some graphitization of the PG along with analysis oversimplification.

In the free-standing approach taken here, no substrate was used so that the conditions leading to residual stresses on cooldown were simplified. Residual stresses still occur even in the free-standing case. However, experimentally determined residual stresses were compared with analytical predictions as discussed in Section 6.3.3.

Buckling

The coating thicknesses used in the previous program were 60 mils or less. These were deposited on a very low modulus substrate which, in compression, could provide little structural support to the coating. Although stresses were similar to smaller diameter nozzles that performed successfully, failures occurred. No attempt was made to perform a stability analysis in the previous program. In the present program, much thicker coatings were considered. Also, a buckling analysis was performed to help identify and avoid the possibility of this type of failure. The results of this effort are presented in Section 6.3.5.

Conclusions

These results, together with a reevaluation of the test firing results of the previous program, [3] lead to the following conclusions:

- (1) Compressive failures of the coating occurred in all the test firings. The coatings in the first two firings also experienced massive delaminations due to poor microstructure and striations. Compressive type failures were confirmed by microphotographs of the failed coatings, the stress analysis performed, and by the fact the substrate experienced a reduction in OD after the test firing.
- (2) Several shortcomings in the analysis approach and material properties used were identified. However, the probable major contributor to the failures was an underestimation of the magnitude of compressive stresses resulting in the inadequate allowance for radial growth into the design. The conclusion is based on data that now shows the coefficient of linear expansion for the Atlantic Research PG to be twice that used in the original analysis and 1.5 times the average value found in the literature for continuously nucleated PG deposited at vacuum conditions.
- (3) There is a strong possibility that pressure bleeding to the backside of the substrate caused massive compressive failure for some cases.
- (4) In general, the basic incompatibility in thermal expansion characteristics between the AGSR and pyrolytic graphite causes compressive cooldown stresses in the coatings which are additive to the stresses induced during motor firing.

4.3.2 Marquardt Free-Standing Chamber Programs

Marquardt conducted a number of AFRPL and NASA-funded programs [8,9,10,11,12] over a period of years ranging from 1962 to 1968. These programs were aimed at the development of liquid rocket combustion chambers for long operational durations utilizing high temperature propellants.

Many tubes and chambers were fabricated with both substrate and continuously nucleated microstructures and with process interruptions. Some of the conclusions which resulted from these programs are:

- The highest rupture pressures of PG tubes tested were attained with a continuously nucleated microstructure.
- b. Continuously nucleated PG is the best type of microstructure for minimization of axial residual stresses in the throat region.
- c. This microstructure was not tested in firings because of an inability to control wall thickness in a limited number of furnace runs.
- d. PG tubes containing carefully controlled delaminations can currently be produced to carry about 1,000 psig internal pressure at room temperature.
- e. When developing new configurations, it is best to make short furnace runs to make thin deposits for the determination of axial variation of deposition rates.

As with all the other work performed on the development of PG rocket nozzle components, the thermal-structure analysis techniques were not adequate.

4.3.3 Pfizer Bulk PG Program

The results of this program indicated that large, thick, free-standing a-b plane PG parts could be fabricated. The size of the parts fabricated and tested in this effort were not adequate to allow the concept of interrupted deposition to be successfully demonstrated. In addition, property data and analytic techniques were not available to fully understand the rationale required to convert the concept to a viable design approach.

5.0 PYROLYTIC GRAPHITE PROPERTIES

5.1 Available Property Data

For the design analysis of a-b plane PG throats for nozzles, it is necessary to have available the thermal and mechanical properties for the material. The property data which exist in the literature were obtained over a number of years. The materials used in those test activities represent a very wide range of types of pyrolytic graphite materials which is not, in general, representative of the material produced in the program for throat inserts. Also, there is only limited data available on some of the properties. In only a few instances, have stress-strain curves been obtained. Described in Section 5.2 is the testing program which was conducted to fill in areas where existing data are incomplete or suspect and to verify which of the existing data is representative of the actual material being considered for the design.

A review of existing data was performed, and the following baseline properties were established for both SN and CN pyrolytic graphite type materials. Three types of properties are required. These are: (1) compliance properties required to predict stress and strain values in the material, (2) thermal properties to predict erosion and thermal gradients, and (3) uniaxial failure properties to allow the prediction of margins of safety.

The required properties for the stress and strain predictions are modulus of elasticity in tension and compression, shear modulus, Poisson's ratio, and coefficient of thermal expansion in both the a-b and c directions as a function of temperature. To perform nonlinear analysis, the stress-strain curves in each of the directions are also required. Table 1 shows the properties required and the source from which the properties were obtained. As can be seen, most of the data is from the TRW thermal stress response notebook. [15] The table also shows that, in some instances, no distinction between SN and CN properties is made. This occurs when the same reference page is given for both SN and CN materials. In reality, the only data in which a distinction between SN and CN material can be drawn are the modulus of elasticity and the thermal expansion characteristics.

As can be seen, no data for c direction tensile properties are available. This is due to the difficulty in obtaining a sufficient gauge length for PG in the c direction. In order to establish this property for analysis input, the constituent relationships of Poisson's ratios and the a-b direction modulus which is known are used to solve for the modulus in the c direction. That is:

$$E_c = \frac{vca}{vac} E_a$$

The above value is that to be used in the analysis.

Also, the c direction compressive data are only for room temperature conditions. An assumption has been made that the compressive modulus changes as a function of temperature proportionate to that of the a-b plane compressive modulus.

TABLE 1. MATERIAL PROPERTIES PYROLYTIC GRAPHITE.

			SN material	CN material
Мо	dulu	s of elasticity	nar pullates significances	
a-b	-	tension	Page IIIC-4 ^a	Page IIIC-7 ^a
a-b	-	compression	Fig. 4-7 ^b	Fig. 4-7 ^b
C	-	tension	Page IIIC-4 ^a	Page IIIC-7 ^a
c	-	compression	12-3-1 ^c	12-3-1 ^c
Shear Modulus		odulus	Page IIIC-9 ^a	Page IIIC-9 ^a
Poisson's Ratio			Page IIIC-10 ^a	Page IIIC-10a
The	ermal	Expansion		
a-b			Page IIIC-5 ^a	Page IIIC-8 ^a
c			Page IIIC-5 ^a	Page IIIC-8 ^a
Stre	ss-St	rain Curves		
a-b	_	tension	Page IIIC-3 ^a	Page IIIC-6a
a-b	-	compression	Fig. 4-9 ^b	Fig. 4-9b
c	-	tension	No Data	No Data
c	-	compressions	12-3-1 ^c	12-3-1 ^c

^a Thermal stress response notebook, TRW, 10 January 1975.^[15]

^bPyrolytic Graphite Final Report, Volume I, Lockheed Missiles & Space Company, 1 June 1962.^[16]

^cPyrolytic Graphite Engineering Handbook, General Electric, September 1964.[17]

The next set of properties required are the thermal properties. Table 2 shows the thermal properties presently being used for ATJ, PG/SiC, and pyrolytic graphite. The ATJ properties were obtained from SoRI. The PG/SiC properties were those obtained in the Scale-up Program with the thermal conductivity data being that backed out of the TRW thermal stress test data. The SiC content is 15 percent. The pyrolytic graphite properties are those obtained from the TRW notebook.

Finally, a set of strength properties are required. Tables 3 and 4 show the strength properties for the SN and CN materials. Since the data for PG have some scatter, both a set of minimum strength properties and average strength properties have been constructed. Factors of safety will be calculated based on both the minimum and average properties.

The minimum strengths for the SN and CN materials are the same since they represent a lower bound for all test results. The minimum tensile values were obtained from the TRW notebook, page II-14. The minimum shear and compressive properties were obtained from Reference 17 shown on Table 1.

The average set of strength properties was taken from work published by Gebhardt and Berry. [18]

The results represent at least five tests at each of the individual test temperatures. From these data the effect of the different strengths of SN and CN materials can be evaluated.

5.2 Testing Program

5.2.1 Data Required for Analysis

Thermal and mechanical properties of pyrolytic graphite material have been reported in the literature. However, much of these data were obtained from test results on plate-type pyrolytic graphite. The data exhibit a large amount of "scatter" due to both the method of testing and the varied processes used to manufacture the material. The material property testing performed in this program was performed to obtain certain pertinent material properties for the pyrolytic graphite material manufactured by the Pfizer Corporation intended for use in this program. To this end, the processing parameters, configuration, and test methods were defined to the point that the test results are representative of the material actually used to manufacture components. The individual test specimens were machined from a 7.0-inch-diameter tube, approximately 6 inches long and having a nominal 0.20 inch wall thickness.

For the analysis of axisymmetric bodies of revolution, comprised of an anisotropic material, the elastic constants required for an analysis are shown below in the form of the stress-strain relationships.

TABLE 2. THERMAL PROPERTIES.

	Temperature	Density	СР	CONDUC (10 ⁻² Btu/		
Material	(°R)	(lb/ft ³)	(Btu/lb-°R)	ab*	c**	Emissivity
	460	136.5	0.200	5.64	0.0432	0.850
	1460	136.5	0.380	3.84	0.0252	0.850
Pyrolytic	2460	136.5	0.450	2.40	0.0192	0.850
Graphite	3460	136.5	0.530	1.50	0.0228	0.850
	4460	136.5	0.540	1.20	0.0288	0.850
	6460	136.5	0.560	1.18	0.0450	0.850
	529	146.9	0.160	3.59	0.528	0.850
	960	146.9	0.312	2.77	0.440	0.850
	1460	146.9	0.370	2.22	0.343	0.850
	1960	146.9	0.404	1.81	0.259	0.850
	2460	146.9	0.430	1.62	0.174	0.850
PG/SiC (15%)	2960	146.9	0.450	1.38	0.124	0.850
(1370)	3460	146.9	0.470	1.14	0.132	0.850
	4460	146.9	0.480	0.90	0.151	0.850
	4960	146.9	0.480	0.90	0.151	0.850
	7960	146.9	0.480	0.90	0.151	0.850
	460	109.0	0.283	1.57	2.080	0.850
	960	109.0	0.340	1.18	1.610	0.850
	1460	109.0	0.390	0.938	1.230	0.850
	1960	109.0	0.430	0.759	0.968	0.850
ATJ Graphite	2460	109.0	0.462	0.632	0.799	0.850
Grapinte	3460	109.0	0.505	0.509	0.646	0.850
	4460	109.0	0.521	0.470	0.579	0.850
	5460	109.0	0.525	0.456	0.539	0.850
	6460	109.0	0.525	0.444	0.532	0.850

^{*}ACROSS GRAIN CONDUCTIVITY FOR ATJ GRAPHITE

^{**}WITH GRAIN CONDUCTIVITY FOR ATJ GRAPHITE

TABLE 3. SUBSTRATE NUCLEATED PG.

Stress allowable (psi)

Temperature		(ps	si)		STATE OF THE STATE OF
Property	Tens	ile	Compr	ession	Shear allowable
condition	a-b	С	a-b	С	(psi)
68°					
Minimum	10000.0	420.0	10000.0	42000.0	525.0
Average	18191.0	750.0	11000.0 🛬	50000.0	1522.0
2000°					
Minimum	10500.0	175.0	10250.0	50000.0	525.0
Average	17555.0	312.0	11275.0	55000.0	1448.0
3000°					
Minimum	12000.0	100.0	10500.0	60000.0	525.0
Average	16919.0	178.0	11550,0	65000.0	1374.0
4000°					
Minimum	15000.0	90.0	110,70.0	60000.0	525.0
Average	22095.0	161.0	12100.0	65000.0	1469.0
5000°					
Minimum	23000.0	400.0	7500.0	60000.0	525.0
Average	50525.0	714.0	8250.0	65000.0	1620.0
•					

TABLE 4. CONTINUOUSLY NUCLEATED PG.

Stress allowable

Temperature		(p:	si)		Shear
Property	Ten	sile	Compre	ssion	allowable
condition	a-b	С	a-b	С	(psi)
68°					
Minimum	10000.0	420.0	10000.0	42000.0	525.0
Average	17818.0	750.0	14500.0	50000.0	2578.0
2000°					
Minimum	10500.0	175.0	10250.0	50000.0	525.0
Average	18153.0	312.0	14862.0	55000.0	2615.0
3000°					
Minimum	12000.0	100.0	10500.0	60000.0	525.0
Average	18488.0	178.0	15225.0	65000.0	2652.0

11000.0

15950.0

7500.0

10875.0

60000.0

65000.0

60000.0

65000.0

525.0

525.0

3155.0

3135.0

90.0

161.0

400.0

714.0

4000° Minimum

Average

Minimum

Average

5000°

15000.0

27525.0

23000.0

55275.0

$$\begin{cases} \epsilon_{\mathsf{r}} \\ \epsilon_{\theta} \\ \epsilon_{\mathsf{z}} \\ \gamma_{\mathsf{rz}} \end{cases} = \begin{bmatrix} 1/\mathsf{E}_{\mathsf{r}} & -\nu_{\mathsf{r}\theta}/\mathsf{E}_{\theta} & -\nu_{\mathsf{r}\mathsf{z}}/\mathsf{E}_{\mathsf{z}} & 0 \\ -\nu_{\theta\mathsf{r}}/\mathsf{E}_{\mathsf{r}} & 1/\mathsf{E}_{\theta} & -\nu_{\theta\mathsf{z}}/\mathsf{E}_{\mathsf{z}} & 0 \\ -\nu_{\mathsf{z}\mathsf{r}}/\mathsf{E}_{\mathsf{r}} & -\nu_{\mathsf{z}\theta}/\mathsf{E}_{\theta} & 1/\mathsf{E}_{\mathsf{z}} & 0 \\ 0 & 0 & 0 & 1/\mathsf{G}_{\mathsf{r}\mathsf{z}} \end{bmatrix} \begin{bmatrix} \sigma_{\mathsf{r}} \\ \sigma_{\theta} \\ \sigma_{\mathsf{z}} \\ \tau_{\mathsf{r}\mathsf{z}} \end{pmatrix} + \begin{bmatrix} \alpha_{\mathsf{r}}\mathsf{T} \\ \alpha_{\theta}\mathsf{T} \\ \sigma_{\mathsf{z}} \\ \tau_{\mathsf{r}\mathsf{z}} \end{bmatrix}$$

As shown, there are seven independent elastic constants when one realizes that

$$\frac{\nu_{r\theta}}{E_{\theta}} = \frac{\nu_{\theta r}}{E_{r}}, \frac{\nu_{rz}}{E_{z}} = \frac{\nu_{zr}}{E_{r}}, \text{ and } \frac{\nu_{\theta z}}{E_{z}} = \frac{\nu_{z\theta}}{E_{\theta}}$$

and three thermal expansion terms. For pyrolytic graphite, there is a transversely isotropic plane, and the elastic constants reduce to five, the thermal expansion coefficients to two. These are two elastic moduli, two Poisson's ratios, and one shear modulus. These material properties must be evaluated for the temperature range 70 to $6,000^{\circ}$ F over which the material is to be utilized. In addition, the material exhibits different properties for tension and compression loading.

Stress-strain curves for the pyrolytic graphite exhibit a degree of nonlinearity, especially at the higher temperatures. Because of this, entire stress-strain curves are required to perform an analysis. Also testing of the materials under multiaxial stress fields is required to establish interaction constants for both yield and failure criteria. Uniaxial and biaxial strength values are required.

The evaluation and determination of properties over the entire temperature range and in both material property directions is beyond the scope of this program. In fact, testing techniques for the evaluation of c direction tensile properties in relatively thin coatings where gauge lengths are necessarily very small are essentially nonexistent. Multiaxial testing techniques are very expensive, if even available. For most such tests, testing techniques would need to be developed.

Therefore, the testing performed was limited to obtaining properties which have considerable influence on the calculated stress and strain states and are determinable by relatively straightforward testing techniques. Sufficient tests were performed to establish representative material properties over the temperature range of interest in each of the material property directions. Elastic modulus, stress-strain curves and uniaxial strain and stress allowables for both tension and compression loading were measured at a number of temperatures. Shear modulus, Poisson's ratio, shear strength, and c direction compressive strength were measured at ambient temperature conditions. Coefficients of linear expansion were determined in both the a-b and c directions over a temperature range of 70 to 5,000°F.

The scope of testing performed is shown in the following section and is adequate to characterize the material to determine whether it is more like existing data for CN or SN type materials. With this measured data and the available data from the literature, the properties are available to provide a basis for an engineering judgement on the degree of structural success expected for the a-b plane insert.

5.2.2 Testing Accomplished

Based on the need for certain critical properties identified in previous analyses, cost effectiveness, and the availability of testing techniques, a material property testing plan was established. Southern Research Institute performed the detailed testing. Table 5 shows the test matrix for the testing at Southern Research Institute.

As shown, tension and compression properties in the a-b plane, coefficient of thermal expansion in both the a-b and c planes and shear strengths and shear modulus were obtained. These properties have all been shown to have a strong influence on stress and strain states and resulting failure of a-b plane pyrolytic graphite components.

5.2.3 Summary of Test Data

The evaluation matrix presented in Table 6 represents the experiments actually performed for property determination. This is slightly different from the specification in the original test matrix presented in the previous section. Three interlaminar shear evaluations at 1,500°F and two at 3,500°F were added to the matrix, and three tensile tests were deleted. The additional shear tests were performed to resolve the ambiguity in the results obtained from tests performed on specimens with two different gage lengths. This will be discussed later. The five additional shear specimens were made from the deleted tensile specimens.

A detailed presentation of the cutting patterns and testing techniques are presented in Appendix A, Southern Research Institute's Letter Report to Atlantic Research. A summary of the data obtained is presented here.

The nomenclature adopted for this program assigns the material a-direction parallel to the cylinder axis (z), the b-direction as circumferential (θ) and the c-direction as radial (r). Since the material properties are considered to be the same in the a and b directions and the evaluation of circumferential specimens will present unique specimen problems, all a-b specimens were taken with the test direction along the a (z) axis. For shear modulus, determinations were made for $G_{\theta z}$ and $G_{rz} = G_{r\theta}$. For axisymmetric problems, the shear modulus required for analysis is G_{rz} .

Figure 5 shows the data obtained for the tensile modulus in the a-b direction. Test data are shown at two temperatures, 70 and 3.500° F. Average values for modulus are 3.36×10^{6} psi at 70° F and 4.49×10^{6} psi at 3.500° F.

TABLE 5. PRE-TEST PG CYLINDER EVALUATION MATRIX.

Evaluation		Tempera	ture in °F	
type	RT	1500	3500	5000
Compression — a-b	2		2	2
Compression — c	3	_	_	-
Tension — a-b	3	_	3	3
Unit Thermal Expansion — a-b ^a	2	2	2	2
Unit Thermal Expansion — c ^a	2	2	2	2
Shear Strength Interlaminar	3	_	3	3
Shear Modulus	3	_		E -

TABLE 6. ACTUAL PG CYLINDER EVALUATION MATRIX.

Evaluation		Tempera	ture in °F	
type	RT	1500	3500	5000
Compression — a-b	2		2	2
Compression — c	3	_		-
Tension — a-b	3	ngati May Androne I	3	-
Unit Thermal Expansion — a-b ^a	2	2	2	2
Unit Thermal Expansion — c ^a	2	2 10 2	Haray 2 minist	2
Shear Strength Interlaminar	3	3	5	3
Shear Modulus	3	_	_	-

^aUnit thermal expansion measurements were conducted twice on these specimens to evaluate the effects of a repeated thermal cycle.

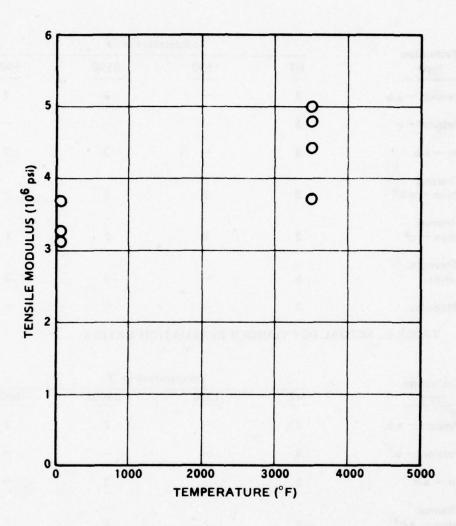


Figure 5. Tensile Modulus for Pyrolytic Graphite, a-b Plane.

Figure 6 shows the a-b direction tensile strength data results. Substantial scatter in the data is apparent and is probably due to three factors. First the tensile specimens had some longitudinal curvature (a bow of approximately 0.017 inch at the middle of the specimen length). Secondly, expansion mismatch between extensometer attachments, and the specimens appeared to cause stress concentrations resulting in specimen failure in these regions. Finally at room temperature, pyrolytic graphite nodule size seemed to influence failure strength since the two lowest strength values were obtained from specimens that fractured near larger than average nodules.

The tensile strength results, therefore, indicate that test methods need to be improved and that strength results at low temperatures may exhibit large data scatter depending on surface roughness and individual nodule sizes.

Figures 7 and 8 show the test results for compressive modulus and compressive strength. These results show that the two data points at each temperature correlate well with little scatter.

Table 7 shows the shear modulus values obtained. Both plate and tension specimens were used to determine these values. A detailed discussion of the tests and theoretical development used to obtain these values are presented in Appendix A.

Figures 9 and 10 show the results of the thermal expansion experiments. The two cycles refer to first performing thermal expansion evaluations from room temperature to 5,000°F, allowing the specimens to cool to room temperature and performing the same evaluations during a second exposure from room temperature to 5,000°F. The purpose of the two tests is to evaluate to some extent the effect of "reordering" of the pyrolytic graphite at temperatures above the deposition temperature. The "reordering" phenomenon has been recognized on other programs involving thermal expansion measurements on pyrolytic graphite and is shown graphically in the values obtained in Figures 9 and 10. Above 3,500 to 4,000°F permanent growth in the a-b plane and contraction in the c plane occur. These growths and contractions are shown to be both time and temperature dependent. For analysis purposes, especially for cooldown analyses, the second cycle data are expected to be more representative of the material behavior since times in a nozzle firing (60 seconds maximum) are much less than the time at temperature used in thermal expansion laboratory testing.

The final data results to be reported are the shear strength data. These data are probably the most difficult to interpret due to the vastly different results obtained using two different specimen configurations. Figures 11 and 12 show the specimen configuration used to measure shear strength. This specimen configuration has been used by SoRI in the past to evaluate carbon/carbon materials. The specimen is loading in compression, and the shear strength is determined by dividing the total load by the gage length area. As shown in the two figures, the only difference in the two specimens was the gage lengths — 0.25 inch long and 0.50 inch long.

Figure 13 shows the results of the tests, shear strength versus temperature. The results obtained with an 0.50-inch gage length specimen are represented by open circles while the 0.25-inch gage length specimen results are represented by solid circles. As shown at 3,500°F, the 0.5-inch gage length results are less than the 0.25-inch results. At 70 and 1,500°F the 0.5-inch gage length results are also lower than was expected. At 5,000°F the test data using the 0.25 gage length is more nearly what was anticipated. One data point was not included in the figure. This was a

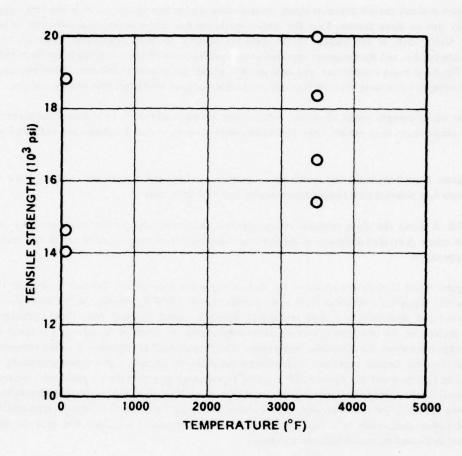


Figure 6. Tensile Strength for Pyrolytic Graphite, a-b Plane.

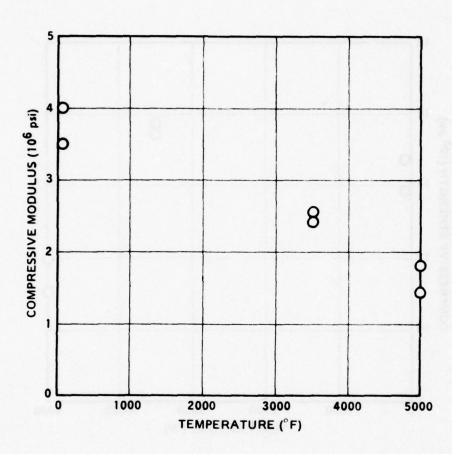


Figure 7. Compressive Modulus for Pyrolytic Graphite, a-b Plane.

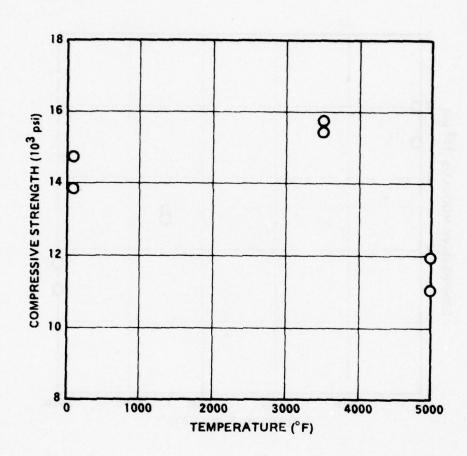


Figure 8. Compressive Strength for Pyrolytic Graphite, a-b Plane.

TABLE 7. RESULTS OF TORSION AND SHEAR MODULUS PLATE EVALUATIONS.

Load direction	Temperature (°F)	Specimen number	Bulk density gm/cm ³	Initial elastic modulus 10 ⁶ psi
$G_{ hetaZ}$	70	SM (P)-1	2.2194	2.02
$G_{\theta Z}$	70	SM (P)-2	2.1987	1.84
G _{RZ}	70	SM-1A	2.2122	0.19
G _{RZ}	70	SM-2A	2.2048	0.18
G _{RZ}	70	SM-4A	2.2093	0.21

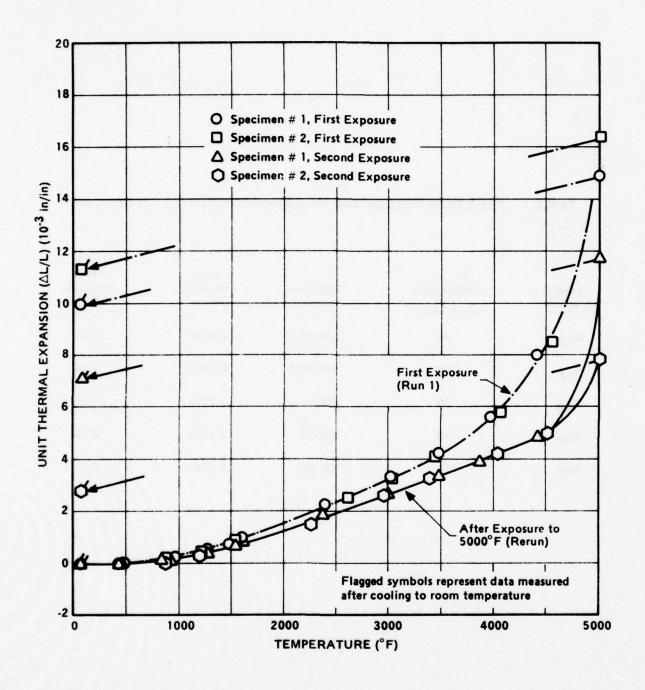


Figure 9. Unit Thermal Expansion for Pyrolytic Graphite, a-b Plane.

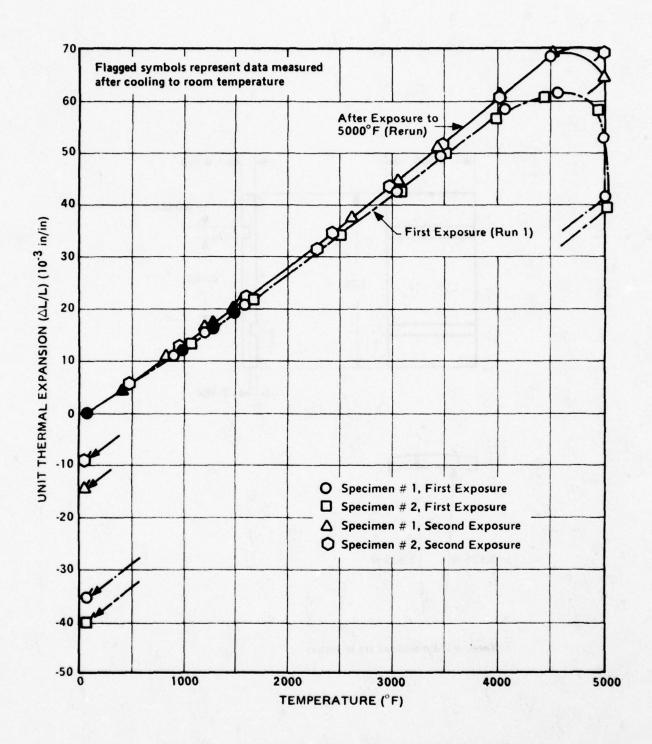
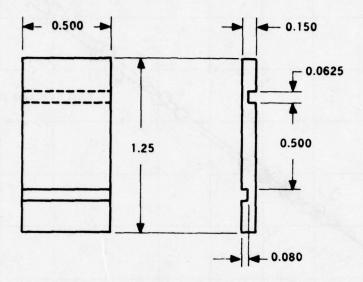
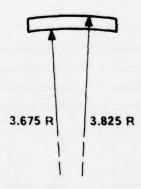


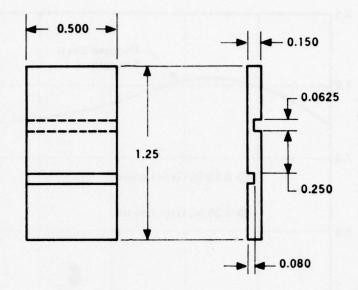
Figure 10. Unit Thermal Expansion for Pyrolytic Graphite, C-direction.

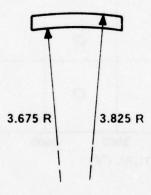




Note: All dimensions are in inches

Figure 11. Interlaminar Shear Strength Test Specimen for Pyrolytic Graphite, 0.5 inch Gage Section.





Note: All dimensions are in inches

Figure 12. Interlaminar Shear Strength Test Specimen for Pyrolytic Graphite, 0.25 inch Gage Section.

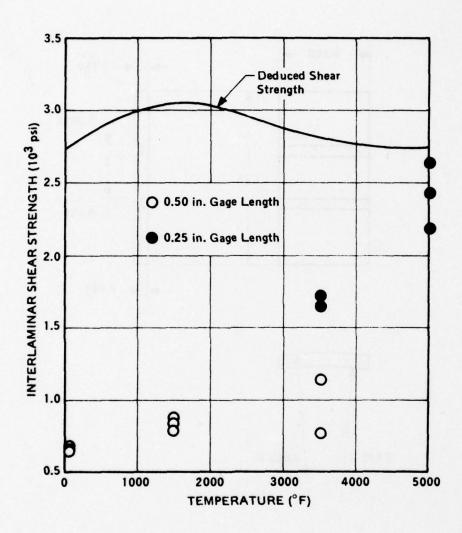


Figure 13. Test Results for Interlaminar Shear Strength of Pyrolytic Graphite.

shear strength value of 640 psi at 3,500°F obtained using an 0.25-inch gage length specimen. Since this data point was completely out of line in reference to all the other data points and to the analysis that follows, it represents a "bad" test and should not be included.

To understand the effect of gage length on the stress results, a finite element structural analysis of the test sample when subjected to a 100-pound load was performed. The TEXGAP computer code was used, and the finite element nodal network used is shown in Figure 14. The analysis was performed using room temperature properties for the pyrolytic graphite. Figure 15 shows the stress distribution along the gage length of the slotted specimen. As shown, a stress concentration occurs near the inside corners of the specimens and results in peak stress value of 2,070 psi for the 0.25-inch gage length specimen and 1,700 psi for the 0.5-inch gage length specimen. Using the average stresses of 800 psi for the 0.25-inch specimen and 400 psi for the 0.5-inch specimen, the stress concentrations are:

$$K_{0.25} = 2.59$$

$$K_{0.50} = 4.25$$

Hence the results indicate that the stress concentration factor for the 0.25-inch specimen is far less than the 0.5-inch specimen. Therefore, if failure occurs due to a maximum stress condition (which is probably true for PG at low temperatures), the 0.5-inch specimen will result in lower apparent shear allowables. As the material is raised in temperature, the stress concentration factor is reduced due to lower stiffness properties and nonlinear effects, although detailed nonlinear analyses should be performed at the higher test temperatures to fully evaluate these effects. This was beyond the scope of the present program. Instead, the assumption was made that the strain at the inner corners remained approximately the same as a function of test temperature but that the stress concentration was reduced due to reduced materials properties at temperature. With this assumption, the shear stress values obtained directly from the test results were increased based on the stress concentration factors determined for each of the test temperatures. These results are represented by the solid line shown on Figure 13. These results compare well with the shear strength values reported in Section 5.2.1 for CN type PG material. In addition, by the use of concentration factors, the seemingly large difference in the test results obtained at 3.500°F for the two gage length specimens is eliminated. The average shear value for the two 0.5-inch specimens tests becomes 2,677 psi and, for the 0.25-inch specimen, the average value is 2,898 psi. Before applying concentration factor, the two values were 1,685 psi and 960 psi, respectively.

Thus, it is postulated that the actual shear strength values for the PG tested are best represented by the solid line shown on Figure 13. It is recommended that further study of stress concentration effects in these specimens be performed and that a redesign of the specimen be performed to minimize stress concentration effects. The entire subject of specimen design should be evaluated with detailed analysis of the specimen in question.

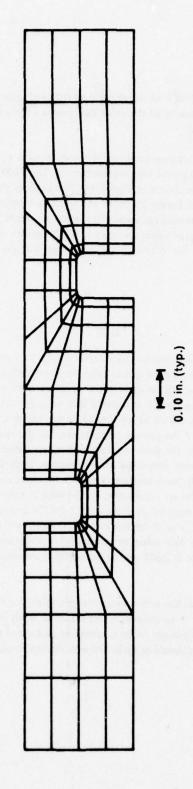


Figure 14. Finite Element Mesh for Shear Strength Test Specimen.

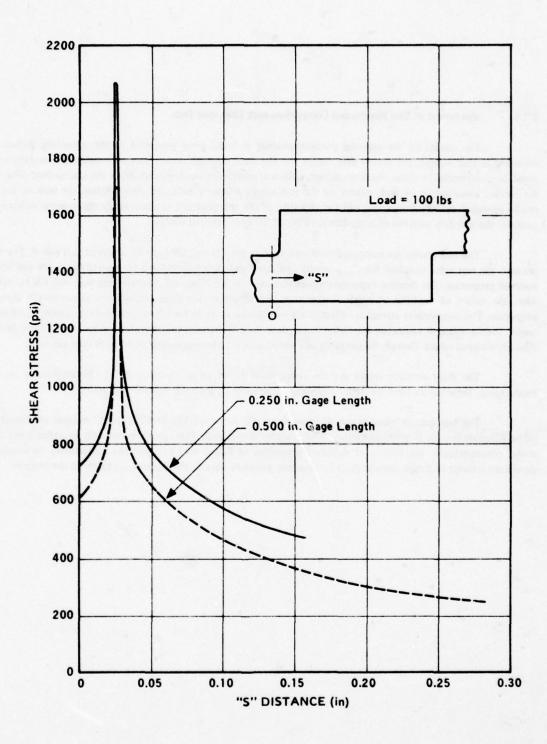


Figure 15. Stress Distribution in Shear Strength Test Specimen.

5.2.4 Assessment of Test Results and Comparison with Literature Data

The results of the material property testing at SoRI were presented in the preceding section. As discussed in that section, the tensile data results and the shear strength results showed considerable scatter, which could be contributed to either specimen design, effects of nodules at low temperature, or the test method. The need for further investigation of such effects on the test results is clearly indicated. Nevertheless, the bulk of the test results provided useful information, and the objective of the test program to characterize the material at hand and compare the test data with the existing data for CN and SN type material was met.

The test results are compared to literature data for CN and SN type PG material in Table 8. The table presents the test value obtained for the property evaluated and values considered representative of CN and SN PG material properties. The thermal expansion values obtained for the Pfizer PG compare very well with CN PG values. Also, the values of modulus at room temperature and values of the shear strength are closer to CN than SN properties. The compressive strengths obtained are very similar to those for CN material over the entire temperature range. Tensile strength values are somewhat lower than the CN material values; yet, they are more nearly like CN than SN material values. Overall, the property test values appear to be representative of a CN type material.

The shear strength values and the compressive strain values obtained for the Pfizer material are very encouraging. These values meet the design requirements defined by the analysis work that follows.

The test data obtained in this program along with literature data for CN-type PG material are considered to be adequate for use in performing the detail analyses that follow. This approach not only provided a means to study, parametrically, the effects of different properties of PG; it also provided the opportunity to conduct a significant amount of design analysis prior to obtaining property data on the PG produced later in the program.

TABLE 8. COMPARISON OF TEST RESULTS WITH LITERATURE DATA.

		FR			1500			3500			2000	
Property evaluated	Test ^a value	CN	SN material	Testa	CN	SN material	Test ^a value	CN	SN material	Testa	CN material	SN material
28/8 - a-b (in/in)	i	1	•	900000	0.0008		0.0034		0.0018	0.0058	9000	0.0033
DR/k - c (in/in)	ı	1	1	0.020	0.020		0.052		0.051	0.070	0.068	0.077
E _T · a-b (psi X 10 ⁻⁶)	3.35	3.45	4.4	i	1		4.49		3.4	1	1	1
E _C · a-b (psi X 10-6)	3.75	NA A	A N	1			2.52		ď	1.62	ď Z	ď
G - a-b, c (psi X 10-6)	0.19	0.20 ^b	0.20 ^b	i	1	ı	,	ı	1	1	1	1
Fs - a-b, c (psi)	2725 ^c	2578	1522	3000°	2605		2850 ^c		1421	2750 ^c	3155	1620
F _T · a-b (psi)	15,800	17,818	18,191	1	1		17,600		19,507	1	ı	1
F _C · a-b (psi)	14,250	14,500	11,000	ì		ı	15,600		11,800	11,550	10,875	8250
F _C · c (psi)	74,900	20,000	20,000	i	1	t	1		1	1	1	1
(%) q-e - 1 ₉	0.46	0.48	0.44	i	,	•	0.5	0.53	0.75	1	1	i
(%) q-e · Э _э	0.52	0.42 ^b	0.42 ^b	i seles	ı		0.70	ď Z	A N	71.35	ď Z	Š

^aTest values represent average of tests.

^bTypical values in literature.

Corrected shear values — see Section 5.2.3. NA - not available.

6.0 DESIGN ANALYSIS

6.1 Introduction

Before presenting the analytical results, a brief discussion of the analysis plan and objectives is presented here to provide a better understanding of the rationale for the specific analysis tasks that follow.

The program objectives included a series of nozzle tests with nozzle firing durations of 15, 30 and 60 seconds. In Section 4.0, two approaches selected for the a-b plane pyrolytic graphite insert design were presented. These were a dual-layer design consisting of two 0.30-inch-thick layers of pyrolytic graphite and a single layer design which included only one 0.30-inch-thick pyrolytic graphite layer.

As pointed out in the material property section, pyrolytic graphite materials exhibit quite varied properties depending on the process conditions and the type of pyrolytic graphite produced (substrate nucleated, SN, or continuously nucleated, CN). Since representative properties for the Pfizer produced pyrolytic graphite would not be available until later in the program, a representative set of CN and SN properties were obtained from the literature to use in the ensuing analyses.

One of the parameters that was studied is the thermal boundary condition. Thermal analyses have been performed for the following boundary conditions.

- Insert Only, IO Axial conduction from upstream and downstream components is assumed to be zero.
- Nozzle Assembly, NA The entire nozzle assembly is modeled into the thermal analysis, thus allowing conduction from upstream and downstream components.
- c. Nozzle Assembly with Front Edge Heating, NAFE Additional heating from the exposed forward edge is allowed as the upstream component erodes away.

Figure 16 shows a typical design configuration for the a-b plane pyrolytic graphite insert nozzle design. The baseline design includes an insert which is 4.40 inches long. The figure also shows an insert which is extended forward and aft of the baseline length. Residual stresses for larger inserts were determined through analysis since erosion and/or thermal effects may indicate that inserts which extend over a larger area ratio range could be beneficial.

The analysis approach included the following activities:

a. Determine an erosion profile for the nozzle contour for 15, 30 and 60 seconds with upstream and downstream components consisting of ATJ, PG/SiC, carbon/carbon and a-b plane pyrolytic graphite materials.

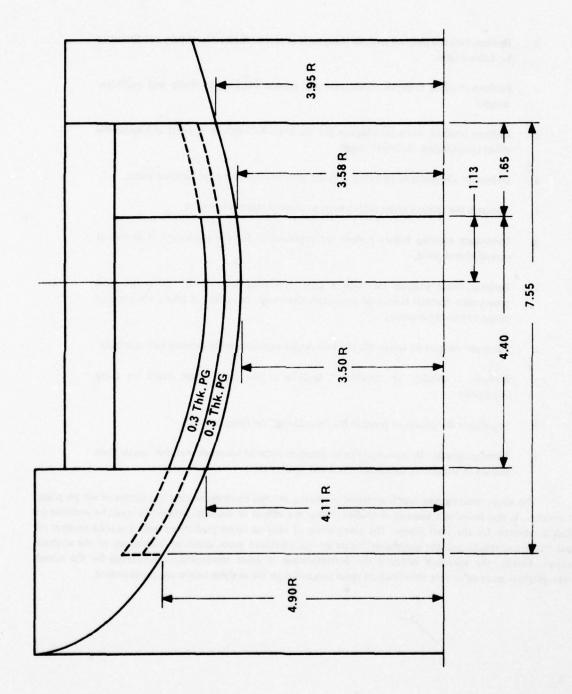


Figure 16. Preliminary A-B Plane Nozzle Insert Configuration.

- b. Perform detailed thermal analysis using each of several thermal boundary conditions to be defined later.
- Perform detailed in-depth conduction and erosion analyses for single- and dual-layer designs.
- d. Perform residual stress calculations for the basic 4.40-inch-long insert and assess the effect of extending the insert length.
- e. Determine the effect of pyrolytic graphite properties on the residual stress states.
- f. Compare the residual stress calculations to residual stress test results.
- g. Investigate existing failure criteria for applicability for the prediction of failure of manufactured parts.
- h. Perform firing analysis for both a dual- and single-layer design using the most appropriate thermal boundary condition. Determine the effect of SN or CN material properties on these results.
- i. Calculate margins of safety for the two design concepts using existing failure criteria.
- Perform a stability or "buckling" analysis of the final design based on firing conditions.
- k. Investigate the effects of possible PG "reordering" on firing stresses.
- When properties for actual pyrolytic graphite material becomes available, assess their impact on previously calculated stress and strain states.

The above analysis plan was formulated to allow a detailed thermostructural assessment of the a-b plane insert concept. It also includes a number of studies so that the effects of essential parameters could be available to establish a rationale for the final design. The comparison of residual stress predictions with a limited number of residual stress test results and the success or failure of manufactured parts allows an assessment of the analysis techniques. Finally, the approach included the determination of some representative properties for the actual pyrolytic graphite material so that the effects of these properties on the analysis results can be quantized.

6.2 Thermal – Erosion Studies

6.2.1 Analysis Techniques

The thermal-erosion prediction techniques used in the following analyses can be summarized by the flow chart shown in Figure 17. The specific areas shown in the chart are a flow field analysis, boundary layer and heat (mass) transfer coefficient analysis, determination of radiation heat fluxes, surface thermochemistry analysis, and an in-depth conduction analysis.

The flow field analysis is performed by using the Atlantic Research in-house Transport Properties Program. The essential output is Mach number versus nozzle station.

The next step is to determine a boundary layer solution for evaluating the heat transfer coefficient distribution throughout the nozzle. The analysis is performed using the TBL computer program (momentum integral technique) defined in Reference 19.

The radiation heat input is in the form of a single gas emissivity. The method of obtaining the total emissivity of an aluminum oxide particle cloud is described in Reference 20, which reports the work performed by Price of Philco-Ford. Basically, the emissivity is shown to be a function of the amount of aluminum oxide, the gas molecular weight, gas temperature, and the local diameter.

The GASKET computer code, Reference 21, is used to provide the necessary thermochemistry and is a program in which the chemical reaction rate for CO₂, H₂O, and H₂ combining with the surface carbon are kinetically controlled. The dimensionless mass removal rate for carbon materials is obtained as a function of temperature from the input of propellant exhaust specie data. This program provides the necessary input for the two dimensional erosion computer code, ASTHMA 3, Reference 22.

Briefly, ASTHMA 3 is an axisymmetric transient heating and materials ablation program. It solves for the thermal response of two-dimensional shapes including variations in local surface regression.

The above methodology and technical approach has given meaningful thermal results for use in the ensuing thermal-structural analyses.

6.2.2 Thermal Properties

A thorough discussion and presentation of pyrolytic graphite properties are presented in Section 5.0. In this section, the thermal properties for PG/SiC and ATJ graphite used to analyze upstream and downstream nozzle components are presented.

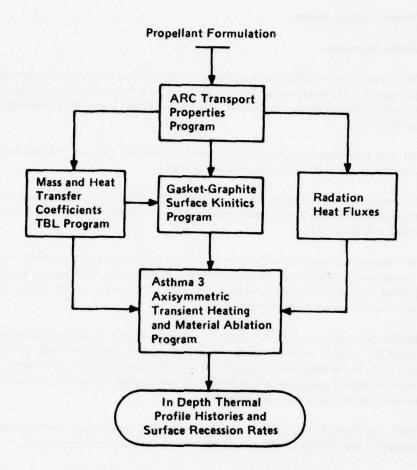


Figure 17. Thermal/Erosion Analysis Flow Chart.

The thermal properties for the PG/SiC material are shown in Figures 18 and 19.

The thermal conductivity in the c direction is shown in Figure 18 versus temperature and SiC content. This parameter has been defined by using the TRW thermal stress testing data. Thermocouple data was obtained for coatings having 6, 9 and 15 percent SiC. An inverse thermal analysis was used to predict the thermal conductivity based on the thermal gradients which existed in the coating. This technique is described in Reference 23. Hence the c direction thermal conductivity has good experimental validation. The thermal conductivity in the a-b direction is shown in Figure 19. The specific heat was taken to be similar to that for pure PG. The density was based on the following formula as a function of SiC content.

$$\rho_{\text{coating}} = \psi \left(\frac{\rho_{\text{PG}}}{\psi - \% \, \text{SiC}} \right)$$

where

 $\rho_{PG} = 2.14 \text{ g/cc}$

 $\psi = 300$ (Experimental Coefficient)

The above formula has been validated by ashing techniques over the range of 10 to 30 percent SiC. It was assumed that variations in density with temperature are small.

Figures 20 through 22 show the thermal properties used for ATJ graphite. The with- and across-grain thermal conductivities are shown in Figures 20 and 21. The specific heat versus temperature is shown in Figure 22.

6.2.3 Boundary Conditions

To perform the in-depth thermal analysis, the boundary conditions must be stipulated. These boundary conditions include convective heat transfer coefficient, radiation flux, surface thermochemistry, and boundary conditions between individual nozzle components. The calculation of transfer coefficients are presented in Section 6.3.4.

For the radiation boundary condition, a gray body model was used. The radiation flux is then given by

$$Q_{rad} = \epsilon_s \sigma T_s^4 - \epsilon_w \sigma T_w^4$$

where

 $\epsilon_{\rm e}$ = stream emissivity

 $\epsilon_{\mathbf{w}}$ = wall emissivity

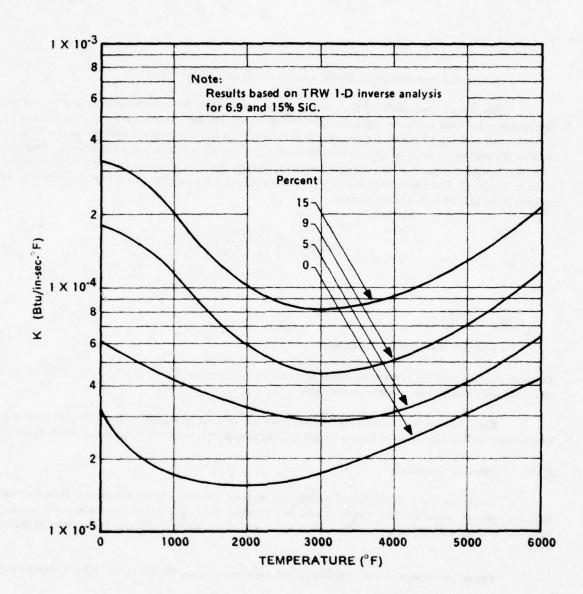


Figure 18. C-Direction Thermal Conductivity for PG/SiC.

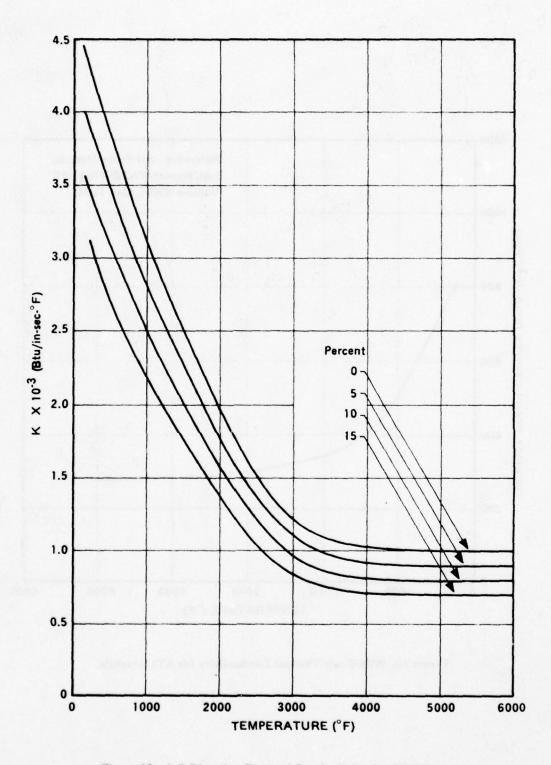


Figure 19. A-B Direction Thermal Conductivity for PG/SiC.

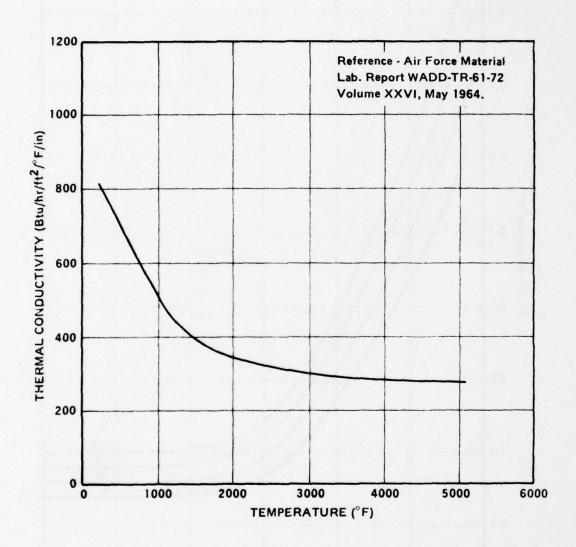


Figure 20. With-Grain Thermal Conductivity for ATJ Graphite.

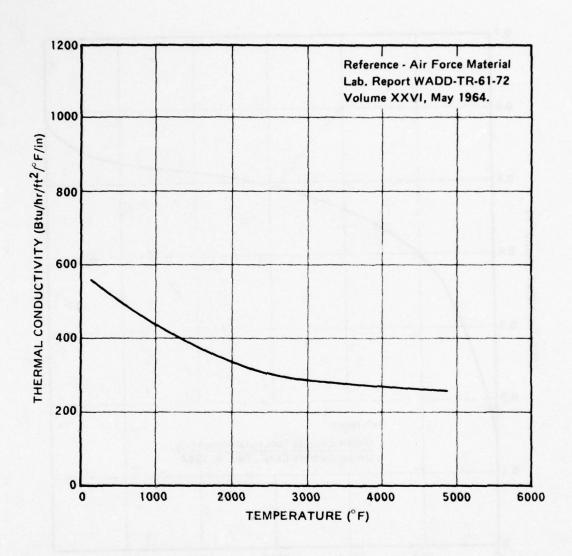


Figure 21. Across-Grain Thermal Conductivity for ATJ Graphite.

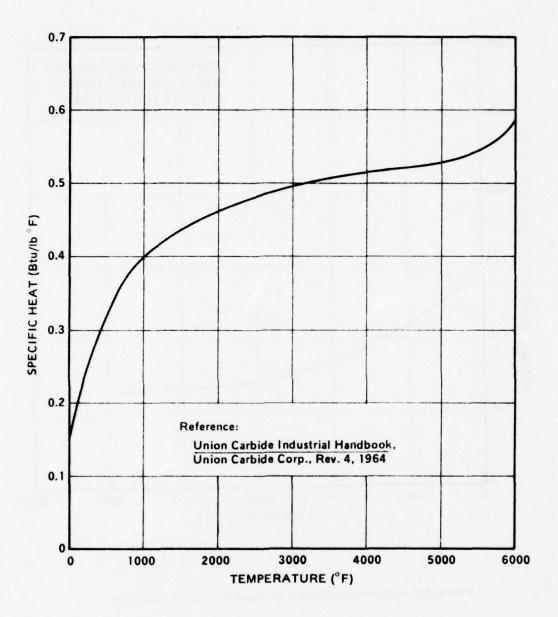


Figure 22. Specific Heat for ATJ Graphite.

 σ = Stefan-Boltzman constant

 $T_e = Free-stream temperature$

 $T_w = Wall temperature$

The particle laden stream emissivity is determined using the work of Price. [20]

Three geometric boundary conditions were studied to determine their influence on the resulting thermal gradients. Figure 23 shows graphically these boundary conditions. Figure 23A shows the insert only, Model IO, where the influence of upstream and downstream components are not included in the model; and, hence, no axial conduction from these components is considered.

The nozzle assembly model, NA, is shown in Figure 23B. This model includes upstream and downstream components and axial conduction from these components are included.

Figure 23C shows the nozzle assembly model with a front face step due to the erosion of the upstream component (NAFE). Each of these models will be analyzed in the thermal analysis section.

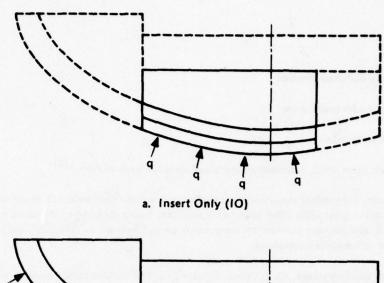
The surface thermochemistry analysis was performed using the Graphite Surface Kinetics (GASKET) computer program. The propellant formulation used for these studies was the HTPB (90 percent solids, 18 percent Al) propellant. The chamber pressure was taken to be 1,000 psi.

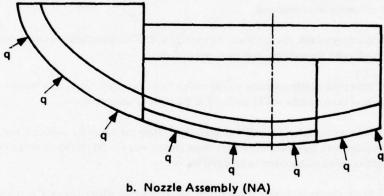
Figure 24 shows the basic nozzle contour and the area ratios where analyses were performed. The upstream and downstream components were assumed to be either a-b plane PG, ATJ graphite, PG/SiC coating or carbon/carbon material. Table 9 shows the matrix of GASKET runs performed. Also shown is the area ratio, Mach number, and mass transfer equation used in the analysis. The built-in kinetic rates in the GASKET Program were used in the analysis. For ATJ, bulk graphite kinetic rates were used. For the a-b plane pyrolytic graphite and PG/SiC materials, the layered and edge kinetic rates were used, respectively. Although additional work on kinetic rates for the PG/SiC material was being performed at Aerotherm, this work was not available at the time of these studies. Based on the success in predicting erosion using pyrolytic graphite edge kinetics in the Atlantic Research Scale-Up Program, [23], the pyrolytic graphite edge kinetics were used in the following analysis.

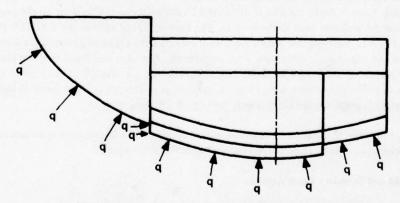
Figures 25 through 27 show the nondimensionalized erosion versus temperature at an area ratio of 1.267 for the three sets of kinetic constants. These curves represent typical results obtained.

6.2.4 Flow Field and Boundary Layer Analysis

To perform the flow field analysis, the Atlantic Research Transport Properties computer code was used. The program calculates individual specie and gas composition properties based on statistical mechanics. Also output is the pressure, temperature, and velocity parameters as a function of nozzle area ratio. The Turbulent Boundary Layer computer code, [19] is used to perform a boundary layer analysis. Basic inputs into the program are nozzle







c. Nozzle Assembly with Front Edge Heating (NAFE)

Figure 23. Thermal Boundary Condition Model Geometries.

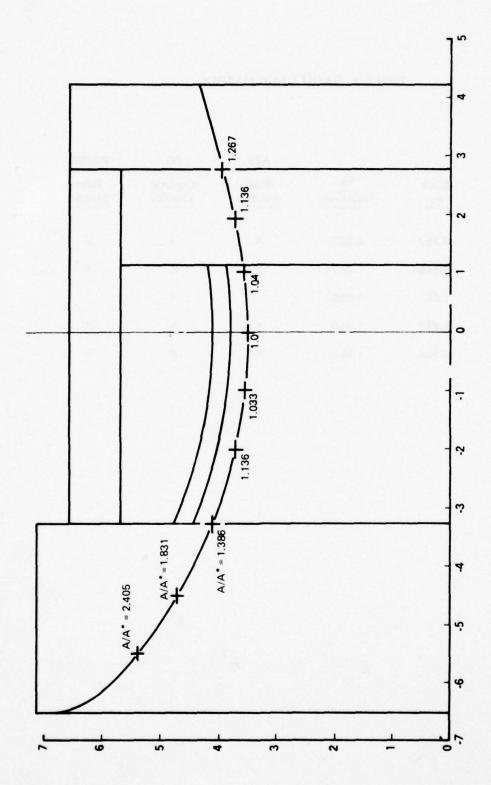


Figure 24. Nozzle Geometry Used for Thermal Analysis.

TABLE 9. GASKET RUN MATRIX.

Area ratio A/A*	Mach no.	C _h lb/ft ² -sec	Bulk kinetics	PG Layered kinetics	PG/SiC Edge kinetics
-1.386	0.488	1.219	×	×	×
1.00	1.00	1.4567		×	
1.04	1.212	1.346	×	×	×
1.267	1.552	1.052	×	×	x

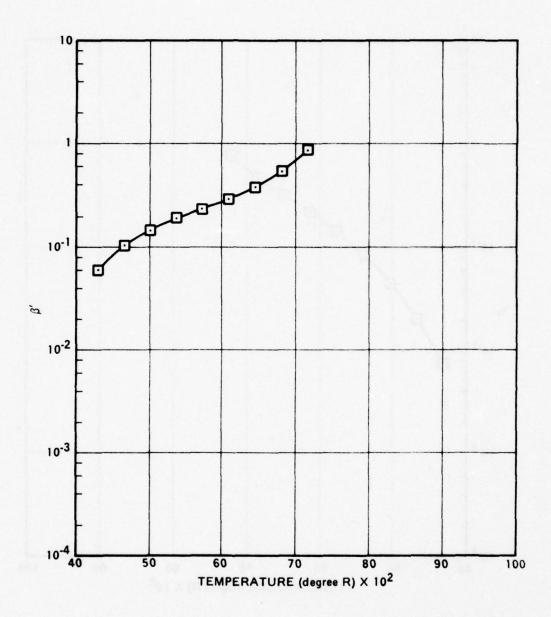


Figure 25. Nondimensionalized Erosion Versus Temperature Using Bulk Graphite Kinetic Constants.

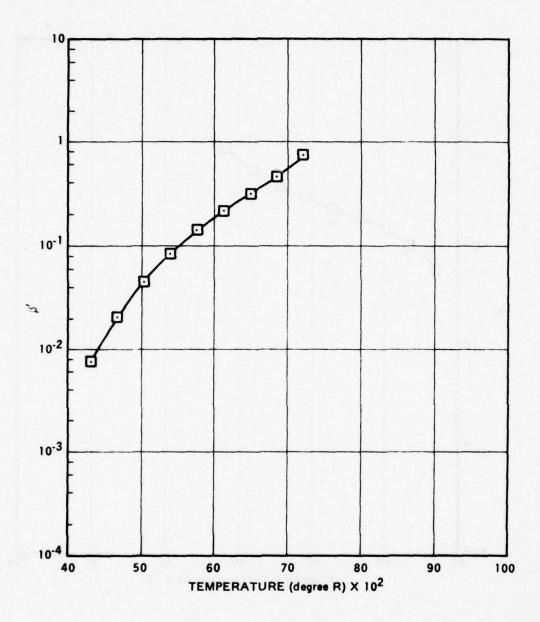


Figure 26. Nondimensionalized Erosion Versus Temperature Used Edge PG Kinetic Constants.

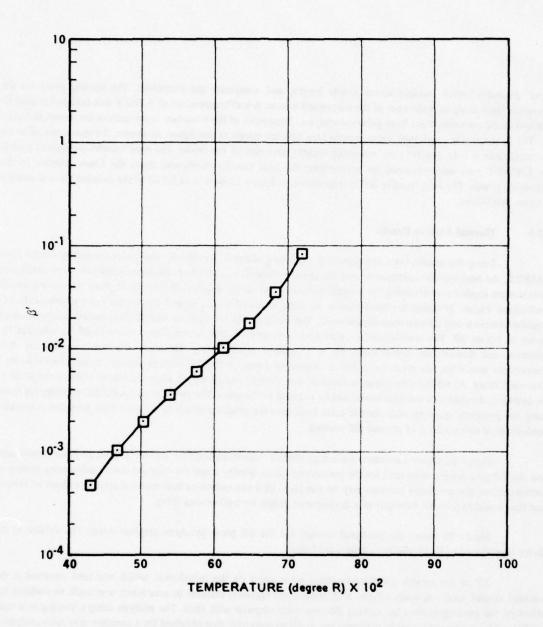


Figure 27. Nondimensionalized Erosion Versus Temperature Using A-B Plane PG Kinetic Constants.

initial geometry, Mach number versus nozzle length, and composite gas properties. The starting point for the boundary layer analysis is the nose of the submerged nozzle. A wall temperature of 5,700°F was used in the analysis and was based on estimations from previous analyses. The results of the boundary layer analysis are shown in Figure 28. The heat transfer coefficient versus nozzle area ratio are shown in this figure. As shown, the maximum value for the coefficient is 1.46 lbm/ft² - sec occurring slightly upstream of the throat. The mass transfer coefficient used in the GASKET runs were obtained by multiplying the heat transfer coefficient times the Lewis Number to the two-thirds power. The heat transfer coefficients shown in Figure 28 were used for all of the detailed thermal-erosion analyses that follow.

6.2.5 Thermal Analysis Results

Using the results from the boundary condition analyses, specifically the thermochemistry results from GASKET, the heat transfer coefficients, and the radiative heat flux, a series of one-dimensional runs were performed to determine erosion profiles along the internal surface of the nozzle. Figures 29 through 31 show the erosion profile predictions. Figure 29 shows the total erosion for firing times of 5, 15, 30 and 60 seconds for a nozzle with ATJ graphite upstream and downstream components. The same results for a nozzle with PG/SiC coated components are shown in Figure 30. The results indicate that both ATJ and PG/SiC coated components could be used for the upstream and downstream components for a 15-second nozzle firing. However, the total erosion for ATJ components would be too great for a 30- or 60-second firing. A PG/SiC coating appears to be acceptable for a 30-second firing. At 60 seconds a large amount of the forward end of the a-b plane dual layer would be exposed to the gases but the substrate material would not be exposed to the gases. The predictions for PG/SiC coatings are made using the pyrolytic graphite edge kinetic rates built into the program which in the past have provided reasonable predictions of erosion for a 15 percent SiC coating.

Figure 31 shows the results for a high density carbon-carbon (1.9 gm/cm³). Bulk graphite kinetic rates and the 1.9 g/cc density were used for the predictions. Since density is not the only parameter influencing erosion in carbon-carbon, the predicted erosions may be too high. Still the carbon-carbon material appears to have an erosion rate that would expose the substrate of a dual-layered design for a 60-second firing.

Figure 32 shows the predicted erosion for the a-b plane pyrolytic graphite insert. The erosion at the throat is predicted to be 39 mils for a 60-second firing.

All of the erosion profiles presented were based on the initial ratio which was held constant as the material eroded away. A study of the ATJ component (greatest increase in area ratio) was made to evaluate the affect of the eroding surface by varying the area ratio stepwise with time. The analysis using a varying area ratio predict a 25 percent reduction in total erosion at 60 seconds over that obtained for a constant area ratio analysis at the station adjacent to the a-b plane insert. Based on these results, upstream and downstream components of ATJ graphite are adequate for a 15-second nozzle firing. For the longer times, a PG/SiC coated nosecap and exit ring would be necessary.

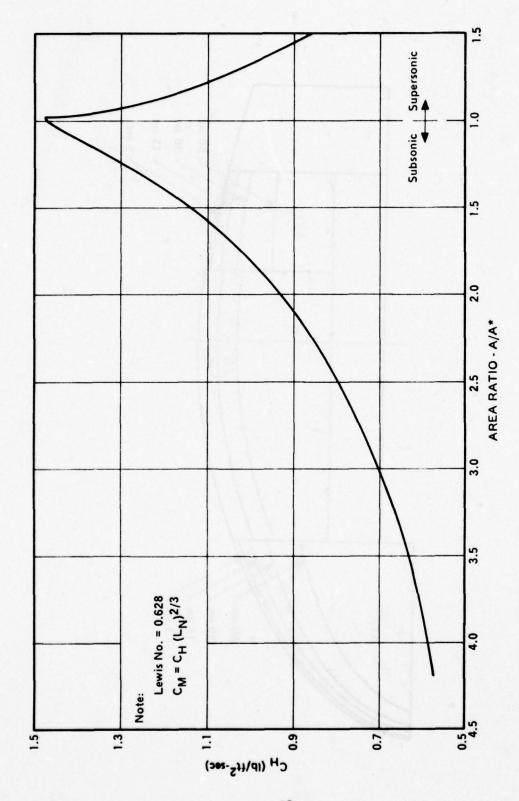


Figure 28. Heat Transfer Coefficient Versus Nozzle Area Ratio.

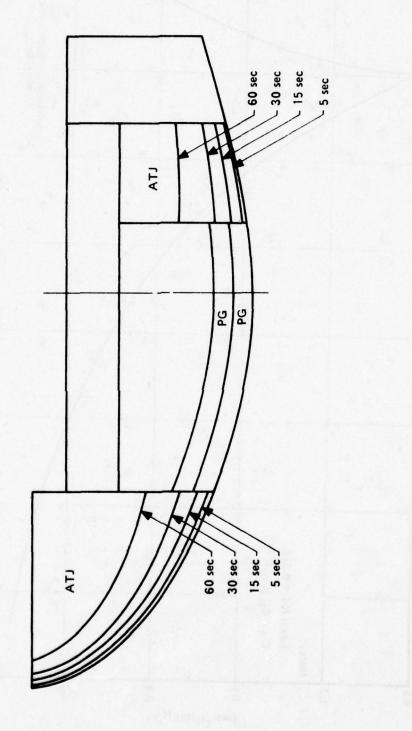


Figure 29. Predicted Erosion Profiles for ATJ Graphite Entrance Cap, and Exit Ring.

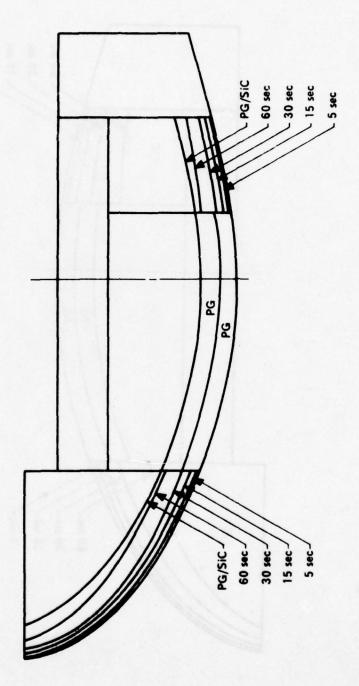


Figure 30. Predicted Erosion Profiles for PG/S.C. Entrance Cap and Exit Ring.

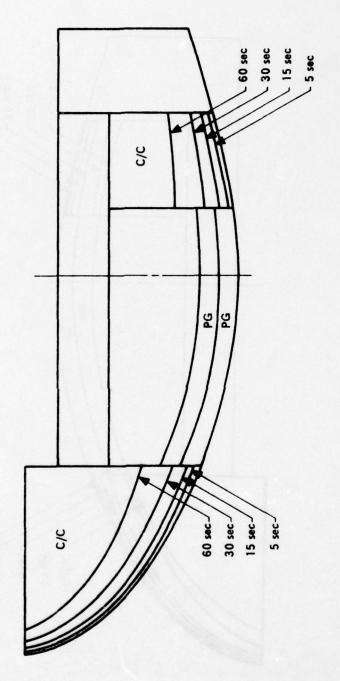


Figure 31. Predicted Erosion Profiles for 1.9 g/cc Carbon/Carbon Entrance Cap and Exit Ring.

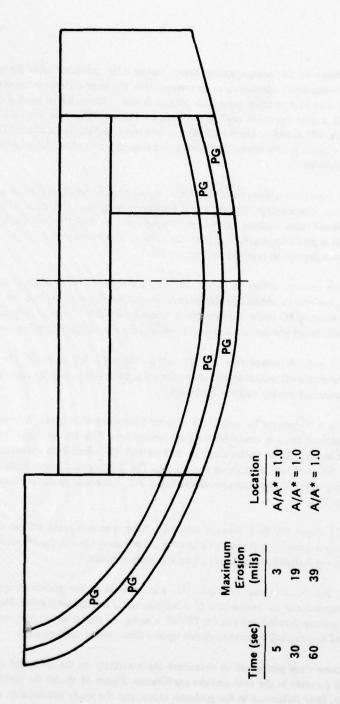


Figure 32. Predicted Erosion for a-b Plane PG Insert.

The durability of the nosecap-throat insert leading edge protector must be considered. Although the erosion predictions presented are considered to be conservative, the large difference between erosion resistances of a-b plane PG and the next best material presents a definite design problem. Better leading edge protection might be obtained with the PG washer approach used in the Scale-up Program. However, for a 60-second test using HTPB propellant, the nosecap will ablate or erode excessively, creating a potentially intolerable flow discontinuity. Based on the results of the erosion profile study, five nosecap/leading edge protector concepts were considered. These are shown in Figures 33 through 37.

Figure 33 presents a schematic of an "ideal" throat package which utilizes an integral nosecap and fully extended throat section. This concept requires a split backup support ring; and, in addition, results in the nosecap portion having a different radial back-up stiffness as compared to the throat region which is contained by the steel housing. This concept is probably impractical from the current state-of-the-art of PG processing when considering the problems of uniform deposition rate and microstructure.

The second concept shown in Figure 34 utilizes a separate PG nosecap which tends to eliminate the differential stiffness problem. In addition, a silicon carbide exit insert is used so that the support structure can be slipped onto the free-standing PG shells. This concept is "more producible" than the ideal concept. However, there is a large risk factor in the design and analysis required to assure primary success of the nosecap.

Figures 35 and 36 present two concepts which utilize PG/SiC nosecaps. The only difference in these concepts is that one utilizes a PG washer to provide leading edge protection assuming superior erosion resistance over the coating. Three options of coating makeup are shown.

The first is a 10 percent by weight SiC content homogeneous coating. A lower SiC content is desirable but probably not practical from a structural integrity standpoint. With this in mind the other options consider graded coatings. The second option grades from 15 to 5 percent SiC which is an approach which should ensure the standard needle-like SiC structure throughout the coating. The third option grades from 15 w/o percent to 0 w/o percent SiC continuing with a finite thickness of unalloyed PG. A thermal stress specimen similar to this has been successfully tested by TRW.

Figure 37 shows the fifth concept evaluated. This approach again utilizes a PG washer. However, a carbon/carbon nosecap is considered in place of a coating. As in concept No. 4, the PG washer is assumed to be more erosion resistant than the high density carbon/carbons currently available.

Concept No. 3, as shown in Figure 35, was selected as the preferred approach with the options considered for coating makeup an erosion rate of 5 mils/second is considered feasible. Hence, this value for erosion will be used in the ensuing detailed analysis for PG/SiC coating. As stated earlier, test results for a 15-second firing using a PG/SiC coated nosecap will be used to decide upon a final coating configuration.

Calculations were performed to determine the sensitivity of the predicted thermal gradients to a 35 percent increase and decrease in the heat transfer coefficients. Figure 38 shows the thermal gradients obtained for each case. As shown, little difference in the gradients exists, and the study indicates an insignificant affect on the analysis results.

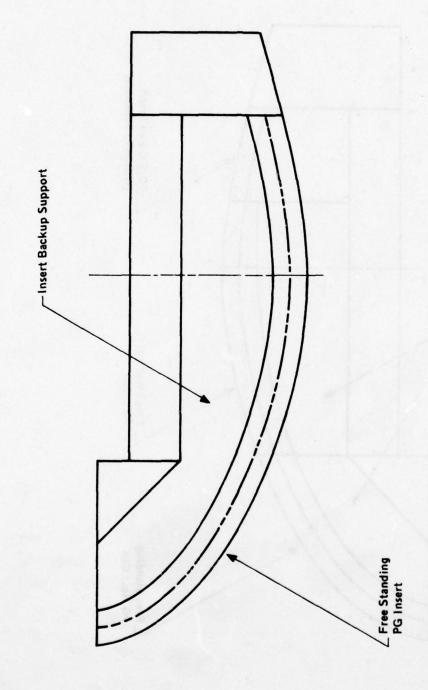


Figure 33. Integral PG Insert/Nose Cap Design.

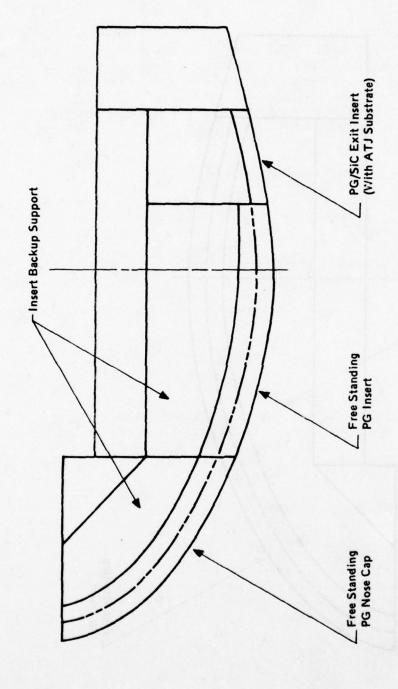


Figure 34. PG Insert with Separate PG Nose Cap.

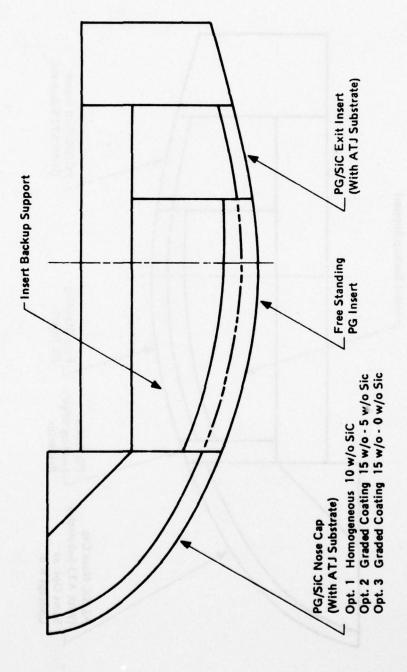


Figure 35. PG Insert with PG/SiC Nose Cap.

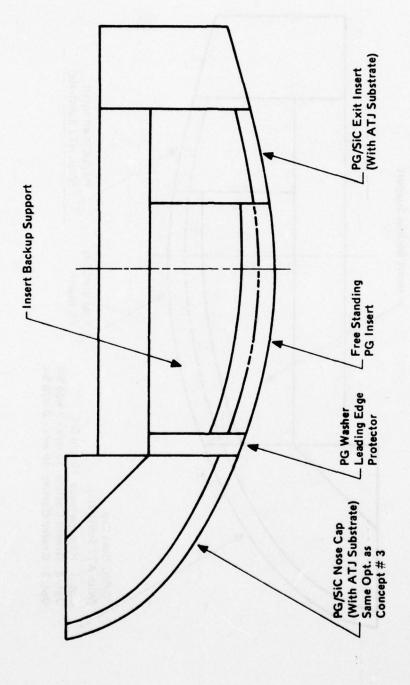


Figure 36. PG Insert with PG Washer and PG/SiC Nose Cap.

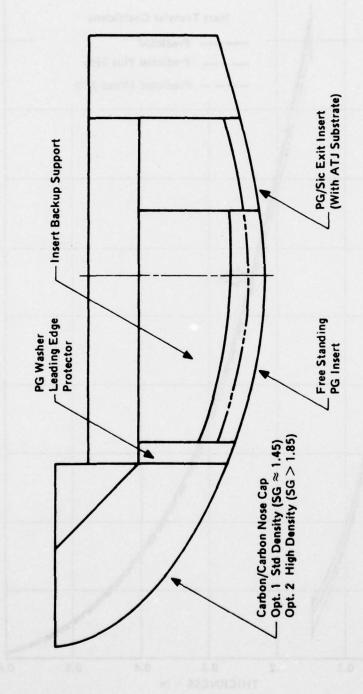


Figure 37. PG Insert with PG Washer and Carbon/Carbon Nose Cap.

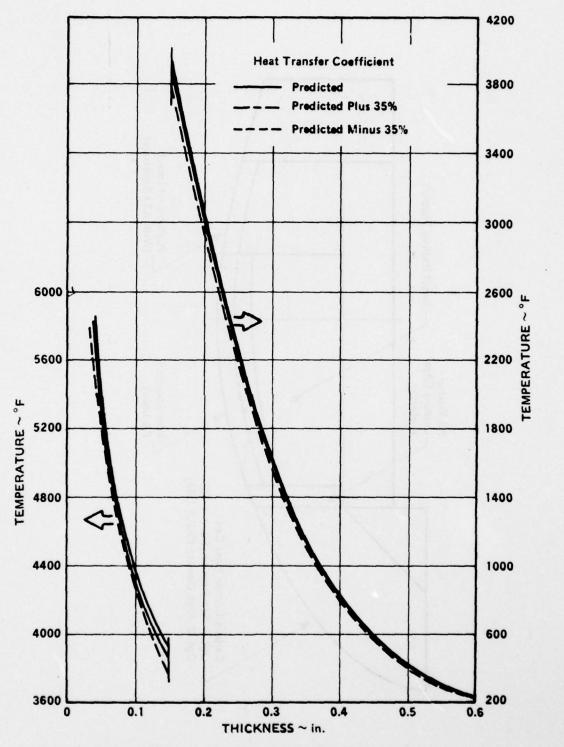


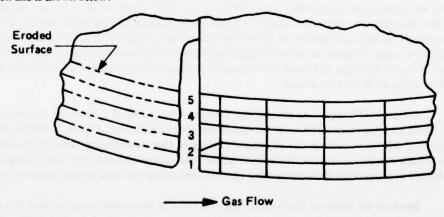
Figure 38. Effects of 35% Change in Heat Transfer Coefficient on Temperature Profile.

Once the design configurations were selected, detailed thermal analyses were performed to define the thermal gradients for use in the structural analyses. As discussed earlier, three thermal analysis models were studied to determine their effects on the resulting thermal gradients. These were as follows:

- a. IO Insert Only
- b. NA Nozzle Assembly
- c. NAFE Nozzle Assembly with Front Edge Heating

The model which best represents the actual conditions during a nozzle firing is the NAFE model. However, the complexity and cost of such an analysis is much greater than that for the *O model. The above factors (cost and complexity) apply not only for the thermal analysis but also for the ensuing saturational analyses. Therefore, a thermal analysis study was performed to determine the relative effects of each model on the predicted temperature distributions.

Before presenting the results of the analysis, a discussion of the technique used to perform the analysis for front edge heating is given. For this analysis, a special model of the region in question was created to overcome a restriction of the ASTHMA computer code. The restriction is that for an eroding inner surface, the second node from the surface cannot be heated in a back face or sidewall mode. Hence, a nodal network was devised to overcome this restriction and is shown below.



Sides 1 and 2 were not heated from the forward face. Side 1 represents a depth equal to the total crosion predicted. Side 2 is only 0.005 inch wide and is also modeled to accept the restriction that the second node could not be heated. Sides 3, 4 and 5 were heated by the use of heat transfer coefficient and temperature source boundary conditions. The heat transfer coefficient was varied as a function of time, being approximately zero until the face was initially exposed, increasing linearly until the face was completely exposed and then remaining constant after that. Other assumptions for the variation of heat transfer coefficient could be made. For instance, an increase in heat transfer coefficient with increased erosion and hence greater depth of mismatch. In addition, if a greater number of nodes were used, a better time dependence of heating could be effected.

An attempt was made to account for front edge heating of the insert. Other more sophisticated methods could be used; however, with the uncertainties involved, the degree of improvement in accuracy would probably not be determinate. No attempt was made to enforce conduction from the entrance cap; however, this assumption is considered to be valid since a gap and filler will be required to account for axial expansion between the two components.

A review of related literature indicates that, in subsonic regions, local heat transfer coefficients may be increased by a factor of 4 to 6 due to local "tripping" of the boundary layer. [24] Hence, analyses were performed with an amplification of the local heat transfer coefficient of 1.5 and 6.0. Figure 39 shows the comparison of the two analyses. The temperature versus distance from the forward end at the backside node and one node from the backside of the PG layer is shown at 30 and 60 seconds. The solid line represents the results of the analysis for a heat transfer coefficient (HTC) multiplied by 6.0 while the dashed line represents the results using a 1.5 factor.

Except for a small region at the extreme forward end of the insert, little increase in temperature results from the higher HTC. So that even though the real increase in HTC may be difficult to analytically calculate, the temperature distribution is not significantly changed by a factor of 6.0 increase in heat transfer coefficient.

The results of the thermal analysis for the IO and NA models are shown in Figures 40 and 41. As shown, the temperature distributions obtained using the two models are quite different. The figures show the isotherms that exist at 5 and 15 seconds, respectively, for the two models. When axial conduction of heat into the insert from the upstream and downstream components is accounted for, the temperatures in the insert are higher throughout the insert. Near the ends of the insert, the increase in temperature with axial conduction is even greater. Figure 41 shows the temperature reached as a function of insert length at a distance 0.225 inch back from the initial internal surface for each of the cases. It shows the effects of axial conduction on the backside temperature distribution of the first a-b plane PG layer. The large difference in temperature profiles has a significant affect on the resulting stress states. This will be discussed in the next section.

For the NAFE model, an analysis was performed that included a 15-second time duration with an ATJ graphite upstream component which eroded at approximately 16 mils/second. Figures 42 and 43 show the isotherms that exist at 5 and 15 seconds in the PG insert. Comparing these isotherms to those for the IO and NA models (Figures 39 and 40), it may be seen that a much higher axial gradient exists for the NAFE model. The higher axial gradients tend to increase the shear stresses that are developed during the firing, as will be shown in the next section.

Based on the results of the thermal analysis for each of the models, it was decided that the NAFE model should be used for determining the temperature distributions since the distributions were significantly different with this model, and the model is considered to be a more representative description. The significance of model selection is definitely established with the previous thermal analyses. To provide temperature profiles for the input to structural analysis, a detailed thermal analysis was performed using the NAFE model. In addition to the 15-second time duration analysis, a second analysis using a 60-second time duration and a PG/SiC coated entrance cap was performed. The PG/SiC coating erosion rate was assumed to be 5 mils/second. Figure 44 shows the nodal column network used for the analysis. Figures 45 through 54 show the temperature distributions through the first layer of PG coating at times of 1, 5 and 15 seconds at the different axial stations defined in Figure 1. ATJ was used for the upstream component in these calculations. Figures 55 through 57 show the isotherms for each of the firing times. The temperature distributions for the second layer of PG vary insignificantly except at the ends and are not shown here.

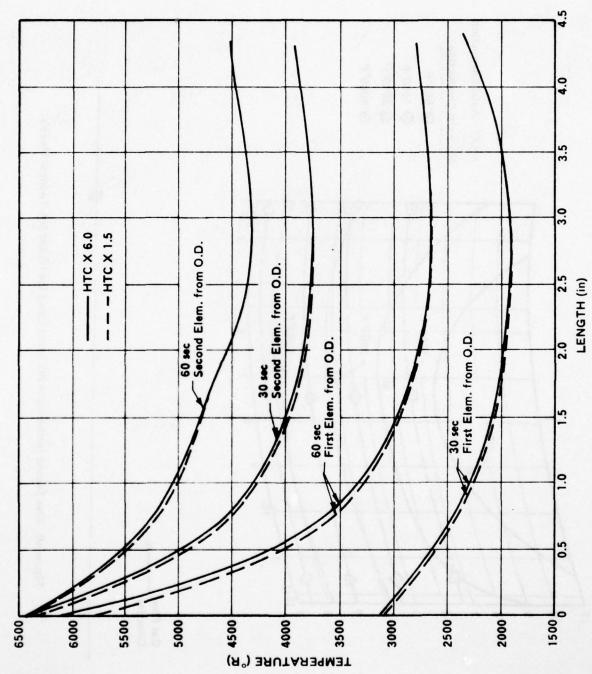
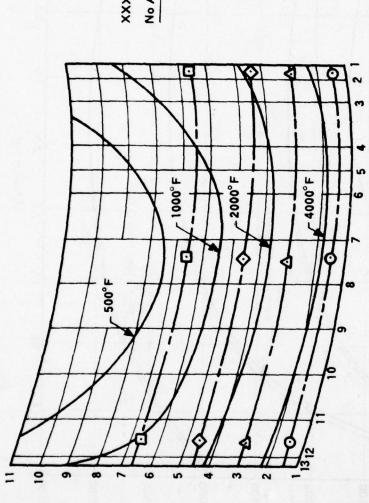
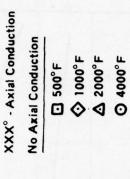


Figure 39. Effect of Increase of Heat Transfer Coefficient on Temperatures Near the Insert OD.







Gas Flow Direction

Figure 40. Five Second Isotherms in PG Insert Using the IO and NA Thermal Models.

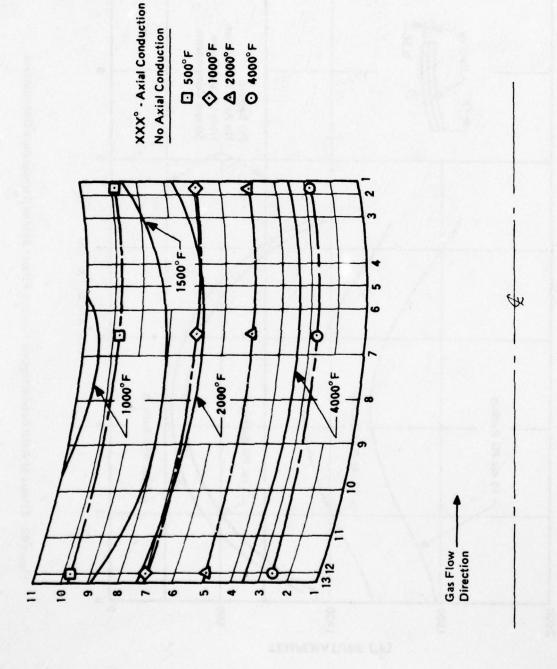


Figure 41. Fifteen Second Isotherms in PG Insert Using IO and NA Models.

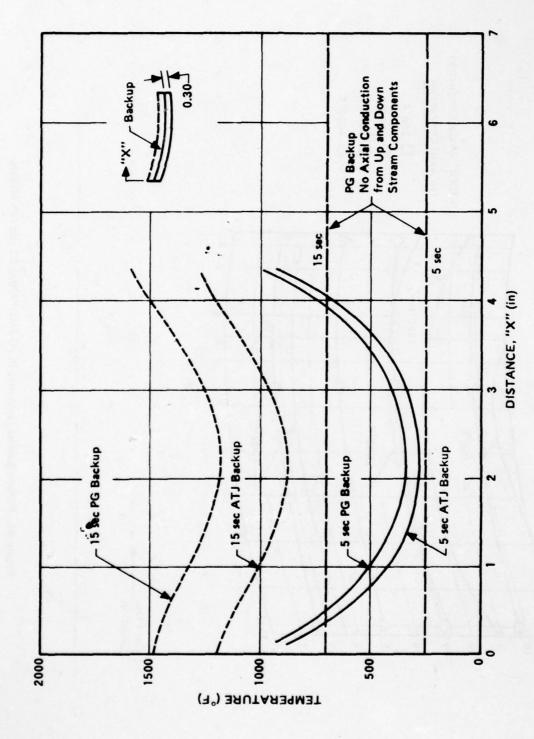


Figure 42. Effects of Axial Conduction on Five and Fifteen Second Temperature Distributions.

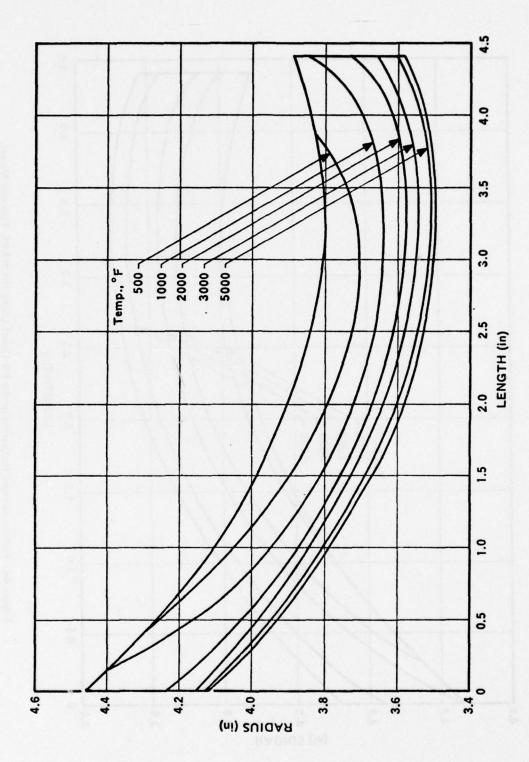


Figure 43. Five Second Isotherms in PG Insert Using NAFE Thermal Model.

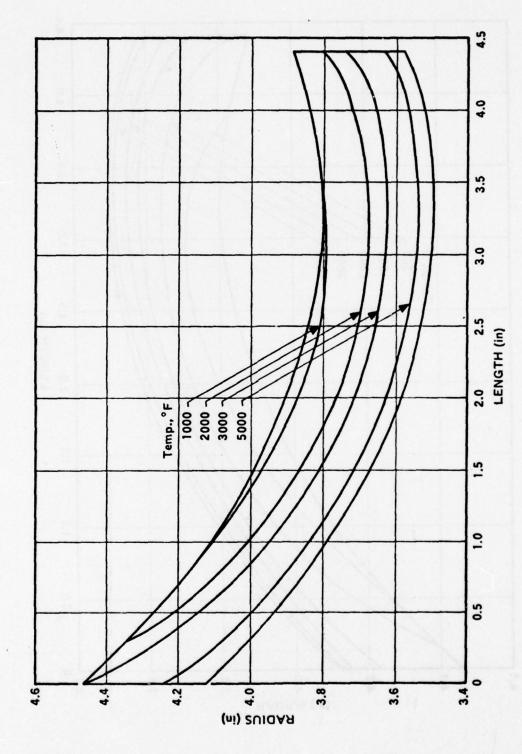


Figure 44. Fifteen Second Isotherms in the PG Insert Using the NAFE Thermal Model.

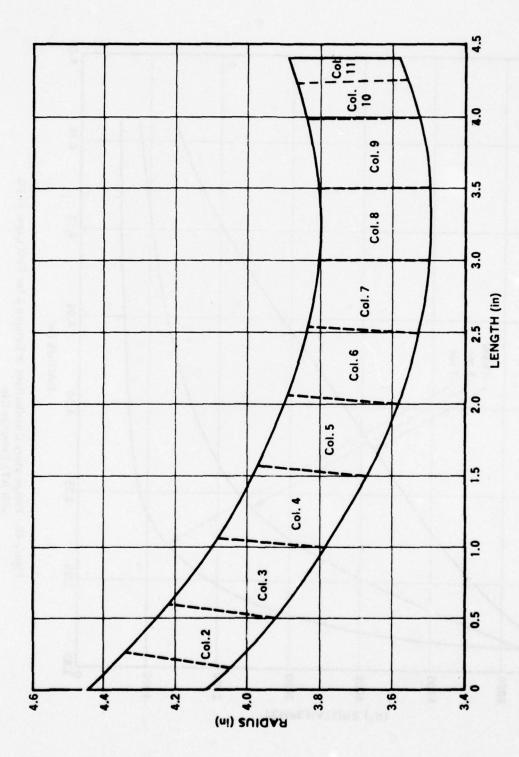


Figure 45. Model Used for Thermal Analysis of PG Insert.

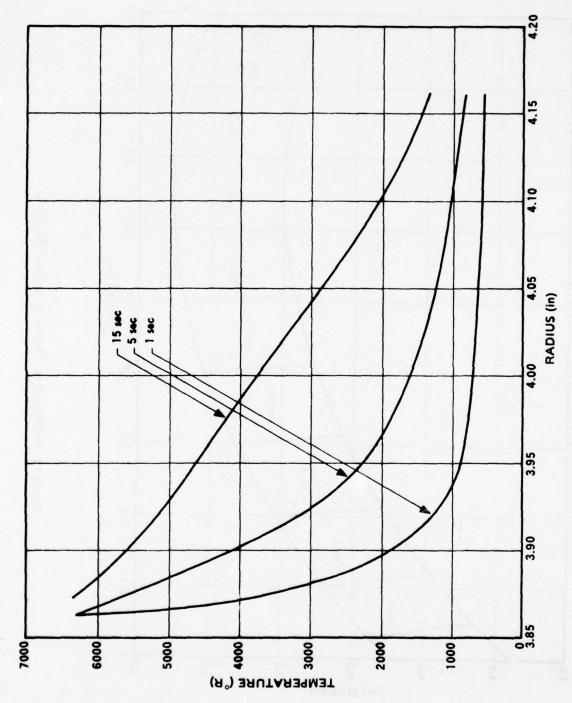


Figure 46. Temperature Distributions in Column 2 for First Layer of PG with ATJ Entrance Cap.

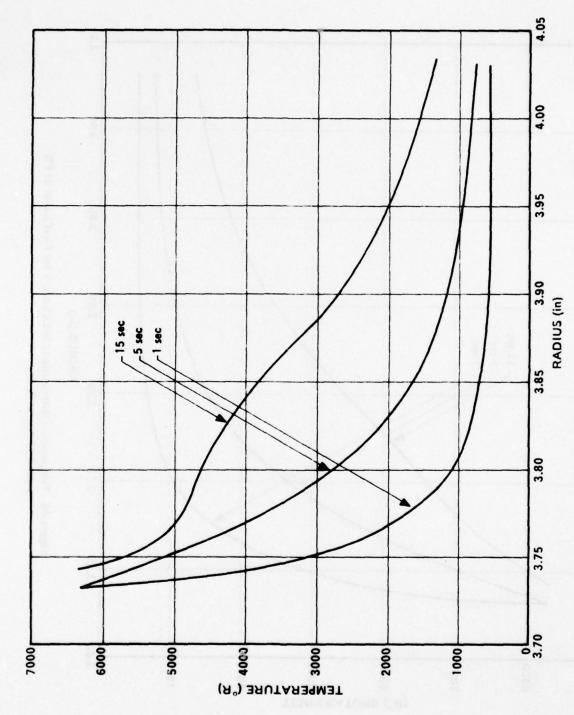


Figure 47. Temperature Distributions in Column 3 for First Layer of PG with ATJ Entrance Cap.

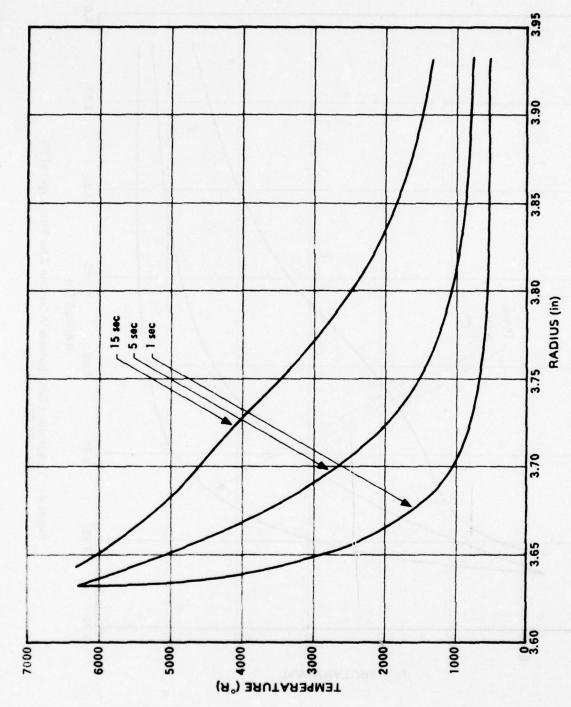


Figure 48. Temperature Distributions in Column 4 for First Layer of PG with ATJ Entrance Cap.

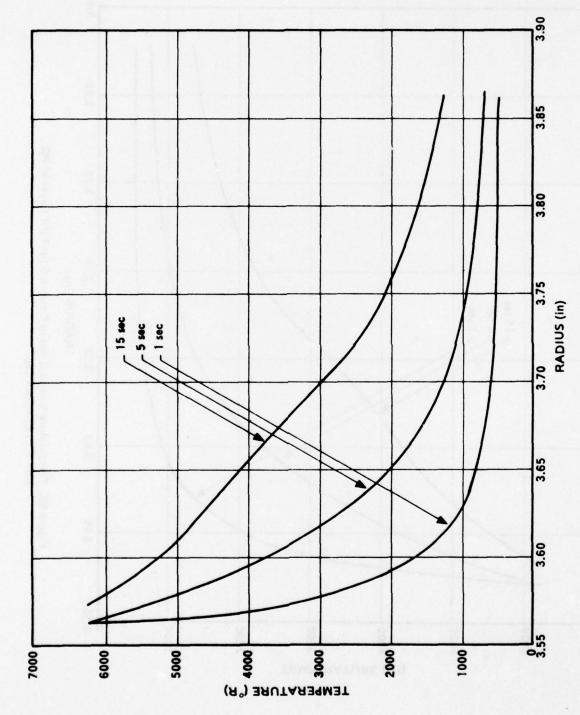


Figure 49. Temperature Distributions in Column 5 for First Layer of PG with ATJ Entrance Cap.

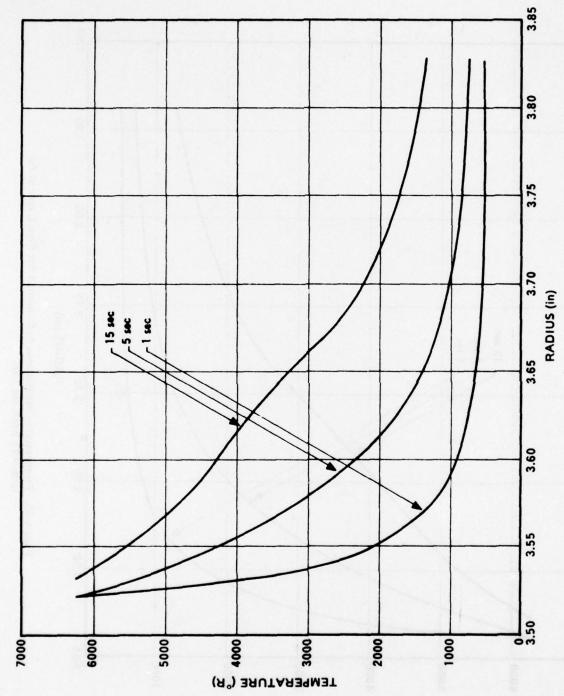


Figure 50. Temperature Distributions in Column 6 for First Layer of PG with ATJ Entrance Cap.

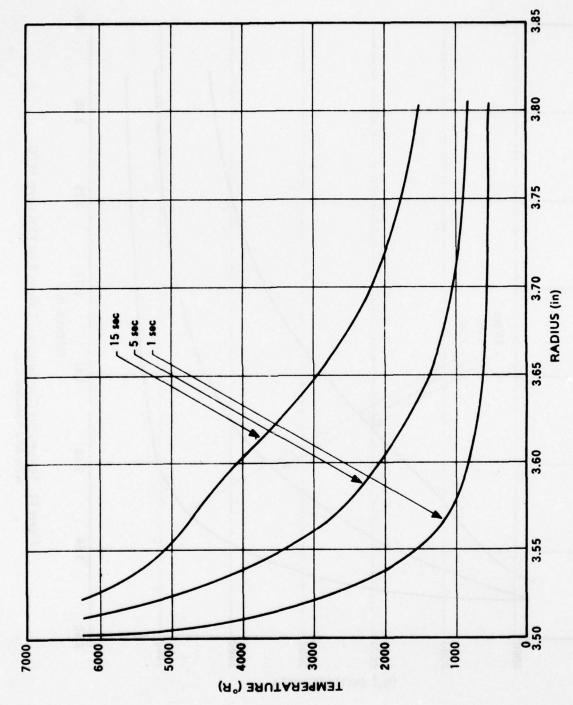


Figure 51. Temperature Distributions in Column 7 for First Layer of PG with ATJ Entrance Cap.

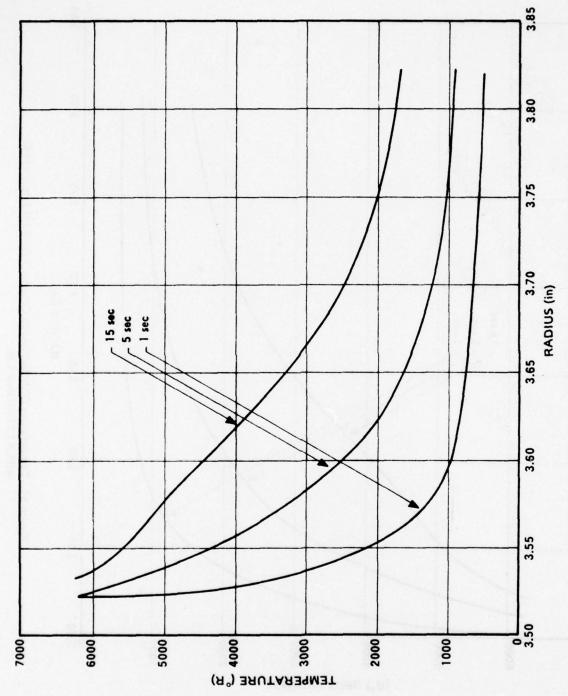


Figure 52. Temperature Distributions in Column 8 for First Layer of PG with ATJ Entrance Cap.

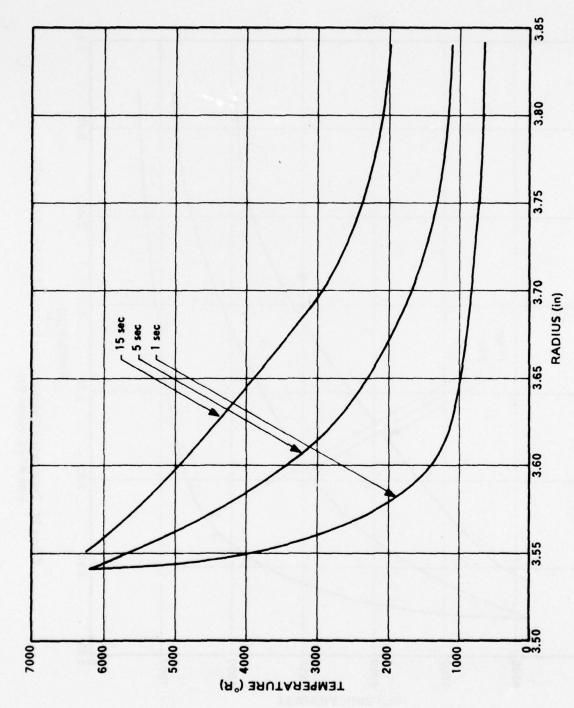


Figure 53. Temperature Distributions in Column 9 for First Layer of PG with ATJ Entrance Cap.

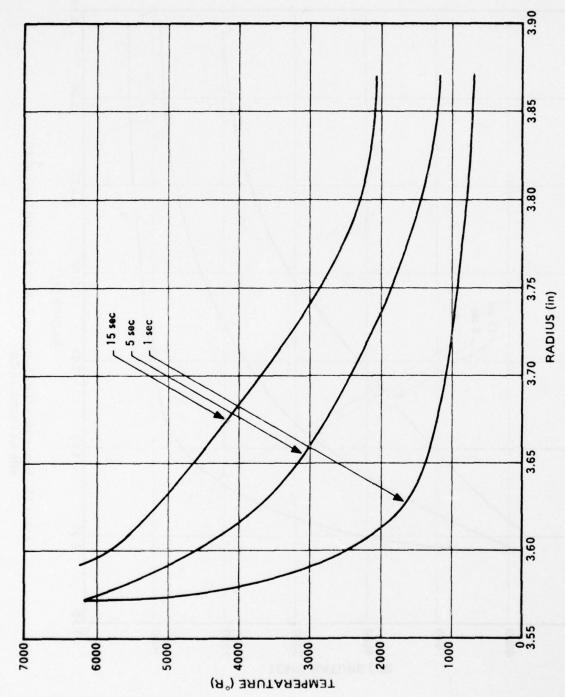


Figure 54. Temperature Distributions in Column 10 for First Layer of PG with ATJ Entrance Cap.

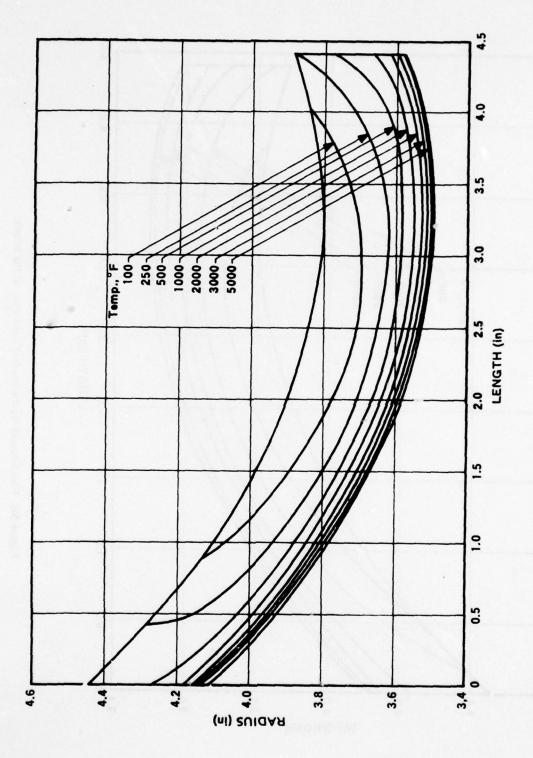


Figure 55. One Second Isotherms in First Layer of the PG Insert.

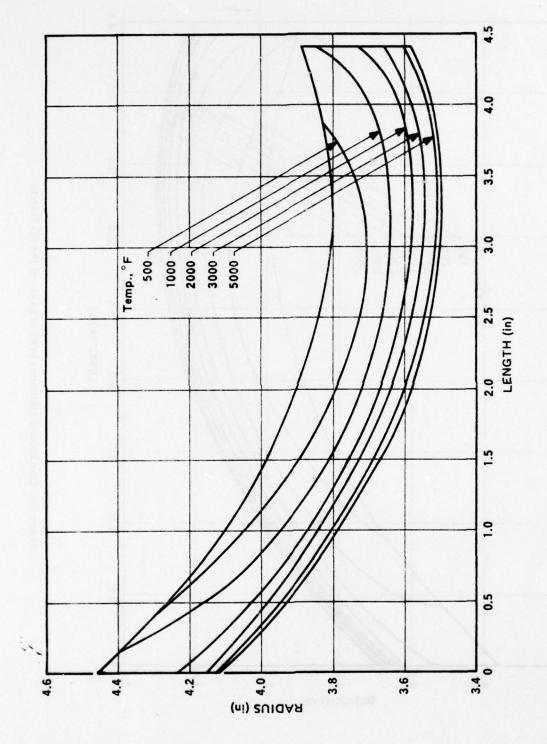


Figure 56. Five Second Isotherms in First Layer of PG Insert.

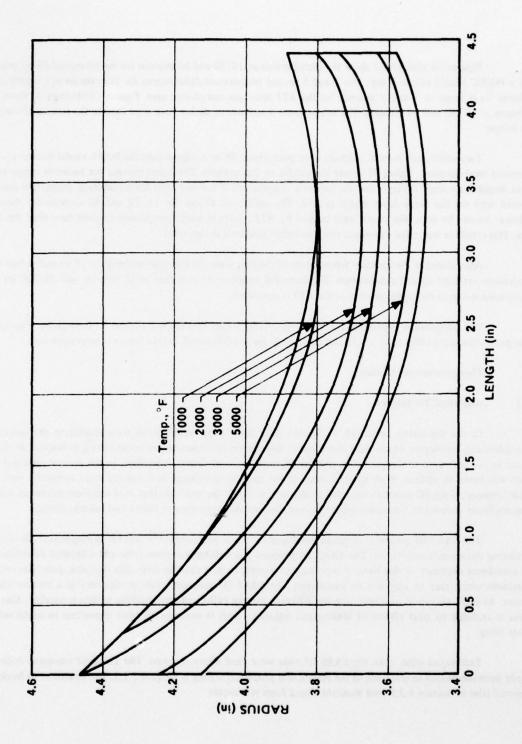


Figure 57. Fifteen Second Isotherms in the First Layer of the PG Insert.

Figures 58 through 67 show the distributions at 15, 30 and 60 seconds for the 60-second firing analysis with a PG/SiC coated entrance cap. The 1 and 5-second temperature distributions for this case are not significantly different from those at 1 and 5 seconds for the ATJ upstream component case. Figures 68 through 70 show the isotherms at 15, 30 and 60 seconds. The temperature distributions shown here were used in the structural analyses that follow.

Two additional thermal analyses were performed. These analyses used the NAFE model for the 15- and 60-second time duration. Figure 71 shows the results of this analysis. The figure present the backside temperature versus length for a single PG layer and the backside temperature of the first layer for a dual-layer design. The backup material used for the single layer design is ATJ. The results are shown for 15, 30 and 60 seconds for the two analyses. As can be seen, the single layer backed by ATJ results in lower temperatures versus time than the dual layer. This results in less radial expansion and also higher gradients in the insert.

Also shown is the backside temperature of the first layer for a dual-layer design at 15 seconds when ATJ components are used up and downstream. The increased temperature over that at 15 seconds with PG/SiC up and downstream is due to the higher erosion of the ATJ components.

The temperature distributions for the one PG layer case are shown in Figures 72 through 81. Figures 82 through 84 show the isotherms at 15, 30 and 60 seconds for the 60-second, PG/SiC coated component case.

6.3 Thermostructural Studies

6.3.1 Analytical Techniques

In the discussion presented in Section 4.0, there were several areas with respect to the analytical approaches and techniques which were identified as being areas of weakness and contributing to the lack of earlier success in the attempts to design, build, and fire PG nozzle throat inserts. Therefore, in the present approach, an effort was made to address those specific areas of the analysis and design in a manner more consistent with the actual behavior of the PG material. Included in this were not only the consideration of stresses and strains calculated using nonlinear techniques, but also consideration of the important question of failure and failure criteria.

The SAAS III computer program developed by Crose and Jones [14] was the principal analysis tool for calculating the stresses and strains. The SAAS III program is a well-known stress code and a detailed description is not considered necessary at this time. It is perhaps of interest to note that the code, like all codes, does have certain limitations which may or may not be significant. The SAAS III program treats nonlinearity in a bilinear elastic manner. As such, no means of accounting for different loading paths and any resulting effects is possible. Also, no means is available to treat effects of loading and unloading such as occur in PG from deposition to cooldown to nozzle firing.

Techniques other than the SAAS III code were used where required. The TEXGAP computer code has already been mentioned in reference to the mechanical properties testing in Section 5.2.3. The treatment of buckling presented later in Section 6.3.5 used standard closed form techniques.

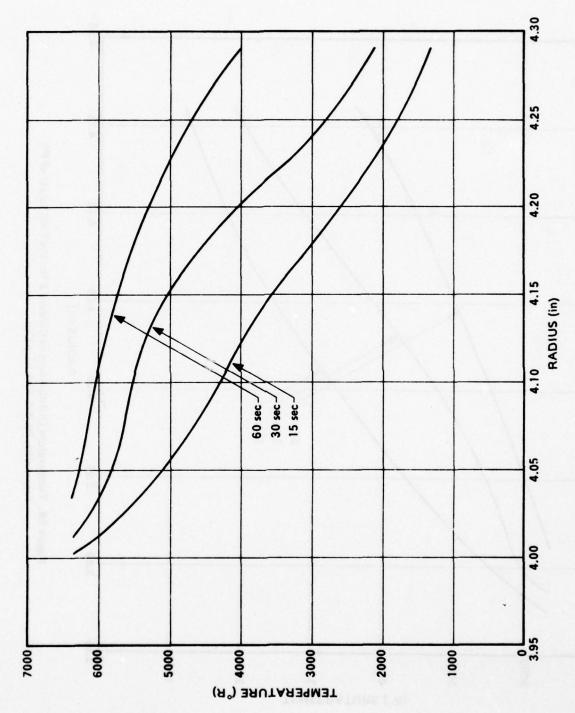


Figure 58. Temperature Distributions in Column 1 for the First Layer of PG Insert with PG/SiC Entrance Cap.

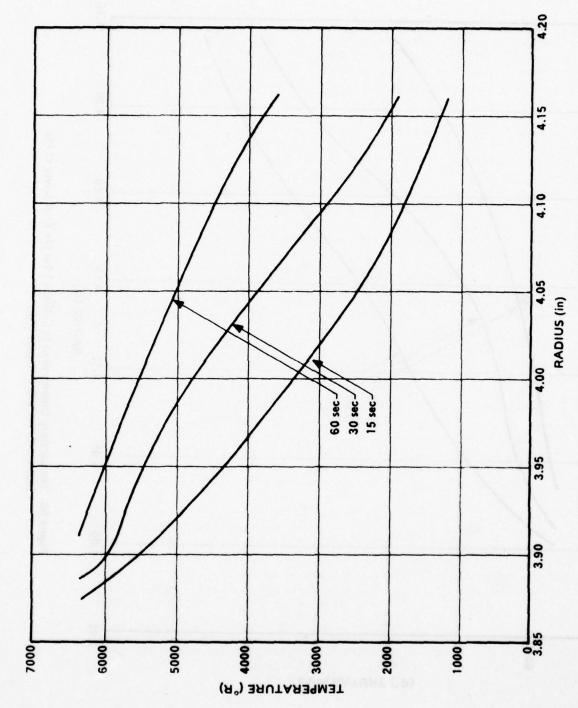


Figure 59. Temperature Distributions in Column 2 for the First Layer of PG Insert with PG/SiC Entrance Cap.

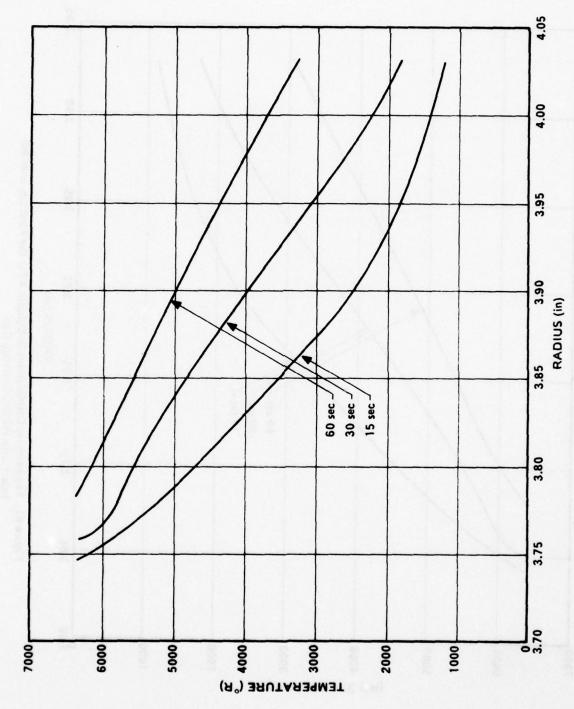


Figure 60. Temperature Distributions in Column 3 for the First Layer of PG Insert with PG/SiC Entrance Cap.

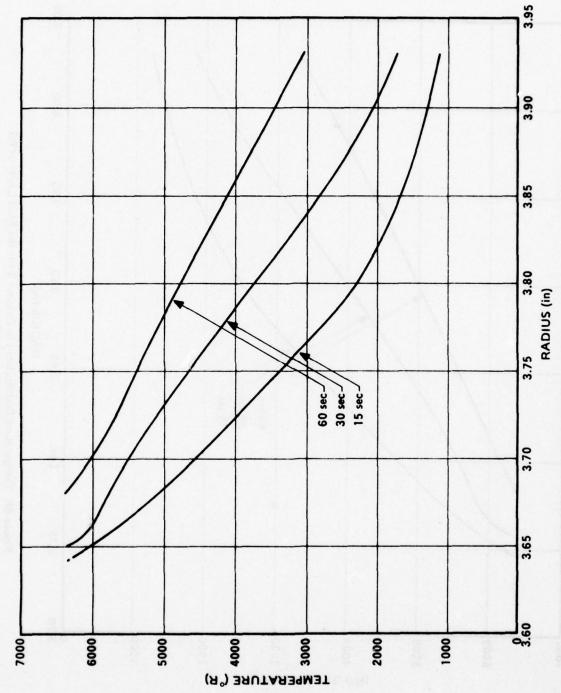


Figure 61. Temperature Distributions in Column 4 for the First Layer of PG Insert with PG/SiC Entrance Cap.

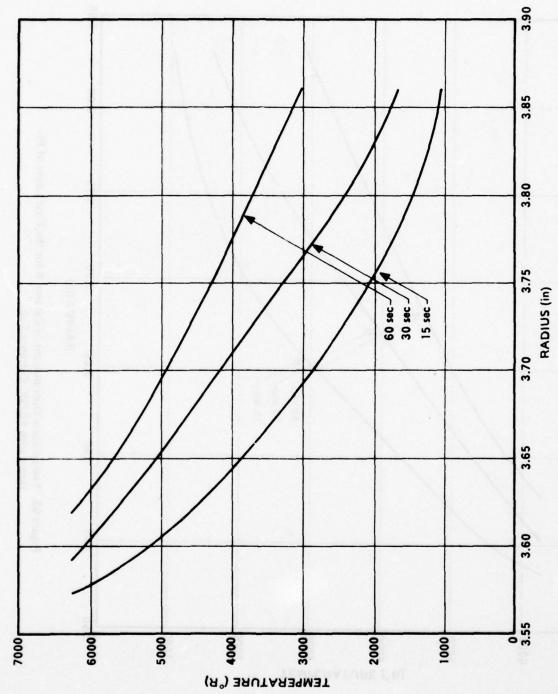


Figure 62. Temperature Distributions in Column 5 for the First Layer of PG Insert with PG/SiC Entrance Cap.

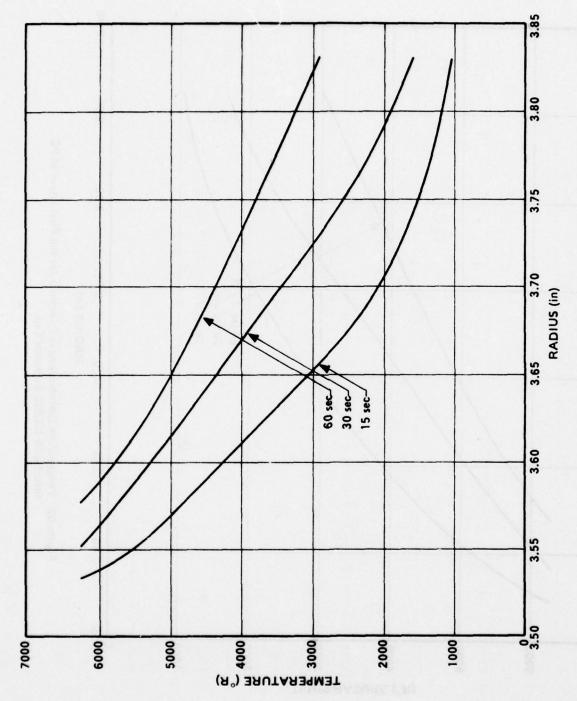


Figure 63. Temperature Distributions in Column 6 for the First Layer of PG Insert with PG/SiC Entrance Cap.

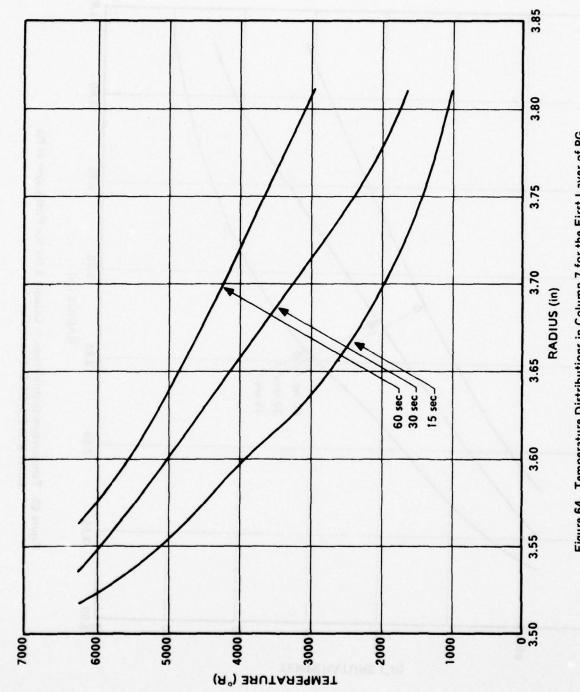


Figure 64. Temperature Distributions in Column 7 for the First Layer of PG Insert with PG/SiC Entrance Cap.

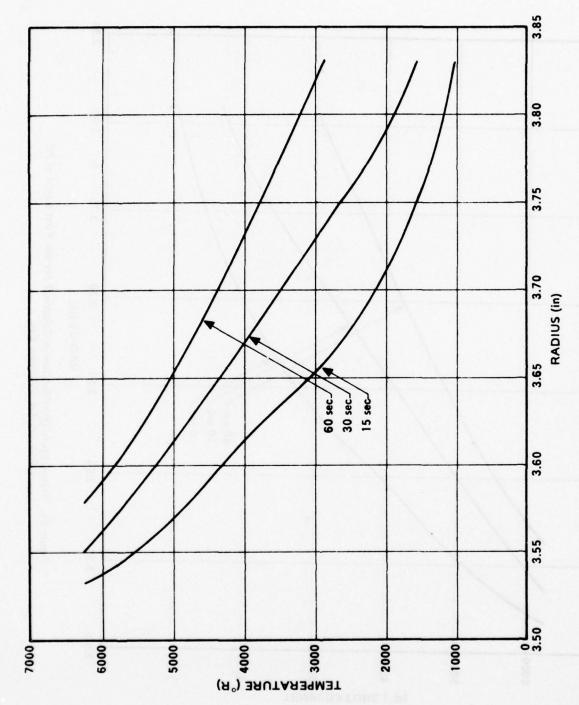


Figure 65. Temperature Distributions in Column 8 for the First Layer of PG Insert with PG/SiC Entrance Cap.

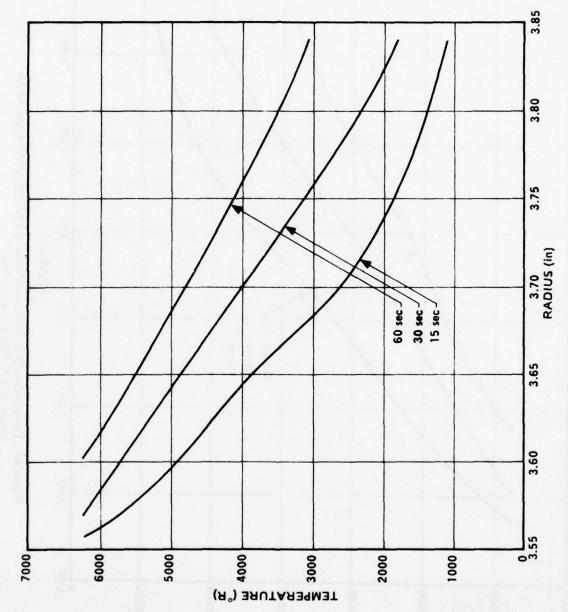


Figure 66. Temperature Distributions in Column 9 for the First Layer of PG Insert with PG/SiC Entrance Cap.

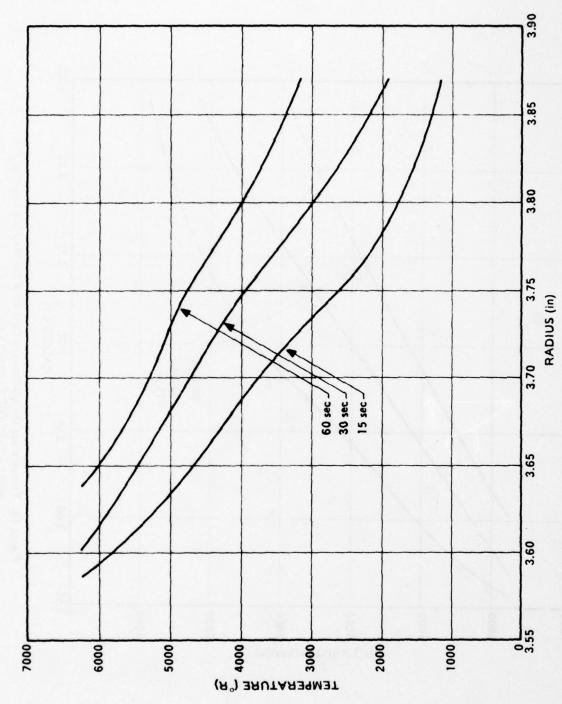


Figure 67. Temperature Distributions in Column 10 for the First Layer of PG Insert with PG/SiC Entrance Cap.

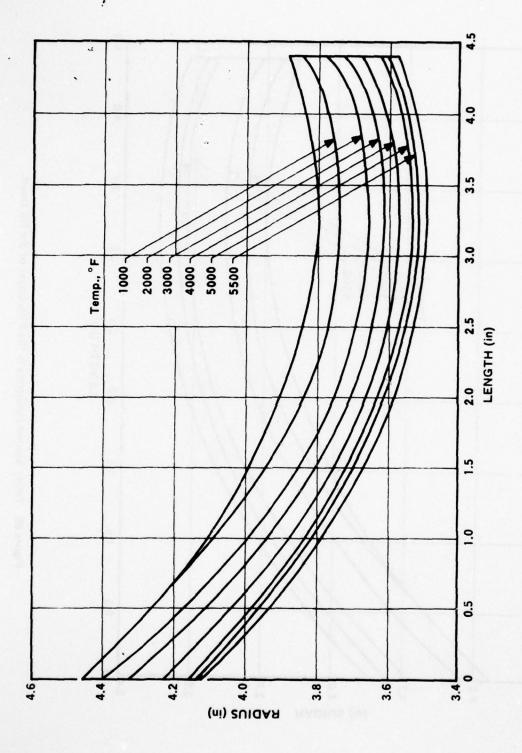


Figure 68. Fifteen Second Isotherms in the First Layer of the PG Insert.

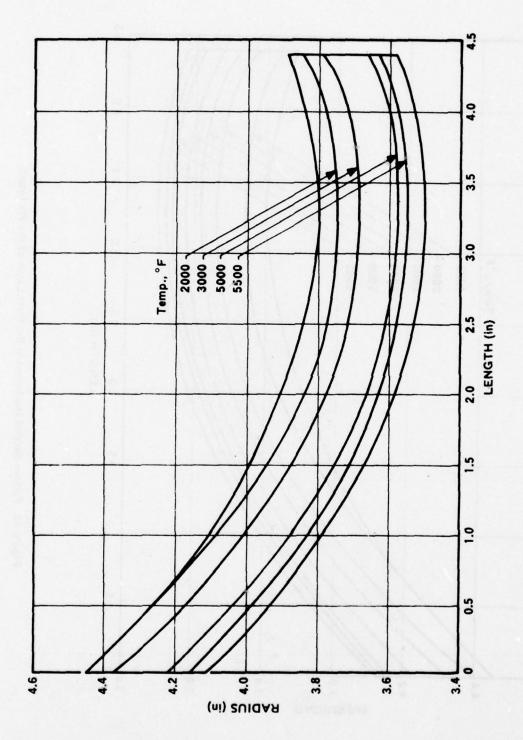


Figure 69. Thirty Second Isotherms in the First Layer of the PG Insert.

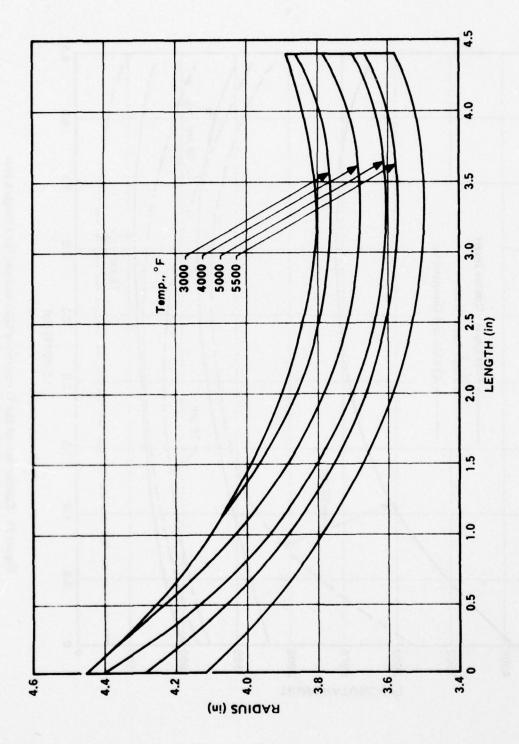


Figure 70. Sixty Second Isotherms in the First Layer of the PG Insert.

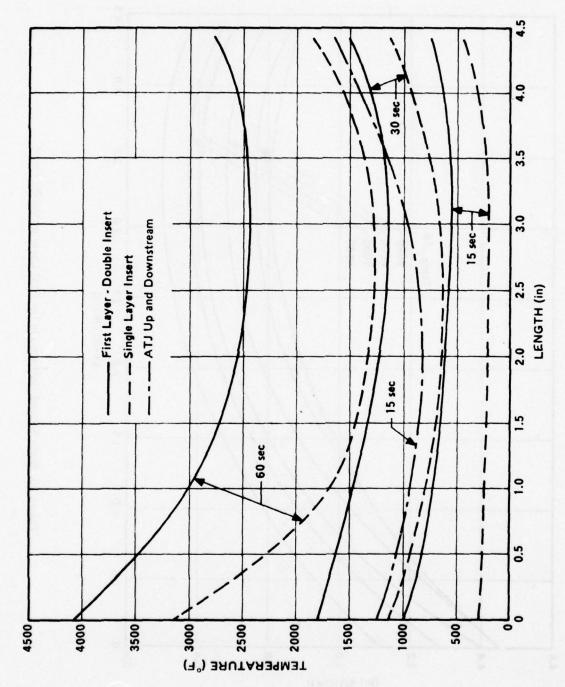


Figure 71. Comparison of the Temperature Distributions for a Single Layer Insert and a Dual-Layer Insert.

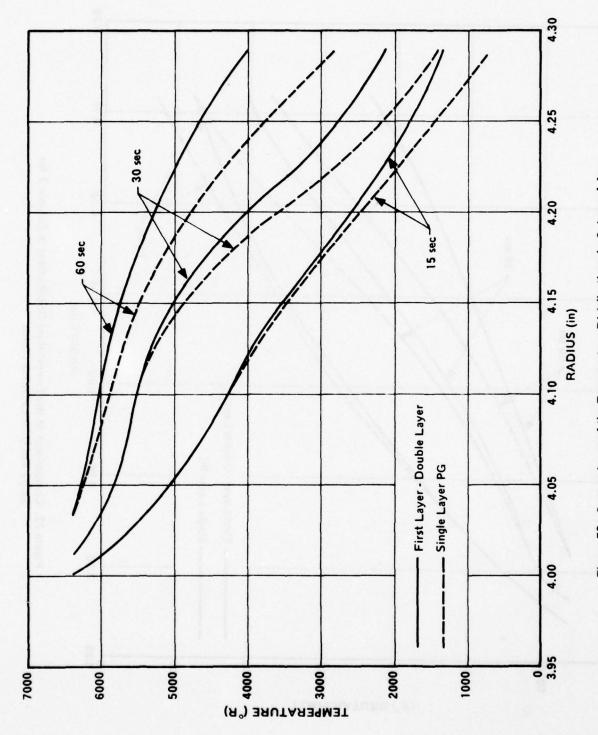


Figure 72. Comparisons of the Temperature Distributions in Column 1 for Single and Dual Layer PG Insert.

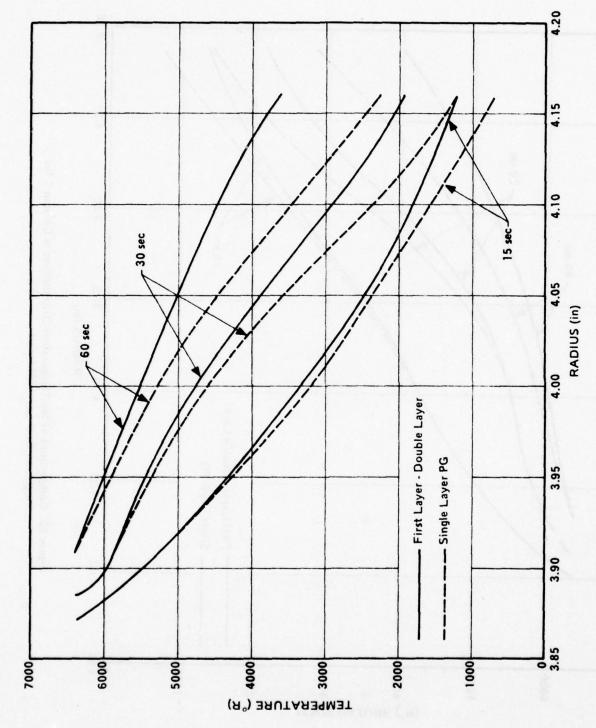


Figure 73. Comparisons of the Temperature Distributions in Column 2 for Single and Dual Layer PG Insert.

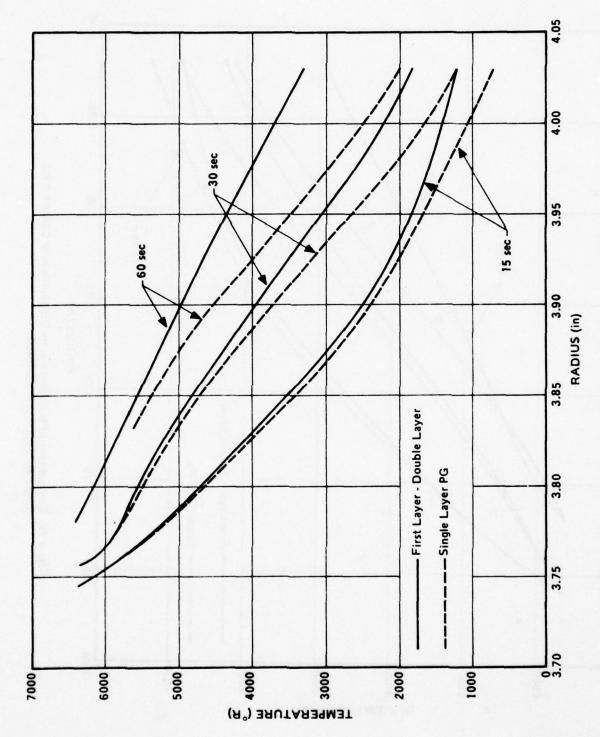


Figure 74. Comparisons of the Temperature Distributions in Column 3 for Single and Dual Layer PG Insert.

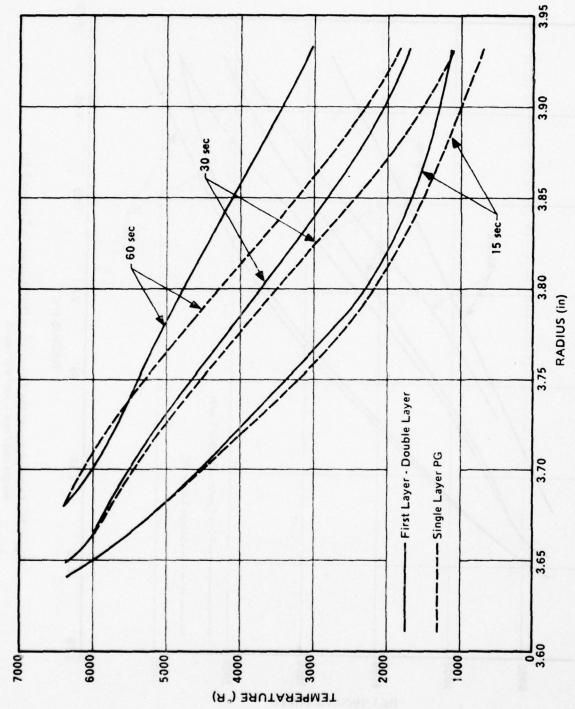


Figure 75. Comparisons of the Temperature Distributions in Column 4 for Single and Dual Layer PG Insert.

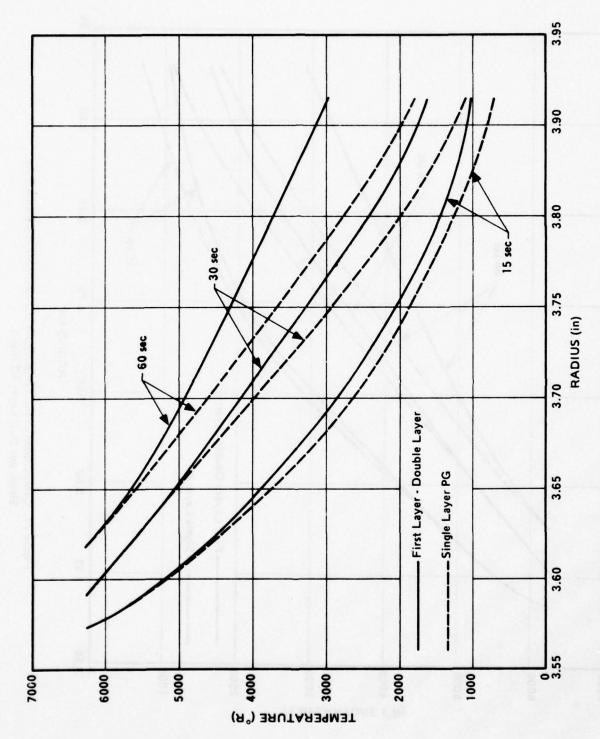


Figure 76. Comparisons of the Temperature Distributions in Column 5 for Single and Dual Layer PG Insert.

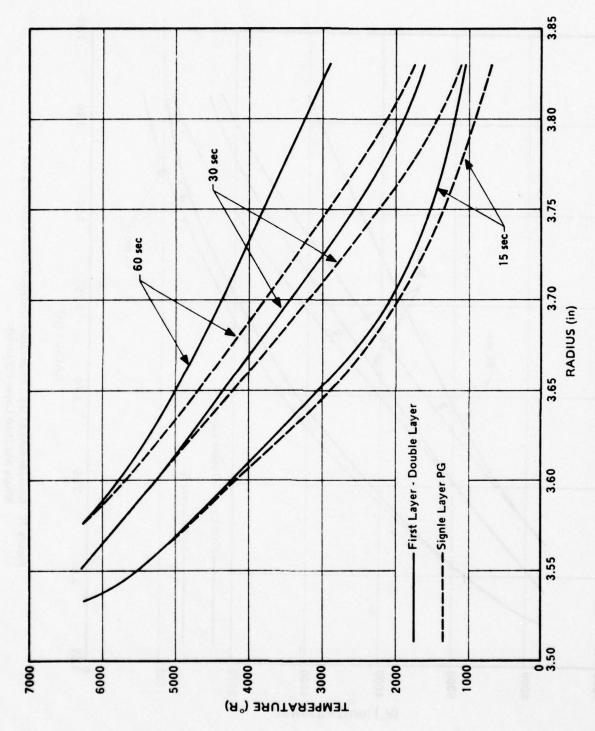


Figure 77. Comparisons of the Temperature Distributions in Column 6 for Single and Dual Layer PG Insert.

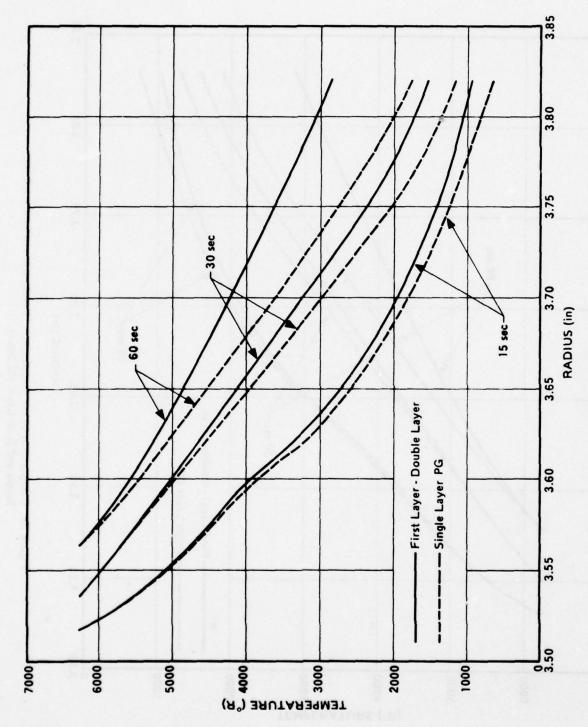


Figure 78. Comparisons of the Temperature Distributions in Column 7 for Single and Dual Layer PG Insert.

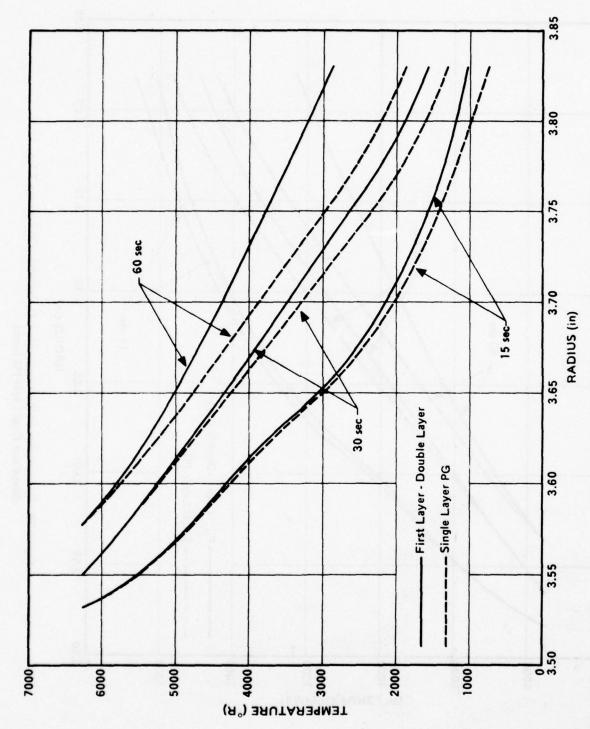


Figure 79. Comparisons of the Temperature Distributions in Column 8 for Single and Dual Layer PG Insert.

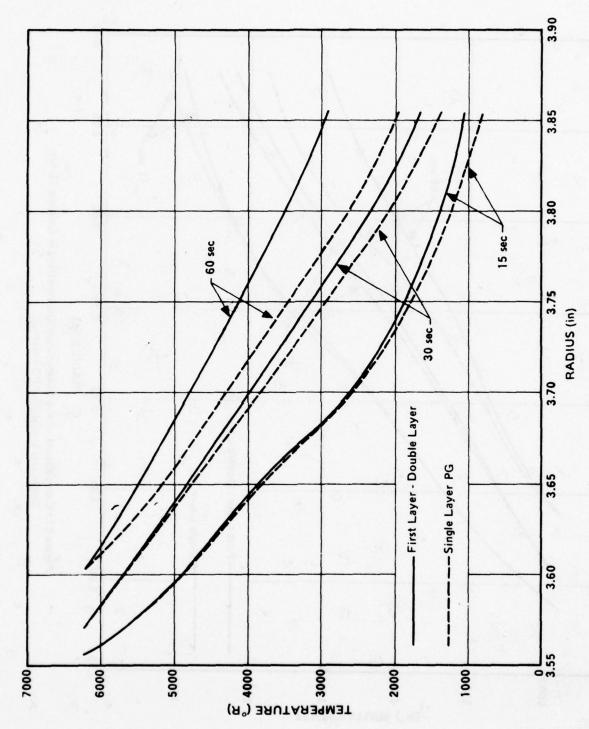


Figure 80. Comparisons of the Temperature Distributions in Column 9 for Single and Dual Layer PG Insert.

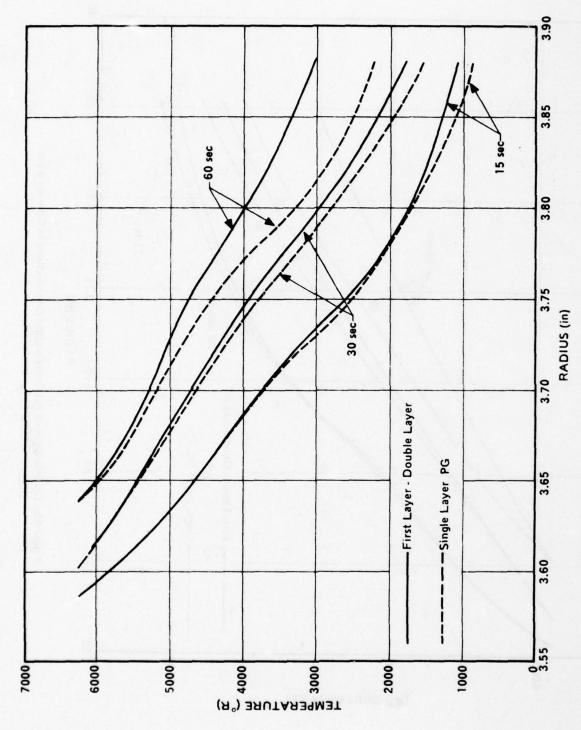


Figure 81. Comparisons of the Temperature Distributions in Column 10 for Single and Dual Layer PG Insert.

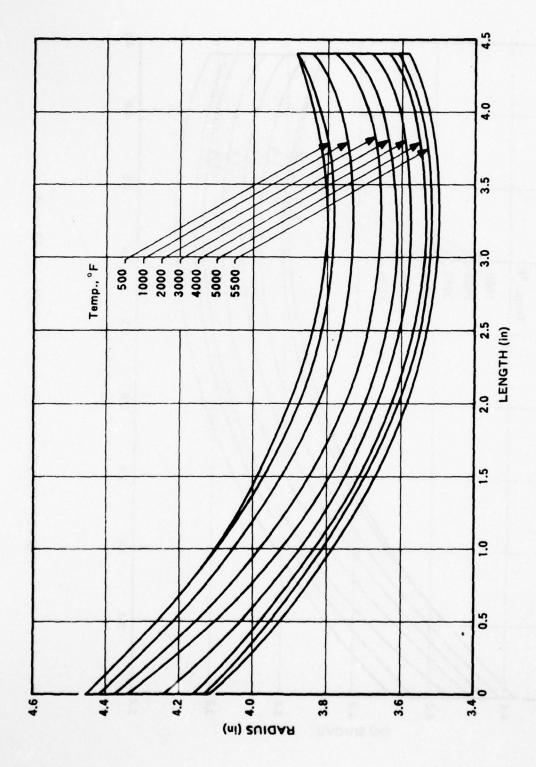


Figure 82. Fifteen Second Isotherms for the Single Layer PG Insert.

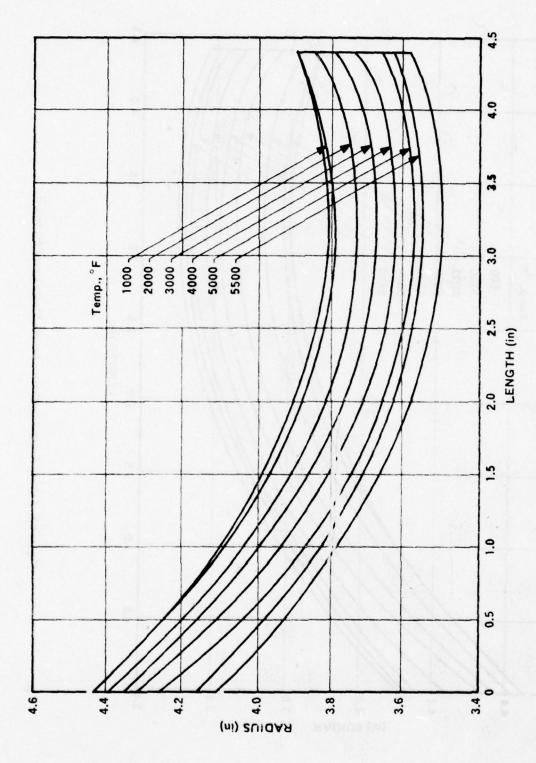


Figure 83. Thirty Second Isotherms for the Single Layer PG Insert.

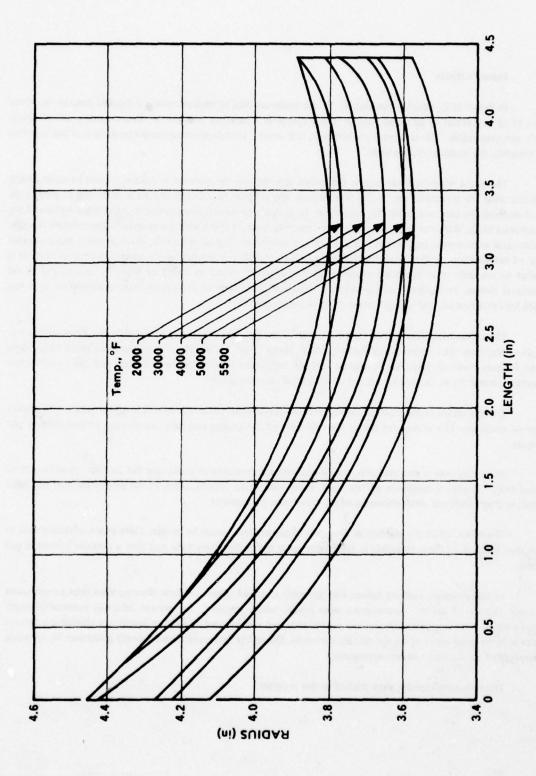


Figure 84. Sixty Second Isotherms for the Single Layer PG Insert.

6.3.2 Failure Criteria

Professor D.C. Drucker has stated, "If the understanding of fracture means a detailed description of the position of all key atoms at all stages leading to the complete separation of material, the atomistic point of view is the only one permissible." He continues on, however, and states, "If understanding means prediction of the behavior of the material, the situation is debatable."

The point which is made here is that when approaching the question of failure, it must be made clearly understood what the objectives are. In the present case, the purpose of a failure criteria is to be able to predict the onset of material fracture and, with this prediction, to design a structural component to adequately withstand the environmental loads. With our present knowledge of material fracture (even with the enormous literature on fracture mechanics and microscopic approaches to fracture), the phenomenological approach, which requires the minimum amount of information, is the most practical approach to realistically predicting the adequacy of structures. It is important to recognize that the phenomenological mathematical model, as stated by Wu[25] "is intended to aid experimental design, to facilitate interpolation, correlation, and retrieval of experimental observations; it is not intended for extrapolation and interpretation of mechanisms of failure."

The assumption here is that fracture occurs when the flow curve, or its generalization in more than one dimension, intersects the corresponding fracture curve. Hence, both knowledge of the stress and strain states along with the fracture curve are required. Nonlinear analysis techniques provide the overall stress and strain states while the fracture curve must be defined by a series of multiaxial laboratory tests.

The definition of the fracture surface in three-dimensional space has been defined for only a very limited number of materials. The reason for this is the difficulty of the testing and even the absence of well-defined test techniques.

Since this data is not available, purely analytical approaches to predicting the fracture curve have been proposed which require a minimum of test data. Even with these criteria, some of the properties have not been obtained, so that additional assumptions based on experience are required.

Therefore, while the validity or accuracy of the criteria cannot be proven, there exists sufficient data to suggest that fracture of these materials is dependent upon the entire stress state and that a uniaxial criteria is not sufficient.

In this program, existing failure theories were reviewed. Some of these theories were then programmed to provide factors of safety. Assumptions were made, where required, for certain inherent material strength properties which were not available, and the results obtained can be used to neither justify nor eliminate a theory. This can only be done by tests on the specific materials. The safety factors obtained provide guidelines for assessing the adequacy of the structure under investigation.

The following theories were studied in this program:

- a. Minimum uniaxial stress ratio
- b. Puppo and Evensen [26]
- c. Interaction theory [27]
- d. Tsai-Wu theory [28]
- e. Priddy theory [29]

The Puppo and Evensen theory was considered as three distinct criteria since the equations have not been extended to three-dimensional space. The results for PG were very eratic and possibly were due to a violation of certain stability conditions on the magnitude of the interaction terms. The causes of this instability was not pursued in this program, and no further consideration is given here.

The Tsai-Wu theory criteria assumes that there exists a failure surface expressible in the following form:

$$F_i \sigma_i + F_{ij} \sigma_i \sigma_j = 1$$

where

$$F_{ij} = \frac{1/\sigma_{Ti} - 1/\sigma_{Ci}}{= \begin{cases} \text{interaction terms obtained from multiaxial or off-axis test results for } i \neq j \\ 1/\sigma_{Ti} \sigma_{Cj} \text{ for } i = j \end{cases}$$

 σ_{T_i} = uniaxial tensile or shear strength

 $\sigma_{\mathbf{C}}$ = uniaxial compressive or shear strength.

Because the data necessary to determine the interaction terms F_{ij} have not been obtained, it was necessary to make certain assumptions. Conditions of stability require that the inequality

$$F_{ii} F_{jj} - F_{ij}^2 \ge 0$$
; i & j not summed,

be satisfied for the constants \boldsymbol{F}_{ij} entering the equation. It was assumed, therefore, that

$$F_{ij}^2 = F_{ii} F_{jj}$$
; i & j not summed.

It must be emphasized that this is merely an assumption about the interaction and that experimental results are required to determine the actual value. It is apparent that either a positive value or a negative value for F_{ij} will be satisfied by the above equation. The effect of both positive and negative values were considered, with minimum

factors of safety being produced by positive values. The fracture theory of Priddy is similar to the Tsai-Wu theory except that it allows the interaction terms for tension-tension and compression-compressions interactions to be independent of each other. The theory assumes failure to be describable as follows:

$$F_i \sigma_i + F_{ij} \sigma_i \sigma_j + F_{ijk} \sigma_i \sigma_j \sigma_k = 1$$

As can be seen, a cubic term is added in the Priddy theory. However, additional data are required over that for the Tsai-Wu theory. For the studies here the following assumptions were made:

- The ratio of biaxial compressive strength to uniaxial compressive strength was taken to be 1.
- The triaxial tensile strength factor was taken to be equal to the biaxial strength factor.

Both of the above assumptions are thought to be reasonable in light of limited test data on other brittle materials. With the above assumptions and the six biaxial normal stress conditions, all of the terms in the theory were then calculated.

The following equations for the "interaction theory" are presented to show that the interaction terms in this theory are assumed to be a function of the uniaxial strengths only.

$$\left(\frac{\sigma_1}{T_1}\right)^2 - \frac{\sigma_1 \sigma_2}{T_1 T_2} + \left(\frac{\sigma_2}{T_2}\right)^2 + \left(\frac{\tau_{12}}{T_6}\right)^2 = 1$$

$$\left(\frac{\sigma_2}{T_2}\right)^2 - \frac{\sigma_2 \sigma_3}{T_2 T_3} + \left(\frac{\sigma_3}{T_3}\right)^2 + \left(\frac{\tau_{23}}{T_5}\right)^2 = 1$$

$$\left(\frac{\sigma_3}{T_3}\right)^2 - \frac{\sigma_3 \sigma_1}{T_3 T_1} + \left(\frac{\sigma_1}{T_1}\right) + \left(\frac{\tau_{31}}{T_4}\right)^2 = 1$$

The publication by E.M Wu^[25] has considered the question of representation of failure from the general point of view of tensor polynomials and therefore includes as special cases most of the theories considered here.

where

 σ_i = applied stress in the ith direction

T_i = strengths in the ith direction

A point to be noted in the interaction theory is that since only uniaxial tension, compression, and shear strengths appear in the equations, there is no requirement for assumptions about biaxiality. This does not mean that the representation of failure of materials is any more or less reliable than other theories used.

Each of the failure theories were programmed and were used in conjunction with the SAAS III stress program to calculate a safety factor for each of the elements in the component being analyzed. The results of these calculations are presented in the following sections.

6.3.3 Residual Stresses

The design and analysis of all PG components must be concerned not only with the thermal and mechanical loads imposed by the application duty cycle, but with residual stresses that exist in the material in the absence of any applied loads. In closed shapes such as the nozzle throat inserts of Figures 2, 3, and 4, the residual stresses may be on the same order of magnitude as the firing stresses. The residual stresses may be due to several factors. These are as follows:

- a. Anisotropic material properties
- b. Nonhomogeneity in microstructure
- c. "Growth stress" effects due to thermal instability of the material structure
- d. Effect of substrate or mandrel stiffness and thermal expansion characteristics.

The largest factor causing the residual stresses in closed shapes is the anisotropic material properties together with the change from the deposition temperature (4,000°F) to room temperature. The other factors listed can, according to the results of earlier studies, [30] be significant and should therefore be considered. Unfortunately, the effects of these other factors have been quantitatively evaluated for only a limited number of cases, and no general procedure exists to treat the effects analytically.

The approach taken here was to evaluate the residual stresses assuming that the residuel stress resulting from effects other than anisotropy could be ignored. The validity of this assumption was then checked using results of strain gage measurements in residual stress tests and by correlation with manufactured parts. For reasons of this assumption and for other reasons as well, an objective of the deposition effects was to obtain a homogeneous microstructure. Also studies performed and reported in Reference 30 indicate that growth stress effects are minimal

when a frangible mandrel is used and breaks away during the cooldown process. The major unknown was then the exact microstructure that would be obtained by Pfizer for their pyrolytic graphite material. Two extremes were considered in the preliminary residual stress calculations. These were the microstructures obtained from a continuously nucleated and a substrate nucleated deposition process. Material properties, such as modulus and thermal expansion, were used in the studies that were considered representative of each of these PG types for calculating the residual stresses. The purpose of these preliminary studies was to define a reasonable bound on the thickness-to-radius ratio for both a CN and SN type pyrolytic graphite closed shape representative of an a-b plane nozzle insert. These thicknesses were to be used as a guideline for beginning the deposition studies. In addition to determining the stress state, a realistic failure criteria needed to be used for predicting the allowable thicknesses.

Based upon the data presented in Section 5.0, two sets of strength properties were considered. The first set of strength properties was based on average properties found in the literature for CN- and SN-type PG. The second set, in an effort to be as conservative as possible, was based on minimum strength properties reported irrespective of the test method or the material microstructure.

The failure theories discussed in Section 6.3.2 were used in conjunction with the two sets of strength properties to define a failure envelope. Once material properties for the particular PG material manufactured by Pfizer became available, a reanalysis of the residual stress state was performed. Limited residual stress tests using strain gages were also performed. The interaction of stress states, strength properties, and failure theories were then evaluated based on the results obtained for the actual manufactured parts.

6.3.3.1 Effects of Insert Length and Shape

The baseline a-b plane insert design was taken to be a 7.0-inch-diameter throat insert 4.40 inches long and 0.30 inch thick. The residual stresses in PG are very much dependent upon the shape of the part. Since insert designs which were longer than the baseline design were considered, residual stresses due to cooldown were determined to obtain the influence of the added length. Similarly, the possibility of using PG for the entrance cap offered definite advantages over materials. The residual stresses due to cooldown for entrance cap shapes were calculated to determine the effects of curvature.

Specifically the following cases were analyzed:

- a. 4.40-inch-long dual-layered insert
- b. 7.55-inch-long dual-layered insert
- Complete length PG shape which includes the entrance cap, insert, and exit piece all in one PG shape
- d. An entrance cap constructed of free-standing pyrolytic graphite.

Figure 85 shows the typical finite element nodal network used for the analysis. Included in the model is a special node located between the two layers which does not transfer loads. The reference temperature used for the analysis is 4,000°F.

The 4.40- and 7.55-inch long configurations were analyzed using both CN and SN properties. The entrance cap and complete length configurations were analyzed for CN material only.

For all the analyses, the inner layer exhibited the higher stresses although the outer layer had stress levels very similar to the inner layer.

The results of the calculations are summarized in Table 10 which presents the maximum radial stress, maximum shear stress, and maximum tensile and compressive hoop stresses which were obtained for each of the cases. For each of the first two cases, namely the 4.40-inch insert and the 7.55-inch insert, lower residual stresses are developed in the CN material than in the SN material. Increasing the length from 4.40 inches to 7.55 inches resulted in lower maximum hoop tension and compression for the CN material.

The maximum radial stress and maximum shear stress was increased. The same effect is observed for the case of the SN material with the exception of the maximum hoop compressive stresses which showed a very small increase.

In the case of the full length insert, the maximum hoop tension and compression are the same as those for the 4.40-inch insert. The maximum radial stress and maximum shear stress are less in the full length insert.

In the last case, entrance cap only, the maximum residual stresses, with the exception of the shear stress, are the lowest of all the cases considered.

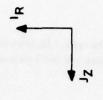
Therefore, for the CN material, the increased length and the entrance cap shape, result in similar or lower residual stresses than the baseline 4.40-inch insert, with one exception. The maximum radial and the maximum shear stress in the 7.55-inch insert are higher than the baseline 4.40-inch insert. On the bases of the test data presented in Section 5.0, all of these values appear to fall within the strength values for the material listed.

These results indicate that on the basis of residual stresses, no additional difficulties would be encountered by increasing the baseline 4.40-inch length.

6.3.3.2 Insert Thickness and Material Effects

As discussed earlier, the analytical definition of closed shape pyrolytic graphite component geometry based on residual stress calculations is dependent on the interaction of many parameters. An analytical study was performed whereby the following parameters were evaluated.

- a. Material properties CN- and SN-type PG material.
- Component thickness 0.15-inch to 0.45-inch thicknesses for the basic 4.40-inchlong insert.



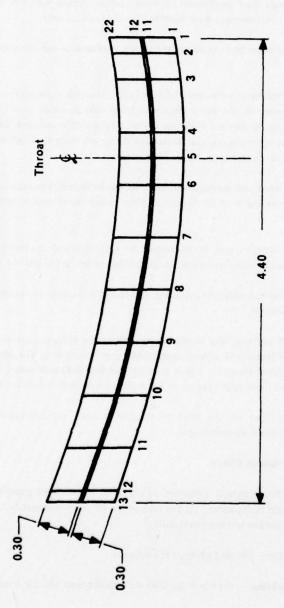


Figure 85. Typical Finite Element Mesh Used for the Stress Analysis of the PG Insert.

TABLE 10. STRUCTURAL COOLDOWN RESULTS.

Configuration	Nucleated Material	Max. Stress		Ноор	
		Radial	Shear	Tensile	Compression
4.40" Long	Substrate	425	388	12500	9200
	Continuous	305	289	8500	7200
7.55" Long	Substrate	699	625	10500	9500
	Continuous	524	520	7500	6500
Full Length	Continuous	258	198	8500	7200
Entrance Cap Only	Continuous	175	250	6500	4500

- c. Material strengths.
- Failure criteria.

The results of the study were used to define a thickness goal for the basic 4.40-inch-long insert assuming that the material exhibited was either CN or SN microstructure.

Figures 86 through 91 show typical stress distributions that were obtained for each of the analyses. Although the magnitudes of stress varied as thicknesses and/or material properties were varied, the following figures show the typical stress types and distributions obtained. The stress values are for a 0.30-inch-thick CN-type material. Figure 86 shows the axial (SIGN) and hoop (SIGT) stresses at the inner surface of the first layer. The maximum tensile stresses occur at the inner surface. Figure 87 shows the radial (SIGM) and shear (TAUMN) stresses at a point close to the middle of the inner layer. This is where the maximum radial stress and the maximum shear stress occurs. Finally, Figure 88 shows the hoop and axial stresses at the outer surface. This is the region where the maximum compressive stresses occur in the insert.

It is also of interest to note that the axial stress is of the opposite sign from the hoop stress at the inner and outer surfaces. Although the maximum stress on the OD of the insert is compressive hoop, the maximum tensile axial stress also occurs at the OD.

Figures 89 through 91 show the same results for a SN-type material. The stresses are all higher for the same thickness for the SN material as compared to the CN-type material.

One other point will be made about the stress fields, although it may be obvious. As the thickness is decreased for the same radius, the stresses are decreased. The effect of all the parameters considered in the analysis can best be shown by the set of plots presented in Figures 92 through 111. These plots show the safety factor distribution at the inner and outer surfaces of the insert as a function of both insert thickness and the failure theory used. The first series of plots are based on minimum strength values. The second set shows the effect of using an average set of strength properties as obtained from the literature.

Four failure theories are presented. These are the minimum stress ratio (MPFM), Priddy (PSFM), Tsai-Wu (TWFM), and the interaction theory (ITSFM). The letter M refers to minimum strength properties while the letter A refers to average strength properties. Referring to the figures, several trends about the calculated safety factors may be observed.

First, the Tsai-Wu theory results in the minimum safety factor for any insert configuration. The minimum stress ratio theory results in the highest factor — the other two theories being in between. The use of a minimum stress ratio, therefore, results in a very nonconservative approach to predicting failure. The interaction of stresses, particularly in the tension-compression, are shown to have a very significant effect. In fact for a 0.30-inch-thick insert, the MPFM factor is 1.2 while the TWFM is 0.91, as shown in Figure 93.

From Figures 92 through 97 another significant result is apparent. The safety factor using the TWFM theory is less at the OD of the insert than at the ID. For a 0.3-inch-thick insert, Figure 96, the minimum factor at the OD is 0.85 while at the ID the factor is 0.91, Figure 93. This suggests an OD failure for the insert, and this fact will be discussed later in relation to the manufactured parts.

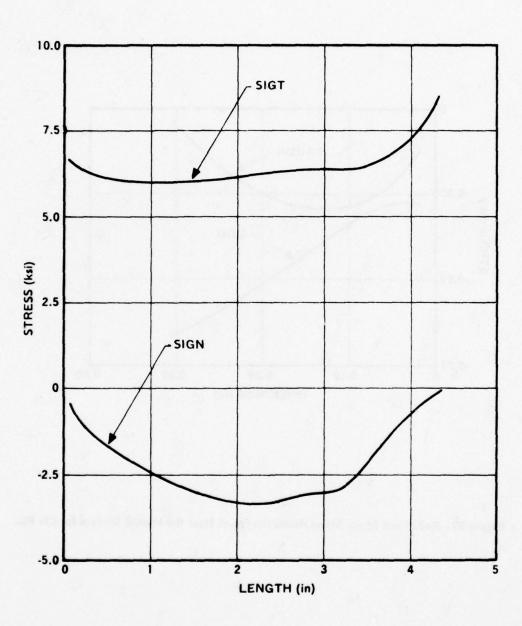


Figure 86. Axial and Hoop Stress Along the Inner Surface of the Insert for CN PG.

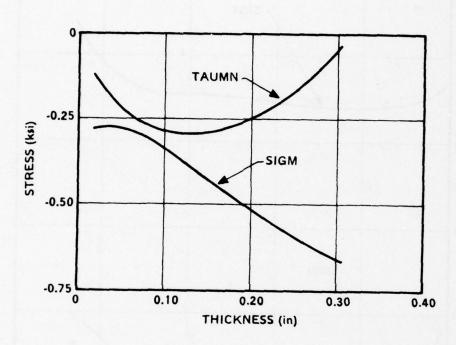


Figure 87. Radial and Shear Stress Along the Insert Near the Middle Surface for CN PG.

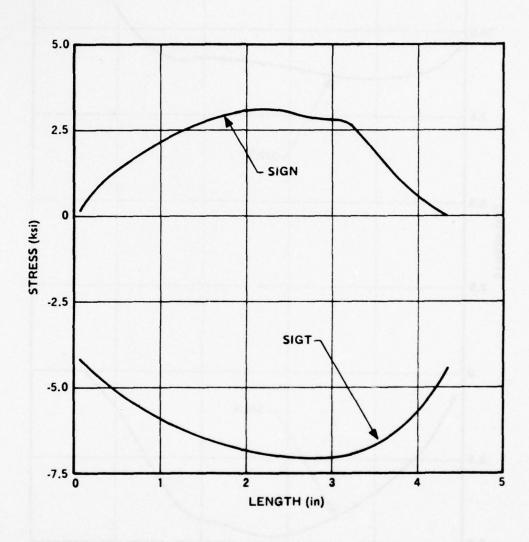


Figure 88. Axial and Hoop Stress Along the Outer Surface of the Insert for CN PG.

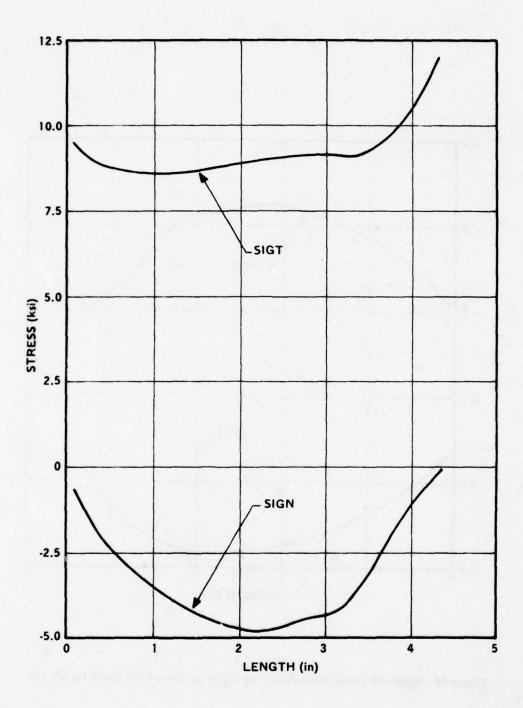


Figure 89. Axial and Hoop Stress Along the Inner Surface of the Insert for SN PG.

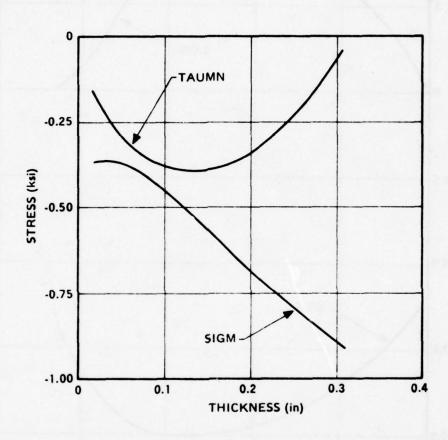


Figure 90. Radial and Shear Stress Along the Insert Near the Middle Surface for SN PG.

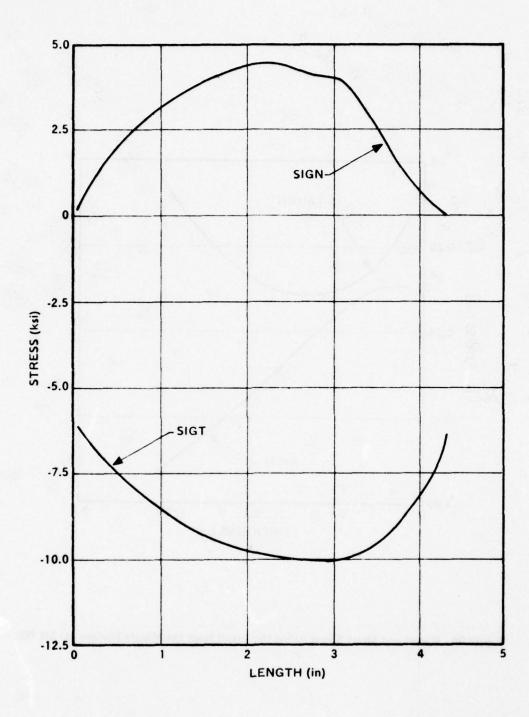


Figure 91. Axial and Hoop Stress Along the Outer Surface of the Insert for SN PG.

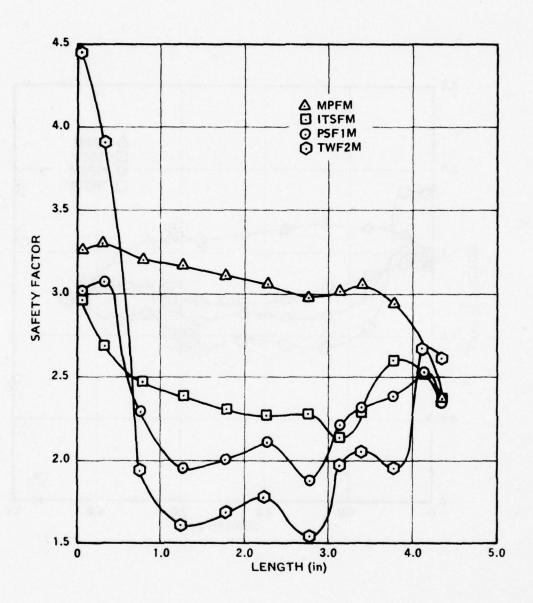


Figure 92. Safety Factors Along Inner Surface for 0.150 inch Thick CN PG.

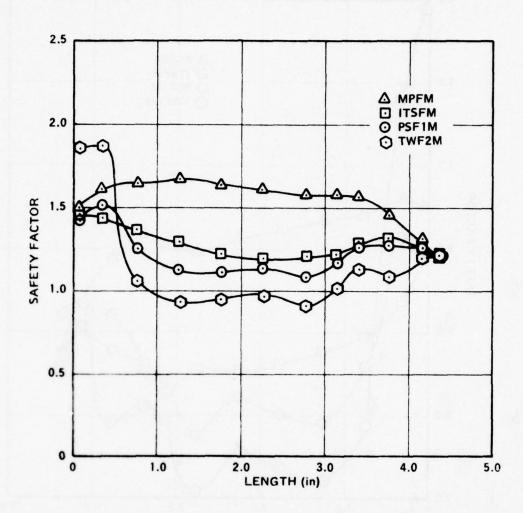


Figure 93. Safety Factors Along Inner Surface for 0.300 inch Thick CN PG.

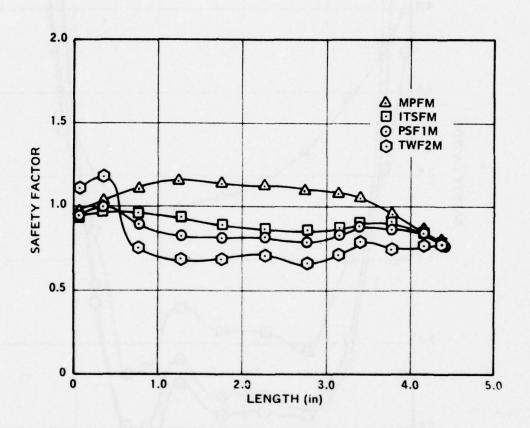


Figure 94. Safety Factors Along Inner Surface for 0.45 inch Thick CN PG.

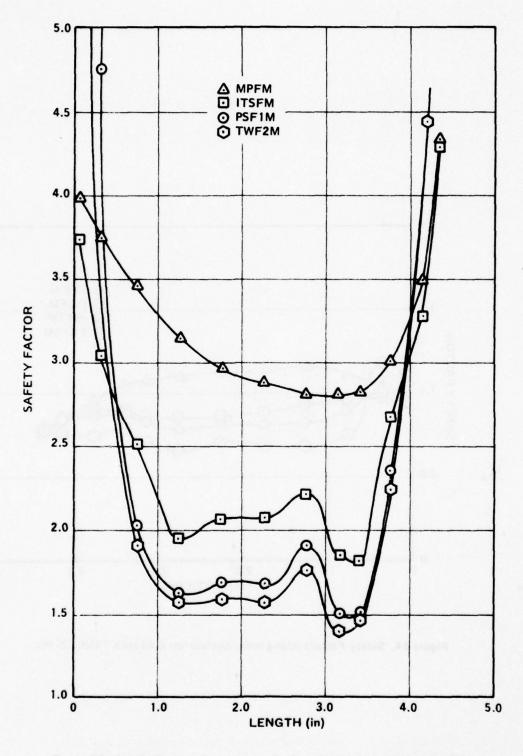


Figure 95. Safety Factors Along Outer Surface for 0.15 inch Thick CN PG.

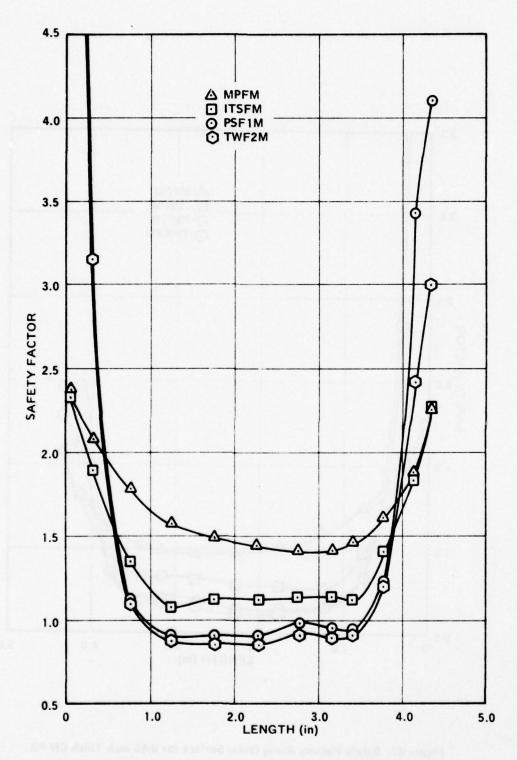


Figure 96. Safety Factors Along Outer Surface for 0.30 inch Thick CN PG.

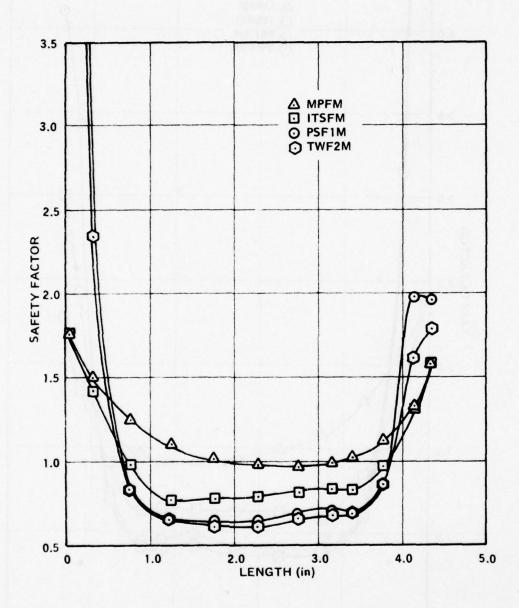


Figure 97. Safety Factors Along Outer Surface for 0.45 inch Thick CN PG.

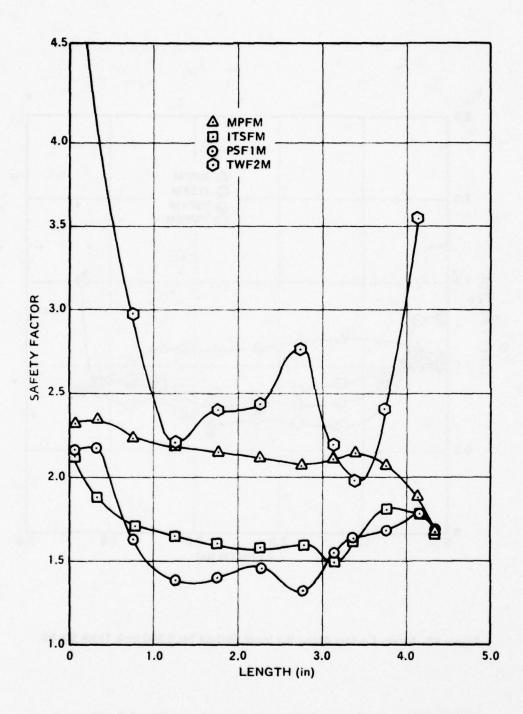


Figure 98. Safety Factors Along the Inner Surface for 0.15 inch Thick SN PG.

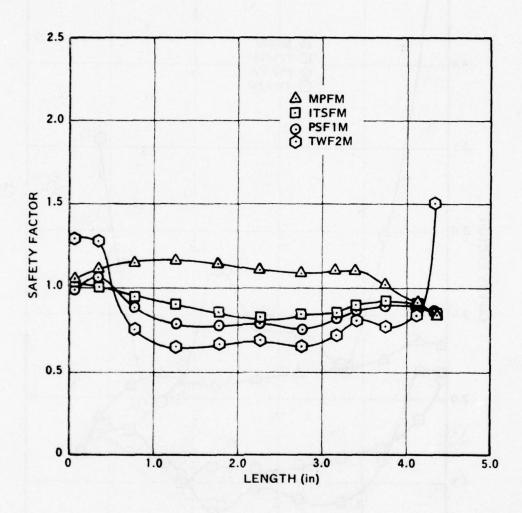


Figure 99. Safety Factors Along the Inner Surface for 0.300 inch Thick SN PG.

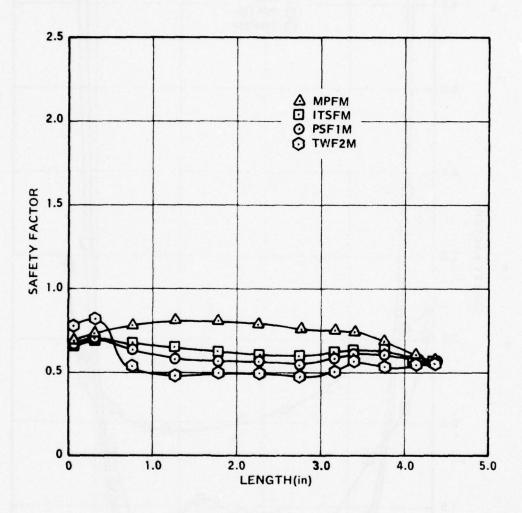


Figure 100. Safety Factors Along Inner Surface of 0.45 inch Thick SN PG.

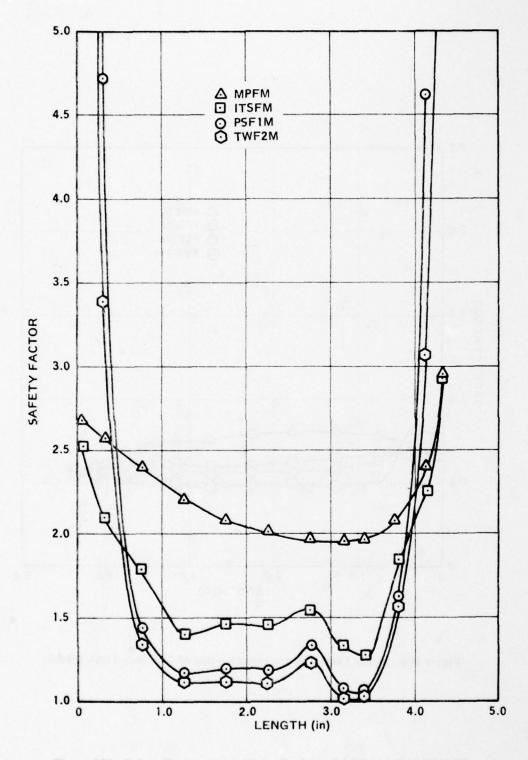


Figure 101. Safety Factors Along Outer Surface of 0.15 inch Thick SN PG.

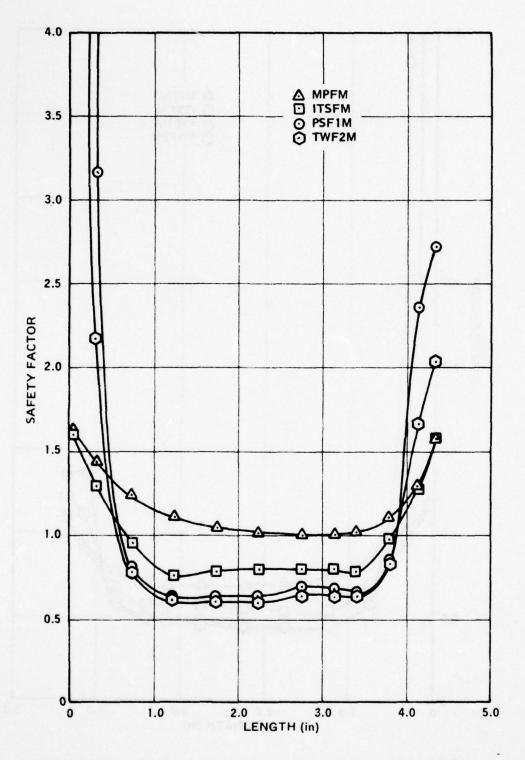


Figure 102. Safety Factors Along Outer Surface of 0.30 inch Thick SN PG.

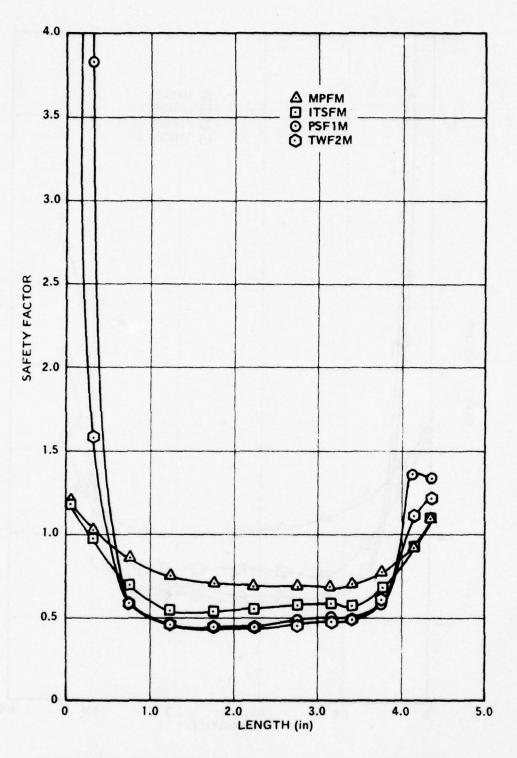


Figure 103. Safety Factors Along Outer Surface of 0.45 inch Thick SN PG.

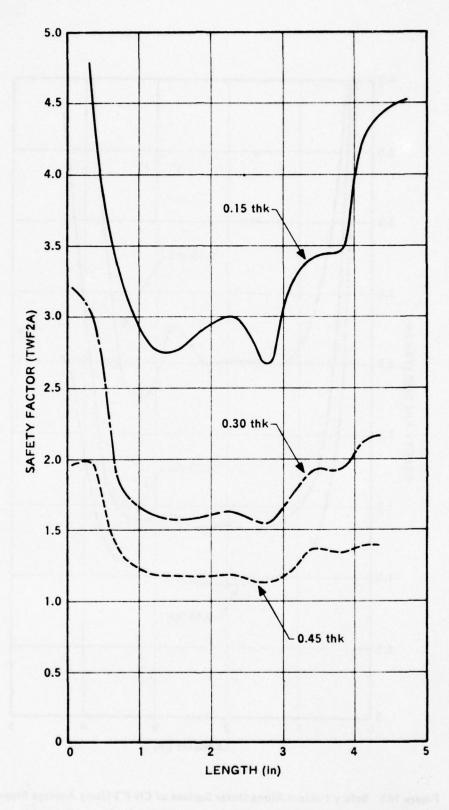


Figure 104. Safety Factors Along Inner Surface of CN PG Using Average Properties.

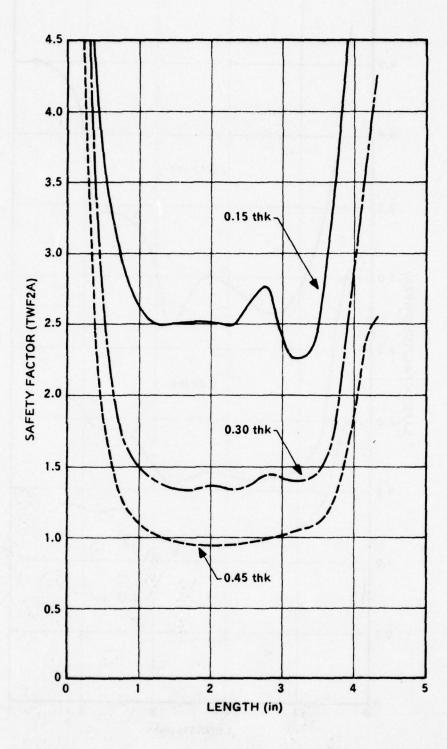


Figure 105. Safety Factors Along Outer Surface of CN PG Using Average Properties.

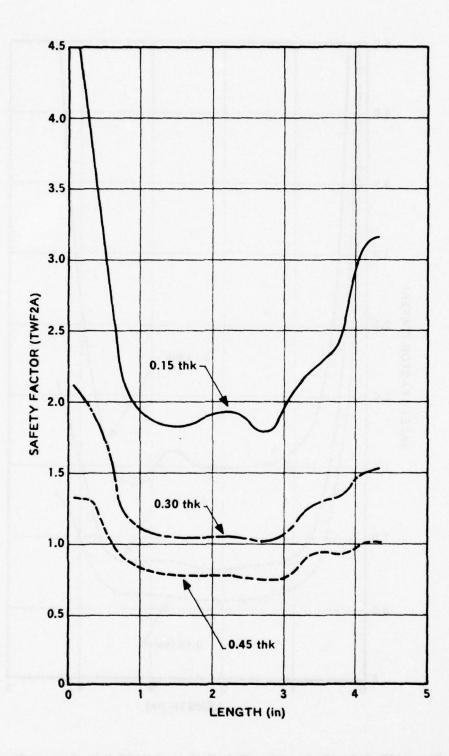


Figure 106. Safety Factors Along Inner Surface of SN PG Using Averages Properties.

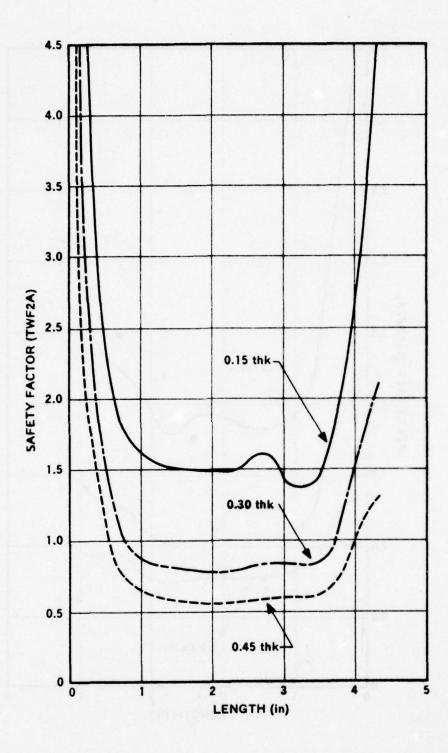


Figure 107. Safety Factors Along Outer Surface of SN PG Using Averages Properties.

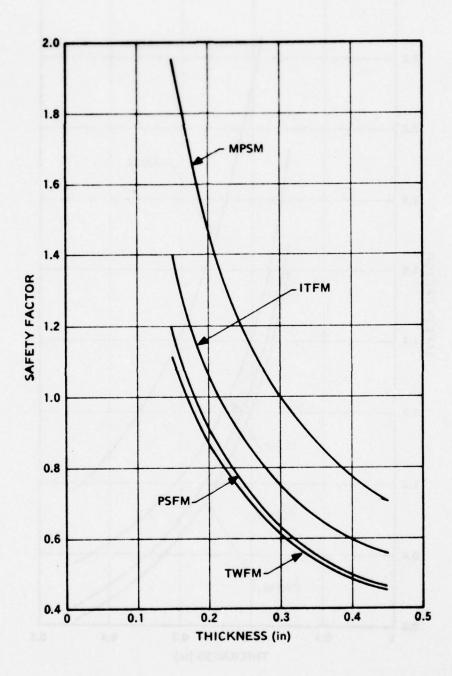


Figure 108. Minimum Factors vs Thickness for SN PG.

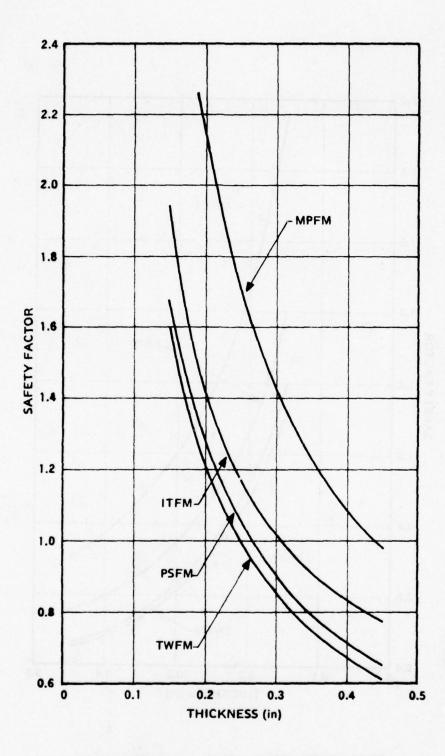


Figure 109. Minimum Factors vs Thickness for CN PG.

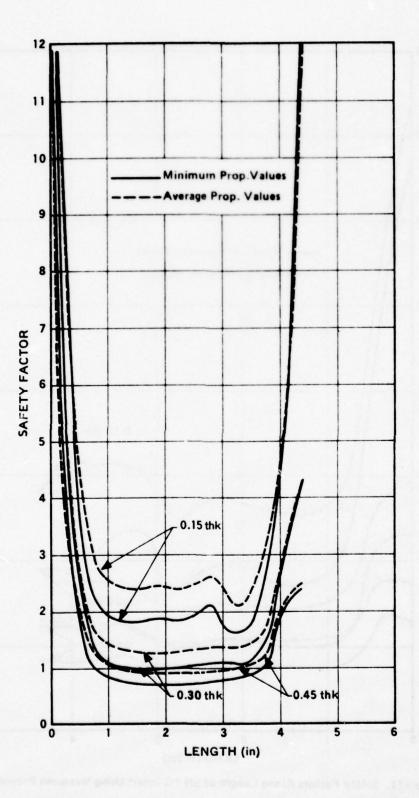


Figure 110. Safety Factors Along Length of CN PG Insert Using Measured Properties.

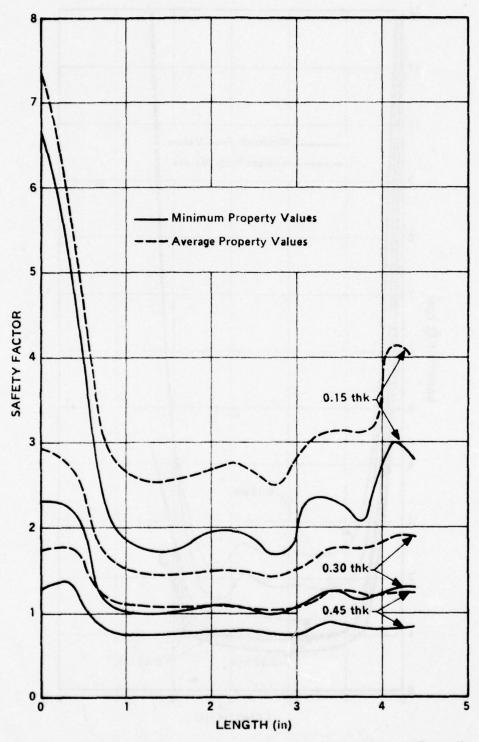


Figure 111. Safety Factors Along Length of SN PG Insert Using Measured Properties.

The results presented in Figures 98 through 103 show the factors of safety to be less for the SN-type material than for the CN-type material of Figures 92 through 97.

All of the above results are based on the minimum set of strength properties. Figures 104 through 107 show the safety factor distribution versus insert length at the ID and OD surfaces and as a function of thickness. These safety factors are shown for the TWFA theory only (the theory predicting minimum safety factors) and are based on the set of average strength allowables. As shown, the safety factors for a 0.30-inch-thick insert comprised of CN-type material are higher than the safety factors for an SN-type material with the same thickness. The minimum factor at the OD is 1.33 for a CN-type material, and only 0.79 for the SN-type material at the OD.

Completely different conclusions can be drawn from the following results depending on the set of parameters one uses to define an insert thickness.

A reasonable thickness assuming a CN-type PG and an average set of properties would be 0.30-inch. This was selected as the basis for beginning the deposition work.

However, based on the large scatter of strength data obtained for pyrolytic graphite and the other unknowns such as homogeneity of microstructure, type of microstructure, and possible thickness variations, a lower bond on thickness was desirable. Figures 108 and 109 show the minimum safety factor as a function of insert thickness using minimum strength properties. Figure 108 is for SN-type PG material while Figure 109 is for CN-type PG material.

The differences in predictions of the different failure theories is even more drastically shown in this figure. If one accepts a factor of 1.0 since minimum strength properties are assumed, the allowable thickness (Figure 109) for the CN material using the MPFM theory is approximately 0.43 inch. However, the TWFM theory results in a minimum thickness of approximately 0.25 inch.

Figure 108 shows the same results for the SN material. For the MPSF theory, the allowable thickness is 0.30 inch while for the TWFM theory the allowable thickness is approximately 0.17 inch.

The following study indicates that, based on a conservative approach to determining thicknesses, the maximum thickness for a CN material insert is approximately 0.25 inch. For a SN material this thickness is 0.170 inch. The analysis has pointed out that many parameters affect the above conclusion, and a foundation has been laid for a methodology that indicates the need for further study of failure and failure theories.

6.3.3.2.1 Reanalysis with Properties Obtained for the Pfizer Material

As stated in Section 5.0, the properties obtained for the Pfizer material were very similar to those for a CN material. However, strength data exhibited some degree of scatter. A reanalysis of the 4.40-inch-long insert was performed using the data obtained from the Pfizer material test program. Figures 110 and 111 show the factor of safety results obtained from this analysis.

The Tsai-Wu theory with assumptions as defined in Section 6.3.2 were used for calculating the factors of safety. Again two sets of strength properties were used. The first set was based on the mean strength values obtained

for the Pfizer material. The second set was based on the -2 σ variation and is called a minimum set of strength properties. Sufficient data was not available to do a meaningful statistical analysis, but a standard deviation was calculated to indicate the type of strength values one might obtain.

Again the minimum factor occurs at the outer surface. Based on mean strength values, the minimum factor of safety for the 0.30-inch-thick insert comprised of Pfizer material is 1.25. Based on the minimum strength value, the factor is approximately 1.0. The analysis predicts that an 0.30-inch-thick insert is very marginal and is subject to failure if minor changes in the stress state are imposed.

6.3.3.3 Residual Stress Tests

Two residual stress tests were performed using strain gage techniques. The procedure for performing the test was to bond strain gages to the ID of a pyrolytic graphite ring and to measure the strain relief obtained as material was removed from the OD of the ring.

Atlantic Research performed one residual stress test using a ring machined from the full scale deposited insert. The material was used from Pfizer Run number M-220. The ring configuration is shown in Figure 112. Four biaxial strain gages were bonded to the internal surface of the ring approximately 90 degrees apart. Fifty mils were removed from the external surface of the ring and strain gage readings were recorded. An additional 100 mils were removed from the external surface and strain gage readings were repeated. Finally the ring was split and the strain gages were isolated by machining away all surrounding material. The results of the strain gage readings are presented in Figure 113. This figure shows the hoop strain relief measured as a function of thickness of material removed. One of the gages was inoperative and therefore the results represent an average of the three remaining gages.

An analysis of the strain relief versus the thickness of material removed was performed using the SAAS III computer program and the properties obtained for the Pfizer material. These results are also shown on the figure.

Comparing the analytical and strain gage results, one sees that the total strain relief from the analysis was approximately 0.083 percent while the test indicated a total value of 0.077 percent. This represents approximately 7 percent difference.

Based on the many parameters involved in the analysis and the strain gage test itself, this agreement is very encouraging. In fact the difference is insignificant in comparison to the scatter that exists in the strength data. This agreement in results indicates that the assumptions in regard to minimum growth stress effects and uniformity in microstructure are fairly reasonable.

The other strain gage test was performed by the Aerospace Corporation. This test was performed on a 1.00-inch-long cylindrical ring with an inner diameter of approximatey 7.85 inches and a well thickness of 0.2 inch. The ring was machined from a cylinder of material made early in the program by Pfizer and the material was not considered to be representative of the final insert material.

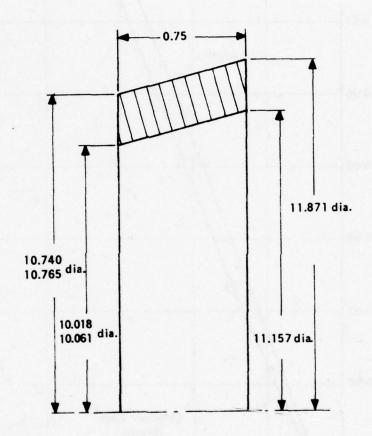


Figure 112. Residual Stress Test Ring Specimen Configuration.

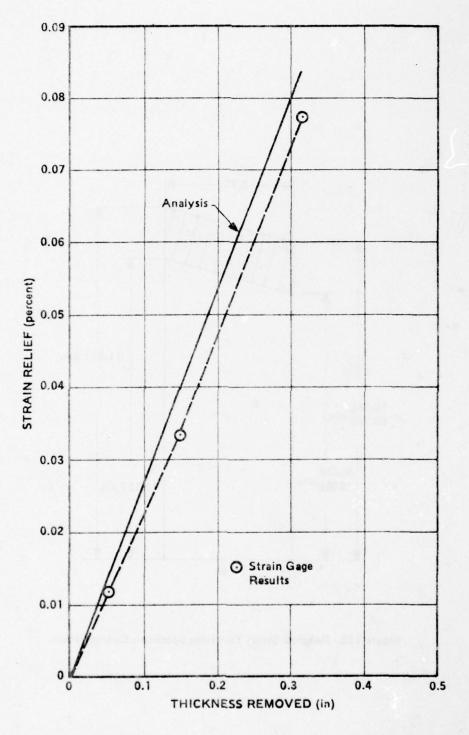


Figure 113. Strain Relief vs Material Removal in Residual Stress Test.

The results of the strain gage test performed by the Aerospace Corporation were "clouded" by the fact that the ring shattered during the final machine cut so the total strain relief could not be measured. An extrapolation of the data was made by Aerospace and a minimum and maximum bound on the total strain relief was projected. The results for total strain relief were approximately one-half of that predicted by analysis. Possible nonuniformity in microstructure could explain the above discrepancy. Also, a high degree of scatter in the strain gage readings were obtained.

6.3.3.4 Comparison of Analysis Results to Manufactured Component Behavior

A total of thirteen deposition runs were made by Pfizer in an attempt to manufacture the free-standing PG insert. Of the thirteen runs, eight runs were aborted due to processing problems. Run M-220 and Run M-224 resulted in inserts with abnormalities. In the case of M-220, a local spalling (surface release) of material occurred at the small diameter end. A longitudinal crack originated in the area of the spall.

A dense soot bridge, which had grown between the separator ring and the ID shape, initiated a crack in the part made from Run M-224. Hence, only the parts obtained from Run M-218, M-222, and M-225 can be discussed in relationship to their structural integrity based on residual stress effects.

Part M-218 was removed from the furnace, and initial visual inspection indicated no cracks. The average thickness of the part in the usable insert region was approximately 0.32 inch. The procedure at the time provided for removing the end separator rings by tapping the rings since the ring and insert were joined together by bridging of the deposited PG. This left a "ragged" edge on the insert component. After about 72 hours an OD spiral-type crack was observed. The crack initiated from the edge of the component. It was theorized that a flow, caused by the separation of the end rings from the insert component, grew under the residual stress field to its critical size and caused the crack. Flaw growth under a stress field has been observed in PG and is not uncommon. Based on the above assumption, a machining procedure was devised in which the ends of the insert were removed as soon as possible after cooldown of the insert. It should be pointed out that no cracking of the other remaining inserts can be attributed to time-dependent cracking. This leaves two inserts which should be discussed: Run M-222 and Run M-225.

This as-deposited part, M-222, was examined upon removal from the furnace, and no visual cracks were found on the ID or OD.

Both end rings were machined off the part, and the OD was machined to size. At this point, no cracks or delaminations were apparent. After final OD machining, a cut was made on the small diameter end of the trimmed part to permit it to fit inside the aluminum fixture. At this time the part cracked longitudinally at the ID, and a spiral crack occurred on the OD.

The as-deposited part, M-225, also contained no visual cracks upon removal from the furnace. Upon machining, a delamination and two hairline cracks occurred at the ID of the insert.

Both of the parts, M-222 and M-225, had average thicknesses greater than 0.30 inch. Based on the parametric residual stress studies, a maximum insert thickness of 0.27 inch was specified for Runs M-223, M-224, and M-225. However, this reduced thickness was never achieved. (Further discussions of the deposition conditions and results are discussed in Section 7.0.)

It is clear, based on the residual stress results and the behavior of the manufactured parts, that the 0.32-inch-thick insert was highly marginal. It is also clear that the residual stresses can be reduced by decreasing the insert thickness. The survivability of parts M-218, M-222 and M-225 indicate that the analysis results adequately predicted the residual stress fields. Also the failure of parts M-222 and M-225 can be attributed, in part, to increased stresses during machining.

The conclusion drawn here is that, with a reduced thickness insert (0.27 inch) and improved machining procedures, the residual stresses can be reduced by approximately 25 percent and a usable, structurally adequate free-standing insert is feasible.

6.3.4 Firing Stresses

6.3.4.1 Throat Insert Analysis

Extensive structural analyses were conducted for the baseline nozzle throat insert subjected to the nozzle pressure and temperature environment of the test firing conditions. The baseline insert was the insert shown in Figure 3, Section 4. That insert consists of two layers of pyrolytic graphite. Considered in this analysis effort were the effects of different temperature distributions (resulting from the different thermal boundary conditions discussed previously), the effects of material properties, and the effects of using only one layer of pyrolytic graphite for the insert.

Specifically, the following analyses were conducted:

- a. A comparative structural analysis in which the results at 15 seconds for a dual-layer concept were compared using temperature distributions obtained from: (1) an insert only thermal analysis, (2) a nozzle assembly thermal analysis, and (3) a nozzle assembly with front edge heating thermal analysis.
- An analysis of the dual-layer system for firing times of 2, 5, 15, and 60 seconds using CN PG material.
- c. An analysis of the above system for 15 and 60 seconds using SN material properties.
- d. An analysis of a single-layer system for firing times of 15 and 60 seconds using CN PG properties.

In all of the analyses which were performed, the following assumptions were made:

- a. The microstructure of the PG is homogeneous and residual stresses are only the result of anisotropic properties.
- b. Gap filler materials between layers of PG or between the PG and backup components remain essentially unchanged up to a temperature of 500°F. The filler materials then decompose to produce an effective gap equal to 60 percent of the assembly gap at a temperature of 1,000°F.

- c. The stress and strain states in the inner layer (the layer next to the exhaust gases) of a dual-layer design are much more critical than those in the second layer. Hence the analysis includes only one layer of PG with a boundary condition applied at the outer surface based on the temperatures of the second layer.
- d. Effects of microstructure "reordering" are small at temperatures of 5,700°F for the short nozzle firing times, and therefore may be neglected.

This baseline ab plane "free-standing" pyrolytic graphite insert nozzle design concept used for thermal-structural analysis is the dual-layer design using CN PG type material. The other cases analyzed are then compared with the baseline design. The SAAS III thermostructural analysis code was used for all of the firing stress predictions presented here. The properties used for these calculations are the preliminary properties established from the various literature sources and presented in Section 5.0. The material properties obtained from the results of the tests conducted at Southern Research Institute and presented in Section 5.0 were not available at the time these calculations were performed. The temperature distributions used for these analyses are those based upon the NAFE thermal model presented in Section 6.2.5. The erosion values for the inserts are the values presented earlier in this section.

For the nonthermal boundary conditions it was assumed that the bond line between the single layer PG insert and the ATJ backup material, or the bond line between the first and second PG layers of the dual layer design, decomposed at 500°F. Above 500°F, therefore, the bond line was assumed to be incapable of sustaining tensile or shear loads. In effect a sliding boundary was imposed at bond lines that exhibited temperatures above 500°F. This was accomplished by using thin finite elements with the appropriate stiffness characteristics (low shear and hoop moduli). Also the skew boundary option of the SAAS III program was utilized at the bond lines to direct the backside boundary displacements along the actual geometric shape of the PG layer.

Pressure distributions along the length of the inserts were calculated assuming an isentropic expansion of the gases through the nozzle. The values of pressure applied to the ends of the insert were based on the local area ratio at the particular axial location.

The results of the thermostructural analysis of the firing conditions for the baseline dual layer insert configuration with CN pyrolytic graphite are presented in Figures 114 through 145. The results which are shown in these figures summarize the conditions which arise in the regions of the insert which are or could be critical areas of the insert from a structural integrity point of view. That is, in certain key regions of the nozzle insert, relatively high stress (or strain) levels are developed which could lead to failure. For example, excessive compressive stresses or strains at the inner surface of the insert are a likely cause for failure. Hence, the hoop (SIGT) and axial (SIGN) stresses at the ID of the insert versus insert length are shown. The shear (TAUMN) and radial (SIGM) stresses are, on the other hand, insignificant at the ID of the insert, and therefore are not presented.

Delaminations of the PG represent another likely failure mode. Conditions leading to delaminations are considered to be those which cause excessive interlaminar shear stresses within the insert. The peak shear stresses occur at the entrance and exit ends of the insert at a distance approximately one-half the thickness from the inner surface. Therefore, the hoop (SIGT), axial (SIGN), shear (TAUMN), and radial (SIGM) stresses versus insert thickness are plotted for the regions near the entrance and exit planes for each of the firing times.

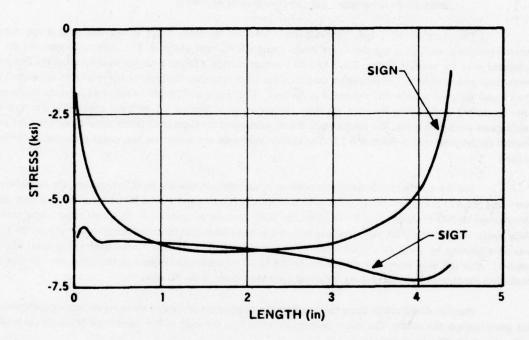


Figure 114. Axial and Hoop Stress Along the Inner Surface of the Insert at 5 Seconds for CN PG.

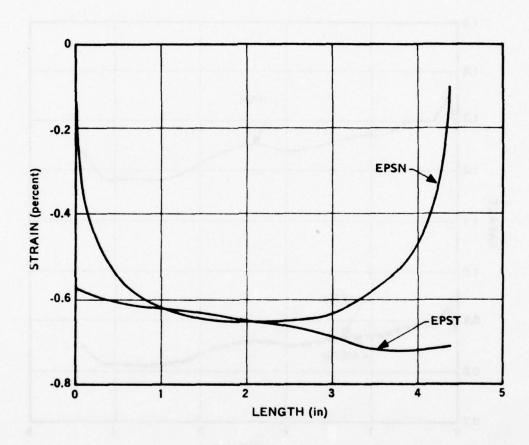


Figure 115. Axial and Hoop Strain Along the Inner Surface of the Insert at 5 Seconds for CN PG.

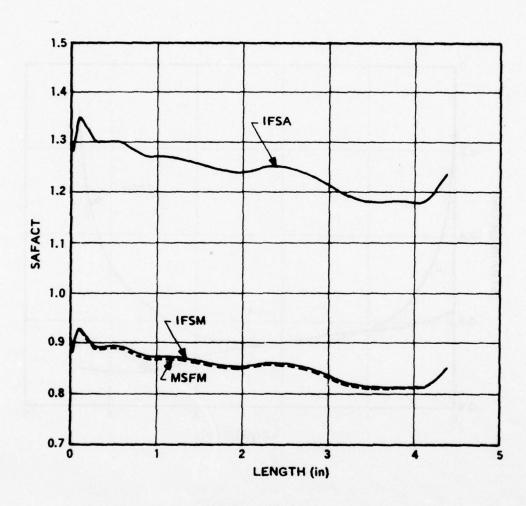


Figure 116. Safety Factors Along the Inner Surface of the Insert at 5 Seconds for CN PG.

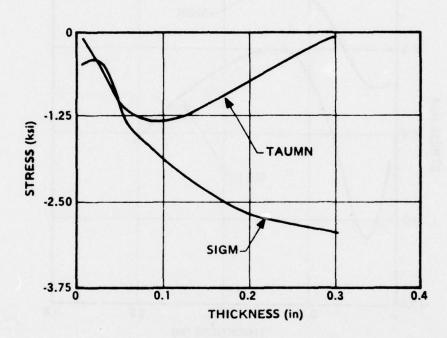


Figure 117. Shear Stress and Radial Stress at the Entrance End of the Insert at 5 Seconds in CN PG.

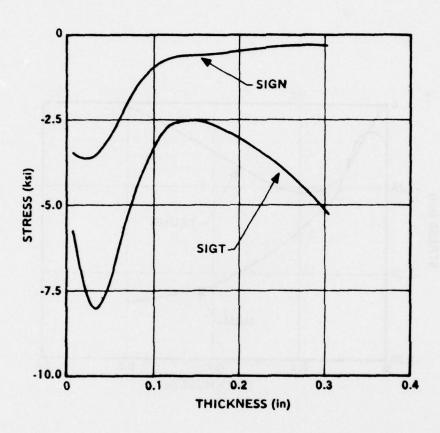


Figure 118. Axial and Hoop Stress at the Entrance End of the Insert at 5 Seconds in CN PG.

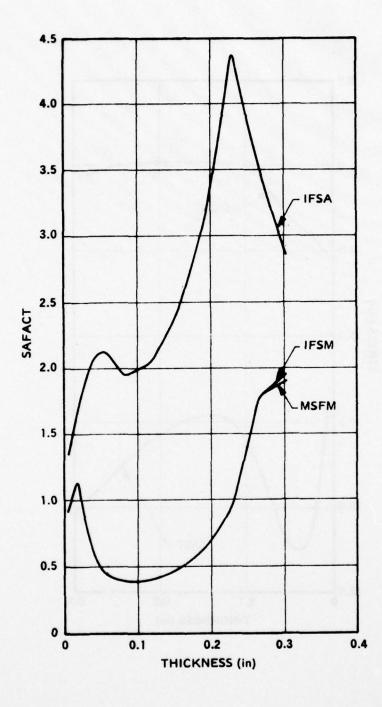


Figure 119. Safety Factors at the Entrance End of the Insert at 5 Seconds in CN PG.

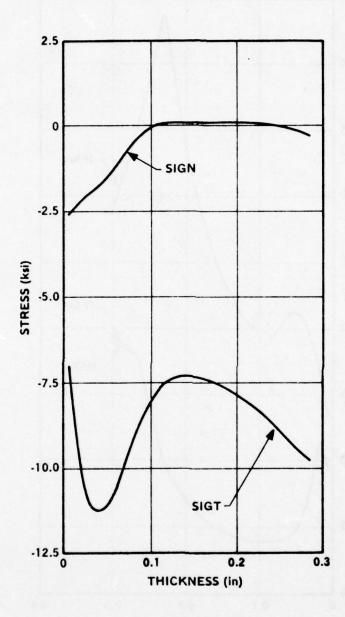


Figure 120. Axial and Hoop Stress and the Exit End of the Insert at 5 Seconds in CN PG.

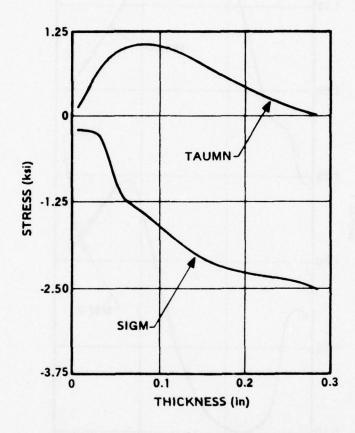


Figure 121. Shear and Radial Stress at Exit End of the Insert at 2 Seconds for CN PG.

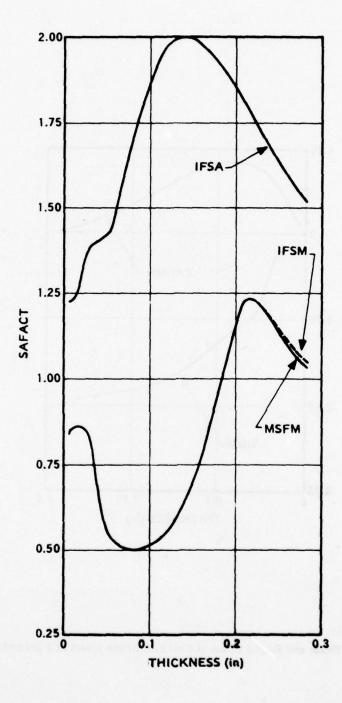


Figure 122. Safety Factors at Exit End of the Insert at 5 Seconds in CN PG.

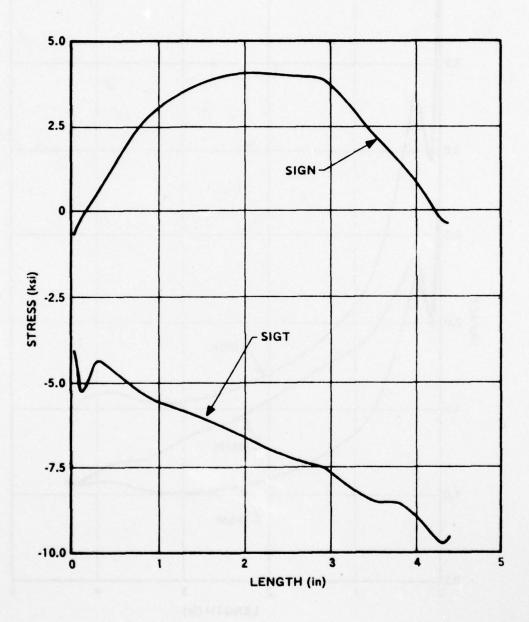


Figure 123. Axial and Hoop Stress Along Outer Surface of the Insert at 5 Seconds in CN PG.

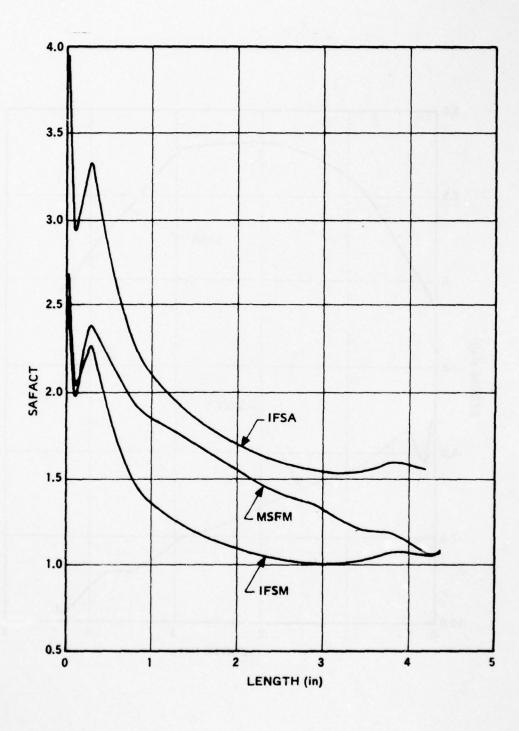


Figure 124. Safety Factors Along Outer Surface of the Insert at 5 Seconds in CN PG.

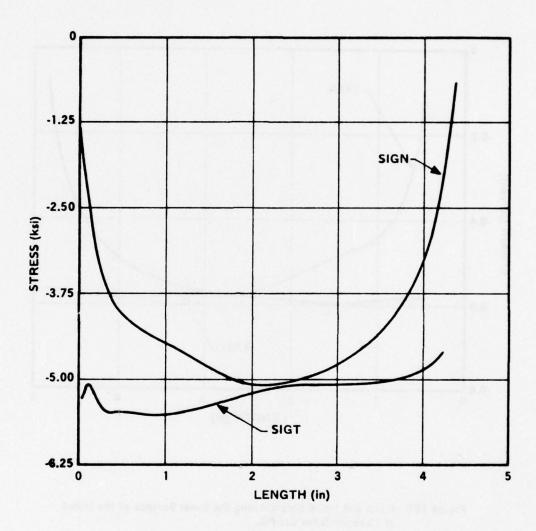


Figure 125. Axial and Hoop Stress Along the Inner Surface of the Insert at 15 Seconds for CN PG.

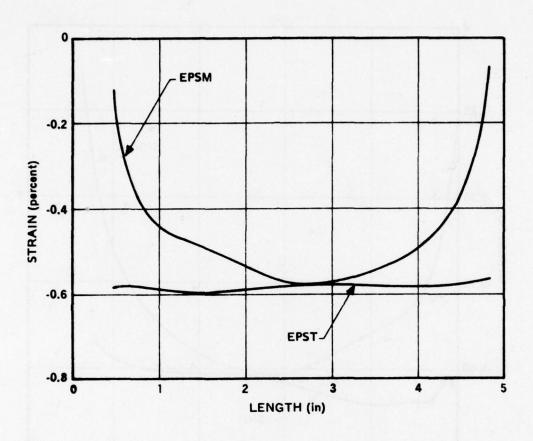


Figure 126. Axial and Hoop Strain Along the Inner Surface of the Insert at 15 seconds for CN PG.

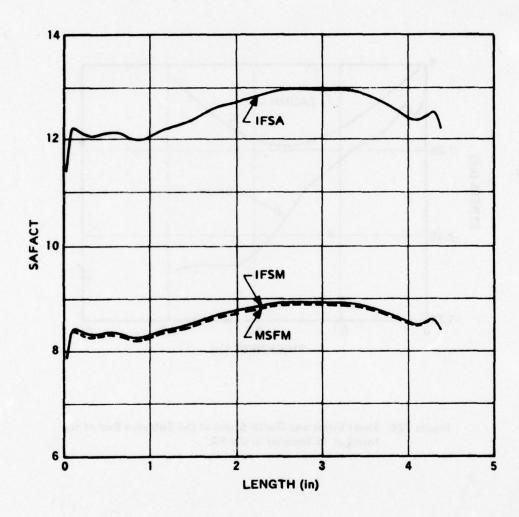


Figure 127. Safety Factors Along the Inner Surface of the Insert at 15 Seconds for CN PG.

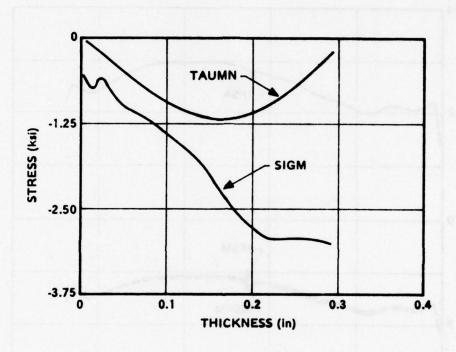


Figure 128. Shear Stress and Radial Stress at the Entrance End of the Insert at 15 Seconds in CN PG.

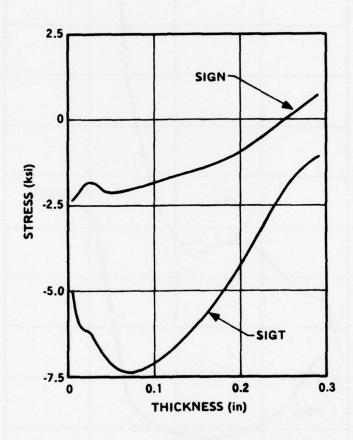


Figure 129. Axial and Hoop Stress at the Entrance End of the Insert at 15 Seconds in CN PG.

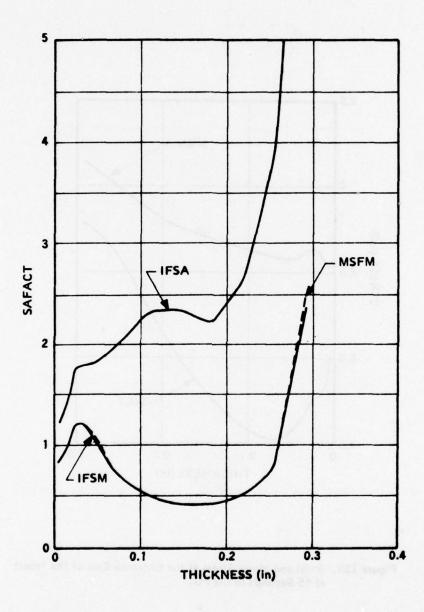


Figure 130. Safety Factors at the Entrance End of the Insert at 15 Seconds in CN PG.

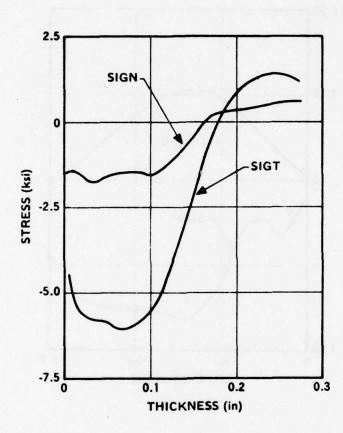


Figure 131. Axial and Hoop Stress and the Exit End of the Insert at 15 Seconds in CN PG.

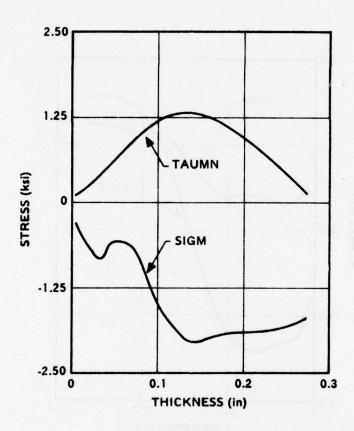


Figure 132. Shear and Radial Stress at Exit End of the Insert at 15 Seconds for CN PG.

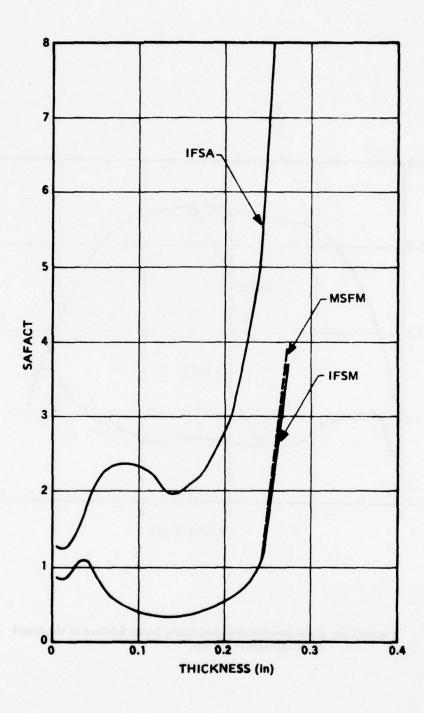


Figure 133. Safety Factors at Exit End of the Insert at 15 Seconds in CN PG.

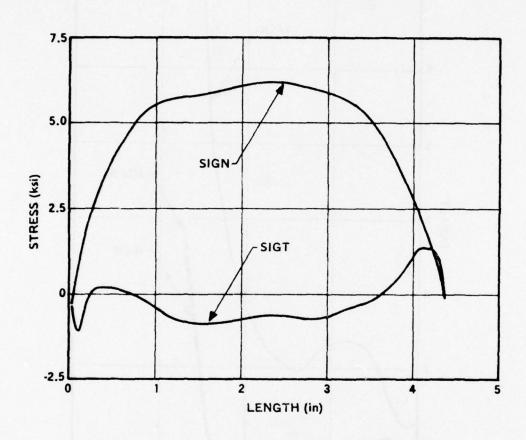


Figure 134. Axial and Hoop Stress Along Outer Surface of the Insert at 15 Seconds in CN PG.

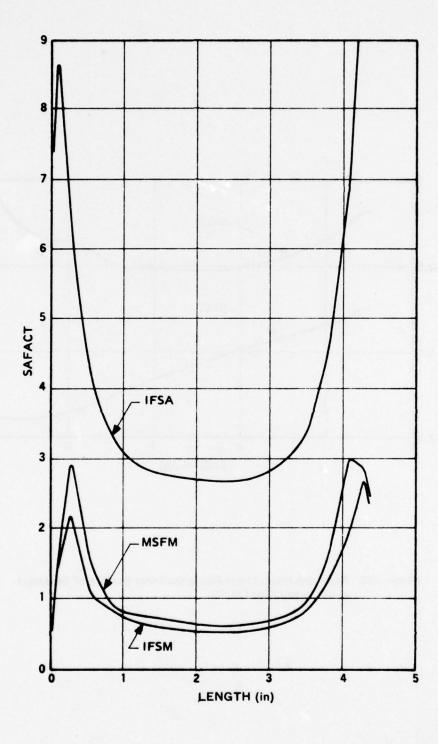


Figure 135. Safety Factors Along Outer Surface of the Insert at 15 Seconds in CN PG.

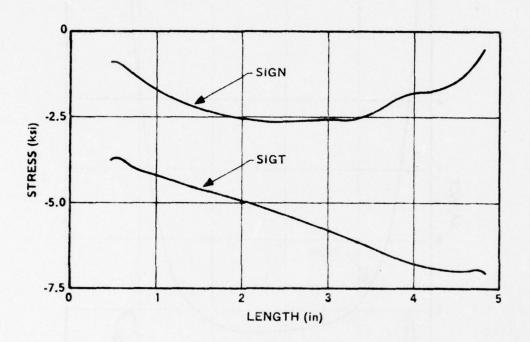


Figure 136. Axial and Hoop Stress Along the Inner Surface of the Insert at 60 Seconds for CN PG.

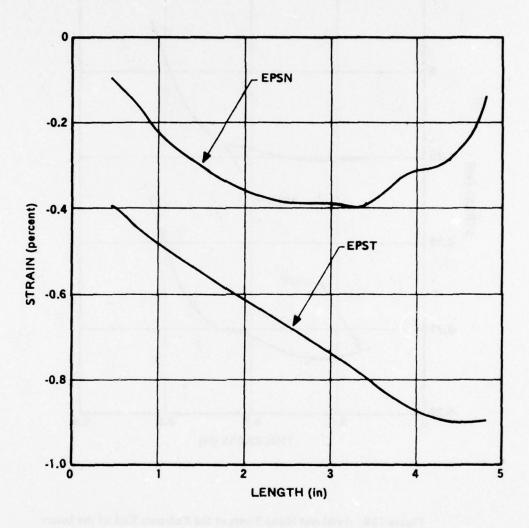


Figure 137. Axial and Hoop Strain Along the Inner Surface of the Insert at 60 Seconds for CN PG.

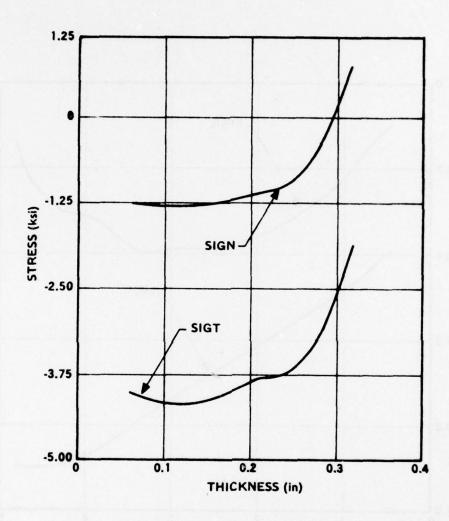


Figure 138. Axial and Hoop Stress at the Entrance End of the Insert at 60 Seconds in CN PG.

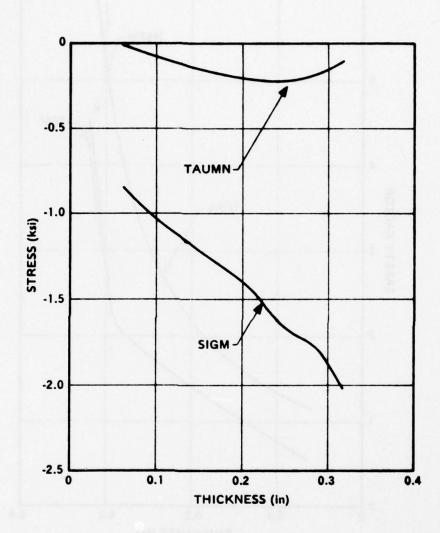


Figure 139. Shear Stress and Radial Stress at the Entrance End of the Insert at 60 Seconds in CN PG.

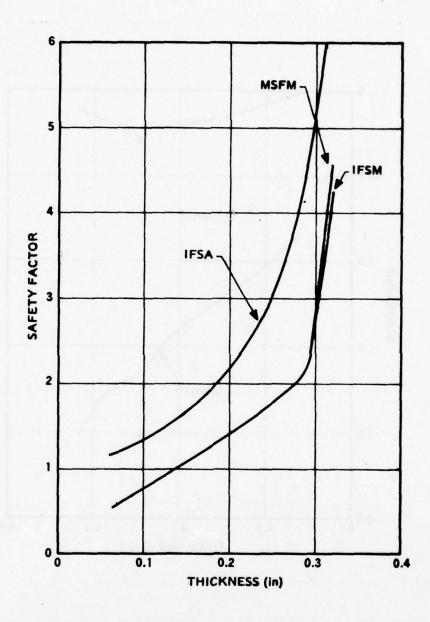


Figure 140. Safety Factors at the Entrance End of the Insert at 60 Seconds in CN PG.

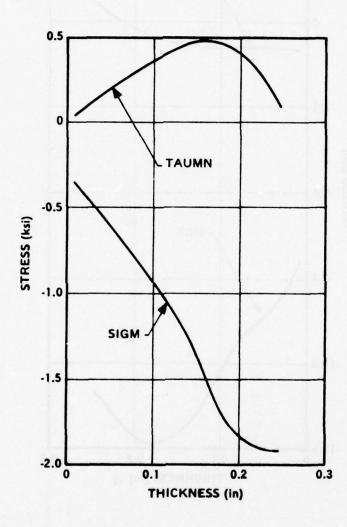


Figure 141. Shear and Radial Stress at Exit End of the Insert at 60 Seconds for CN PG.

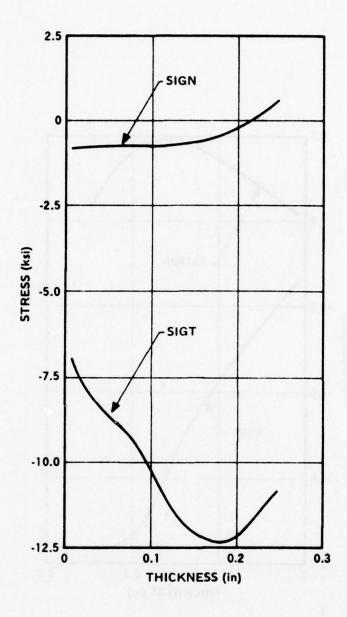


Figure 142. Axial and Hoop Stress and the Exit End of the Insert at 60 Seconds in CN PG.

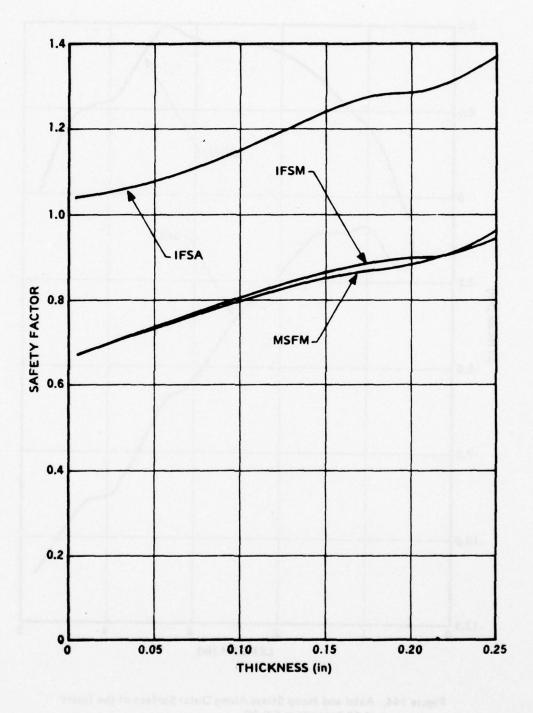


Figure 143. Safety Factors at Exit End of the Insert at 60 Seconds in CN PG.

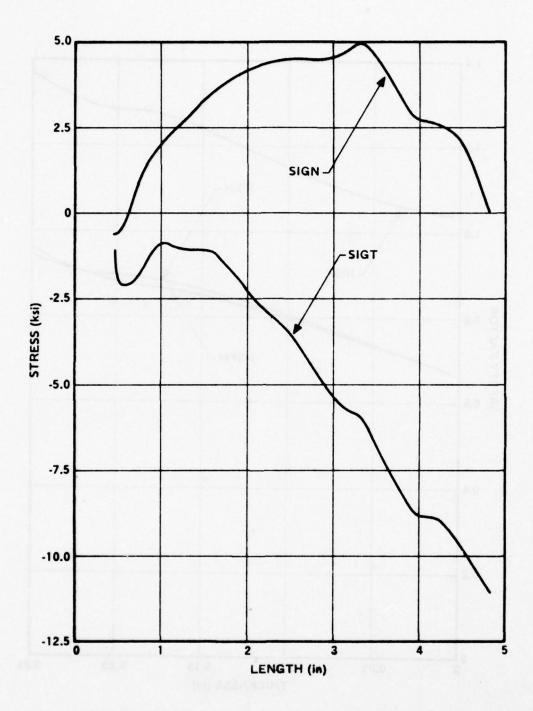


Figure 144. Axial and Hoop Stress Along Outer Surface of the Insert at 60 Seconds in CN PG.

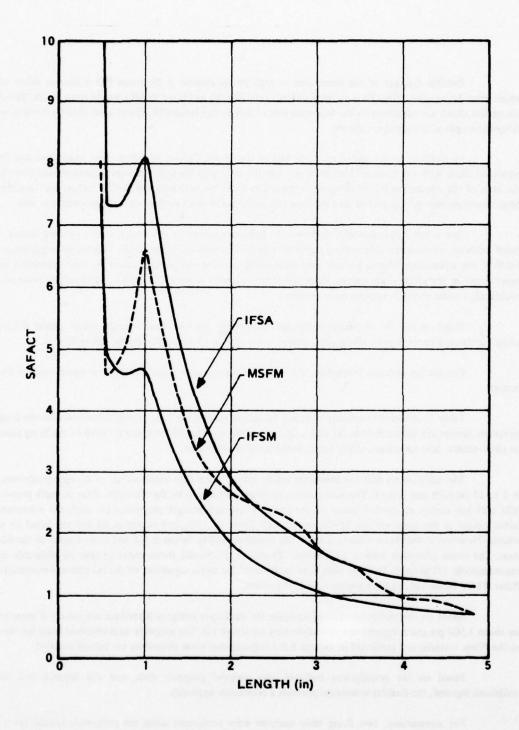


Figure 145. Safety Factors Along Outer Surface of the Insert at 60 Seconds in CN PG.

Possible fracture of the insert due to high tensile stresses at the insert OD is another mode of failure which must be avoided. The OD is a region of both axial (SIGN) and hoop (SIGT) tensile stress states. Therefore, in the results which are presented in the following sets of figures, the hoop (SIGT) and axial (SIGN) stress distribution along the length of the insert are shown.

In addition to the states of stress and/or the strain, factors of safety were calculated and these are presented along with the stress and strain values. For the most part the safety factors presented were determined on the basis of the interaction failure criterion or the minimum stress ratio criterion. Safety factors are calculated based upon minimum strength properties, and they are calculated based upon average strength properties as well.

One other criterion was considered. At the inner surface of the insert, where yielding occurs, a strain based criterion was used to determine a factor of safety. The reason for this is the fact for at temperatures above 5,000°F the stress-strain curves are not well established and the stresses calculated are very dependent upon the exact shape of the stress-strain curves. Since the strain is largely thermally induced and therefore more accurately calculated, a strain criterion appears more realistic.

Based on the set of minimum strength properties, the low shear strength values greatly influence the safety factors and hence regions where shear stresses are significant result in the lowest safety factors.

For average strength properties, the regions of maximum compressive stress or strain result in the lowest factors.

Table 11 shows the summary of safety factors calculated for 2, 5, 15, and 60 seconds for the design. The minimum factors are shown for the ID, OD, exit, and entrance planes of the insert for each of the firing times based on stress results. Also shown is a safety factor based on allowable strain.

The table shows that the minimum safety factor, based on a minimum set of strength properties, occurs at 2 to 15 seconds and is 0.33. This safety factor is mostly influenced by the allowable shear strength property used (525 psi) and occurs at the exit plane of the insert. If average strength properties are used, the minimum safety factor occurs at the inner surface of the insert. This factor is 1.03, and occurs at 60 seconds based on strength criteria. However, if the strain criteria is used, the minimum safety factor is 1.1 and occurs again at the 60-second time. The strain allowable used is 1.0 percent. Therefore, 60-second strain states require an allowable strain of approximately 1.0 percent. Material tests have determined the strain capability of the PG material manufactured by Pfizer. These values obtained are greater than 1.35 percent.

Based on the thermal-structural analysis, the dual-layer design will perform adequately if shear strengths are above 1,500 psi and compressive strain allowables are above 1.0. The property data obtained from the test results on the Pfizer material and presented in Section 5.3.3 indicate that these allowables are indeed satisfied.

Based on the assumptions outlined, the material property data, and the thermal and boundary conditions inputed, the dual-layer concept provides a reasonable approach.

For comparison, two firing time analyses were performed using the properties typical for a SN PG material. These analyses were performed at firing times of 15 and 60 seconds. The same stress, strain, and safety

TABLE 11. SUMMARY OF SAFETY FACTORS DUAL LAYER DESIGN - CN MATERIAL.

Time (Sec)	SFE	SFID*	SFOD*	SFENT*	SFEXT*
2	0.62 ^Δ	0.98	1.05	0.46	0.33
	(1.61)	(1.42)	(1.58)	(1.68)	(1.50)
5	0.73 [△]	0.81	1.0	0.405	0.5
	(1.36)	(1.18)	(1.5)	(1.35)	(1.22)
15	0.6 [△]	0.78	0.52	0.40	0.37
	(1.67)	(1.13)	(2.67)	(1.20)	(1.23)
60	0.9 [△]	0.68	0.76	0.48	0.68
	(1.11)	(1.03)	(1.22)	(1.16)	(1.03)

SFE - Safety Factor Based on Maximum Strain

SFID - Safety Factor at I.D. of Insert

SFOD - Safety Factor at O.D. of Insert

SFENT - Safety Factor at Entrance End of Insert

SFEXT - Safety Factor at Exit End of Insert

- () Indicate S.F. Based on Average Strength
 Properties/Other Factor Based on Minimum Strengths
- * Safety Factor Based on Multi-Axial Stress Failure Criteria
- △ Represents Strain Values & Not Safety Factor

factor results, as shown for the analysis using CN PG material properties, are presented in Figure 146 through Figure 165 for the SN PG material properties.

Table 12 shows the resulting set of safety factors. Again, based on minimum strength properties, the minimum safety factor (0.56) exists at the exit end at 15 seconds. The shear stresses developed are the major contributor to the low safety factors. For the average set of properties, the minimum factor exists at the outer surface at the exit end of the insert. This factor is 0.79, and is due to the high compressive stresses at the OD of the insert. These compressive stresses are greater than for the CN material case since the residual compressive stresses are higher for a SN type PG material. The analysis, therefore, shows that, based on average properties, the hoop compressive stresses result in a factor of safety at 60 seconds which is less than 1.0.

Therefore, a SN PG material insert results in a lower factor of safety than for a CN PG material. Further analyses could be performed, however, with a thinner SN material insert, and a design could result that exhibited acceptable margins of safety. In summary, an insert fabricated with SN PG material will result in a more marginal design than one fabricated with CN PG material.

From a fabrication viewpoint, an insert design consisting of a single layer of a-b plane PG backed up by an ATJ substrate is desirable due to its simplicity. Therefore, an analysis was performed for a single-layer concept, and a comparison of the stress and strain states for the dual and single layer was made.

The results for a single-layer and dual-layer design are presented in Figures 166 through 169. The results are shown for 15 and 60 seconds. Only small differences exist in the results for firing times up to 15 seconds. Figure 166 presents the hoop stress distributions through the coating thickness for a single and dual layer at times of 15 and 60 seconds. These results are shown for the exit plane where the stresses are maximum. The results indicate that the hoop stresses at 15 seconds are much higher for the single-layer design than for the dual-layer design. The reason for this is that the temperature gradients for the single-layer design are greater and the temperatures at the back surface of a single-layer design are less due to the higher conductivity of the ATJ backup material. The lower temperatures result in no degradation of the gap filler material for a single-layer design while, for the dual layer, the gap filler material has completely decomposed. Hence the radial deformation for a single-layer design is less as a function of firing time.

For the 60-second firing time, the hoop stresses for the dual-layer design are greater than those for a single-layer design due to the higher temperature of the inner layer. However, the stresses are not quite as different for the two designs as at the 15-second time.

Figure 167 shows the strain distribution through the thickness. Due to the higher radial restraint, the maximum strain at the inner surface of the coating occurs at 15 seconds for the single-layer design. This value is slightly less than 1.0 percent. The strain is then reduced to approximately 0.8 percent at 60 seconds. For the dual-layer design, the strain increases over the total firing time and is a maximum of 0.9 percent at 60 seconds.

The above results are based on an effective gap of 10 mils behind the inner-layer insert and a gap decomposition temperature of $500^{\circ}F$.

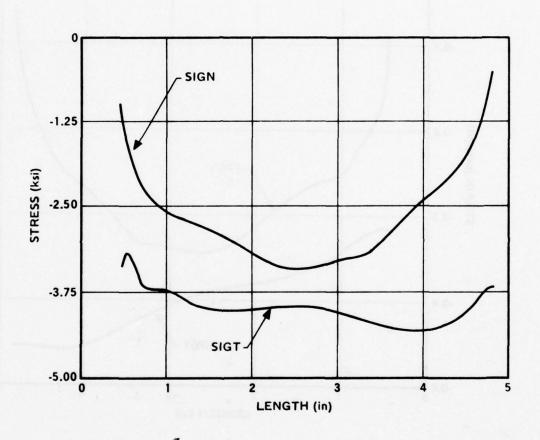


Figure 146. Axial and Hoop Stress Along the Inner Surface of the Insert at 15 Seconds for SN PG.

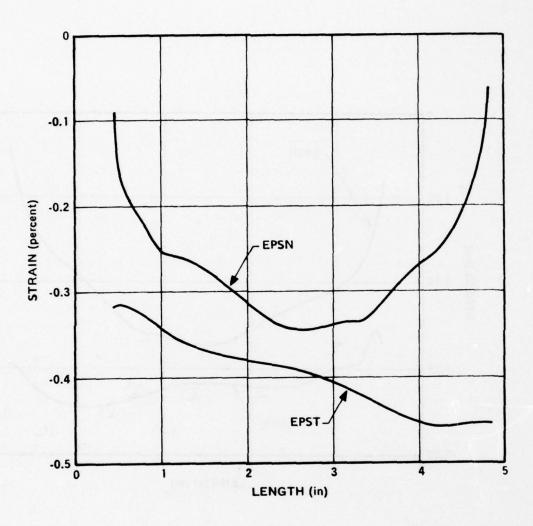


Figure 147. Axial and Hoop Strain Along the Inner Surface of the Insert at 15 Seconds for SN PG.

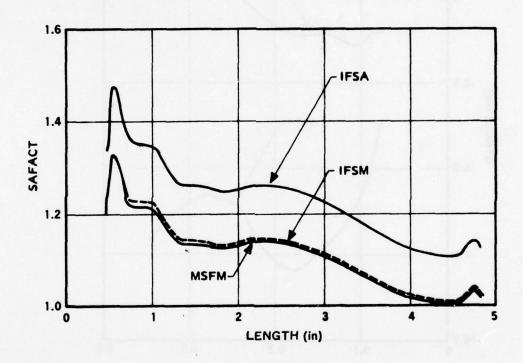


Figure 148. Safety Factors Along the Inner Surface of the Insert at 15 Seconds for SN PG.

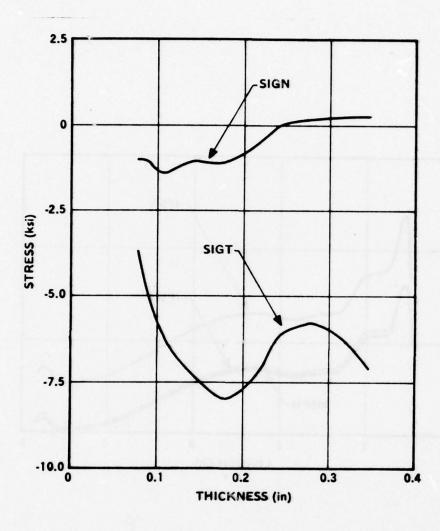


Figure 149. Axial and Hoop Stress and the Exit End of the Insert at 15 Seconds in SN PG.

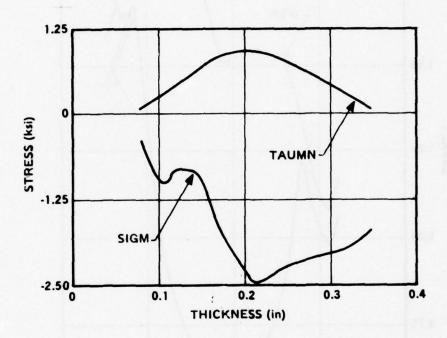


Figure 150. Shear and Radial Stress at Exit End of the Insert at 15 Seconds for SN PG.

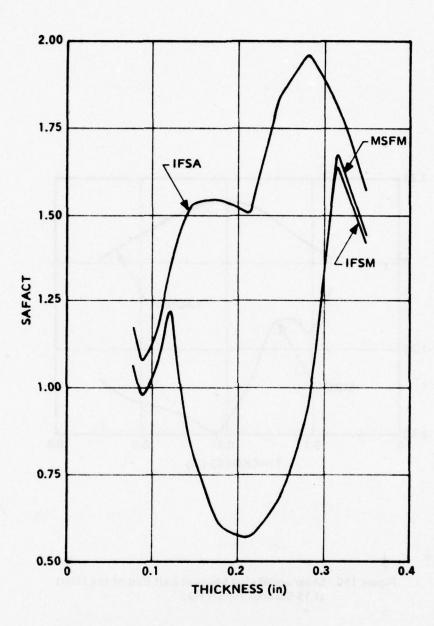


Figure 151. Safety Factors at Exit End of the Insert at 15 Seconds in SN PG.

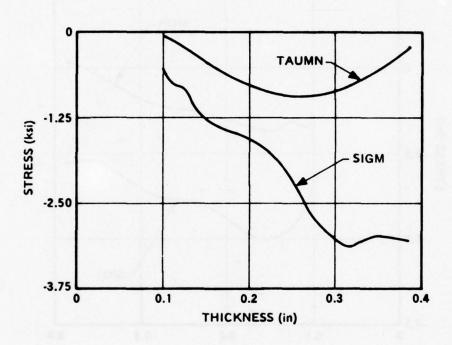


Figure 152. Shear and Radial Stress at Entrance End of the Insert at 15 Seconds for SN PG.

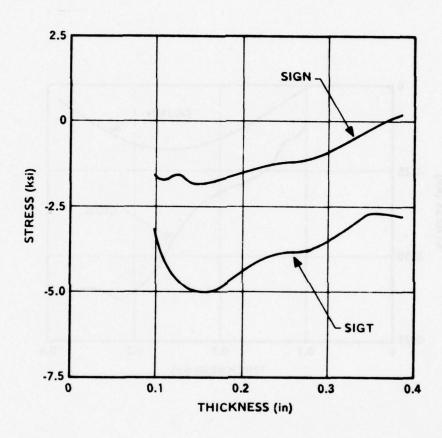


Figure 153. Axial and Hoop Stress and the Entrance End of the Insert at 15 Seconds in SN PG.

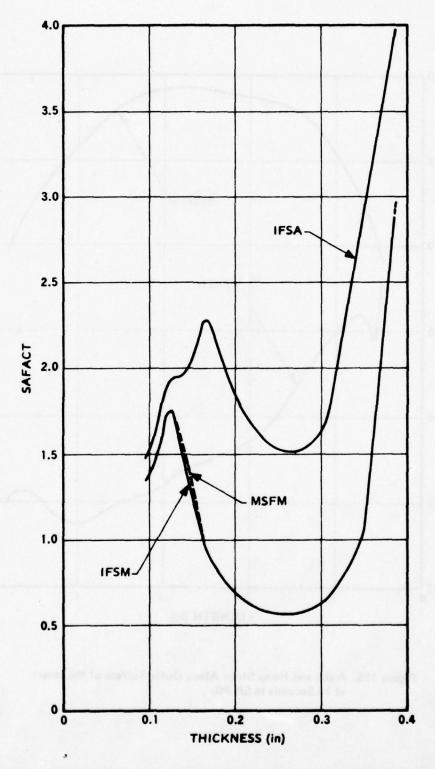


Figure 154. Safety Factors at Entrance End of the Insert at 15 Seconds in SN PG.

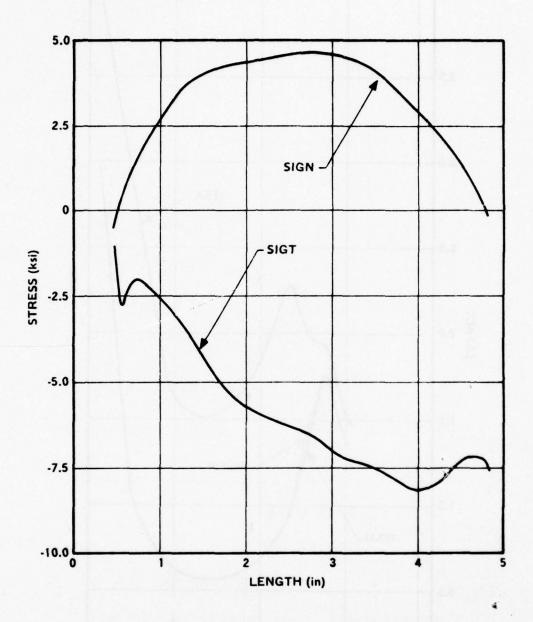


Figure 155. Axial and Hoop Stress Along Outer Surface of the Insert at 15 Seconds in SN PG.

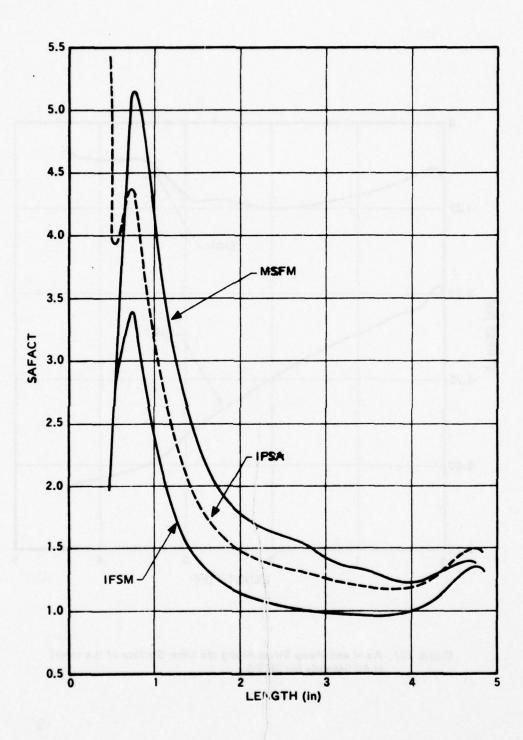


Figure 156. Safety Factors Along Outer Surface of the Insert at 15 Seconds in SN PG.

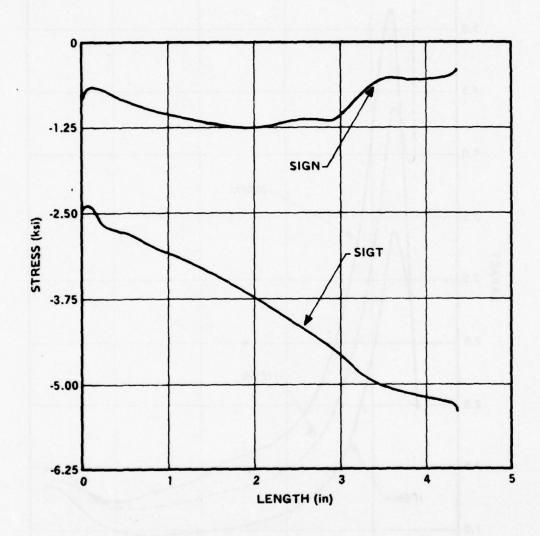


Figure 157. Axial and Hoop Stress Along the Inner Surface of the Insert at 60 Seconds for SN PG.

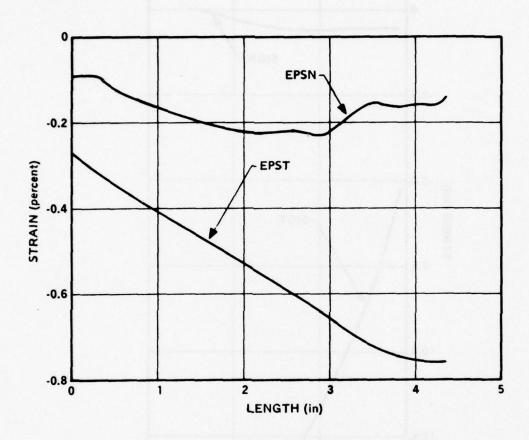


Figure 158. Axial and Hoop Strain Along the Inner Surface of the Insert at 60 Seconds for SN PG.

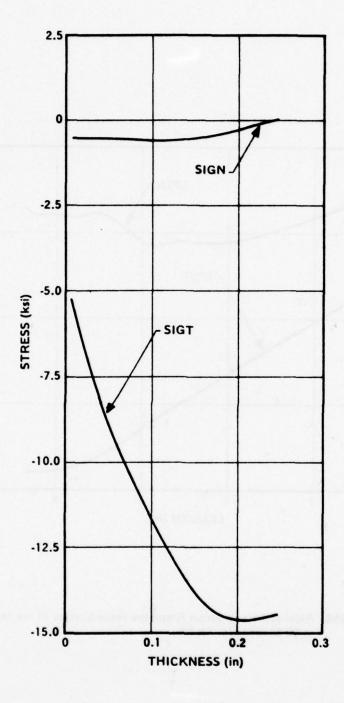


Figure 159. Axial and Hoop Stress and the Exit End of the Insert at 60 Seconds in SN PG.

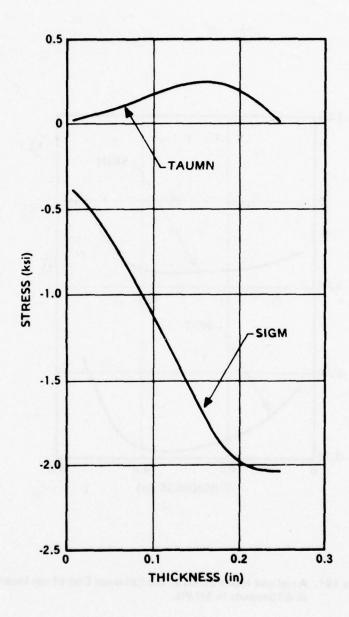


Figure 160. Shear and Radial Stress at Exit End of the Insert at 60 Seconds for SN PG.

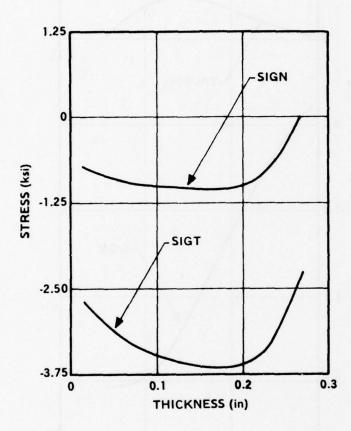


Figure 161. Axial and Hoop Stress at the Entrance End of the Insert at 60 Seconds in SN PG.

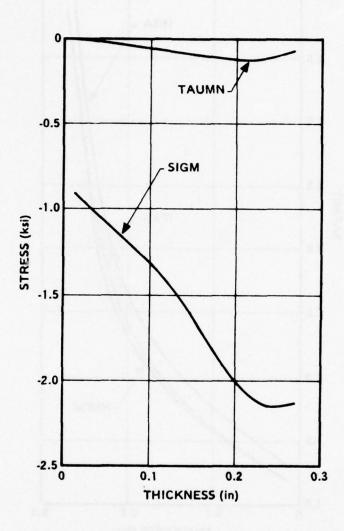


Figure 162. Shear Stress and Radial Stress at the Entrance End of the Insert at 60 Seconds in SN PG.

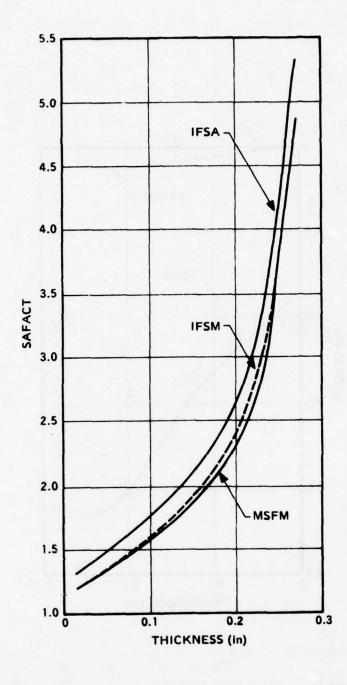


Figure 163. Safety Factors at the Entrance End of the Insert at 60 Seconds in SN PG.

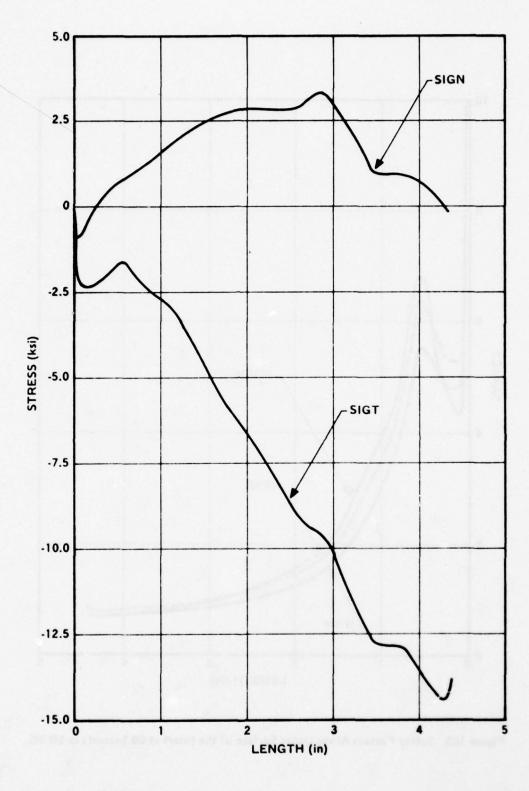


Figure 164. Axial and Hoop Stress Along Outer Surface of the Insert at 60 Seconds in SN PG.

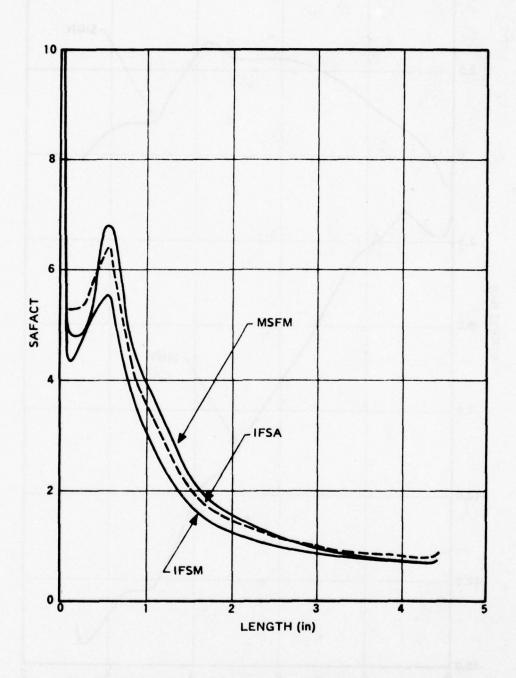


Figure 165. Safety Factors Along Outer Surface of the Insert at 60 Seconds in SN PG.

TABLE 12. SUMMARY OF SAFETY FACTORS DUAL LAYER - SN MATERIAL.

Time (Sec)	SFE	SFID	SFOD	SFENT	SFEXT
15	0.46	1.01	0.97	0.58	0.56
	(2.19)	(1.11)	(1.19)	(1.46)	(1.06)
60	0.76	0.86	0.76	1.22	0.76
	(1.31)	(1.03)	(0.80)	(1.33)	(0.79)

SFE - Safety Factor Based on Maximum Strain

SFID - Safety Factor at I.D. of Insert

SFOD - Safety Factor at O.D. of Insert

SFENT - Safety Factor at Entrance End of Insert

SFEXT - Safety Factor at Exit End of Insert

() - Indicate S.F. Based on Average Strength
Properties/Other Factor Based on Minimum Strengths

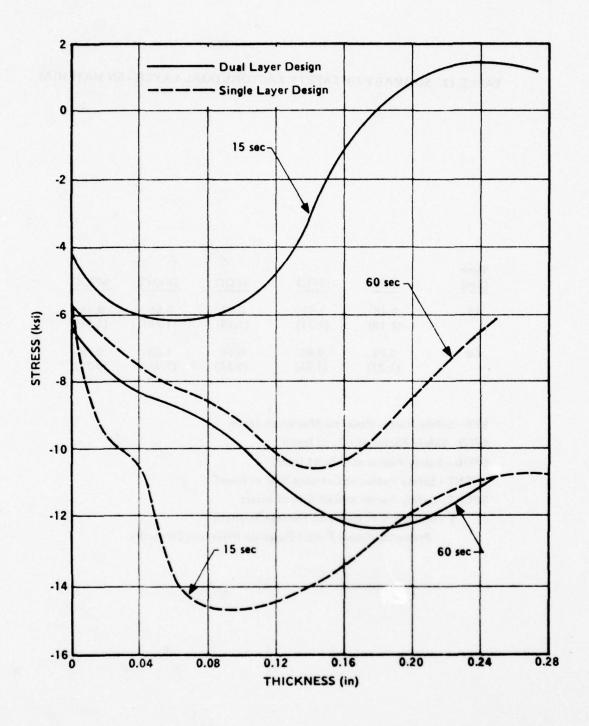


Figure 166. Comparison of Hoop Stress Distributions for Single and Dual Layer Designs.

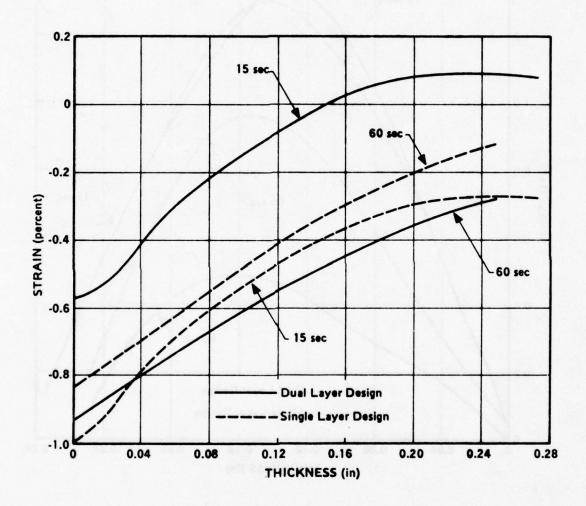


Figure 167. Comparison of Hoop Straim Distributions for Single and Dual Layer Designs.

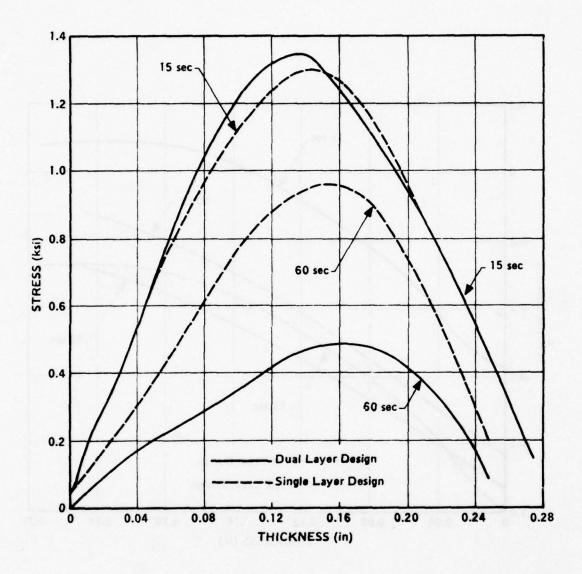


Figure 168. Comparison of Shear Stress Distributions for Single and Dual Layer Designs.

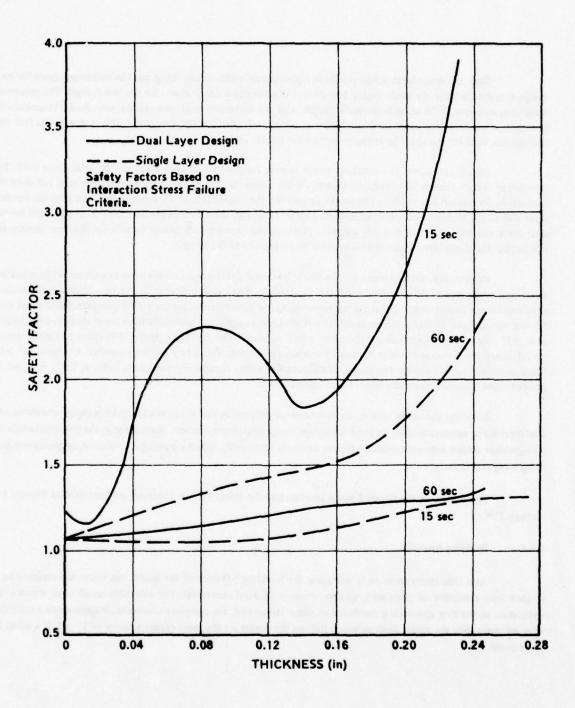


Figure 169. Comparison of Factors of Safety for Single and Dual Layer Designs.

Thus the single-layer design results in higher strains earlier in the firing, but the maximum strain for each design is approximately the same. Figure 168 shows the shear stress distributions for the two designs. The maximum shear stresses occur at 15 seconds for both designs, and the maximum shear stresses are very similar in magnitude. The shear stresses for the single layer are higher at 60 seconds than for the dual layer. This is due to the fact that thermal gradients for the single layer remain somewhat greater during the firing duration.

Figure 169 shows the resulting safety factors for the two designs based on the total stress field. The interaction failure criteria was used. As shown, all the safety factors at the inner surface approach 1.0 since the material in this region has yielded. The safety factors for the single layer at 15 seconds are lower than for the dual layer due to the higher compressive stresses that exist. However, these factors are similar to those that exist for the dual layer and the single layer at 60 seconds. Therefore, again minimum safety factors for the two designs are similar; but the single-layer design results in lower factors earlier in the firing.

In summary, shear stresses for the single layer and dual layer are of the same magnitude while minimum strain and stress factors are also similar for the two designs. The basic difference in the two designs is the time at which minimum factors exist. The stress states presented are highly dependent on the temperature profiles that exist for the two designs. If the backup material for a single-layer design was a material with a lower thermal conductivity than ATJ, then the temperature distributions would approach the dual-layer design. The stress and strain results would, therefore, be somewhere in between the results presented. The safety factors presented in Figure 169 were based upon stresses. If strains are used to determine the safety factors, the minimum factor is 1.35, or about 35 percent higher than the minimum factor based upon stresses.

Based on the above results, current material properties, and strength allowables, a design consisting of a dual-layer insert appears to offer no great advantage over a single-layer concept. Significantly, the previous results for a single-layer design indicate minimum factors at about 15 seconds, thereby making a 15-second, single-layer nozzle firing a key test milestone.

The results of the detailed stress analysis and the safety factors obtained are presented in Figures 170 through 199.

o.3.4.2 Buckling Analysis

As a first approximation in analyzing the buckling behavior of the insert, the insert was assumed to be divided into a number of rings with various amounts of axial constraint. For relatively small axial stresses, the stress-state in the ring approach a condition of plane stress; and, for complete constraint, it approaches a condition of plane strain. For the elastic analysis which follows the results are the same except a factor of $1 - \nu_{ab}^2$ is applied for plane strain.

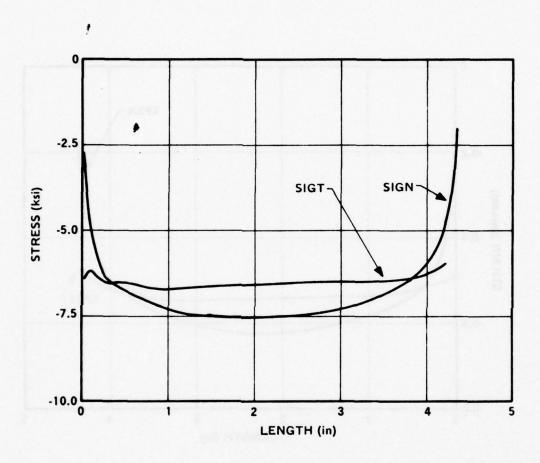


Figure 170. Axial and Hoop Stress Along the Inner Surface at 2 Seconds for a Single Layer CN PG Insert.

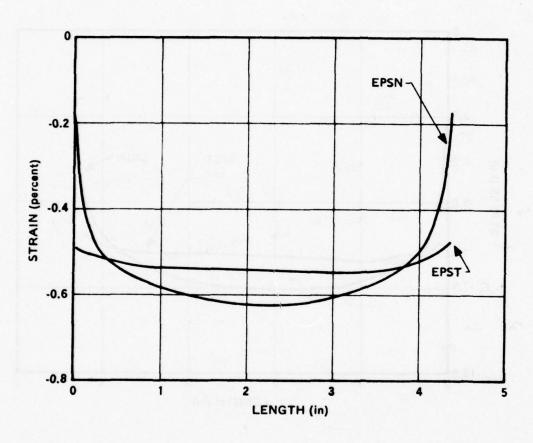


Figure 171. Hoop and Axial Strain Along the Inner Surface at 2 Seconds for a Single Layer CN PG Insert.

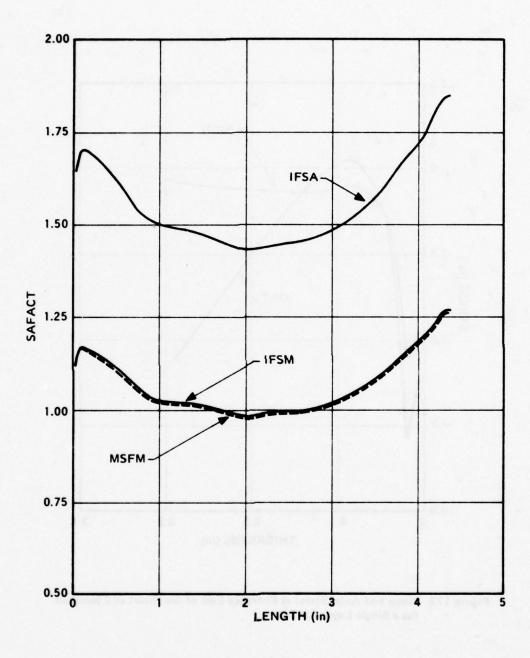


Figure 172. Safety Factors Along the Inner Surface at 2 Seconds for a Single Layer CN PG Insert.

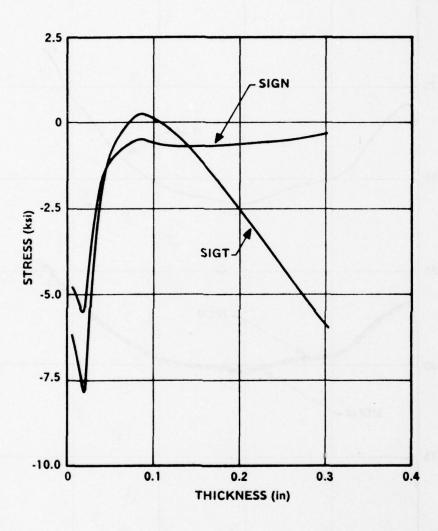


Figure 173. Hoop and Axial Stress at Entrance End of the Insert at 2 Seconds for a Single Layer CN PG.

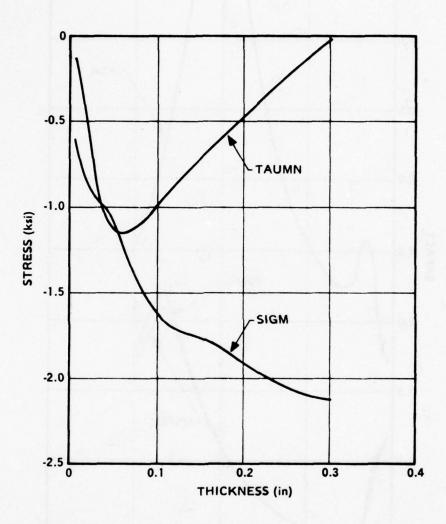


Figure 174. Shear and Radial Stress at Entrance End of the Insert at 2 Seconds for a Single Layer CN PG.

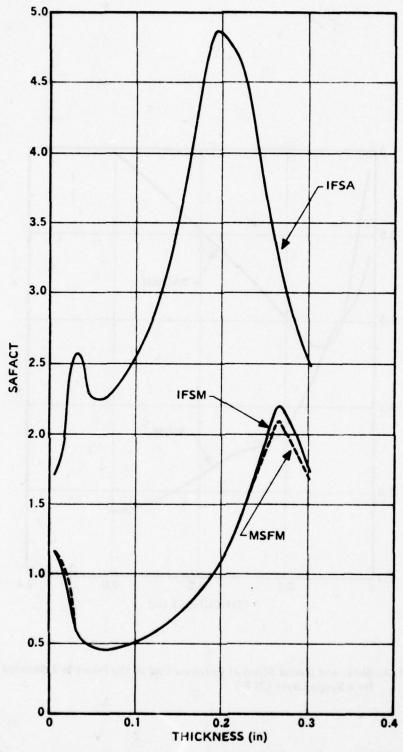


Figure 175. Safety Factor at Entrance End of the Insert at 2 Seconds for a Single Layer CN PG.

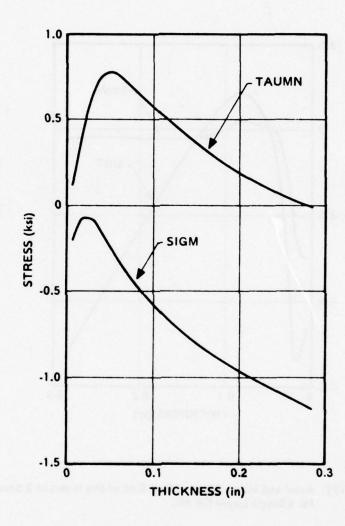


Figure 176. Shear and Radial STress at Exit End of the Insert at 2 Seconds for a Single Layer CN PG.

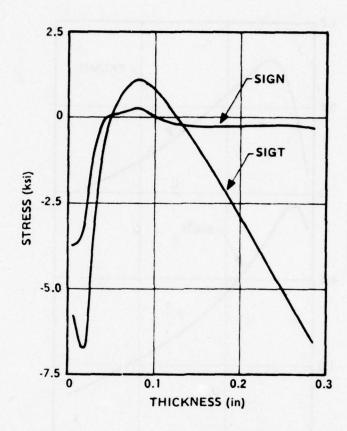


Figure 177. Axial and Hoop Stress at Exit End of the Insert at 2 Seconds for a Single Layer CN PG.

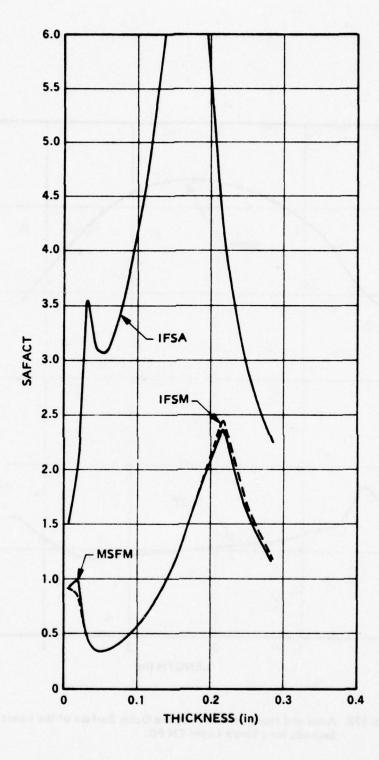


Figure 178. Safety Factors at the Exit End of the Insert at 2 Seconds for a Single Layer CN PG.

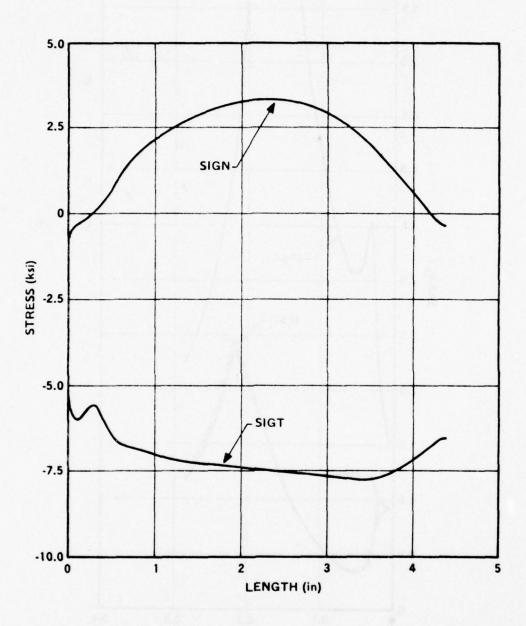


Figure 179. Axial and Hoop Stress Along the Outer Surface of the Insert at 2 Seconds for a Single Layer CN PG.

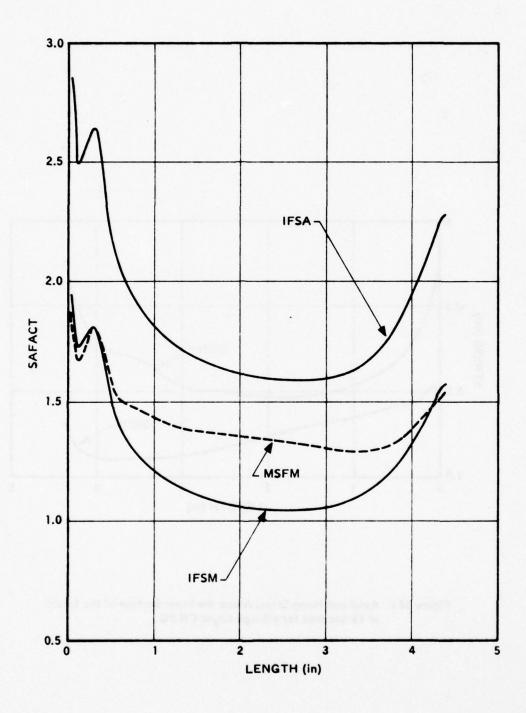


Figure 180. Safety Factors Along the Outer Surface of the Insert at 2 Seconds for a Single Layer CN PG.

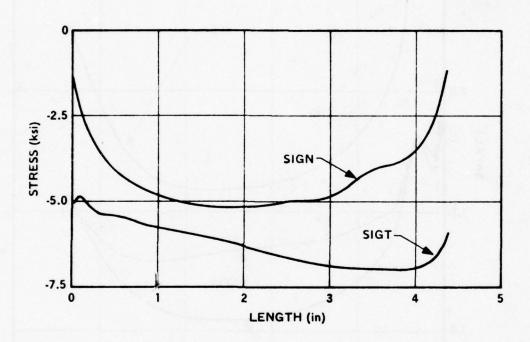


Figure 181. Axial and Hoop Stress Along the Inner Surface of the Insert at 15 Seconds for a Single Layer CN PG.

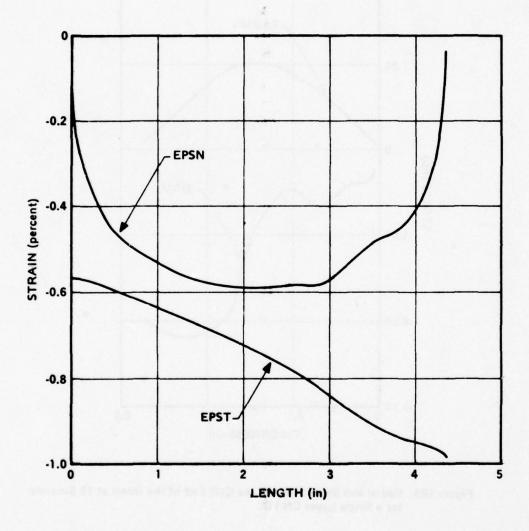


Figure 182. Axial and Hoop Strain Along the Inner Surface of the Insert at 15 Seconds for a Single Layer CN PG.

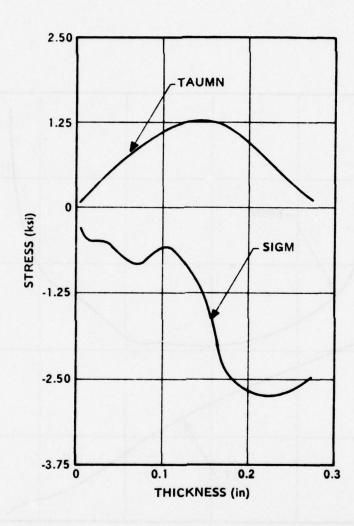


Figure 183. Radial and Shear Stress at the Exit End of the Insert at 15 Seconds for a Single Layer CN PG.

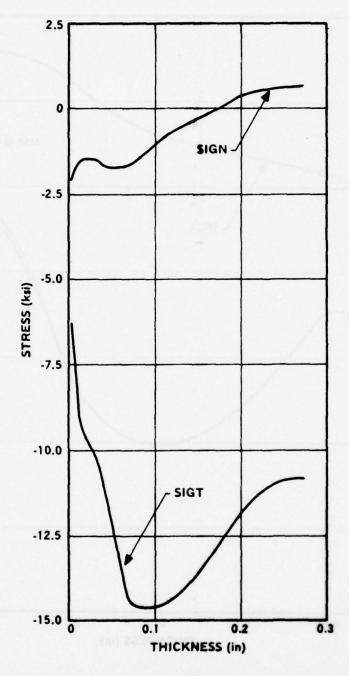


Figure 186. Axial and Hoop Stress at Exit End of the Insert at 15 Seconds for a Single Layer CN PG.

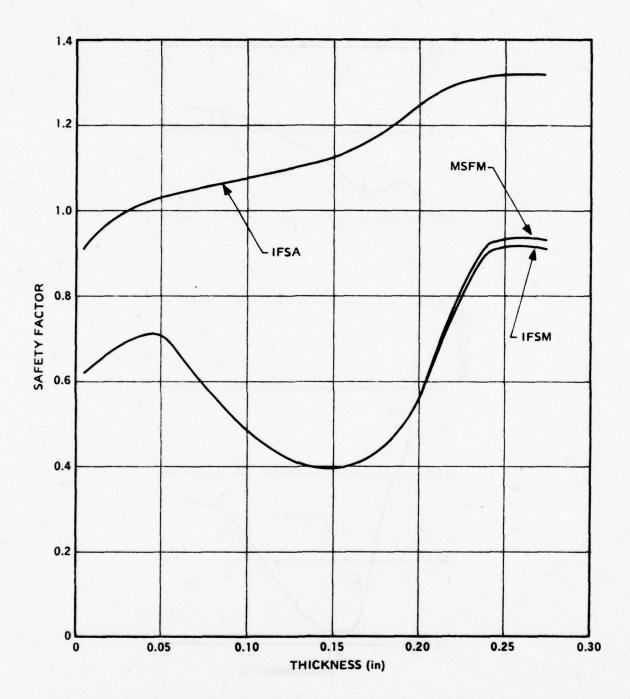


Figure 185. Safety Factors at Exit End of the Insert at 15 Seconds for a Single Layer CN PG.

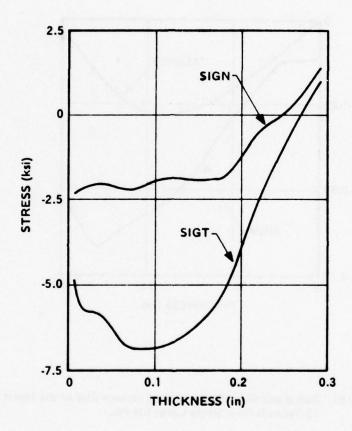


Figure 186. Axial and Hoop Stress at the Entrance End of the Insert at 15 Seconds for a Single Layer CN PG.

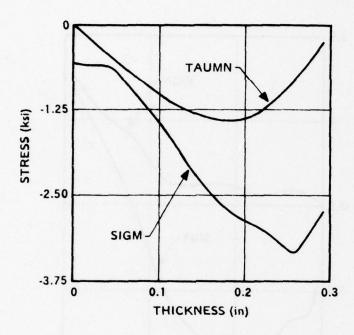


Figure 187. Radial and Shear Stress at the Entrance End of the Insert at 15 Seconds for a Single Layer CN PG.

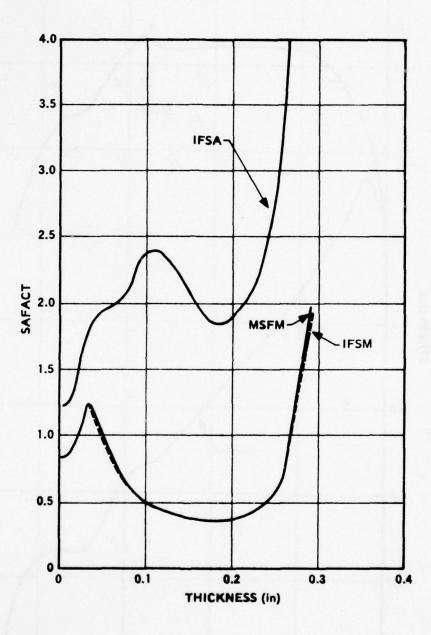


Figure 188. Safety Factors at the Entrance End of the Insert at 15 Seconds for a Single Layer CN PG.

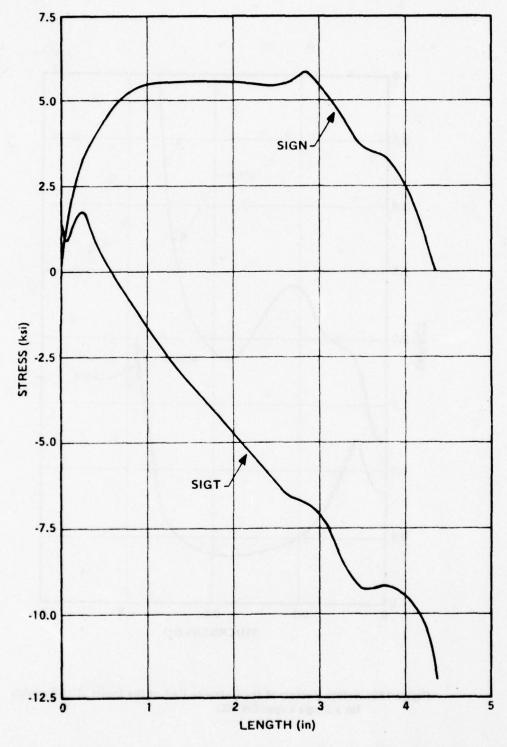


Figure 189. Axial and Hoop Stress Along Outer Surface of the Insert at 15 Seconds for a Single Layer CN PG.

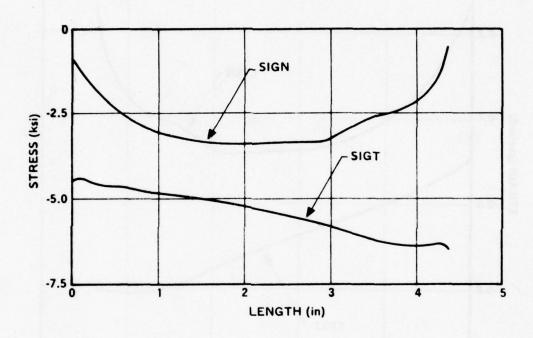


Figure 190. Axial and Hoop Stress Along the Inner Surface of the Insert at 60 Seconds for a Single Layer CN PG.

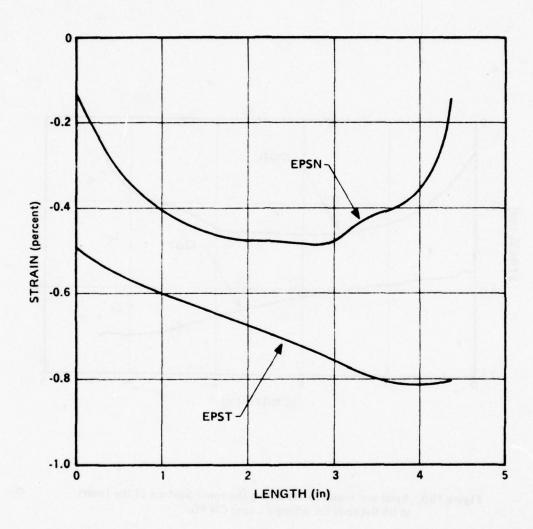


Figure 191. Axial and Hoop Strain Along the Inner Surface of the Insert at 60 Seconds for a Single Layer CN PG.

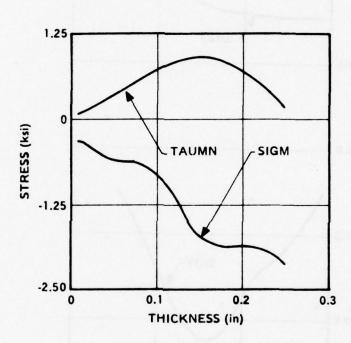


Figure 192. Radial and Shear Stress at the Exit End of the Insert at 60 Seconds for a Single Layer CN PG.

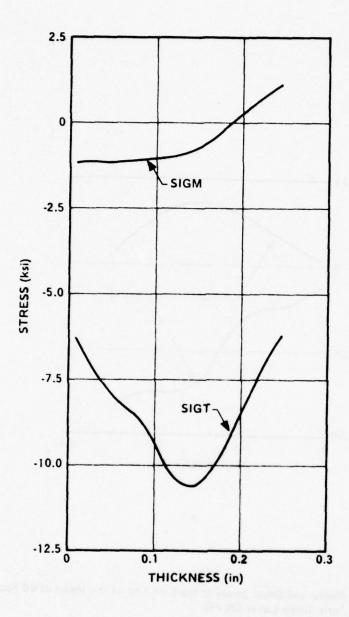


Figure 193. Axial and Hoop Stress at the Exit End of the Insert at 60 Seconds for a Single Layer CN PG.

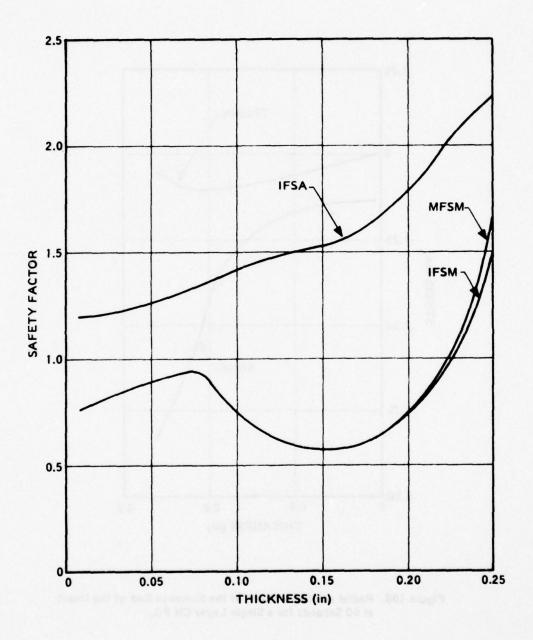


Figure 194. Safety Factors at the Exit End of the Insert at 60 Seconds for a Single Layer CN PG.

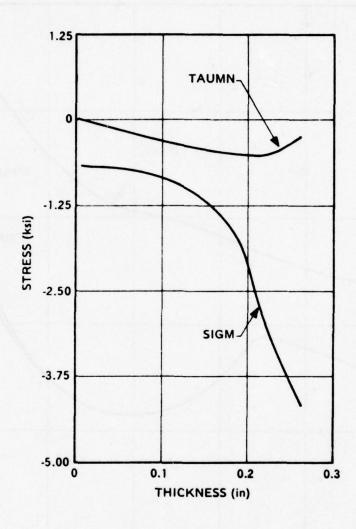


Figure 195. Radial and Shear Stress at the Entrance End of the Insert at 60 Seconds for a Single Layer CN PG.

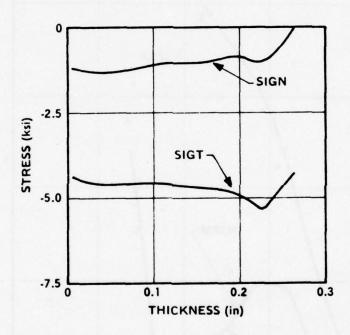


Figure 196. Axial and Hoop Stress at the Entrance End of the Insert at 60 Seconds for a Single Layer CN PG.

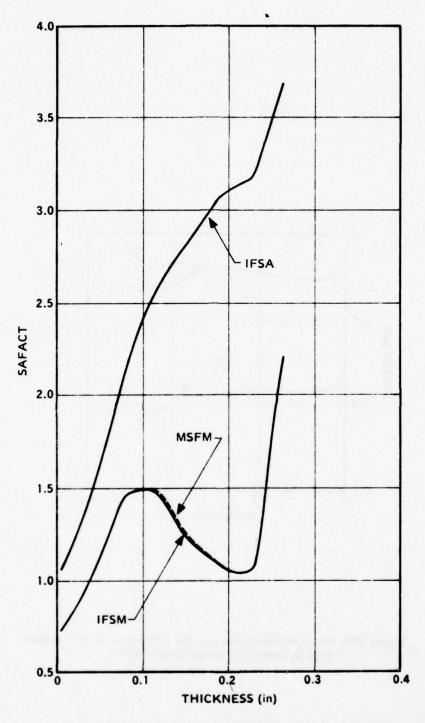


Figure 197. Safety Factors at the Entrance End of the Insert at 60 Seconds for a Single Layer CN PG.

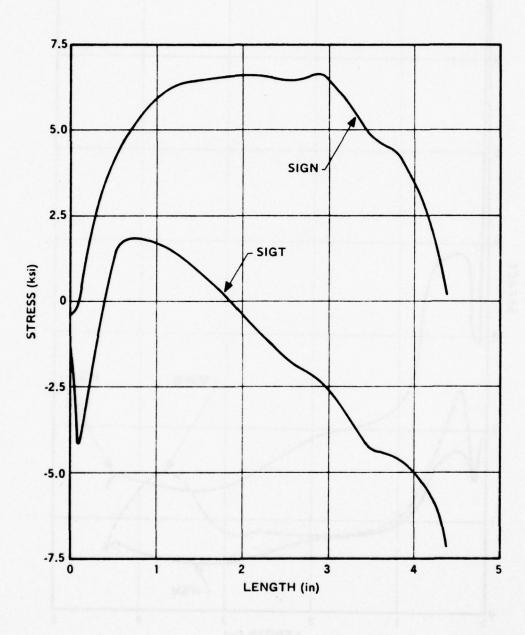


Figure 198. Axial and Hoop Stress Along the Outer Surface of the Insert at 60 Seconds for a Single Layer CN PG.

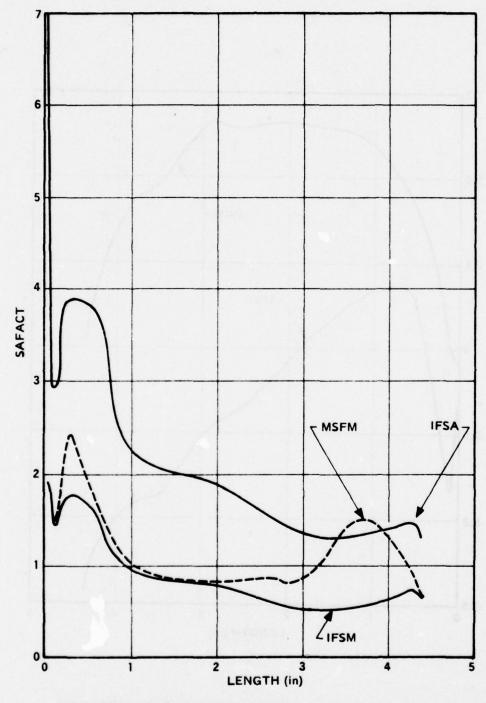
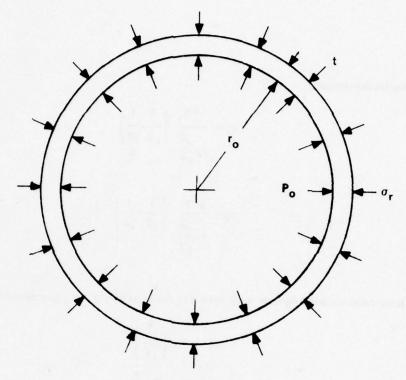


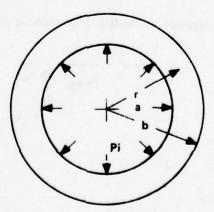
Figure 199. Safety Factors Along the Outer Surface of the Insert at 60 Seconds for a Single Layer CN PG.



Ring Under Buckling Load

The condition which is analyzed is shown in the sketch above. It is assumed that there exists some critical combination of ring thickness, t, and pressure $(\sigma_r - P_0)$ which produces buckling. (The contribution of P_0 to σ_r varies with the radius, but is a weak function of the radius. Hence for this analysis, the contribution of P_0 to σ_r is assumed constant.)

If u is the radial deflection of the ring, then the surrounding material exerts a resisting force Ku per unit outer circumference of the ring. The spring constant, K, can be expressed in terms of familiar material properties by using the solution for a thick cylinder subjected to internal pressure as shown in the sketch below.



Thick Cylinder Under Internal Pressure

The solution for the stresses is

$$\sigma_{\rm r} = \frac{{\rm a}^2 \, {\rm Pi}}{1 - \frac{{\rm a}^2}{{\rm b}^2}} \, \left(\frac{1}{{\rm b}^2} - \frac{1}{{\rm r}^2} \right)$$

$$\sigma_{\theta} = \frac{a^2 P_i}{1 - \frac{a^2}{b^2}} \left(\frac{1}{b^2} + \frac{1}{r^2} \right)$$

where $\sigma_{\rm r}$ is the radial stress and σ_{θ} is the hoop stress. For the insert b >>>a and approximately

$$\sigma_{\rm r} = -Pi \left(\frac{a^2}{r^2} \right)$$

$$\sigma_{\theta} = P_i \left(\frac{a^2}{r^2} \right)$$

The hoop strain is

$$\epsilon_{\theta} = \frac{u}{r} = \frac{\sigma_{\theta}}{E_{\theta}} - \nu_{\theta r} \frac{\sigma_{r}}{E_{r}}$$

where the effect of $\sigma_{\!Z}$ has been neglected. Substituting for the stress and noting that

$$\& = \frac{P_i}{u} = \frac{E_{\theta}}{1 + \nu_{\theta r}} \frac{1}{E_{\theta}} \frac{1}{r_0}$$

per unit axial length of the ring. For convenience write

$$\ell_c = c \frac{E_a}{r}$$

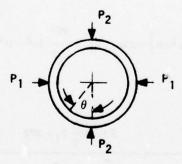
We can now proceed to the buckling analysis. The strain energy in the ring is given by

$$V = \frac{EI}{2_0^r} \int_0^2 \left(\frac{d^2u}{d\theta^2} + u \right)^2 d\theta - \frac{q}{2} \int_0^2 \left(\frac{d^2u}{ds^2} + \frac{u}{r_0^2} \right) u d\theta$$
 (a)

where s is the coordinate measured along the ring centerline. The work done by the surrounding medium is

$$W_{e} = -\frac{\ell_{c}}{2} \int_{0}^{2\pi} u^{2} \cdot r_{o} d\theta$$
 (b)

Assume that small perturbations in the load applied to the ring may be represented by concentrated forces as shown in the sketch below 1



It will be shown later that these forces may be of negligible magnitude. They are needed only to induce the buckling instability.

The work performed by the concentrated forces is

$$W_1 + W_2 = P_1(U)_{\theta} = \pi/2 + P_2(u)_{\theta} = \pi$$
 (c)

The general expression for the radial displacement of the ring is

$$u = \sum_{n=1}^{\infty} a_n \cos n\theta + \sum_{n=1}^{\infty} b_n \sin n\theta$$
.

However, symmetry requires that the sine terms be omitted and only even values of the cosines terms are used

$$u = \sum_{n=0}^{\infty} a_n \cos n\theta \quad (n \text{ even}). \tag{d}$$

The method of virtual work will be used to solve for the critical value of buckling pressure, q. For a virtual radial displacement

$$\delta u = \delta a_n \cos n\theta$$

the strain energy must be equal to the work done by the forces, so that

$$+ P_2 \delta a_n \left(\cos n\pi + \cos^2 n\pi \right) - \pi \ell c r_0 a_n = \frac{\pi EI}{r_0^3} (n^2 - 1)^2 a_n - \pi (n^2 - 1) q a_n$$

solving for an,

$$a_{n} = \frac{2(-1)\frac{n}{2}P_{1} + 2P2}{\frac{\pi EI}{r_{0}^{3}}(n^{2} - 1)^{2}\left[1 - \frac{qr_{0}^{3}}{(n^{2} - 1)EI} + \frac{kr_{0}^{4}}{EI(n^{2} - 1)^{2}}\right]}$$
 (e)

Recalling that a_n is the coefficient in Equation (d) for radial displacement, u. the displacement increases without limit when the denominator of Equation (e) becomes equal to zero. Notice that P_1 and P_2 can be very small, representing small perturbations in the loading of the ring.

For $a_n \to \infty$,

$$q_{cr} = \frac{1}{n^2 - 1} \left[kr_0 + (n^2 - 1)^2 \frac{EI}{r_0^3} \right]$$

The E in this equation is E_{θ} or for pyrolytic graphite E_{θ} @ E_a . Using $k = c E_a/r_o$, and $I = t^3/12$ where t = ring thickness, the above equation becomes

$$q_{cr} = \frac{E_a}{n^2 - 1} \left[c + \frac{(n^2 - 1)^2}{12} \left(\frac{t}{r_o} \right)^3 \right]$$
 (f)

The value of c for pyrolytic graphite is approximately 1/2 and Equation (f) becomes

$$q_{cr} = \frac{E_a}{2(n^2 - 1)} \left[1 + \frac{(n^2 - 1)^2}{6} \left(\frac{t}{r_o} \right)^3 \right]$$

There are several observations with respect to Equation (f). First, the value of the critical buckling pressure takes on discrete values for each buckling configuration, determined by the value of n, which must be an even number. Second, for each value of the thickness ratio, t/r_0 , there is a value of n for the minimum buckling pressure. This value may be found by taking

$$\frac{\partial q_{cr}}{\partial n} = -\frac{E_a}{2(n^2 - 1)^2} + \frac{E_a}{12} \frac{t^3}{r_0} = 0$$

or

$$n^2 = 1 + \frac{\sqrt{6}}{\left(\frac{t}{r_0}\right)^{3/2}} \text{ n even}$$

The nondimensionalized critical buckling pressure versus thickness ratio is shown in Figure 200. The nondimensional plot is presented since, for a given thickness of the insert, the thickness ratio varies due to a variation in the internal radius along the axis of the insert and the value of E_a varies with temperature. The solid lines in Figure 200 show the minimum values for $q_{C\Gamma}$; the dotted lines representing the pressure required for buckling in a given nodal configuration.

Figure 201 shows the buckled configuration as viewed on a plane normal to the axis of the insert for n = 10 which occurs for a thickness ratio of 0.1.

Figure 202 is a plot of buckling pressure versus thickness for E_a at room temperature and E_a at 6,000°F. The internal radius at the throat (3.50 inch) was used for these plots. For the entrance and exit ends of the inserts, the internal radii are somewhat greater and, therefore, the values of the buckling pressure are a little less at these two locations.

The possibility of buckling can be assessed if the radial stresses are compared with the critical buckling pressure as given by Equation (f).

Using the equation for n for critical buckling pressure

$$n^2 = 1 + \frac{\sqrt{6}}{\left(\frac{t}{r_0}\right)^{3/2}}$$

a value of n is calculated for each selected value of t/r_0 . This value will, in general, not be an even whole number, and hence the closest even whole number must be selected. The value of n is substituted into Equation (f) to obtain the critical buckling pressure. The value used for E_a is that for the average temperature across the thickness under consideration. Three locations along the insert axis are selected: the entrance end, minimum cross-section, and exit end. The results are shown in Figures 203, 204, and 205 for a 60-second firing time. For these conditions the greatest possibility for buckling exists at the exit end of the insert.

Referring to Figure 205, it is apparent that the critical thickness for buckling is approximately 0.10 inch. Due to the many uncertainties and assumptions related to the buckling analysis, a minimum factor of 1.5 was assumed. Hence, an insert thickness greater than 0.15 inch should eliminate structural stability as a possible failure mode.

It should be pointed out that the 60-second firing time results in the "worst" case condition since the material is the "hottest" (minimum modulus), the thickness has been reduced due to erosion, and the radial compressive stresses are at the maximum.

The conclusions of the "buckling" analysis are as follows:

The critical buckling conditions for the insert is significantly different as compared to
the case of a ring subjected to pressure with no resistance backup material. For no

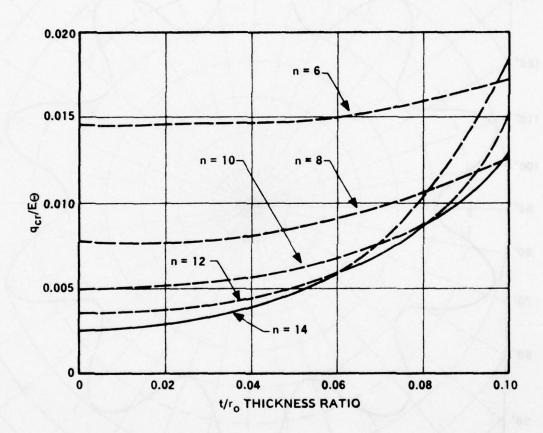


Figure 200. Critical Buckling Pressure vs. Thickness Radios Ratio.

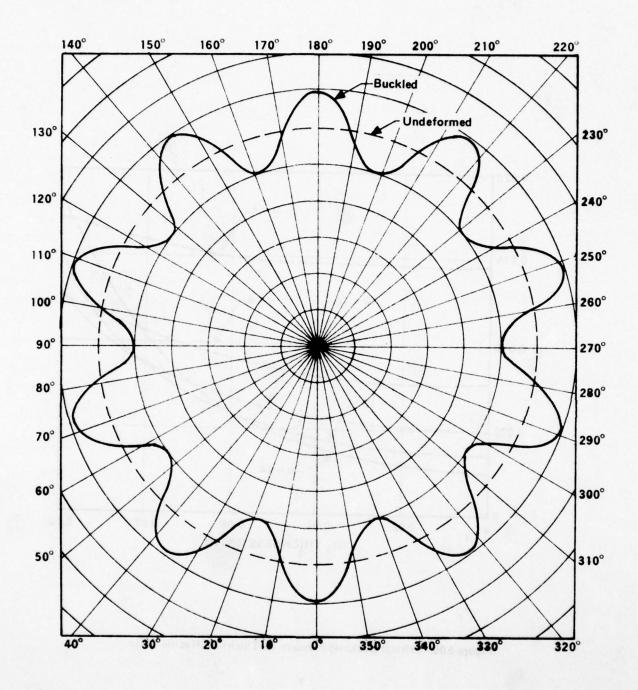


Figure 201. Mode Shape for Buckling Due to External Pressure for $t/r_0 = 0.1$ and n = 10.

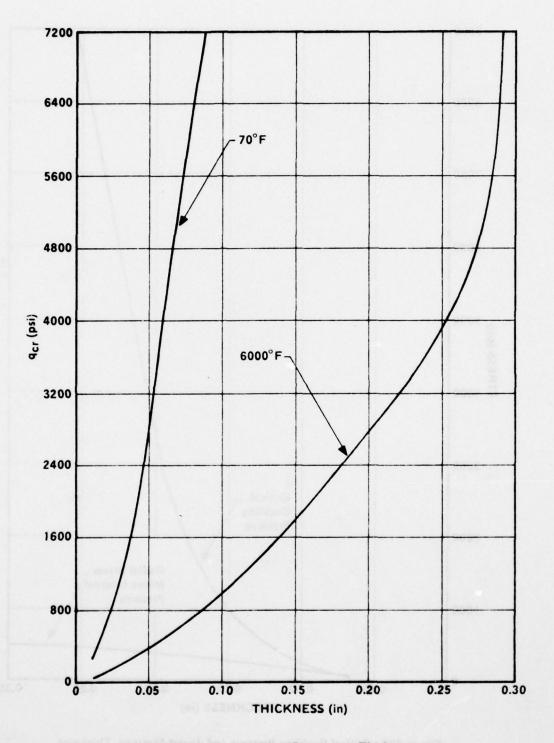


Figure 202. Critical Buckling Pressure vs. Thickness.

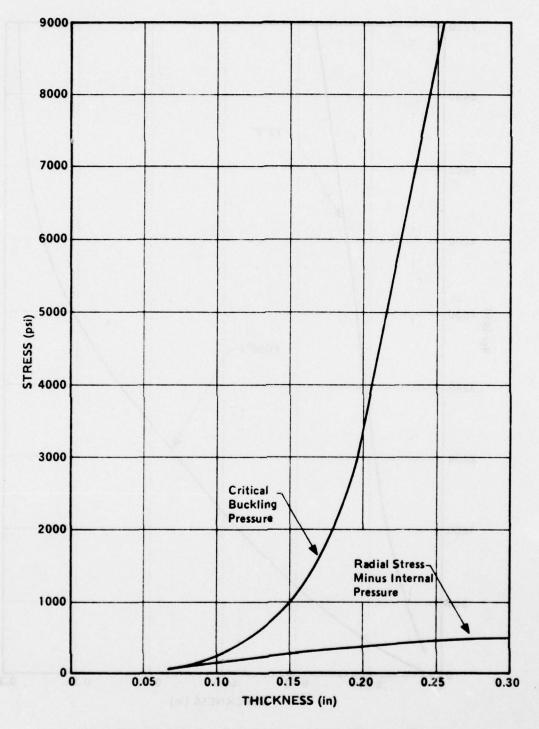


Figure 203. Critical Buckling Pressure and Insert Stress vs. Thickness at 60 Seconds for the Entrance End.

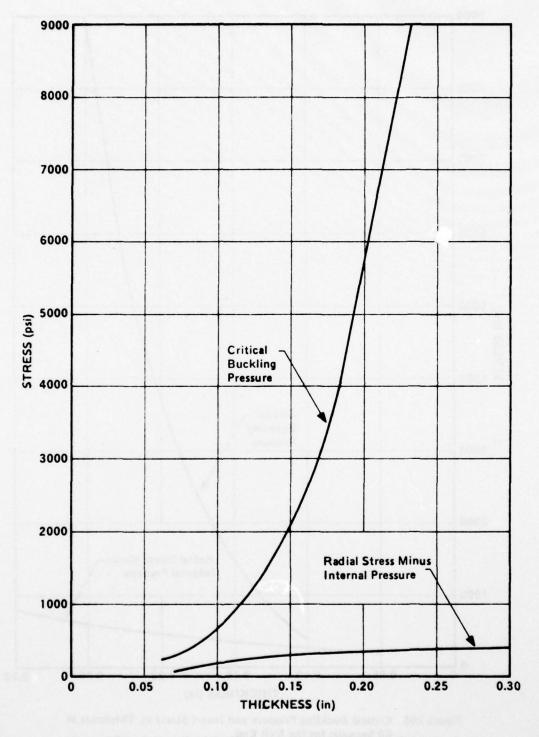


Figure 204. Critical Buckling Pressure and Insert Stress vs. Thickness at 60 Seconds for the Throat Plane.

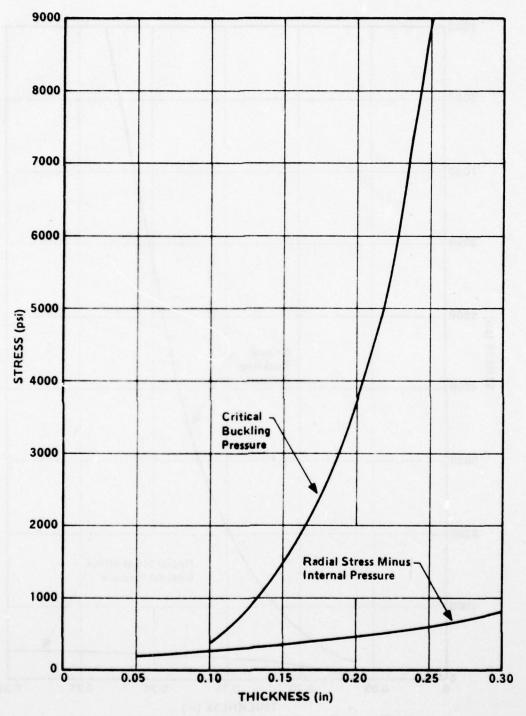


Figure 205. Critical Buckling Pressure and Insert Stress vs. Thickness at 60 Seconds for the Exit End.

backup material the minimum critical buckling pressure occurs for n = 2 (one complete sine wave) and n is not dependent on thickness as it is in the insert situation.

An insert thickness greater than 0.15 inch is required to eliminate possible buckling of the "free-standing" a-b plane insert.

6.3.4.3 PG/SiC Coated Components

For the 30- and 60-second nozzle firings, PG/SiC coated components are recommended. No thermal or structural studies have been performed in this program for these components; however, detailed analyses were performed in a previous program. [31] Positive margins of safety were predicted for the entrance cap in these studies.

6.3.4.4 ATJ Graphite Components

Figure 206 shows the upstream ATJ entrance cap and downstream ATJ component considered for the 15-second nozzle test. The ATJ entrance cap was modeled for analysis with the SAAS III structural computer code. Analyses were performed for firing times of 5 and 15 seconds (firing duration). The temperature distributions were obtained from the nozzle assembly thermal analysis.

Figures 207 and 208 show the stress distributions at the inner surface of entrance cap. The sketch below shows the region where stresses are plotted.

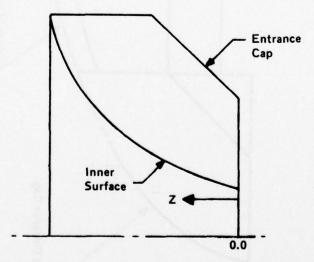


Figure 207 shows the hoop and axial stresses while Figure 208 shows the radial and shear stresses. Figures 209 and 210 show the strain distributions. Figure 211 shows the safety factors for the same inner surface. The interaction failure criteria is used to calculate the factors of safety based on the average strength properties for ATJ. Based on the average properties the minimum factor is 1.74.

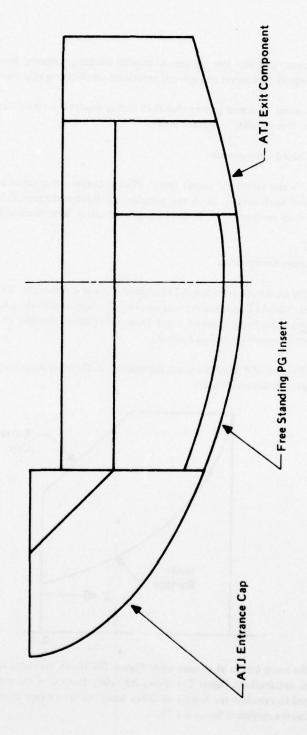


Figure 206. ATJ Graphite Entrance Cap and Exit Ring for the 15 Second Nozzle Design.

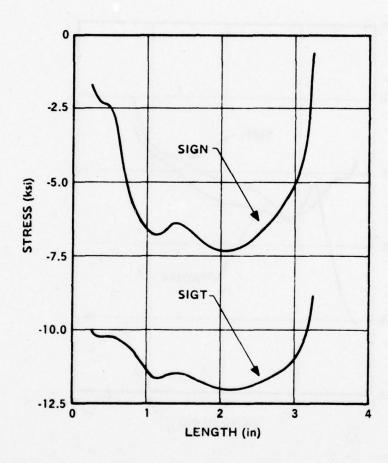


Figure 207. Axial and Hoop Stress Along the Inner Surface of the Entrance Cap at 5 Seconds.

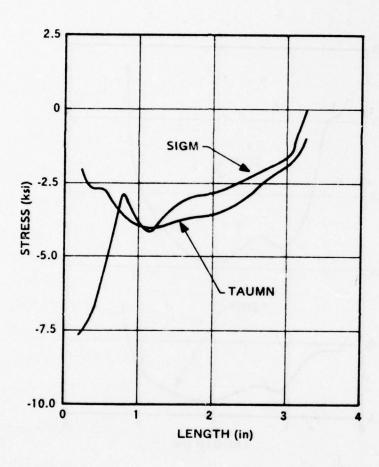


Figure 208. Radial and Shear Stress Along the Inner Surface of the Entrance Cap at 5 Seconds.

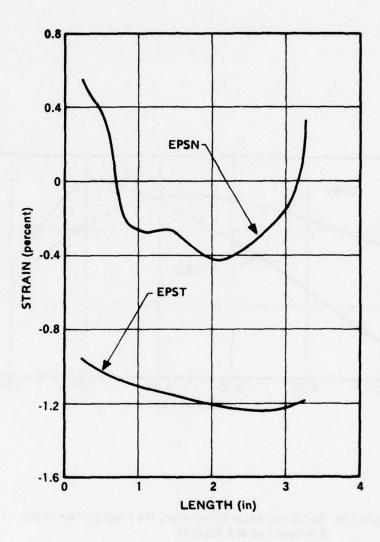


Figure 209. Axial and Hoop Strain Along the Inner Surface of the Entrance Cap at 5 Seconds.

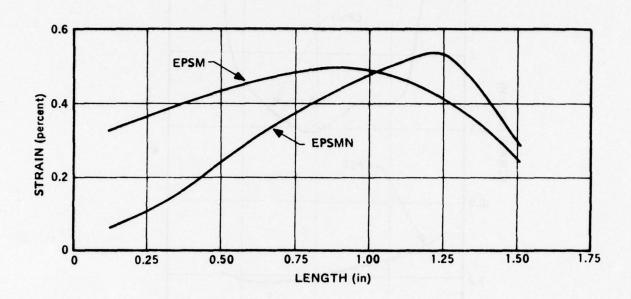


Figure 210. Radial and Shear Strain Along the Inner Surface of the Entrance Cap at 5 Seconds.

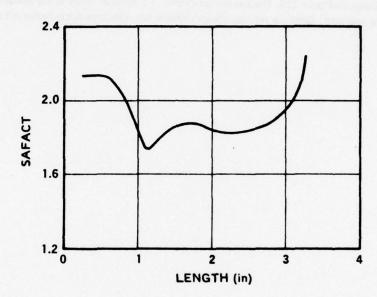


Figure 211. Safety Factors Along the Inner Surface of the Entrance Cap at 5 Seconds.

Figure 212 shows the safety factor results for 15 seconds. Significantly the safety factors are increased at 15 seconds, and the minimum factor based on average properties is 2.25. Based on these results, the entrance cap would perform successfully.

Figures 213 through 224 show the hoop and axial stress and strain distributions versus length for the ID and OD of the ATJ exit component for 2, 5, and 15 seconds. The factors of safety calculated for the inner surface at the 5-second time are shown in Figure 225. The stresses developed at 5 seconds result in the minimum factors of safety for the three cases analyzed. Based on average strength values, the minimum safety factor is 1.45.

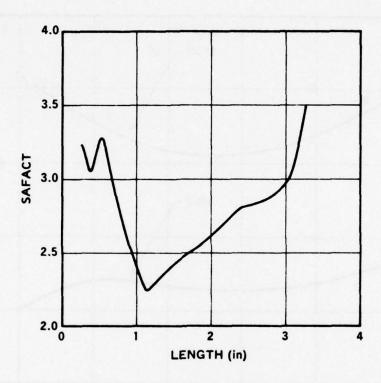


Figure 212. Safety Factors Along the Inner Surface of the Entrance Cap at 15 Seconds.

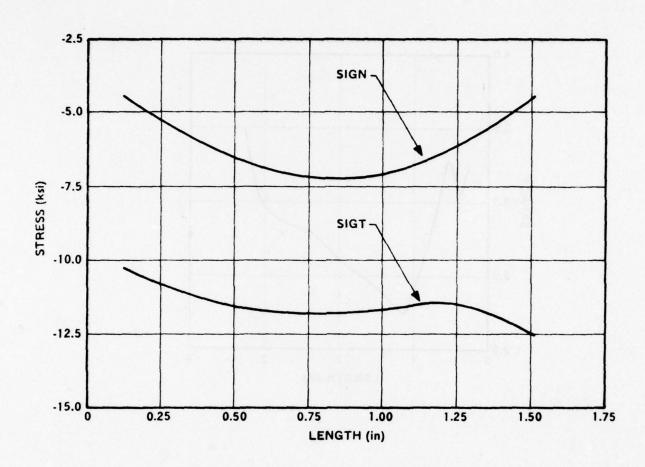


Figure 213. Axial and Hoop Stress Along Inner Surface of the Exit Ring at 2 Seconds.

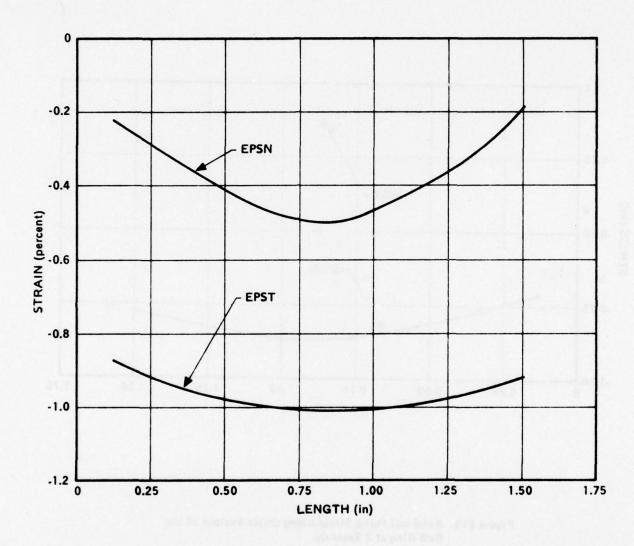


Figure 214. Axial and Hoop Strain Along the Inner Surface of the Exit Ring at 2 Seconds.

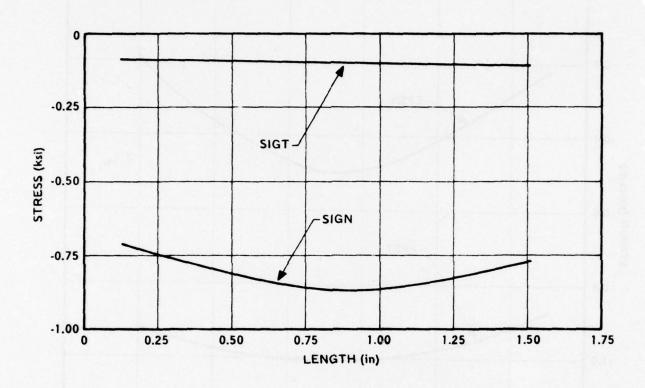


Figure 215. Axial and Hoop Stress Along Outer Surface of the Exit Ring at 2 Seconds.

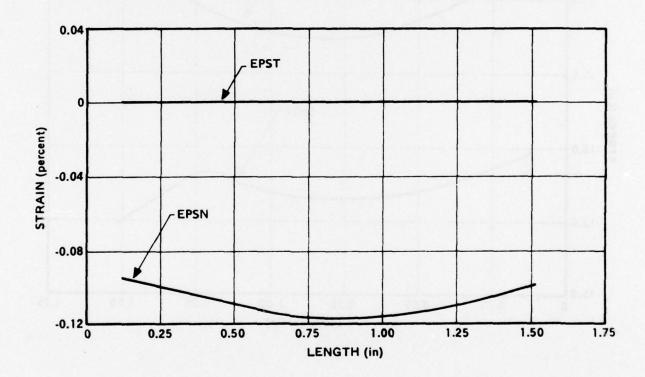


Figure 216. Axial and Hoop Strain Along Outer Surface of the Exit Ring at 2 Seconds.

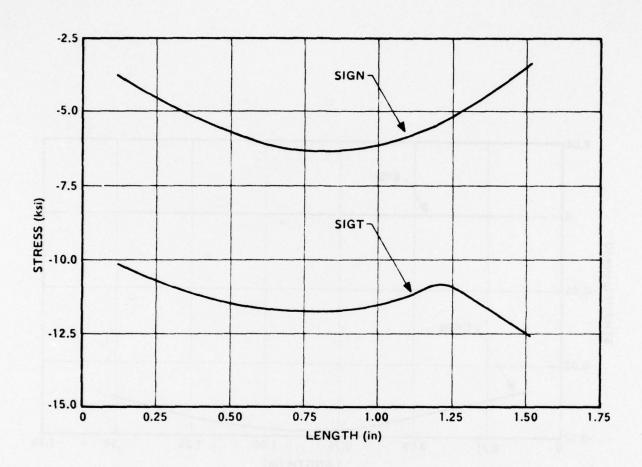


Figure 217. Axial and Hoop Stress Along the Inner Surface of the Exit Ring at 5 Seconds.

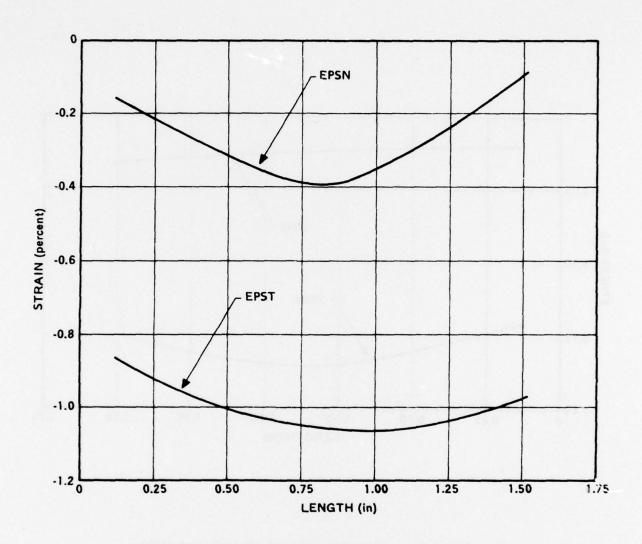


Figure 218. Axial and Hoop Strain Along the Inner Surface of the Exit Ring at 5 Seconds.

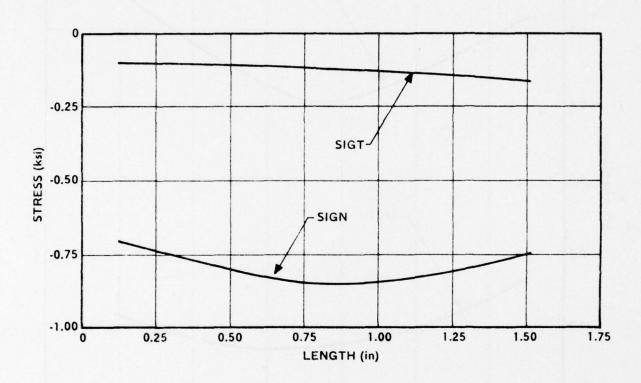


Figure 219. Axial and Hoop Stress Along the Outer Surface of the Exit Ring at 5 Seconds.

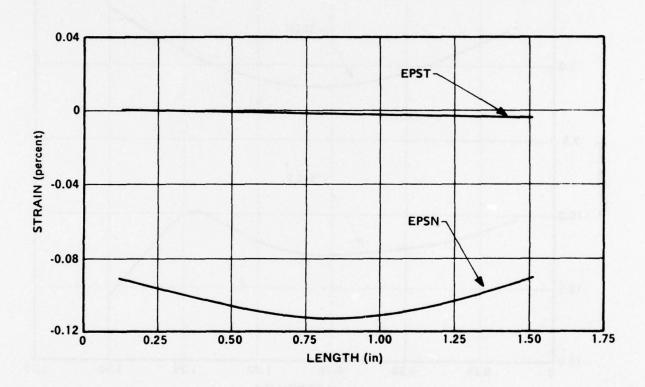


Figure 220. Axial and Hoop Strain Along Outer Surface of the Exit Ring at 5 Seconds.

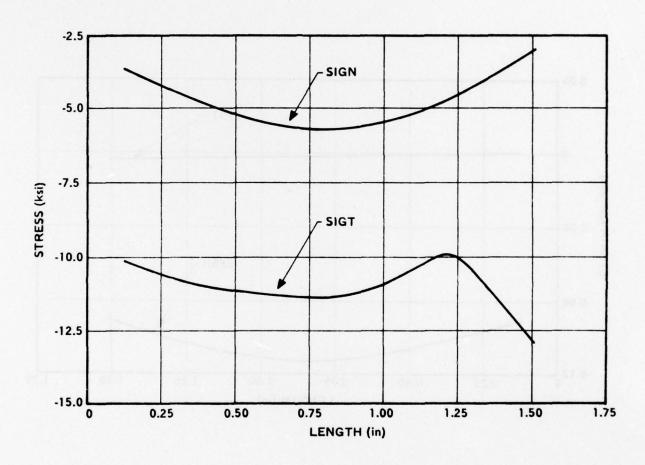


Figure 221. Axial and Hoop Stress Along the Inner Surface of the Exit Ring at 15 Seconds.

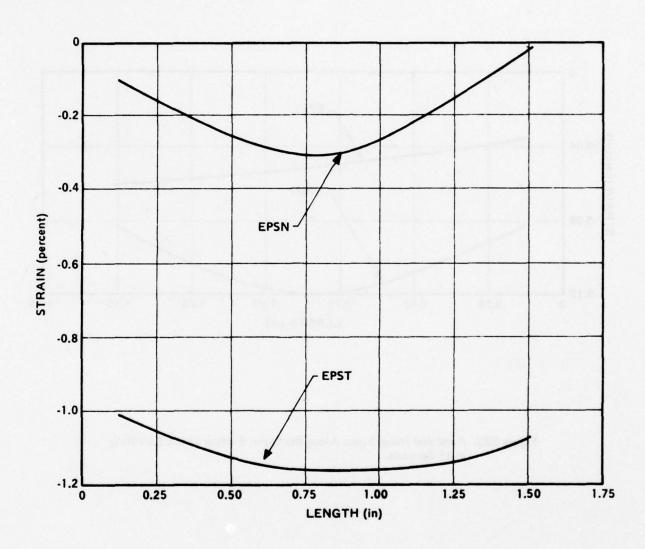


Figure 222. Axial and Hoop Strain Along the Inner Surface of the Exit Ring at 15 Seconds.

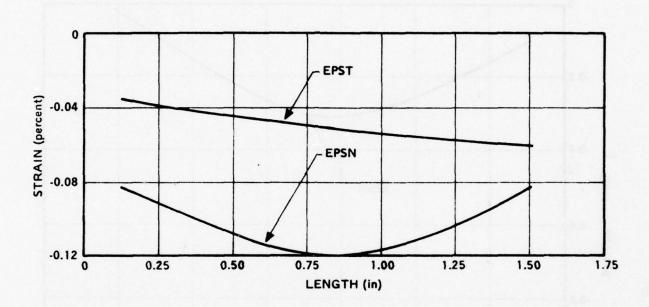


Figure 223. Axial and Hoop Stress Along the Outer Surface of the Exit Ring at 15 Seconds.

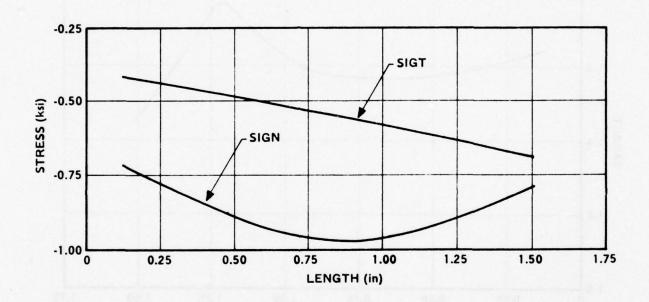


Figure 224. Axial and Hoop Strain Along the Outer Surface of the Exit Ring at 15 Seconds.

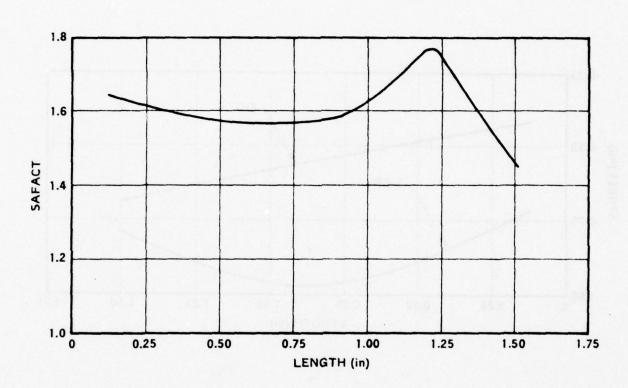


Figure 225. Safety Factors Along the Inner Surface of the Exit Ring at 5 Seconds.

7.0 AB PLANE PG FABRICATION

7.1 Introduction

A total of fifteen deposition runs was conducted by the Pfizer Corp., Easton, Pa., in an attempt to fabricate a nominal 7-inch throat diameter, free-standing, pyrolytic graphite throat insert with a nominal wall thickness of 0.300 inch.

An objective within this phase of the effort was to develop a material specification for free-standing a-b plane pyrolytic graphite shapes for rocket nozzle applications. The preliminary specification which was established is given in Appendix B.

The specified deposition shape is shown in Figure 226 and a typical throat insert deposition assembly is shown in Figure 227. All graphites used were purified electrode grade material (to minimize metal contamination) except for the mandrel which was machined from ATJ graphite.

The first six throat insert deposition runs were conducted to develop process parameters. Two tubular deposition runs were also conducted, during this developmental phase, to fabricate free-standing tubes from which test specimens could be removed and utilized for characterizing the physical properties of the material produced. The second of these two runs was of the desired microstructure and was the material used for characterization. The last seven deposition runs utilized the same deposition conditions as the second materials characterization tube fabrication run (M-217) and nozzle development run (M-218) and were conducted in an attempt to fabricate the required free-standing nozzle shapes for test firing.

7.2 Results

The initial deposition conditions selected yielded a banded microstructure. These bands resulted from changes in the deposition pressure and were in the form of abrupt changes in microstructure from a highly regenerative to a sooty material. To eliminate this problem changes were made in the process parameters to reduce the sensitivity of the deposition process to minor changes in deposition pressure. These changes resulted in a uniform, moderately regenerative, microstructure with the desired physical properties.

Minor changes in the initial deposition geometry were required to obtain a uniform deposition rate along the axial length of the mandrel. The only assembly changes during the course of the program involved relative stand-off distances of the internal baffle plates and exhaust tube bore.

Although the desired coating microstructure and thickness was achieved, all of the throat inserts fabricated were cracked to an extent that they were considered to be unsuitable for test firing.

7.3 Conclusions

Free-standing PG throat inserts of the required shape, sufficient thickness and specified microstructure were fabricated, but none survived the cooldown stresses inherent in the fabrication process.

The last deposition run made before the program was halted, number M-225, and run number M-222 produced shapes which contained no visual cracks upon removal from the furnace, but cracks occurred in both parts during the machining operation.

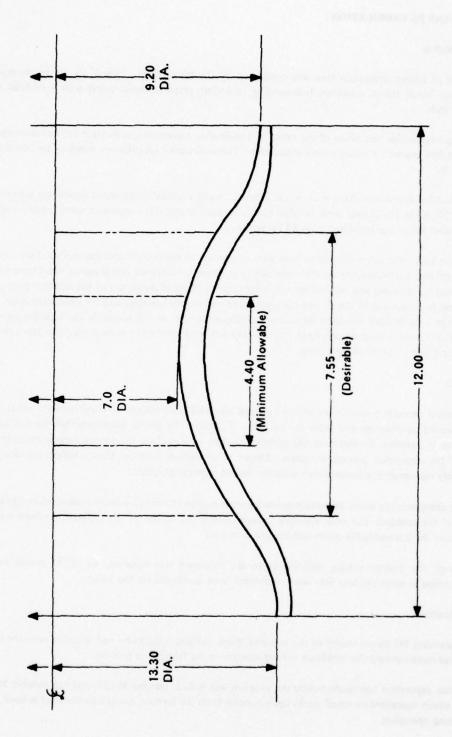


Figure 226. Specified Deposition Shape.

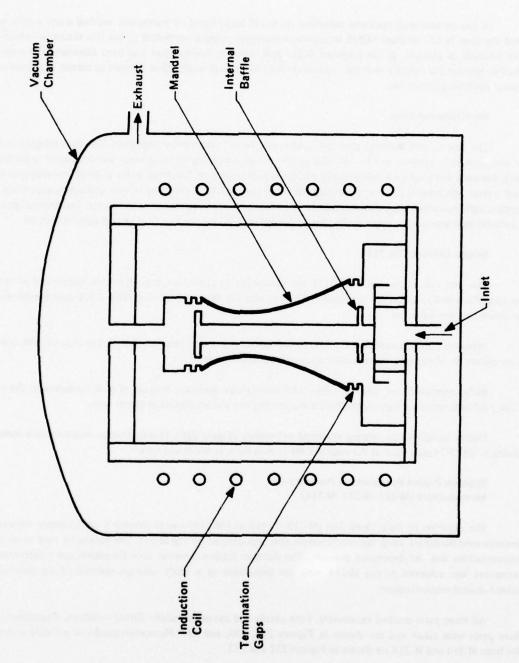


Figure 227. Typical Deposit Assembly.

A ten percent wall thickness reduction (to 0.270 inch) based on parametric residual stress studies was specified for runs M-223 through M-225 to reduce stresses and increase survivability, but this thickness reduction was not achieved as planned. If the proposed 0.270-inch wall (or thinner) part had been fabricated the analysis described in Section 6.0 indicate that the reduced residual stress level would allow the part to survive cooldown and subsequent machining operations.

7.4 Developmental Runs

The seven developmental runs are divided into three categories by objectives. The first category is for system checkout and consisted of one run. The second group, consisting of three runs, was conducted to establish process parameters and produce a continuously nucleated microstructure. The third series of developmental runs was for final system adjustments prior to producing the scheduled inserts. It consisted of two runs which were made in conjunction with two other runs used to produce cylinders for microstructural characterization. Information gained in the cylinder runs was used to upgrade the process conditions used for the two final system adjustment runs.

7.4.1 System Checkout (M-211)

The first run of the series (M-211) was conducted to check out the deposition system and to assess process conditions and resultant microstructure. This run was the first attempt at making a full-scale curved shape and no usable part was expected.

Based on previous experience a 1.00-inch-diameter restriction plug was installed in the exit tube as part of the procedure for obtaining a continuously nucleated microstructure.

Early termination of this run (after 13.5 hours) was necessary because of soot formation at the exit tube. The 1.00-inch restrictor was responsible for the sooting and was eliminated in future runs.

During cooldown the coating shattered extensively (Figure 228), Post-deposition measurements showed the coating to be 15-24 mils thick at the ends and 40-41 mils thick in the throat area.

7.4.2 Establish Process Parameters to Produce a CN Microstructure (M-212, M-213, M-214)

The objective of these three runs (M-212, M-213 and M-214) was to develop a continuously nucleated and uniform microstructure using the configuration that was defined by run M-211. The parameter used to control the microstructure was the deposition pressure. The delicate balance between soot formation and a regenerative microstructure was achieved in run M-214 with the deposition of a fairly uniform material of the previously determined desired microstructure.

All three parts cracked extensively, both axially and circumferentially during cooldown. Photographs of the three parts were taken and are shown in Figures 229, 230, and 231. Photomicrographs of polished material samples from M-213 and M-214 are shown in Figures 232 and 233.

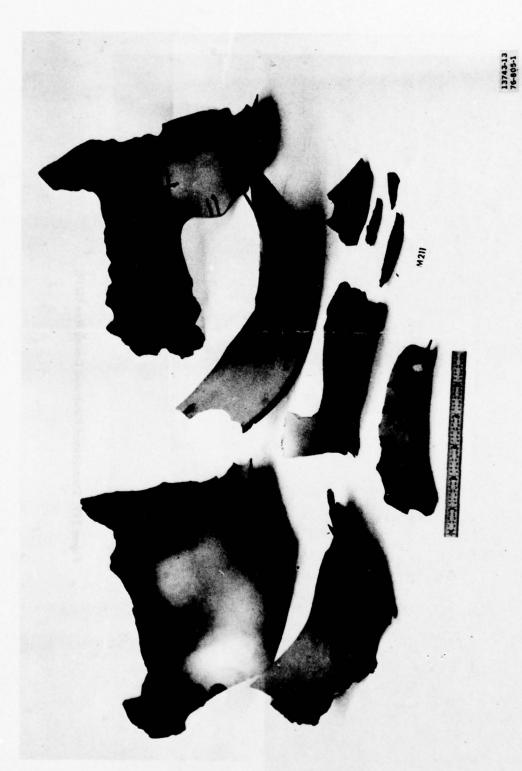


Figure 228. Throat Insert Fabricated During Run M211.



Figure 229. Throat Insert Fabricated During Run M212.



13743-8

Figure 230. Throat Insert Fabricated During Run M213.

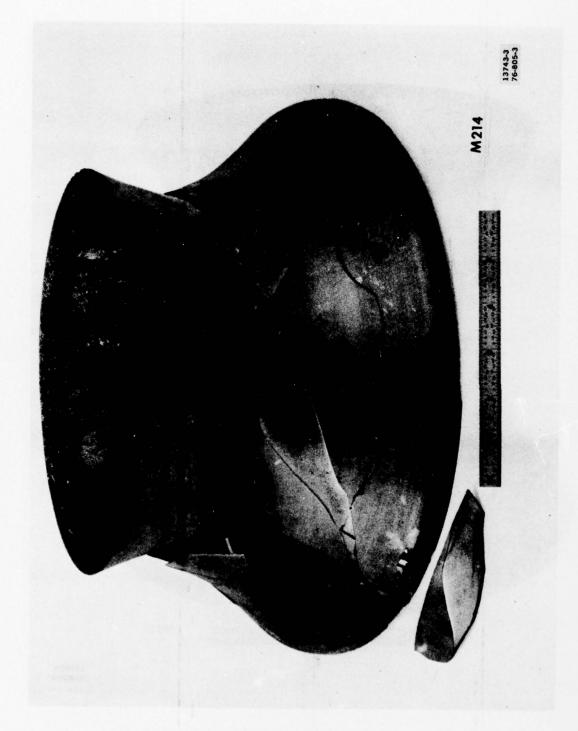


Figure 231. Throat Insert Fabricated During Run M214.

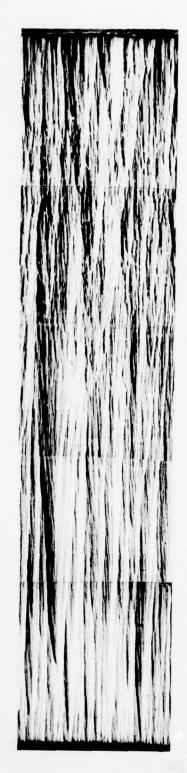


Figure 232. Microstructure of Throat Insert Fabricated During Run M213.50X.



Figure 233. Microstructure of Throat Insert Fabricated During Run M214.50X.

M-212 and M-214 were extremely rough in surface texture indicating a high degree of sooting in the gas phase during deposition. M-213 was somewhat smoother but contained many large nodules; again an indication of excessive gas phase sooting.

Microscopic examination of the polished coating samples showed the degree of renucleation to have varied during deposition in all three runs. The most abrupt change occurred about half way through M-212 where the microstructure changed from moderately regenerative to highly regenerative. A similar but less abrupt change occurred in M-213, in which instance the microstructure changed from substrate nucleated to moderately regenerative about half way through the thickness. M-214 showed the least change in microstructure with deposition time starting with a substrate nucleated material and changing gradually to a moderately regenerative structure about one-fourth of the way through the thickness.

The wall thickness, in all three parts, was approximately 0.300 inch in the throat area and 0.150 inch at the ends.

7.4.2.1 Final System Adjustments (M-216, M-218)

Deposition runs M-216 and M-218 were made in order to adjust the process as necessary to produce the required 0.300-inch wall throat inserts. Beginning with run M-216 the set-up was redesigned for a 0.300-inch wall rather than the 0.600-inch wall allowance on mandrels used in the previous runs. Additional changes introduced successfully in run M-216 were modifications of the top and bottom chambers of the set-up to minimize sooting, and addition of baffles within the part to improve axial coating thickness distribution.

Post deposition examination of M-216 showed the part to be crack-free on removal from the furnace. At this time the part was still quite warm. The upstream (large diameter) end of the part released immediately from the end ring. However, the downstream ring would not release and consequently restrained this end of the part causing it to crack during cooldown to room temperature. Figure 234 shows this part after a section of the downstream end had been removed. The spiraling crack is evident.

M-218 was crack-free on removal from the furnace at 110 to 120°F and both end rings were readily removed. After subsequent cooldown (100 hours) the part had developed several spiraling cracks starting at the upstream end. These cracks initiated at small notches that formed at the edge when the end ring was broken away from the part. Efforts to stop the largest crack by drilling a hole in its path were unsuccessful. Figure 235 shows the part after the cracks had fully developed.

A full coating thickness profile was made of both M-216 and M-218 and this is shown in Table 13.

Figure 236 shows the coating microstructure achieved in M-218.

7.4.2.2 Cylinders for Characterization (M-215, M-216)

To produce material of the desired regenerative microstructure for physical properties testing, two deposition runs were conducted in the furnace used for fabricating the throat insert shapes utilizing similar deposition parameters. These two runs used cylindrical mandrels sized such that processing information gained in

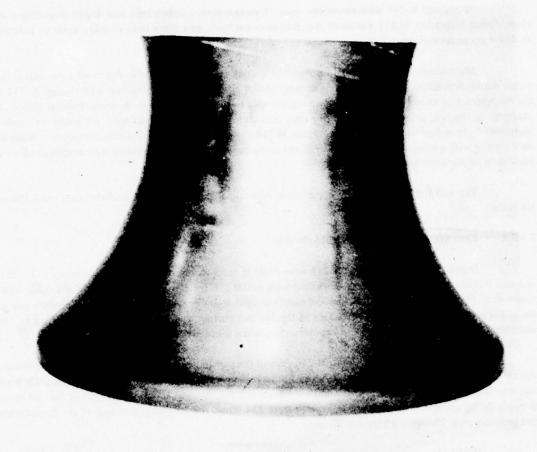


Figure 234. Throat Insert Fabricated During Run M216. Downstream End Removed.

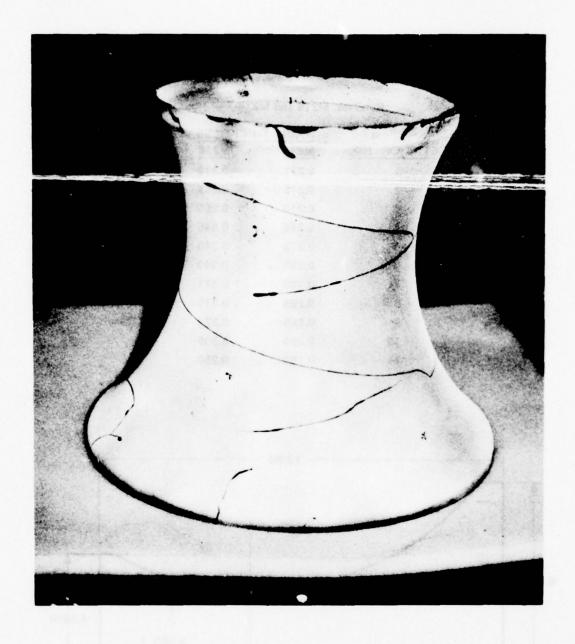


Figure 235. Throat Insert Fabricated During Run M218.

TABLE 13. ATLANTIC RESEARCH CORPORATION 0.300" WALL PG SHAPE.

Run Nos. M216 and M218

STATION NO.	WALL THICKNESS	
	M216	M218
1	0.225	0.310
2	0.315	0.355
3	0.310	0.350
4	0.310	0.345
5	0.315	0.340
6	0.330	0.340
7	0.300	0.325
8	0.295	0.315
9	0.285	0.320
10	0.280	0.305
11	0.180	0.260

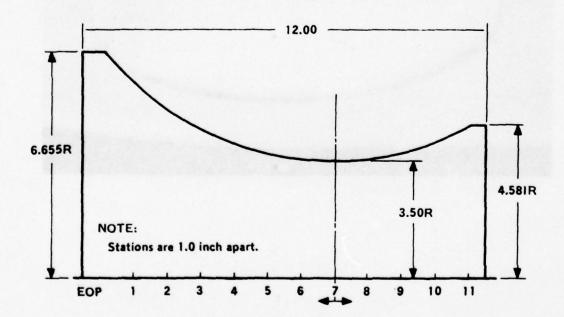




Figure 236. Microstructure of Throat Insert Fabricated During Run M218.50X.

making these cylindrical parts would be of direct use in the final adjustment phase of the developmental runs which were being conducted concurrently. Photographs of the two tubes fabricated are shown in Figures 237 and 238.

The second of these tubes (M-217) was of the desired microstructure and coating thickness. This tube was sectioned and utilized by SoRI to determine the physical properties of a typical renucleated pyrolytic graphite material manufactured by the same techniques utilized in fabricating the seven subsequent nozzle throat inserts. The physical properties data obtained are reported in Section 5.

7.4.3 Production Runs

The production phase which was intended to produce two throat inserts of 0.300-inch wall thickness included seven furnace runs, three of which were aborted, before the program was halted. The purpose of the first and second of these runs was to achieve process reproducibility and the purpose of the last five runs was to produce the required throat inserts.

7.4.3.1 Achieve Process Reproducibility (M-219, M-220)

The object of conducting Runs M-219 and M-220 was to achieve a high degree of reproducibility in the process conditions used to fabricate the throat inserts. One modification made for these runs was a reduction in diameter of the lower stack ring to improve the wall thickness uniformity. Two runs were necessary in this phase because the first run, M-219, was unsuccessful due to an equipment malfunction.

Deposition Run M-219 was halted after 1.75 hours of deposition due to a vacuum pump malfunction, but the run was restarted a short time later. The temperature had dropped to 1,100°C during the down period and was reestablished before resuming the deposition. The resulting part had a double wall growth due to an undetected mandrel breakage that occurred while the furnace cooled to 1,100°C the first time. Post run calculations estimated that the mandrel broke at about 1,600°C during temporary shutdown. Figure 239 shows the part after it was removed from the furnace.

Run M-220 was completed as planned, but a portion of the PG deposit adhered to the mandrel and was torn from the insert shape. A crack beginning at the torn patch on the external surface at the small end propagated along the internal surface to within a few inches of the large end. Figure 240 shows the crack as viewed from the large end.

This part was also used to establish machining techniques for trimming the ends from the inserts. Figure 241 shows the insert and the ends that were trimmed from it. Also visible in this photograph is the torn patch on the external surface at the small end of the part.

7.4.3.2 Produce Deliverable Parts (M-221, M-222, M-223, M-224, M-225)

The last five deposition runs were made in an attempt to produce the specified free-standing PG throat inserts. Two of the runs, M-222 and M-225, produced insert shapes that were removed from the furnace intact, but

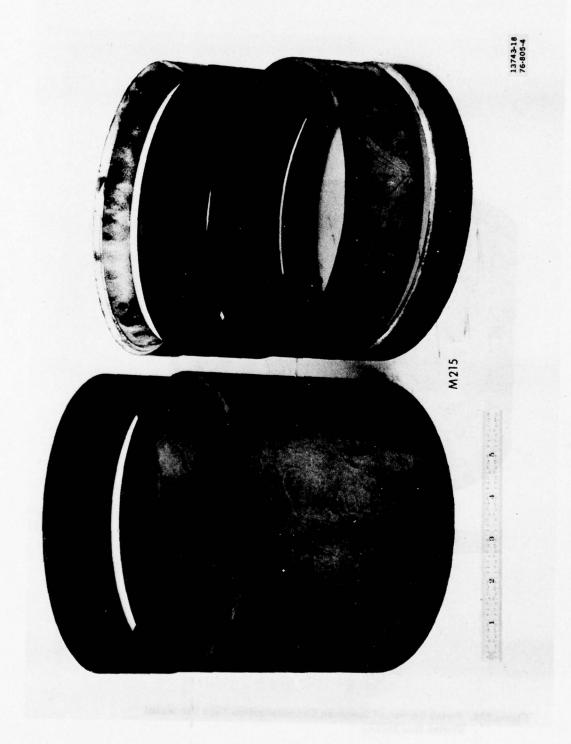


Figure 237. Both Sections of Specimen Characterization Tube Fabricated During Run M215.

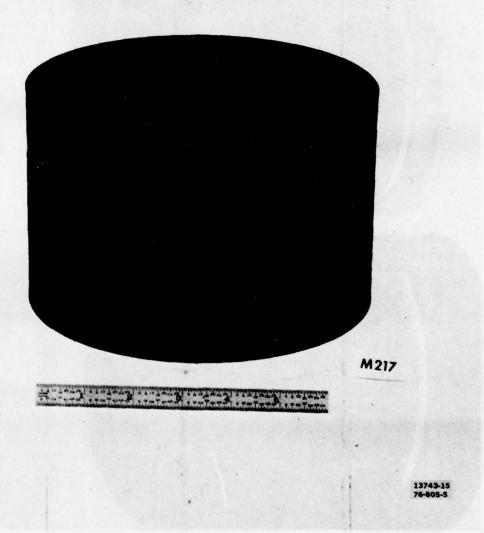


Figure 238. Partial Section of Specimen Characterization Tube Fabricated During Run M217.



Figure 239. Throat Insert Fabricated During Run M219 Showing Separation Due to Extended Process Interuption.

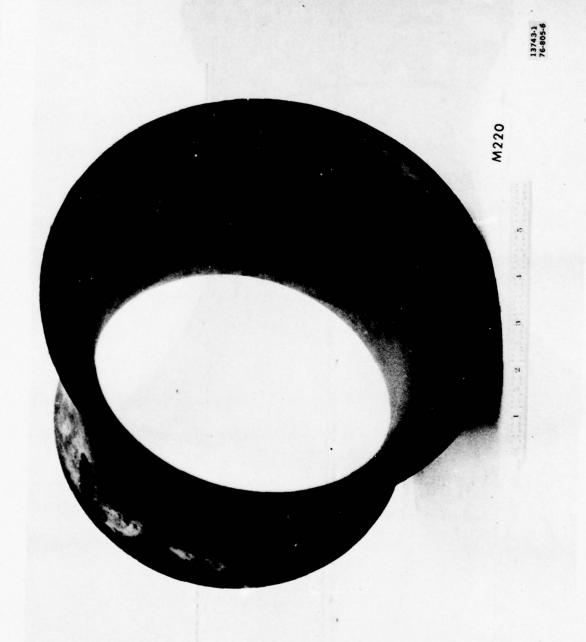


Figure 240. Throat Insert Fabricated During Run M220. Upstream End View.

13743-9

Figure 241. Throat Insert Fabricated During Run M220 Side View.

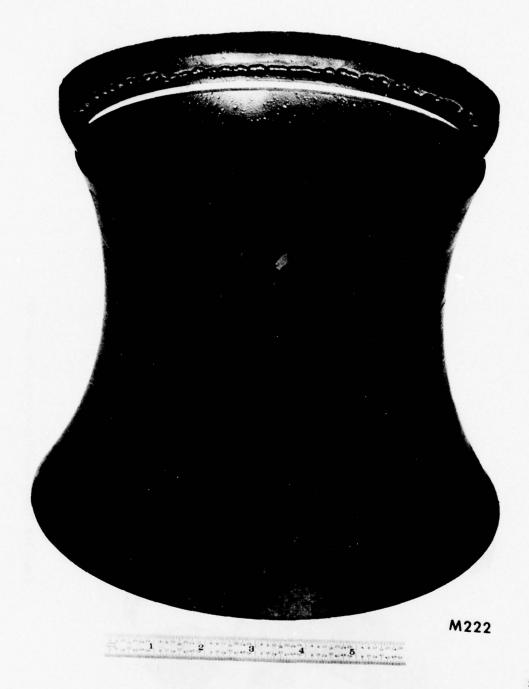
cracked during the subsequent machining process. One run, M-224, produced a part which was cracked before removal from the furnace. The remaining two production runs, M-221 and M-223, were aborted early due to failure of the mandrel to maintain its structural integrity.

Figures 242 through 246 show the parts fabricated in Runs M-221 through M-225.

The part fabricated during Run M-224 was sectioned and across thickness photomicrographs were taken to show the typical moicrostructure achieved during this series. See Figure 247. A definite shift in microstructure from slightly regenerative to a moderatly regenerative can be seen about 15 percent of the way through the coating thickness. An axial coating thickness profile was also constructed and is shown in Figure 248.



Figure 242. Throat Insert Fabricated During Run M221.



13743-7 76-805-9

Figure 243. Throat Insert Fabricated During Run M222.

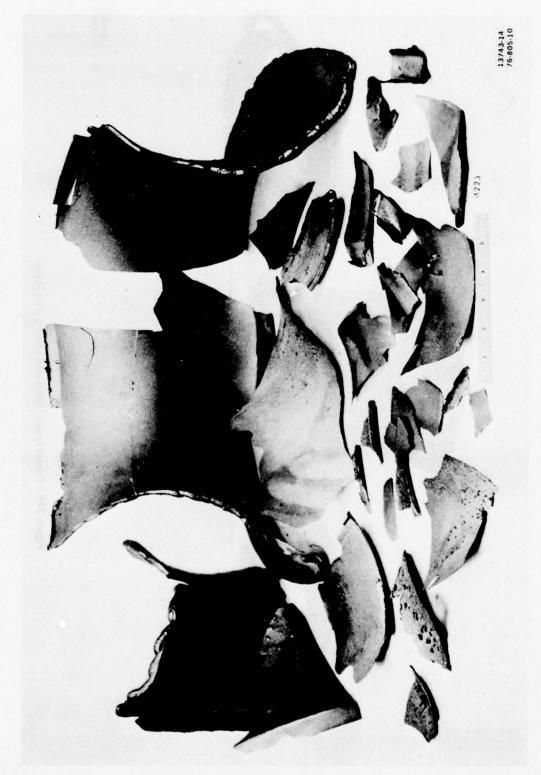


Figure 244. Throat Insert Fabricated During Run M223.

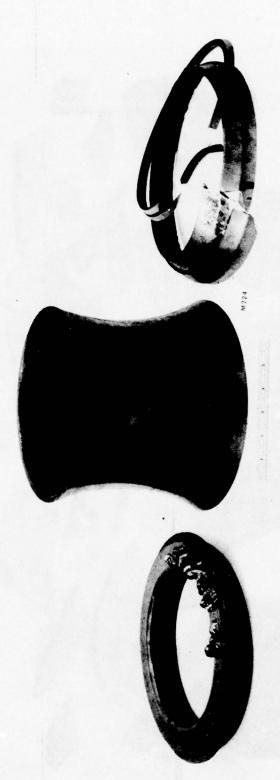


Figure 245. Throat Insert Fabricated During Run M224.



13743-4 76-805-13

Figure 246. Throat Insert Fabricated During Run M225.

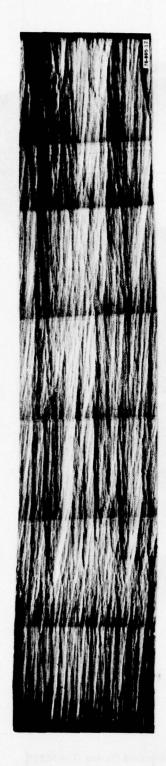
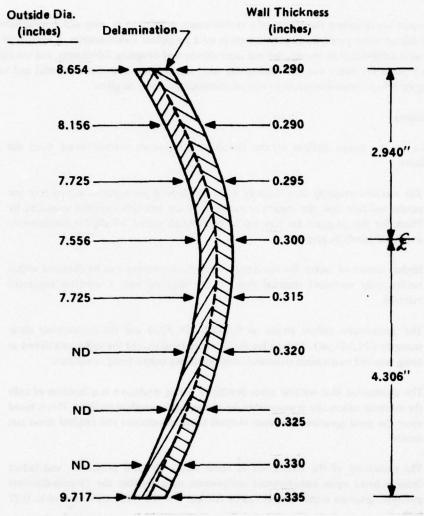


Figure 247. Microstructure of Throat Insert Fabricated During Run M224.50X.



NOTES:

- 1. Measurements taken at 1-inch increments from throat (¢) except at ends.
- 2. Delamination lecated 0.150 0.180 inch from 1D surface.

Figure 248. Coating Thickness Profile of Run M224.

8.0 CONCLUSIONS AND RECOMMENDATIONS

This report has described the efforts of a twelve-month activity to develop and demonstrate the use of commercially available a-b plane pyrolytic graphite inserts in solid propellant rocket nozzles. A number of significant accomplishments were achieved; even though the end item objective of designing, fabricating, and testing a 7.0-inch throat diameter a-b plane PG insert was not successfully met. Based upon both the successful and unsuccessful aspects of the program efforts, several conclusions and recommendations may be given.

8.1 Conclusions

Relative to the design analysis efforts, the major conclusions reached based upon the results are summarized as follows:

- The material property data obtained from the thermal and mechanical property test results indicate that the material properties of the pyrolytic graphite produced by Pfizer for this program are very similar to those identified initially for continuously nucleated pyrolytic graphite.
- Higher factors of safety for the design concepts considered can be obtained with a
 continuously nucleated material than can be obtained with a substrate nucleated
 material.
- 3. The compressive failure strains at 5,000°F (>1.35%) and the interlaminar shear strengths (>1,500 psi) obtained for the Pfizer material exceed the values established as being required to maintain structural integrity during nozzle firing conditions.
- 4. The assumption that residual stress developed during cooldown is a function of only the material anisotropy is acceptable for this pyrolytic graphite material. This is based upon the good agreement between residual stress calculations and residual stress test results.
- 5. The evaluation of the interaction of stress states, strength properties, and failure theories based upon manufactured components indicates that the 7.0-inch-diameter pyrolytic graphite nozzle inserts can be fabricated if the thickness is limited to 0.27 inch.
- 6. Acceptable factors of safety are predicted for both the dual layer and the single layer insert design. Minimum factors of safety for the two concepts are very nearly the same; however, the minimum factor of safety for the single layer design occurs much earlier in the firing.
- Based upon the buckling analysis, with PG thicknesses of 0.150 inch or greater, structural stability of the insert will not present a design problem.

Conclusions relative to the design methodology are summarized as follows:

- 1. Analytical study and evaluation of the shear test specimens and stress distributions in the specimens indicate that property data values are much different from those obtained by assuming an average stress in the gage section.
- Multiaxial failure criteria, as used in this program, predicted the onset of fracture reasonably well. Uniaxial failure criteria predictions were not acceptable. Also conclusions reached on the basis of past failures together with uniaxial failure theories are necessarily suspect.
- For the design concepts considered here, the effects of heat transfer through the
 exposed front edge of the insert have a pronounced influence on the predicted
 in-depth temperature distributions.
- 4. Much of the uncertainty in establishing an acceptable design approach was due to the large scatter in the results of a relatively small number of strength and modulus data.
- 5. In the case of the pyrolytic graphite inserts investigated here, the significant stress levels which developed upon cooldown and the subsequent failure due to those residual stresses provided a means to check certain of the stress and failure predictions prior to actual firing. Additional confidence in the analytical predictions for the behavior of the insert for actual firing conditions was therefore obtained.

Several observations may be made with respect to the efforts to fabricate the desired pyrolytic graphite throat inserts. These are:

- 1. The state-of-the-art of fabrication of pyrolytic graphite in free-standing closed shapes with the double curvature of nozzle inserts is not yet to the point that such parts can be considered as commercially available "off-the-shelf" items.
- 2. Continuously nucleated pyrolytic graphite components having fairly uniform microstructure were fabricated in large sizes with relatively thick walls in cylindrical shapes and in nozzle insert shapes, having very similar microstructures in each. The degree of renucleation, however, was somewhat less than was originally sought because of the sensitivity of the tendency to sooting to the process conditions. The process control requirements necessary to produce the highly continuously nucleated microstructure appear to be outside the limits of those typical for production type deposition equipment. Even so, the microstructure which was obtained consistently was judged to be acceptable for the intended application.
- Relative to the fabrication attempts, then, essentially all objectives of size, shape, microstructure and its uniformity were achieved; a crack-free insert with the desired wall thickness was not achieved, however.

4. On the basis of the results obtained in the last two attempts (M-224 and M-225) to reduce the insert thickness from 0.32 inch to 0.25 inch maximum, the process variables and their influence on deposition rate are not well understood, and the thickness of the deposits apparently can be determined finally only by trial and error.

8.2 Recommendations

Based upon the accomplishments and the conclusions given above, some recommendations about a-b plane pyrolytic graphite throat inserts and about nozzle design analysis in general can be given and are as follows:

- The literature sources for thermal and mechanical properties for pyrolytic graphite
 provide a reasonable starting point as input for analysis. It requires that, in using such
 data, care be exercised in distinguishing between the different types of material that
 can be produced. Characterization of the material is required, of course, but emphasis
 should be placed upon the conduct of tests to obtain data on properties such as
 interlaminar shear, and c-direction tension for which the data is either lacking or
 suspect.
- 2. For all the properties, sufficient testing should be done to establish a reasonable statistical basis for behavior and allowables, particularly the critical ones of compressive strengths and interlaminar shear strengths. Included here also should be the multiaxial properties necessary to establish the constants for the multiaxial failure theories, and to determine the effects, if any, of multiaxial loads on the prediction of stress (and strain) states.
- 3. Although the assumption that the residual stress could be determined by considering only the effects of anisotropy was acceptable for this material, it is known that this may not be the case in general. Therefore, this assumption should not be used unless it is substantiated by actual test data. Moreover, the mechanisms causing residual stress should be investigated, and a consistent approach to treating residual stress in nozzle design analysis should be developed for those situations in which effects other than anisotropy are important.
- 4. Since the dual-layer insert design offered no real advantage, any future attempt to produce and test a free-standing a-b plane PG insert should use the single layer concept. In fact, since minimum factors of safety were developed early in the firing for the single layer design, the test firing duration required to validate the design approach for the single layer design is shorter than that required for the dual-layer design.
- 5. Although the buckling analysis indicated that structural stability for the insert would not be a problem for the design concepts presented here, the possibility of "micro-buckling" of the pyrolytic graphite remains. Further study of buckling at the micro-level is required. Testing approaches developed specifically for this purpose would be necessary. The approaches could perhaps be applied to other materials such as carbon/carbons in which micro-buckling of fibers has been observed.

- 6. The value of test specimen design studies was well illustrated by the results obtained with the finite element analysis of the shear strength specimen. The question of interpretation of test results for other test specimens is one which needs additional study using the available tools of finite element codes, micromechanics analysis and, where available, closed form solutions.
- 7. The question of the right or the acceptable failure criterion for nozzle design analysis is an important one. The results of this study have shown the inadequacy of uniaxial criteria. The multiaxial criteria exhibited more realistic predictions but the correct theory was not defined and fully explored. For rocket nozzle design analysis, a realistic and reasonably accurate means for predicting potential failure is vital.
- 8. In the design and analysis efforts conducted here, the problem of residual stresses and the subsequent failure of parts due to residual stress, was not completely solved. However, the results of the deposition efforts together with the analysis of cooldown did provide a means to validate the analysis techniques at a point intermediate between material characterization and the application of the property test data to the design of actual hardware. It illustrates the value and advantages which can be achieved through the availability of information about the deformation and failure of materials which are to be used in nozzle applications. The same or similar kinds of information could be obtained on PG and other materials such as carbon/carbon composites by developing and using test techniques designed to check the validity of material properties and analysis methods.
- 9. The results of the fabrication efforts point up the fact that very few "advanced" materials can really be considered as commercially available "off-the-shelf" items. For the most part such materials are only commercially available once they have been made to the required specifications, characterized, tested, analyzed, and subjected to the application for which they are intended. Reaching outside the scope of what currently exists must always be approached recognizing that significant developmental efforts will very likely be required.
- 10. As it exists now, if the design, fabrication, and test firing of a-b plane pyrolytic graphite nozzle inserts is pursued, several aspects of fabrication should be recognized at the outset as requiring specific attention. These include the systematic approach to determining the practical limits of continuously nucleated microstructure and thickness, the most appropriate methods of termination for the deposit, improved methods of machining, and other possible mandrel materials.

9.0 REFERENCES

- Carbon/Carbon Substrates for Throat Inserts of Solid Propellant Rocket Motors. (Contract 33615-74-C-5162.)
 Presentation at AFRPL Throat Insert Technology meeting, January 22-23, 1975. TRW Systems Group.
- Thermal/Structural Analysis of Nozzles with "a" Plane Liners. Presentation at AFRPL Throat Insert Technology meeting, January 22-23, 1975. Hercules Incorporated.
- Development of Large Diameter High Chamber Pressure Throat Insert Materials, E.L. Olcott, et al. Final Report AFRPC-TR-72-112, (Contract F04611-70-C-0009) Atlantic Research Corporation, November 1972.
- 4. Cooldown and Motor Firing Thermostructural Analysis of a 7.0-Inch Diameter Pyrolytic Graphite Insert, D.L. Baker, et al. AFRPL-TR-73-72, (Contract F04611-71-C-0023) Aerotherm/Acurex Corp., July 1973.
- Codeposited PG/SiC and PG Nozzle Liners for Advanced ICBM Systems, P.A. Tomlinson, et al. Final Report AFRPL-TR-74-15, (Contract F04611-73-C-0012) Atlantic Research Corporation, November 1974.
- Pyrolytic Graphite Coated Rocket Nozzles: Their Design, Manufacture and Performance in Solid Propellant and Liquid Propellant Rocket Motors, A.C. Parmee. T.T.C.P. D-5 Panel Meeting, Rocket Propulsion Establishment, U.K., June 1971.
- 7. Development and Demonstration of Nozzles Using Bulk Pyrolytic Graphite, W.A. Robba. Final Report AFRPL-TR-67-86, (Contract AF04(611)-9903), Chas. Pfizei & Co., Inc., September 1966 (Confidential).
- Pyrolytic Refractory Thrust Chamber Development, J.G. Campbell, et al. Final Report 5592, (Contract NAS 7-54), Marquardt Corp., August 1963.
- Refractory Thrust Chambers for Spacecraft Engines, J.C. Campbell, C.D. Coulbert. Final Report 6069, (Contract NAS 7-103), Marquardt Corp., July 1964.
- Free-Standing Pyrolytic Graphite Thrust Chambers for Space Operation and Attitude Control, J.G. Campbell, et al. Phase I Analysis and Preliminary Design AFRPL-TR-66-95, (Contract AF04(611)-10790), Marquardt Corp., June 1966.
- Refractory Materials for Spacecraft Thrust Chambers. C.D. Coulbert. Final Report 6115, (Contract NAS 7-373), Marquardt Corp., December 1966.
- Free-Standing Pyrolytic Graphite Thrust Chambers for Space Operation and Attitude Control, J.C. Campbell, et al. Final Report Vol. I & II, AFRPL-TR-68-44 (AF04(611)-10790), Marquardt Corp., September 1968.
- Pyrolytic Graphite, Final Report LMSC 801376, (Contract NORD-17017), Lockheed Missiles and Space Co., June 1962.
- SAAS III Finite Element Stress Analysis of Axisymmetric and Plane Solids with Different Orthotropic, Temperature-Dependent Material Properties in Tension and Compression, J.G. Grose and R.M. Jones, Report No. SAMSO-TR-71-103, The Aerospace Corporation, 22 June 1971.

- Thermal Stress Response Notebook, TRW Systems Group, 10 January 1975; also AFRPL Graphite Thermal Stress Assessment and Inspection Program, Final Report to be published, TRW Systems Group, Redondo Beach, California.
- 16. Pyrolytic Graphite Final Report, Volume 1, Lockheed Missiles and Space Company, 1 June 1962.
- 17. Pyrolytic Graphite Engineering Handbook, General Electric Co., September 1964.
- 18. J.J. Gebhardt and J.M. Berry, "Mechanical Properties of Pyrolytic Graphite," AIAA Journal, Vol. 3, No. 2, February 1965.
- 19. ICRPG Turbulent Boundary Layer Nozzle Analysis Computer Program, July 1968, Pratt & Whitney Aircraft.
- Price, F.C., et al, Internal Environment of Solid Rocket Nozzles, Philo-Ford AF04(611)-9072, W.O. 2104, for Rocket Propulsion Laboratory RPL-TDR-64-140, July 30, 1964.
- 21. Aerotherm Graphite Surface Kinetic Computer Program (GASKET), AFRPL Report TR-72-23, Aerotherm/Acurex Corp., January 1973.
- 22. Aerotherm Axi-symmetric Transient Heating and Material Ablation Computer Program (ASTHMA-3), AFRPL-TR-72-24, Aerotherm/Acurex Corp., January 1972.
- Codeposited PG/SiC and PG Nozzle Liners for Advanced ICBM Systems, Final Report, AFRPL-TR-75-22, September 1975.
- 24. Advances in Heat Transfer, Hartnett, J.P. and Irvine, T.F., Volume 6, 1970, Academic Press, New York.
- 25. E.M. Wu, "Phenomenological Anisotropic Failure Criterion" in *Composite Materials, Vol. 2*, Ed. G.P. Sendecky, Academic Press, New York, 1974.
- Puppo, A.H., and Evensen, H.A., "Strength of Anisotropic Material Under Combined Stresses," AIAA Journal, Vol. 10, No. 4, April 1972.
- Advanced Composites Design Guide, Volume II, Analysis, Third Edition, Air Force Materials Laboratory, January 1973.
- 28. S.W. Tsai and E.M. Wu, "A General Theory of Strength for Anisotropic Materials" J. Composite Materials, Vol. 5, January 1971, pp. 58-80.
- 29. T.G. Priddy, "A Fracture Theory for Brittle Anisotropic Materials," Jour. of Engng. Mat ls. and Tech., April 1974, pp. 91-96.
- 30. T.J. Clark, and R.J. Larsen, Final Report on Work Statement 87, "Residual Stress Studies," General Electric Report P 1-WS-0232, Metallurgical Products Dept., Detroit (1961).

10.0	LIST OF SYMBOLS
1.	a-b (A-B) Direction (Parallel-Circumferential)
2.	a (subscript)
3.	A
4.	A* Throat Area
5.	α
6.	b (subscript)
7.	c (subscript)
8.	Cp Specific Heat
9.	C(subscript)
10.	CH Heat Transfer Coefficient
11.	C _M Mass Transfer Coefficient
12.	E
13.	EPSN
14.	EPST
15.	ϵ
16.	°F Degrees Farenheit
17.	F _s
18.	F _T Tensile Strength
19.	F _C Compressive Strength
20.	G
21.	ID Inner Diameter
22.	ν Poissons' Ratio
23.	OD Outer Diameter
24.	P _O External Pressure
25.	P _i
26.	P
27.	QRAD
28.	$g_{cr}/E_{ heta}$
29.	r
30.	R
31.	r _o
32.	ρ

ecific Gravity	Sp																										 				SG	33.
Axial Stress																													1	GN	SIC	34.
Hoop Stress																													1	GT	SIC	35.
Radial Stress																													1	GN	SIC	36.
bscript, Stress	Su	h	vit	r v	0	nt	ta	ns	oı	C	ar	m	ltz	Во	n-	fa	Ste	. :													σ	37.
Temperature																															T	38.
. Thickness																															t	39.
. Coordinate																															θ	40.
Shear																											 				τ	41.
Shear Stress																												N	M	U	TA	42.
. Coordinate																															7	43

APPENDIX A

THERMAL AND MECHANICAL PROPERTY TEST RESULTS FOR PYROLYTIC GRAPHITE

Final Report

Prepared by:

Gerald W. Driggers

December 31, 1975

Southern Research Institute 2000 Ninth Avenue South Birmingham, Alabama 35205



December 31, 1975

Mr. P. A. Tomlinson Atlantic Research Corporation 5390 Cherokee Avenue Alexandria, Virginia 22314

Dear Mr. Tomlinson:

This is the final report for work done under Purchase Order E-06764 of Prime Contract F09611-75-C-008. The purpose of this program was to evaluate the properties delineated in Table 1 for a Pfizer Pyrolytic graphite in cylindrical form. The cylinder provided by ARC was nominally five inches long (axial dimension) with a 7.8 inch OD and 0.190 inch wall thickness. Examination of the material by photomicrograph or Scanning Electron Microscope was not included in this program. Visual inspection revealed a cone structure evident of some continuous nucleation although this was not dramatic. The structure is best described as between what is generally considered substrate nucleation and continuous nucleation. This is consistent with the verbal description provided by ARC and Pfizer.

As shown on Table 1, several evaluations were required in the "a-b" plane. The nomenclature adopted for this program assigns the material "a" direction parallel to the cylinder axis (Z), the "b" direction as circumferential (θ) and the "c" direction as radial (r). Since the material is considered to be isotropic in the "a-b" plane and evaluation of circumferential specimens would present several unique problems, all "a-b" specimens were taken out with the test direction oriented along the "a" (Z) axis. Interlaminar shear strength was evaluated similarly. The shear modulus determination was conducted in a fashion suitable for determining two values; $G_{\theta Z}$ and G_{rZ} = $G_{r\theta}$. In the material axis system these are G_{ba} and G_{ca} = G_{cb} . Methodologies will be discussed later.

Table \mathbb{R}^2 PG Cylinder Evaluation Matrix

Post local design	Temperature in °F										
Evaluation Type	RT	1500	3500	5000							
Compression-"a-b"	2	-	2	2							
Compression-"c"	3	-		_							
Tension-"a-b"	3		3	23 V 0 0 - 1							
Unit Thermal Expansion-"a-b"*	2 —			-							
Unit Thermal Expansion-"c"*	2			A SECTION							
Shear Strength Interlaminar	3	3	5	3							
Shear Modulus	3	-	-	-							

^{*}Unit thermal expansion measurements were conducted twice on these specimens to evaluate the effects of a repeated thermal cycle

Mr. P. A. Tomlinson Atlantic Research Corporation Page 2 December 31, 1975

The evaluation matrix presented in Table 1 represents the experiments actually performed for property determination. This is slightly different from the specification in the Statement of Work. At the request of ARC three interlaminar shear evaluations at 1500°F and two at 3500°F were added to the matrix and three tensile tests deleted. The five additional specimens were made from the deleted tensile specimen blanks.

The cutting plans used to specify locations for removal of specimens are shown in Figures 1 and 2. Prior to layout of the cylinder for specimen removal, a series of axial cuts were made to stress relieve the part and determine the extent to which it changed dimensionally. This was accomplished by etching marks approximately one-half inch apart on the outside circumference. Single saw cuts were then made between these marks until the cylinder no longer sprang together after a cut. The amount the etched marks came together and the change in ID and OD were then measured. The average OD and ID prior to contraction was 7.838 inches and 7.461 inches, respectively. The measurements were made at four locations and OD varied by ±0.003 inches while ID varied by ±0.006 inches. After the cylinders were cut the OD and ID measurements were 7.675 ± 0.002 inches and 7.301 ± 0.006 inches, respectively. A circumferential contraction of 0.528 inches was measured.

When cutting began for specimen removal two things were noted. First a crack was found near one end of the cylinder which went through the wall. A section about 2-1/2 inches axially and 1-1/2 inch circumferentially was made unusable by the crack. It was necessary to relocate specimens to avoid the cracked area. The general shape and location of the crack is shown on Figure 1.

Mr. P. A. Tomlinson Atlantic Research Corporation Page 3 December 31, 1975

Another unexpected behavior was noted when the tensile specimen blanks were removed. When placed against a flat surface, they exhibited a decided bowing in the axial/radial plane. The center deflection was measured for the ten specimens and averaged 0.0178 inches. Actual measurements by specimen number are given in Table 2. There was no apparent bow in the shorter blanks with the exception of the torsional (SM-shear modulus) specimens. These deflected only 0.001-0.002 inches which was considered negligible in the property measurement. The deflection of the specimen center was toward the axis of the cylinder in all cases.

Specimen Configurations

The axial compressive, tensile, interlaminar shear strength and torsional specimens used for evaluations in this program are shown in Figures 3 through 7. Radial compaction was also evaluated using three 1/4 inch diameter x 0.175 inch thick disks. Shear modulus in the 2θ ("a-b") plane was determined from two curved plates, one 2 inches x 2 inches x 0.150 inches and the second 1.5 inches x 1.5 inches x 0.190 inches. The first plate was more nearly ideal for this measurement but was inadvertently broken after the first measurement. The second plate was taken from the remaining material and evaluated primarily as a check on the single test of the first plate.

Unit thermal expansion specimens for Z direction measurements were 0.175 inches x 0.175 inches x 3.0 inches. Measurement of radial ("c") direction) expansion was accomplished by stacking twenty pieces 1/4 inches x 1/4 inches x 0.150 inches to obtain a three inch specimen.

As reflected by Figures 5 and 6, two gage areas were used for interlaminar shear strength measurements. Pyrolytic graphite generated by continuous nucleation has typically exhibited an increase in interlaminar shear strength with increasing temperature. This necessitated a reduction in gage area to avoid destructing the graphite loading fixture prior to specimen failure.

Mr. P. A. Tomlinson Atlantic Research Corporation Page 4 December 31, 1975

Evaluation Techniques

All tensile evaluations were performed in a gas-bearing tensile facility. This facility utilizes gas-bearings in the load train to eliminate kinking and the introduction of unknown bending stresses in the specimen in order to provide a true uniaxial load. Clip-on strain gage extensometers were attached to graphite clamps on the specimen. Two extensometers (one on each side) were used. These were balanced to compensate as much as possible for specimen bending. This arrangement is shown schematically in Figure 8. The gasbearing tensile facility is described generally in Appendix A.

The cylindrical curvature of the specimen required that special grips be machined from graphite to accommodate them. The load was introduced into the specimen at the tab lip (see Figure 4) as interlaminar shear. The grips were hand fitted to the specimens and worked as anticipated at room temperature. Some wedging and slipping was encountered at 3500°F due to the mismatch of expansion in the grips and specimens. This did not substantially affect the data obtained.

All of the axial compressive evaluations were performed in the gas-bearing compressive facility. Gas-bearings were installed on each end of the load train to permit precise alignment of the load train and the specimen. The gas-bearings and the load train are shown diagramatically in Figure 9. A general description of the gas-bearing compressive facility is included in Appendix B.

The compressive specimens were loaded via graphite anvils with curved slots machined to conform to the specimen. Lateral supports were machined to conform to the convex and concave faces of the specimen in order to delay the onset of buckling. Targets for the optical strain analyzer were attached to the specimen edges via small graphite clamps.

Mr. P. A. Tomlinson Atlantic Research Corporation Page 5 December 31, 1975

The interlaminar shear specimens shown earlier were loaded in compression using graphite anvils slotted to hold the specimen aligned. The anvils were fitted in a special graphite loading sleeve to insure alignment and each gage section was fully supported by close fitting lateral spacers to prevent bending. The sleeve was loaded in a gas-bearing tensile facility.

The shear modulus determinations were conducted using two techniques to isolate individual moduli. Torsion of an axial rectangular specimen about the Z axis and measurement of the resulting angular deflection was conducted as described in our report to ARC under Purchase Order 94561. The report number was SoRI-EAS-74-068, March 1974. This evaluation allowed determination of the relationship between G_{12} and $G_{13} = G_{23}$. That relationship is given by G_{12}

 $\frac{M}{\theta} = G_{12} \text{ ab}^3 \beta(c)$ $C = \frac{a}{b} \frac{G_{23}}{G}$ $C = \frac{a}{b} \frac{G_{23}}{G}$

where

M = applied moment

meters and constants are

 θ = relative rotation of gage

 $a = width (\theta direction) of gage$

b = thickness (r direction) of gage

and $\beta(c)$ is the function shown on Figure 9. The other para-

With G determined from another experiment, G could be isolated.

¹Lekhnitskii, S. G. Theory of Elasticity of an Anistropic Body, Holden-Day, Inc., 1963.

Mr. P. A. Tomlinson Atlantic Research Corporation Page 6 December 31, 1975

The plate test specified by ASTM C3044-72 was used to determine the in-plane (G_{12}) modulus. The geometry of this arrangement is shown in Figure 10. Data obtained in this evaluation consisted of load applied (P) and differential deflection (δ_d) between the probes on the diagonals. The required equation is

$$G_{12} = 3Pd^2/2\delta_dt^3$$

where d is the radius from the center of the plate to the probes and t is the plate thickness. A small Instron Testing machine was used for loading and a differential deflection device built at SoRI used for δ_d measurement.

Thermal expansion measurements were made from about 70°F to 1700°F utilizing the quartz tube dilatometer and a dial gage. The required specimen heat input was obtained from electric resistance heaters and measured via thermocouple.

Thermal expansion measurements were made from 70°F to 5000°F utilizing the graphite dilatometer with a dial gage. The specimen was heated radiantly in a graphite tube furnace.

The uncertainty in measurements for both apparatuses using the standard 3-inch long specimens utilized in this program is estimated at ±5 percent. These apparatuses are described in Appendix C.

Results and Observations

Mechanical Evaluations

The composite results of the tensile, compressive, shear strength and shear modulus evaluations are presented in Figures 11 through 15 and Tables 3 through 6. The raw data curves are included in Appendix D.

Mr. P. A. Tomlinson Atlantic Research Corporation Page 7 December 31, 1975

The tensile data do not exhibit the trend of a highly substrate nucleated PG which usually has a decrease in modulus at 3500°F. The increase in tensile modulus at 3500°F shown in Figure 11 has been noted on some continuously nucleated PG and seems to depend on process variables since other regenerative PG exhibits the opposite character. The average values obtained here were 3.36 x 10^6 psi at room temperature and 4.49 x 10^6 psi at 3500°F. The data curves do not show any discernable effect due to the bow in the specimen.

The strength obtained from the tensile evaluations is presented on Figure 12. Substantial scatter is apparent and probably due to a combination of factors. The stress state in the specimen was complicated by two external factors: the longitudinal curvature and the mismatch in expansion between extensometer attachments and the specimen. This would cause stress concentrations in the area of the flags. Nodule size distribution also appeared to influence the results at room temperature. The two lowest values were obtained from specimens that fractured around larger than average nodules. No similar characteristic was observed at 35()°F since the highest values were obtained from specimens fracturing near larger nodules. Examination of X-Ray, sonic velocity and density data did not reveal any notable relationships to modulus or strength data.

The modulus and strength measurements obtained from compressive evaluations are shown in Figures 13 and 14. The trends of the data obtained are typical of previous measurements reported in the literature for regenerative PG. Some problems were encountered in loading two specimens resulting in breakage prior to test. The third run at 3500°F was deleted in order to run a fourth tensile specimen.

The results of the interlaminar shear strength evaluations are shown on Figure 15 as a function of temperature. The increasing strength at elevated temperature is typical of continuously nucleated PG. Substantial scatter in values is notable at 3500°F and contrasts to the grouping of the other data. As shown on Table 5, a mixture of two gage sections (1/4 inch x 1/2 inch and 1/2 inch x 1/2 inch) was used at this temperature. Specimen numbers IS-14 and IS-15 were added after IS-4 yielded a particularly low value. These yielded intermediate values between IS-4 (1/2 inch x 1/2 inch gage) and IS-2 (1/2 inch x 1/4 inch gage).

Mr. P. A. Tomlinson Atlantic Research Corporation Page 8 December 31, 1975

Previous work with carbon/carbon using mixes of these gage sections has always yielded comparable data between experiments. Since stress concentrations should be largely load and gage section independent there is no apparent analytical explanation for a gage area effect. No correlation between density or sonic velocity values and strength was found. Visual observation of the fracture surfaces of all specimens revealed one observation of interest. All room temperature, 1500°F and low value 3500°F specimens had irregular and random "flecking" ("a-b" plane peeling). The high value 3500°F and all three 5000°F specimens exhibited a regularity in pattern and were generally aligned along lines perpendicular to the load direction. The intermediate 3500°F specimen (IS-15) showed similar characteristics although the regularity was not as pronounced. It is possible that a material transition is taking place fairly rapidly at 3500°F, and the exact state of the material during the experiment is unknown. Additional studies to explore this were not within the scope of this program.

The shear modulus evaluations were conducted only at room temperature. Three torsional rods were used and two plates. The first plate was loaded too high and broke after one test. The second plate was not near optimum from the standpoint of side to thickness ratio. It was used primarily as a check on the first plate and to evaluate orientation (i.e. convex up versus convex down) effects on the data. The measured G modulus was slightly lower than for the larger

plate (1.84 x 10 6 psi versus 2.02 x 10 6 psi) as anticipated. The G values given in Table 6 were calculated using

2.02 x 10 6 psi for G, ..

Thermal Evaluations

The unit thermal expansions of pyrolytic graphite from cylinder S/N M-217 in the "a-b" and "c" directions during first and second cycles up to 5000°F are shown in Figures 16 through 21 and tabulated in Tables 7 through 18. Duplicate data for each exposure were obtained in both orientations.

Mr. P. A. Tomlinson Atalantic Research Corporation Page 9 December 31, 1975

The two cycles refer to first performing thermal expansion evaluations from room temperature to about 5000°F, allowing the specimens to cool to room temperature and performing the same evaluations during a second exposure from room temperature to 5000°F.

Initial exposures to 5000°F in the "a-b" direction on two specimens are shown in Figure 16. During the initial exposure the expansion was relatively low up to about 3500°F, exhibiting a value at that temperature of 4.25 x 10^{-3} in./in. Above 3500°F the value increased sharply to about 16×10^{-3} in./in. at 5000°F, for specimen M-217-CTE-1A. The other specimen exhibited the identical expansion up to about 5000°F, but the value at 5000°F was lower, about 15×10^{-3} in./in. At 5000°F both specimens continued to grow with time indicating that the growth was time as well as temperature dependent.

The difference in the expansion between the two specimens at 5000°F is real as indicated by the high final return values, see Figure 16. This difference is permanent as indicated by the final dial reading and measured length change by a micrometer after the specimen was cooled to room temperature.

Results of the second exposure to 5000°F in the "a-b" direction on the same two specimens are shown in Figure 17. During the second cycle the expansion was slightly lower than that of the first cycle up to about 3500°F. The expansion increased significantly above 4500°F and again at about 5000°F the specimens continued to grow with time. This phenomenon has been recognized on other programs involving thermal expansion measurements on pyrolytic graphite.

This unstable behavior can be explained, in part, in terms of the structure of pyrolytic graphite. The graphitization-annealing temperature of the "as received" material is not known, but the material probably was not well graphitized-annealed, and could be classed as turbostratic in that their crystallites are well oriented in the "a" direction

Mr. P. A. Tomlinson Atlantic Research Corporation Page 10 December 31, 1975

but are rotated about the c-axis with random translation in the "a-b" plane. Further, it probably had "curved" "a-b" planes in the nodules. This is indicated by the fact that the negative expansion (or contraction) was not as great as that exhibited for a well graphitized-annealed and ordered pyrolytic graphite, and the fact of the significant increase in expansion above about 3500°F.

The material showed slight contraction in the "a-b" direction from room temperature to about 900°F. The contraction on conventional pyrolytic graphite is explained in terms of Poisson contraction of the layer planes (basal) associated with large expansion perpendicular to the layer planes (c-axis) as explained by Riley. Above about 1000°F, this effect is assumed to be counteracted by a true thermal expansion of the layer planes to produce a small positive thermal expansion.

The increase in expansion at elevated temperatures, in addition to the time dependence of the elongation and the large permanent growth also suggest the process of annealing. During the annealing process on a poorly graphitized ordered pyrolytic graphite, a restructuring and straightening of the crystallites joined by tilt boundaries or kinks in the basal plane occur. This creates high growth in the "a" direction and contraction in the "c" direction. This is true of the material evaluated on this program as evidence from the composite plots shown in Figures 20 and 21. The second run on the specimens also shows the result of graphitizationannealing, which is the lower expansion at the elevated temperatures. Note that even during the second run, the material was apparently altered as evidenced by the increase in expansion above 4500°F in the "a-b" direction and the continued dependence of growth on time.

²ASD-TDR-63-195, "Pyrolytic Graphite, Its High Temperature Properties", March, 1963.

³Riley, D. P., Phys. Soc. 57, 487 (1945).

Mr. P. A. Tomlinson Atlantic Research Corporation Page 11 December 31, 1975

Figure 18 shows the unit thermal expansion of the "as received" pyrolytic graphite in the "c" direction as a result of the initial exposure, and Figure 19 shows the same for the second exposure to 5000°F. The above discussion also explains the character of the two curves in the "c" direction, large permanent contraction after the initial exposure, and contraction after peak expansion at 5000°F. The thermal expansion increased almost linearly from room temperature to a maximum value of about 62 x 10⁻³ in./in. at about 4500°F, and then a contraction to about 40 x 10-3 in./in. at 5000°F. Repeatability was very good for the measurements as evidenced by the curves.

Figure 20 and 21 are composites showing thermal expansion results of both exposures in the two directions.

In pyrolytic graphite, the structure can range from a material where the growth cone develops from the deposition surface (nonregenerative or substrate nucleated) to a material where the growth cones are regenerated continuously throughout the thickness of the deposition (continuously nucleated). material evaluated on this program exhibited characteristics of a material structured partially by nonregenerative growth cones and partially by regenerative cones. That is, the data lies between that generated on other programs where the material was completely nonregenerative and those where the material was completely regenerative. The large expansion in the "a-b" direction and contraction in the "c" direction at 5000°F represents a response due to time at temperature and graphitizationannealing.

Yours very truly,

Gerald W. Driggers

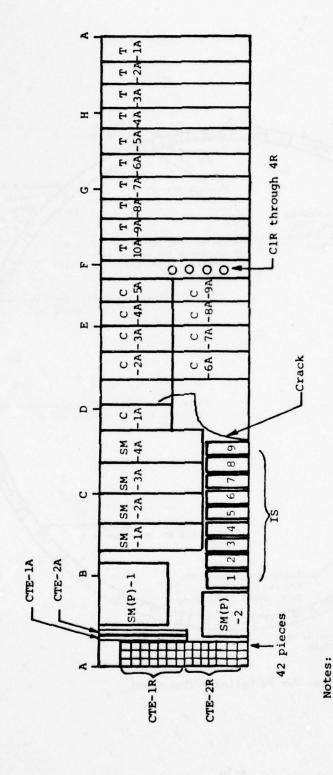
Associate Engineer

Approved by

. D. Pears, Director

Mechanical Engineering Research

GWD: bac SORI-EAS-75-660 3553-I-F (6:14)



A - Axial
R - Radial
First cut along axis at A
Inner radius all curved specimens = 3.750 in.
Outer radius all curved specimens = 3.500 in.

Inside out view - Letters correspond to top view drawing

Figure 1. Cutting Plan for PG Cylinder (Side View)

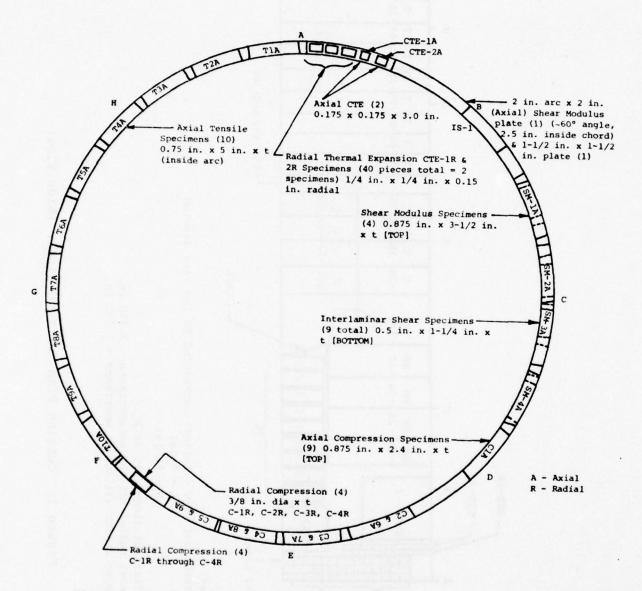
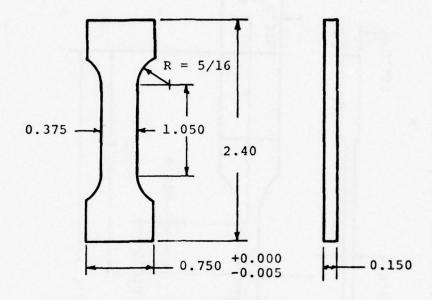
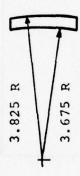


Figure 2. Cutting Plan for PG Cylinder (Top View)





Note: All dimensions are in inches

Figure 3. Axial Compressive Specimen Configuration

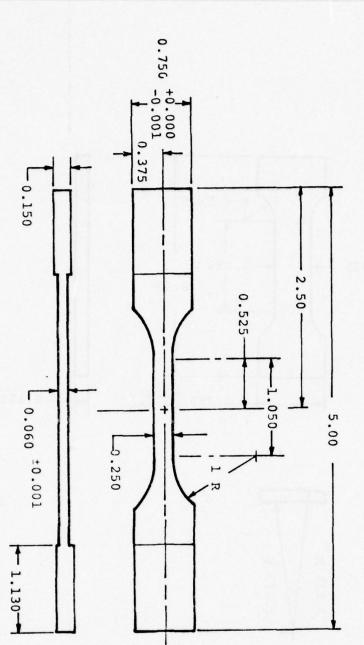
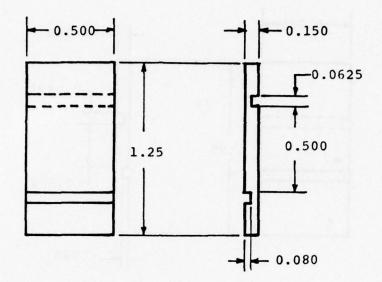
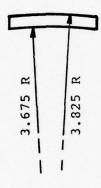


Figure 4. Axial Tensile Specimen Configuration

Note: All dimensions are in inches

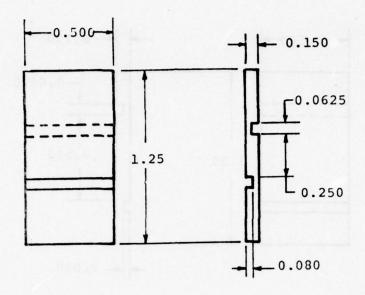
3.675 R 3.720 R 3.780 R

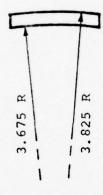




Note: All dimensions are in inches

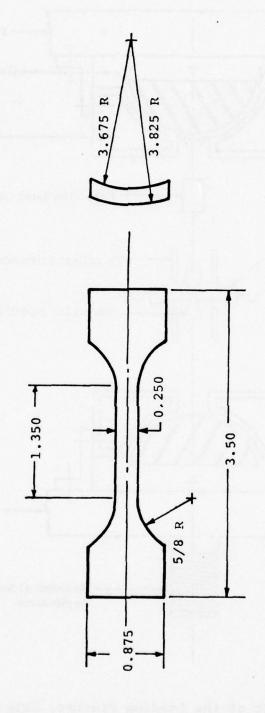
Figure 5. Interlaminar Shear Specimen with a 0.500 inch Gage Length





Note: All dimensions are in inches

Figure 6. Interlaminar Shear Specimen with a 0.250 inch Gage Length



Note: All dimensions are in inches

Figure 7. Axial Torsional Specimen Configuration

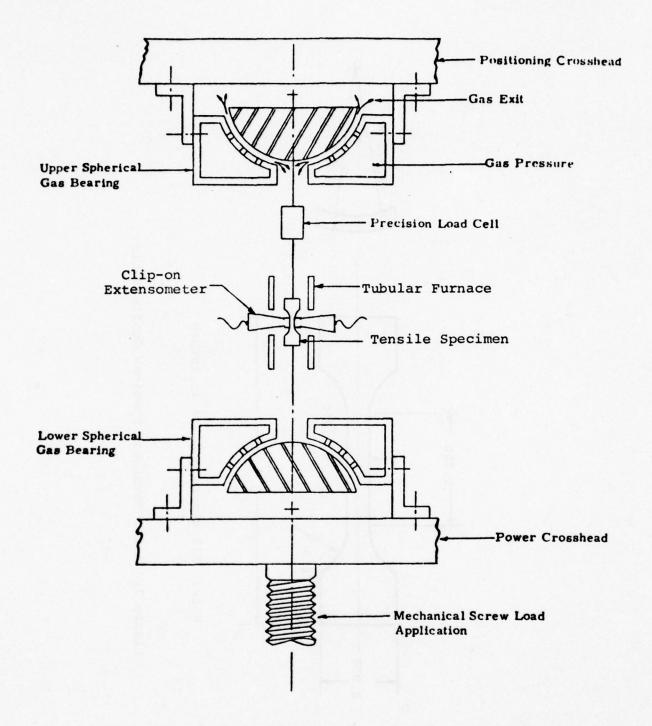


Figure 8. Schematic of the Loading Fixture, Extensometers and Furnace Used for Tensile Evaluations

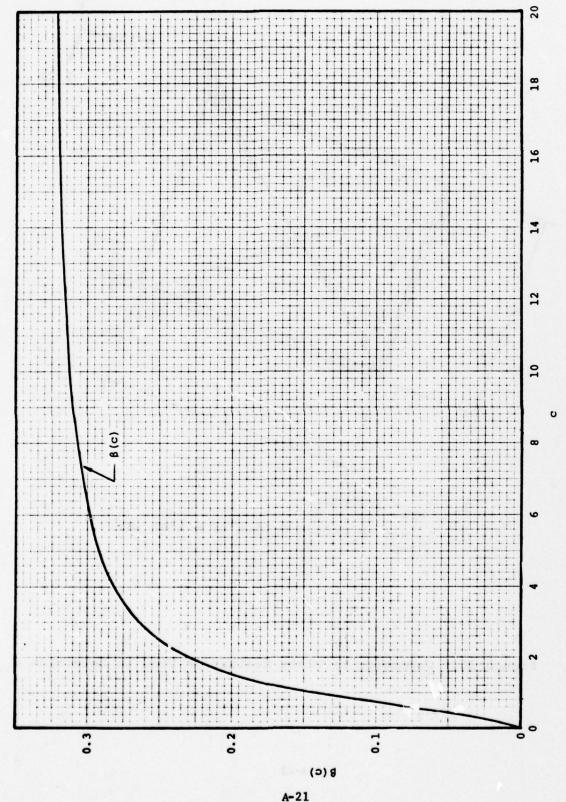
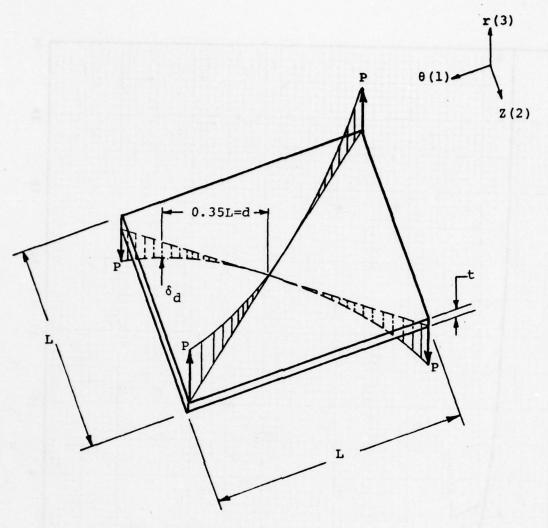


Figure 9. Plot of B(c) versus c for a Rectangular Torsional Specimen



- 1. $G_{xy} = 3Pd^2/2\delta_d t^3$
- 2. δ_d not to exceed 0.10 t ($\sigma \simeq 2000 \text{ psi}$)

Figure 10. Schematic of Plate Evaluation Used to Determine G12

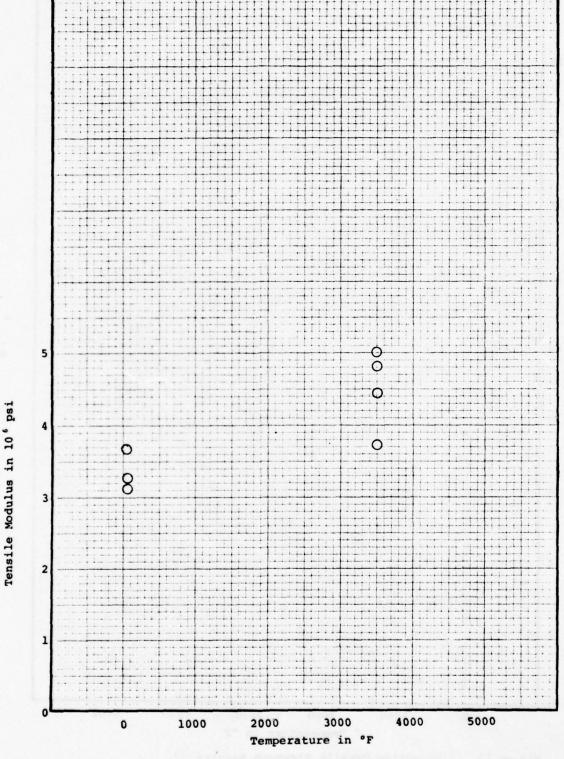


Figure 11. Z Direction Tensile Modulus Results

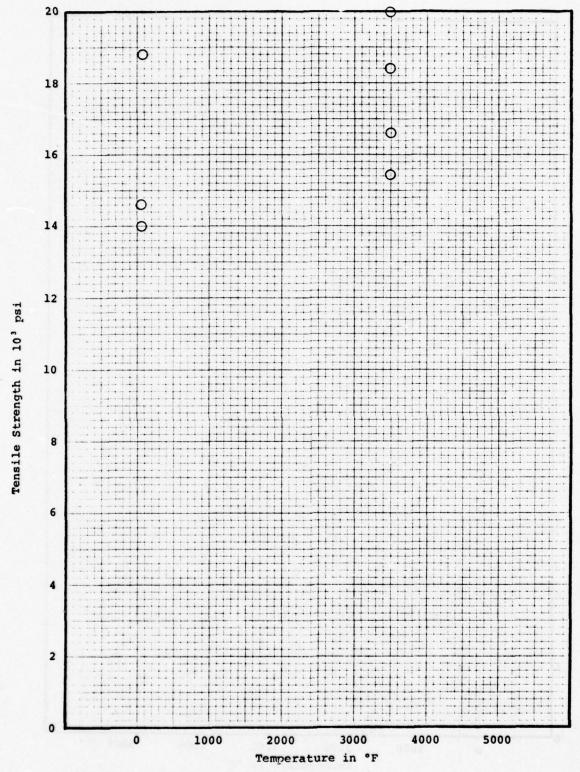


Figure 12. Z Direction Tensile Strength Results
A-24

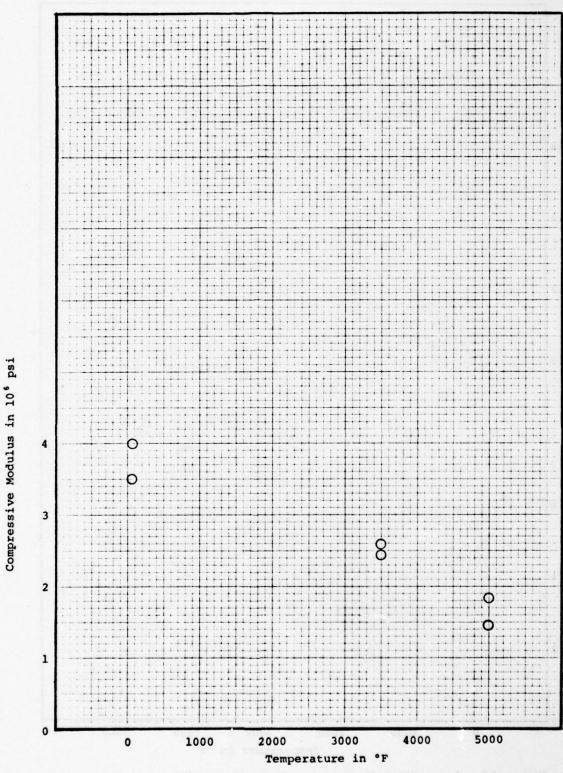


Figure 13. Z Direction Compressive Modulus Results

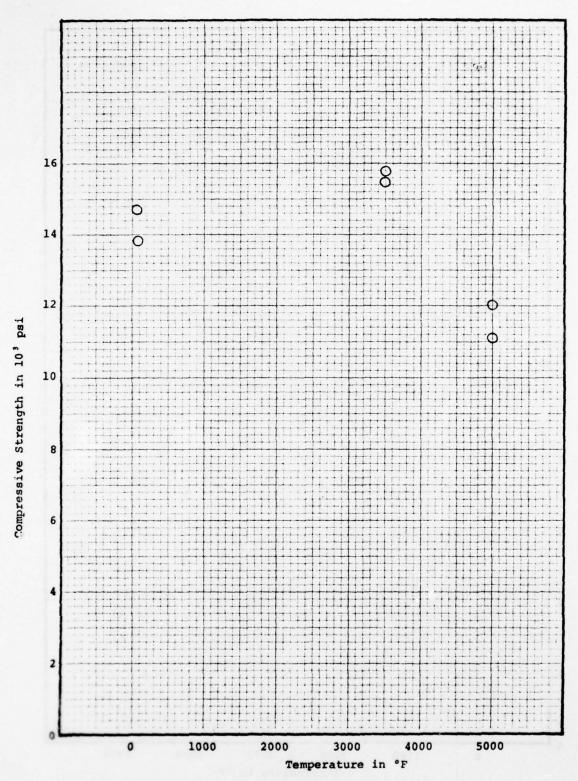


Figure 14. Z Direction Compressive Strength Results

A-26

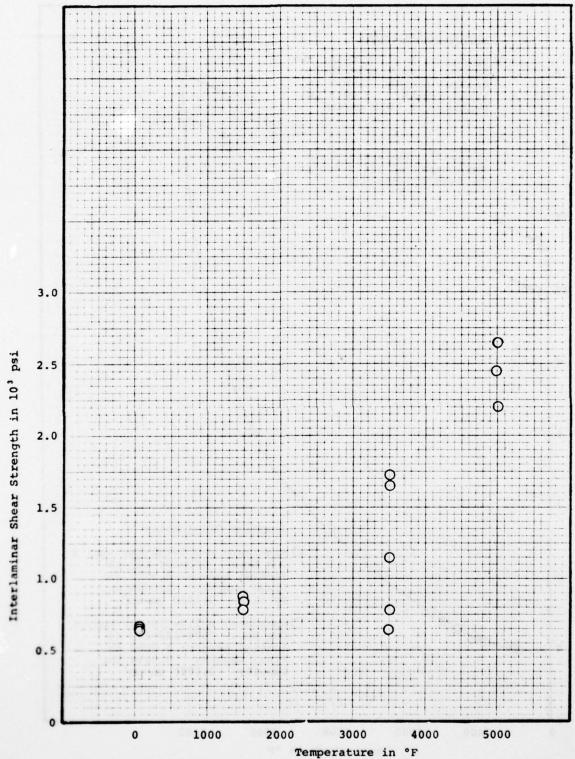


Figure 15. Interlaminar Shear Strength Results

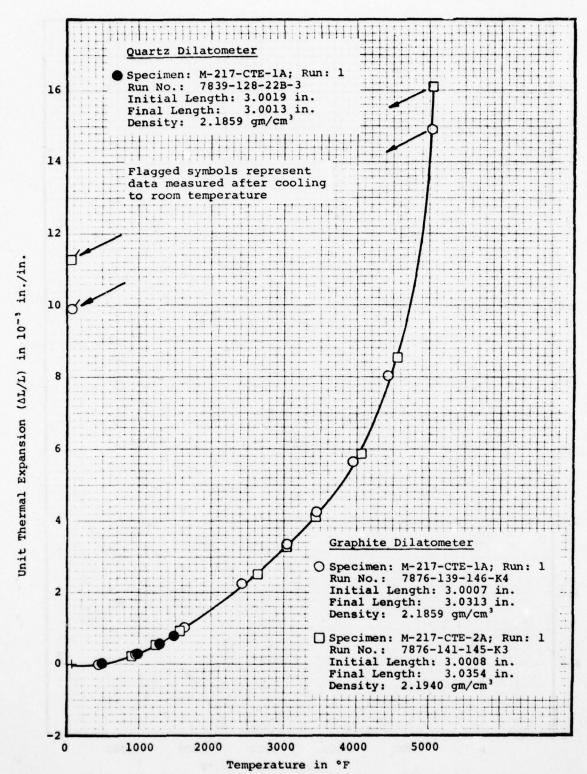


Figure 16. Thermal Expansion of Pyrolytic Graphite (Cylinder S/N M-217) as Received in the "a-b" Direction

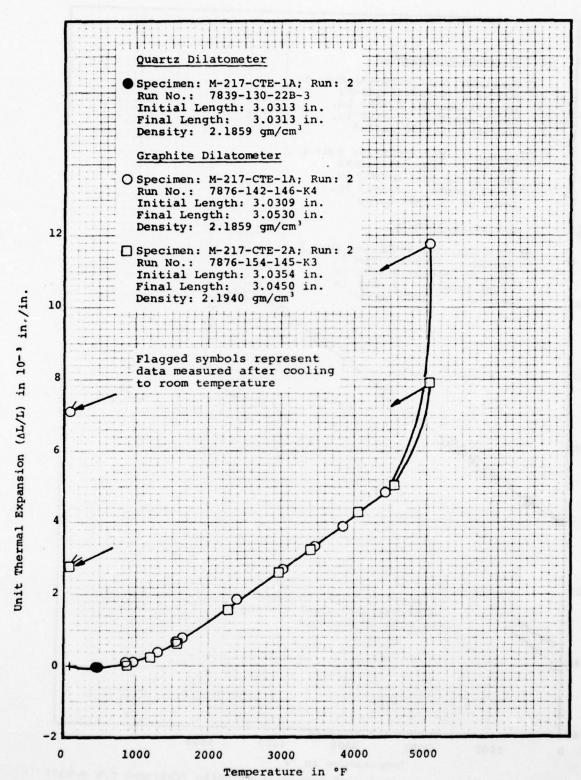


Figure 17. Thermal Expansion of Pyrolytic Graphite (Cylinder S/N M-217)
After Previous Exposure to 5000°F in the "a-b" Direction

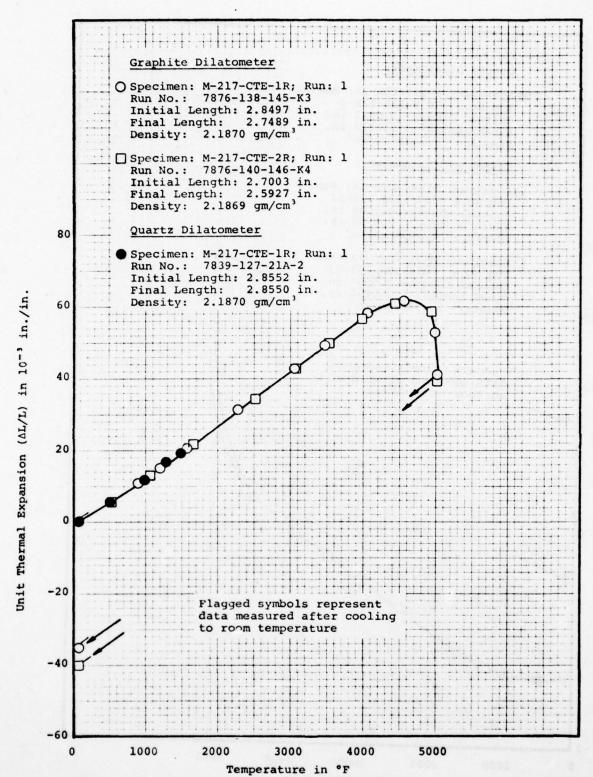


Figure 18. Thermal Expansion of Pyrolytic Graphite (Cylinder S/N M-217) as Received in the "c" Direction

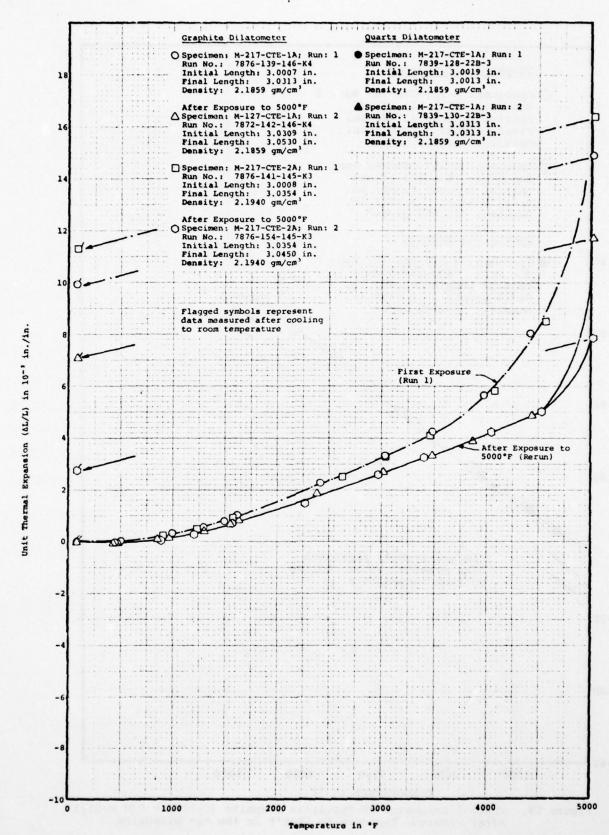


Figure 20. Comparison of Thermal Expansions (Run 1 - as Received, Run 2 - After Being Exposed to 5000°F) of Pyrolytic Graphite Cylinder 5/N M-217 in the "a-b" Direction

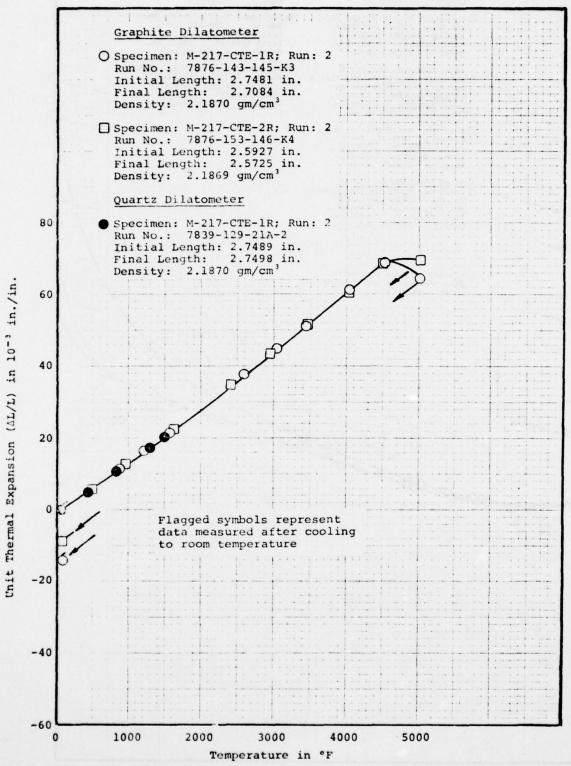


Figure 19. Thermal Expansion of Pyrolytic Graphite (Cylinder S/N M-217)
After Previous Exposure to 5000°F in the "c" Direction

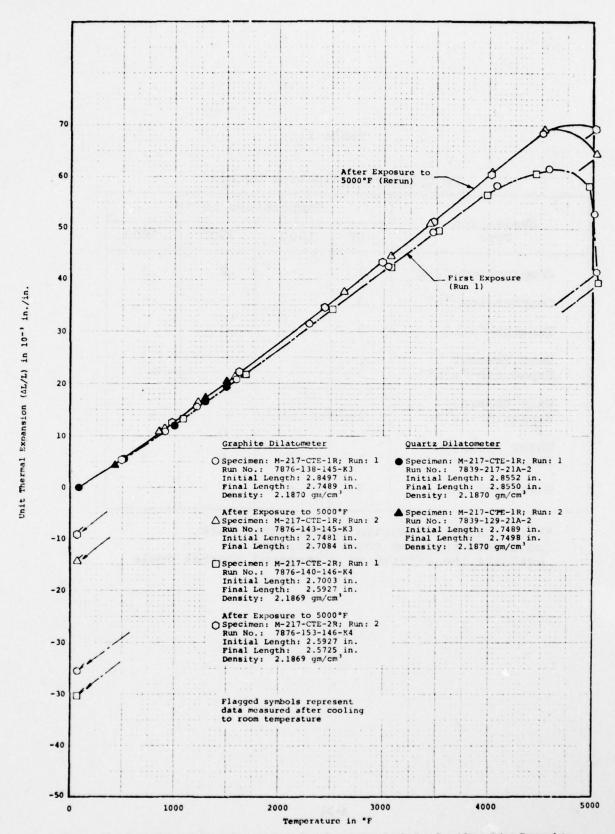


Figure 21. Comparison of Thermal Expansions (Run 1 - as Received, Run 2 - After Jeing Exposed to 5000°F) of Pyrolytic Graphite Cylinder S/N M-217 in the "c" Direction

Table 1
PG Cylinder Evaluation Matrix

Evaluation		Temperat	ure in °1	P
Type	RT	1500	3500	5000
Compression-"a-b"	2	-	2	2
Compression-"c"	3	-	-	-
Tension-"a-b"	3	-	3	-
Unit Thermal Expansion-"a-b"*	2 —			-
Unit Thermal Expansion-"c"*	2			-
Shear Strength Interlaminar	3	3	5	3
Shear Modulus	3	-	-	_

^{*}Unit thermal expansion measurements were conducted twice on these specimens to evaluate the effects of a repeated thermal cycle

Table 2

Deflection of Tensile Specimen Center Relative to Ends

Specimen	Deflection
T-1A	0.0167
T-2A	0.0171
T-3A	0.0188
T-4A	0.0204
T-5A	0.0209
T-6A	0.0141
T-7A	0.0184
T-8A	0.0186
T-9A	0.0170
T-10A	0.0163

Table 3

Failed above flag (at small nodule) Failed at flag (large nodule) Failed at flag (large nodule) Failed between flags (large nodule) Failed between flags (large nodule) Failed at flag (no nodule) Failed at flag (no nodule) Remarks Sonic Velocity in./wsec 0.1814 0.1809 0.1812 0.1823 0.1812 0.1808 0.1813 0.0043 ~0.0055 in./in. 0.0054 0.0043 ~0.0045 Strain Results of Axial (Z) Tensile Evaluations Unit Axial Total Initial Elastic Modulus 10⁶ psi 3.72 3.69 3.27 3.11 4.80 4.44 5.00 Ultimate Strength psi 14600 14000 18400 20000 18800 16600 15400 Bulk Density gm/cm 2.2034 2.2042 2.2023 2.2068 2.2026 2.2064 2.2004 Specimen Number TTA TIA T6A T2A T3A T5A T4A Rate psi/min 10,000 10,000 10,000 10,000 10,000 10,000 10,000 3500 3500 3500 Temp 3500 200 10 Direction "a-p" "a-p" "a-b" "a-p" "a-p" "a-e" "a-b"

Table 4

Results of Compressive Evaluations

Total Unit Axial Strain in./in.	0.0058	0.0073	0.007	>0.013	>0.014							
Initial Elastic Modulus 10 ⁶ psi	3.5	2.59	2.44	1.80	1.43							
Ultimate Strength psi	14,700	15,800	15,450	11,100	12,000	75,000	74,700	75,000			•	
Bulk Density gm/cm³	2.2046	2.2050	2.2018	2.2057	2.2042							
Specimen Number	M-217-C-4A	M-217-C-7A	M-217-C-5A	M-217-C-3A	M-217-C-6A	M-217-C-1R	M-217-C-2R	M-217-C-3R				
Rate psi/min	10,000	10,000	10,000	10,000	10,000	10,000	10,000	10,000	**************************************			
Temp °F	5 5	3500	3500	2000	2000	70	70	70				
Load	"a-b"	"a-b"	"a-b"	"a-b"	"a-b"	.°°	"°	.°°.				Total Total

Table 5 Results of Interlaminar Shear Evaluations

Gage Section	0.5 x 0.5 0.5 x 0.5	0.5 × 0.5 0.5 × 0.5	0.5 × 0.5	0.5 x 0.25 0.5 x 0.25 0.5 x 0.25	0.5 × 0.5	0.5 × 0.5	0.5 x 0.25 0.5 x 0.25 0.5 x 0.25			
Sonic Velocity in./wsec	0.1840 0.1862 0.1885			0.1856 0.1862 0.1874			0.1852 0.1848 0.1859			
Total Unit Axial Strain in./in.										
Initial Elastic Modulus 10 ⁶ psi										
Ultimate Strength psi	630 660 650	830	780	1720 1650 640	1140	786	2440 2640 2200			
Bulk Density gm/cm	2.2030 2.2012	2.2024	2.2024	2.2012 2.2011 2.2052	2.2024	2.2024	2.2011 2.2022 2.2003	1 X 3		
Specimen Number	M-217-IS-9 M-217-IS-3 M-217-IS-1	M-217-IS- 10-T9A M-217-IS-	11-T9A M-217-IS- 12-T9A	M-217-IS-8 M-217-IS-2 M-217-IS-4	M-217-IS-	M-217-IS- 14-T9A	M-217-IS-7 M-217-IS-6 M-217-IS-5			
Rate psi/min	1000	1000	1000	1000	1000	1000	1000			
Temp °F	70 70 70 70	1500	1500	3500 3500 3500	3500	3500	5000		ja A	
Direction	"a-b" "a-b"	"a-b"	"a-b"	" a-b" "a-b"	"a-b"	"a-b"	"a-b" "a-b"			

Table 6

Results of Torsion and Shear Modulus Plate Evaluations

Load Temp Rate Specimen Dulk Ultimate Elastic Axial Direction or psi/min Number Giz							 	
Temp Rate Specimen Density Strength Number Gm/cm³ psi	Total Unit Axial Strain in./in.	2" x 2" x 0.150 plate	1.5" x 1.5" x 0.194 plate					
Temp Rate Specimen Density OFF psi/min Number Gm/cm ³ 70 - SM (P)-1 2.2194 70 - SM-1A 2.2122 70 - SM-2A 2.2048 70 - SM-4A 2.2093	Initial Elastic Modulus 10 psi	2.02	1.84	0.19	0.18	0.21		
Temp Rate Specimen D Number g 70 - SM (P)-1 70 - SM-1A 70 - SM-2A 70 - SM-2A 70 - SM-4A	Ultimate Strength psi	1	1	•	•	1		
Temp Rate of psi/min	Bulk Density gm/cm³	2.2194	2.1987	2.2122	2.2048	2.2093		
Temp 70 70 70 70 70 70 70 70 70 70 70 70 70	Specimen Number	SM (P)-1	SM (P)-2	SM-1A	SM-2A	SM-4A		
	Rate psi/min	•	1	•				
Load Direction G12 G23 G23	Temp °F	02	02	70	02	02		
	Load Direction	G ₁₂	G ₁₂	G ₂ 3	G ₂₃	G _{2 3}		

Table 7

Thermal Expansion of Pyrolytic Graphite (Cylinder S/N M-217) as Received in the "a-b" Direction Measured in Quartz Dilatometer

Corrected	Unit Elongation 10 in./in		0.0	0.03	0.31	0.56	0.78	-0.03	
Unit Elongation Correction for	Dilatometer Motion 10-3 in./in.	e e	0.0	0.17	0.35	0.47	0.56	0.0	TO THE PARTY OF TH
Observed	Unit Elongation 10- in./in.	ght: 3.2888 gm t: 3.2887 gm	0.0	-0.14	-0.04	0.09	0.22	-0.03	
Observed	Total Flongation 10-3 in.	Initial Weight: Final Weight:	0.0	-0.41	-0.12	0.28	99.0	-0.08	
tures - °F	Average	9 in. 3 in.	75	200	1000	1300	1500	75	
Specimen Temperatures	Bottom	gth: 3.0019 h: 3.0013	7.5	200	1000	1300	1500	75	
Speci	Top	Initial Length: Final Length:	75	200	1000	1300	1500	75	
	Time	Init	9:30	10:10	10:50		11:30	8:05	
	Specimen	Specimen: M-217-CTE-1A Run: 7839-	128-22B-3 Density: 2.1859 gm/cm ³	Run: 1					

Table 8

Thermal Expansion of Pyrolytic Graphite (Cylinder S/N M-217) as Received in the "a-b" Direction Measured in Graphite Dilatometer

Corrected Specimen Unit Elongation (10 ⁻³ in. /in.)	0.0 -0.03 0.28 1.04 2.25 3.35 4.22 5.66 8.06 14.93 9.91
Unit Correction for Dilatometer Motion (10 ⁻³ in. /in.)	0.0 0.22 0.83 1.86 3.33 4.56 5.44 6.50 7.45 8.78
Observed Unit Elongation (10 ⁻³ in./in.)	0.0 -0.25 -0.55 -1.08 -1.21 -1.22 -0.85 0.61 6.15 9.91
Observed Total Elongation (10 ⁻³ in.)	0.0 -0.74 -1.66 -3.24 -3.65 -2.56 1.82 18.44 29.74
Time	9:15 9:45 10:15 10:50 11:25 12:25 1:25 7:20
Temp.	75 445 985 1618 2412 3038 3478 3969 4415 75
Specimen and Run No.	Specimen: M-217-CTE-18 Run: 1 Run: 7876-139-146K4 Initial Length: 3.0007 in. Final Length: 3.0313 in. Initial Weight: 3.2887 gm Final Weight: 3.2892 gm Density: 2.1859 gm/cm³

Table 9

Thermal Expansion of Pyrolytic Graphite (Cylinder S/N M-217) as Received in the "a-b" Direction Measured in Graphite Dilatometer

Corrected Specimen Unit Elongation (10-3 in. /in.)	0.0 0.22 0.49 0.91 2.50 3.27 4.10 5.81 8.56 16.39 11.32	
Unit Correction for Dilatometer Motion (10 ⁻³ in. /in.)	0.0 0.66 1.17 1.79 3.81 4.68 5.58 6.92 8.01 9.04	
Observed Unit Elongation (10 ⁻³ in./in.)	0.0 -0.44 -0.68 -0.88 -1.31 -1.41 -1.48 1.11 0.55 7.35 11.32	
Observed Total Elongation (10 ⁻³ in.)	0.0 -1.33 -2.63 -3.92 -4.24 -4.45 -3.33 1.64 22.07	Organ part
Time	9:05 9:40 10:10 10:45 11:20 11:50 12:50 1:20 7:30	
Temp.	75 904 11235 11235 1577 2639 3043 3043 4070 4567 5014	
Specimen and Run No.	Specimen: M-217-CTE-2A Run: 1 Run: 7876-141-145K3 Initial Length; 3.0008 in. Final Length: 3.0354 in. Initial Weight: 3.3021 gm Final Weight: 3.3011 gm Density: 2.1950 gm/cm³	også fambade Fi

Table 10

Thermal Expansion of Pyrolytic Graphite (Cylinder S/N M-217) after Previous Exposure to 5000°F in the "a-b" Direction Measured in Quartz Dilatometer

1	1			-				
		Specim	Specimen Temperatures	tures - °F	Observed	Observed	Unit Elongation	Corrected
Time	ø	Top	Bottom	Average	Total Elongation 10-3 in.	Unit Elongation 10- in./in.	Dilatometer Motion 10-3 in./in.	Unit Elongation 10- 3 in./in
H E	iti	Initial Length: Final Length:	h: 3.0313 in.	in.	Initial Weight: Final Weight:	Weight: 3.2892 ight: 3.2889	2 gm 9 gm	
9:40	0	75	75	75	0.0	0.0	o o	6
10:20	20	431	431	431	-0.55	-0.18	0.14	-0.04
10:45	45	850	850	850	-0.57	-0.19	0.28	0.09
		1300	1300	1300	-0.23	-0.08	0.47	0.39
11:30	30	1550	1550	1550	0.17	90.0	0.59	0.65
8	8:10	75	75	75	-0.10	-0.03	0.0	-0.03
		d H						
		9						

Table 11

Thermal Expansion of Pyrolytic Graphite (Cylinder S/N M-217) after Previous Exposure to 5000°F in the "a-b" Direction Measured in Graphite Dilatometer

				-		
			Observed	Observed		
Speciment	Temn		Flongation	Flongation	Dilatometer Motion	Corrected Specimen
Run No.	·F.	Time	(10-3 in.)	(10 ⁻³ in./in.)	(10 ⁻³ in. /in.)	(10 ⁻³ in. /in.)
Specimen: M-217-CTE-1A	75	9:15	0.0	0.0	0.0	0.0
Run: 2	497	9:45	-0.99	-0.33	0.29	-0.04
Initial Length:	965	10:15	-2.05	-0.68	0.81	0.13
3.0309 in.	1634	10:50	-3.29	-1.09	1.89	0.80
3.0530 in.	2392	11:25	-4.24	-1.40	3.28	1.88
Initial Weight:	3008	11:55	-5.42	-1.79	4.50	2.71
Final Weight:	3478	12:25	-6.32	-2.09	5.44	3.35
3.2991 gm	3868	12:55	-7.36	-2.43	6.29	3.86
- And Const.	4435	1:25	-8.09	-2.67	7.50	4.83
CALL TO SERVE	5014	2:00	60.6	3.00	8.78	11.78
	75	6.50	21.51	7.10	0.0	7.10
				Sales	Barrier Street	
Section 1						
TO TO THE PROPERTY OF THE PARTY						Transfer as
						-

Table 12

Thermal Expansion of Pyrolytic Graphite (Cylinder S/N M-217) after Previous Exposure to 5000°F in the "a-b" Direction Measured in Graphite Dilatometer

Corrected Specimen Unit Elongation (10 ⁻³ in. /in.)	0.0 0.1 0.23 0.64 1.57 2.60 4.23 5.04 7.87
Unit Correction for Dilatometer Motion (10 ⁻³ in. /in.)	0.0 0.65 1.12 1.79 3.11 4.55 5.49 6.87 7.97 9.02
Observed Unit Elongation (10 ⁻³ in./in.)	0.0 -0.89 -1.15 -1.95 -2.23 -2.64 -2.93 -2.93 -2.93
Observed Total Elongation (10-3 in.)	0.0 -1.95 -3.48 -4.68 -5.91 -6.76 -8.88 -3.50 +2.76
Time	8:10 8:45 9:15 9:50 10:25 10:55 11:25 12:25 8:40
Temp.	75 880 1201 1572 2271 2967 3402 4040 4547 5014
Specimen and Run No.	Specimen: M-217-CTE-2A. Run: 2 Run: 7876-154-145K3 Initial Length: 3.0354 in. Final Length: 3.0450 in. Final Weight: 3.3011 gm Final Weight: 3.0009 gm Density: 2.1940 gm/cm³

Table 13

Thermal Expansion of Pyrolytic Graphite (Cylinder S/N M-217) as Received in the "c" Direction Measured in Quartz Dilatometer

		Specia	Specimen Temperatures	atures - °F	0	Observed	Unit Elongation Correction for	Corrected
Specimen	Time	Top	Bottom	Average	Elongation 10-3 in.	Elongation 10- 3 in./in.	Motion Motion 10-3 in./in.	Elongation 10 ⁻³ in./in
	Ini Fin	Initial Length: Final Length:		2.8552 in. 2.8550 in.	Initial Weight: Final Weight:	ht: 6.3835 gm : 6.3824 gm		
Specimen: M-217-CTE-1R Run: 7839-	9:30	75	75	75	0.0	0.0	0.0	0.0
127-21A-2	10:10	530	530	530	16.19	5.67	0.15	5.82
2.1870 gm/cm ³	10:50	1000	1000	1000	33.44	11.71	0.27	11.98
	100 Che 1	1300	1300	1300	45.68	16.00	0.36	16.36
	11:30	1500	1500	1500	53.46	18.72	0.43	19.15
	8:05	75	75	75	0.01	0.0	0.0	0.0
		2 4		3 S 7 Y	3.3		1 0 00 0 00 0 0	
100					2 4	3 5		
					# :	N =	7 0	
					B 8338		Stape of the	
				The same of				

Table 14

Thermal Expansion of Pyrolytic Graphite (Cylinder S/N M-217) as Received in the "c" Direction Measured in Graphite Dilatometer

Corrected Specimen Unit Elongation (10-3 in. /in.)	0.0 10.86 15.28 20.77 31.21 42.87 49.21 58.11 61.60 52.84 41.38 -35.68
Unit Correction for Dilatometer Motion (10 ⁻³ in. /in.)	0.0 0.64 1.17 1.80 3.11 4.68 5.60 6.94 8.07 9.09
Observed Unit Elongation (10 ⁻³ in./in.)	0.0 10.22 14.11 18.97 28.10 38.19 43.61 51.17 53.53 43.80 32.29
Observed Total Elongation (10 ⁻³ in.)	0.0 29.12 40.22 54.06 80.04 108.82 124.28 145.82 152.55 124.81 92.01
Time	9:15 9:50 10:20 10:55 11:30 12:00 1:50 7:20
Temp.	75 903 1213 1213 1593 2291 3048 3473 4070 4587 5014 5034
Specimen and Run No.	Specimen: M-217-CTE-1R Run: 1 Run: 1 Run: 1 2.8497 in. Final Length: 2.7489 in. Initial Weight: 6.3824 gm Final Weight: 6.3818 gm Density: 2.1870 gm/cm³

Table 15

Thermal Expansion of Pyrolytic Graphite (Cylinder S/N M-217) as Received in the "c" Direction Measured in Graphite Dilatometer

							<u>.</u>			
Corrected Specimen Unit Elongation (10-3 in. /in.)	0.0	13.04	34.06	49.52	56.33	58.04	39.28	-40.28	31	
Unit Correction for Dilatometer Motion (10 ⁻³ in. /in.)	0.0	1.00	3.51	5.52	6.52	89.8	8.81	0.0		
Observed Unit Elongation (10 ⁻³ in./in.)	0.0	12.04	30.55	44.00	49.81 53.36	49.36	30.47	-40.28		Total see
Observed Total Elongation (10-3 in.)	0.0	32.50	82.49	118.81	134.49	133.29	82.29	-108.77		
Time	9:35	10:05	11:50	12:52	1:50	2:05	2:20	7:30		
Temp.	75	1686	2503	3513	3989	4963	5044	75		
Specimen and Run No.	Specimen: M-217-CTE-2R Run: 1	Run: 7876-140-146K4 Initial Length: 2.7003 in.	Final Length: 2.5927 in. Initial Weight:		Density: 2.1869 gm/cm ³					

Table 16

Thermal Expansion of Pyrolytic Graphite (Cylinder S/N M-217) after Previous Exposure to 5000°F in the "c" Direction Measured in Quartz Dilatometer

Corrected	Specimen Unit Elongation 10-3 in./in		0.0	4.68	10.60	17.31	20.27	90.0		
Unit Elongation	Correction for Dilatometer Motion 10-3 in./in.	sight: 6.3818 gm ght:	0.0	0.12	0.24	0.36	0.43	0.0		
	Observed Unit Elongation 10-3 in./in.		0.0	4.56	10.42	16.45	19.84	90.0		
	Observed Total Elongation 10-3 in.	Initial Weight: Final Weight:	0.0	12.55	28.63	46.60	54.53	0.17		
tures - °F	age	2.7489 in. 2.7498 in.	75.	431	850	1300	1500	7.5		
Specimen Temperatures	Bottom		Initial Length: 2. Final Length: 2.	75	431	850	1300	1500	75	
Speci	Top	itial I	75	431	850	1300	1500	75		
	Time	In	9:40	10:15	10:45		11:30	8:10		
	Specimen	Specimen: M-217-CTE-1R Run: 7839-129-	37							

Table 17

Thermal Expansion of Pyrolytic Graphite (Cylinder S/N M-217) After Previous Exposure to 5000°F in the "c" Direction Measured in Graphite Dilatometer

Corrected Specimen Unit Elongation (10-3 in. /in.)	0.0 11.12 16.19 21.48 37.76 44.83 51.01 61.13 69.04 64.50 -14.18
Unit Correction for Dilatometer Motion (10 ⁻³ in. /in.)	0.0 0.61 1.18 1.80 3.79 4.70 5.52 6.82 7.96 9.09
Observed Unit Elongation (10 ⁻³ in./in.)	0.0 10.51 15.01 19.68 33.97 40.13 45.49 54.31 61.08 55.41 -14.18
Observed Total Elongation (10-3 in.)	28.88 41.26 54.07 93.35 110.29 125.01 149.26 157.84 152.26 -38.96
Time	9:15 9:50 10:20 10:55 11:30 12:00 1:00 1:30 6:50
Temp.	75 899 1239 1587 2614 3058 3443 4040 4537 5034 75
Specimen and Run No.	Specimen: M-217-CTE-1R Run: 2 Run: 7876-143-145K3 Linitial Length: 2.7481 in. Final Length: 2.7084 in. Initial Weight: 6.3810 gm Final Weight: 6.3811 gm Density: 2.1870 gm/cm³

Thermal Expansion of Pyrolytic Graphite (Cylinder S/N M-217) After Previous Exposure to 5000°F in the "c" Direction Measured in Graphite Dilatometer Table 18

Corrected Specimen Unit Elongation (10 ⁻³ in. /in.)	5.58 12.40 22.20 34.74 43.28 51.41 60.63 68.54 69.46
Unit Correction for Dilatometer Motion (10 ⁻³ in. /in.)	0.0 0.30 1.88 3.39 4.41 5.41 0.0
Observed Unit Elongation (10 ⁻³ in./in.)	0.0 5.28 11.57 20.32 31.35 38.87 46.00 54.03 60.86 60.66 - 9.00
Observed Total Elongation (10 ⁻³ in.)	0.0 13.68 30.01 52.69 81.27 100.78 119.26 140.08 157.78 - 23.34
Time	8:10 8:40 9:10 9:45 10:20 10:50 11:50 12:50 8:40
Temp.	75 505 978 1625 2437 2977 3468 4020 4511 5034 75
Specimen and Run No.	Specimen: M-217-CTE-2R Run: 2 Run: 7876-153-146K4 Initial Length: 2.5927 in. Final Length: 2.5725 in. Initial Weight: 6.0524 gm Final Weight: 6.0528 gm Density: 2.1869 gm/cm ³

2

LIST OF APPENDICES

- A Ultimate Strength, Elastic Modulus, and Poisson's Ratio to 5500°F in Tension
- B Ultimate Strength, Elastic Modulus, and Poisson's Ratio to 5500°F in Compression
- C Thermal Expansion Equipment
 - C-1 Thermal Expansion to 1800°F
 - C-2 Thermal Expansion to 5500°F
- D Raw Data for Mechanical Evaluations (Stress-Strain Curves)

APPENDIX A

ULTIMATE STRENGTH, ELASTIC MODULUS, AND POISSON'S
RATIO TO 5500°F IN TENSION

ULTIMATE STRENGTH, ELASTIC MODULUS AND POISSON'S RATIO TO 5500°F IN TENSION

A typical tensile facility is shown in the photograph in Figure 1 and in the schematic in Figure 2. The primary components are the gas-bearings, the load frame, the mechanical drive system, the 5500°F furnace, the optical strain analyzers and associated instrumentation for measurement of load and strain. The load capacity is 15,000 pounds.

The load frame and mechanical drive system are similar to those of many good facilities. The upper crosshead is positioned by a small electric motor connected to a precision screw jack. This crosshead is stationary during loading and is moved only when assembling the load train. The lower crosshead is used to apply the load to the specimen through a precision screw jack chain driven by a variable speed motor and gear reducer.

Nonuniaxial loading, and therefore bending stresses, may be introduced in tensile specimens not only from (1) misalignment of the load train at the attachment to the crossheads, but also from (2) eccentricity within the load train, (3) unbalance of the load train and (4) external forces applied to the load train by such items as electrical leads and clip-on extensometers. Although the bending moments from some of these sources may seem relatively slight, the resulting stress distortions are quite significant in the evaluation of the extremely sensitive brittle materials. Now consider each individually.

To confirm that the gas-bearings had eliminated nonuniaxial loading at the point of attachment of the load train to the cross-heads, the frictional moment was determined at a load of 5000 pounds by measuring the torque required to produce initial motion within the system with the bearings in operation. This torque was found to be a maximum of 6.6×10^{-3} inch-pounds. The equation

$$M_{O} = \frac{2uP}{3} \qquad \left[\frac{R_{2}^{3} - R_{1}^{3}}{R_{2}^{2} - R_{1}^{2}} \right] \tag{1}$$

was then applied to the system to calculate the kinetic friction where M_O was the resisting moment due to kinetic friction and μ represented the coefficient of kinetic friction. The calculated value of μ was then equal to a maximum of only 4.5 x 10^{-7} .

 $S = \frac{MC}{T} \tag{2}$

was then employed to obtain the stress that could be induced in the specimen due to this bending moment. This value was 0.16 psi, or less than 0.002 percent of the tensile stress produced within a typical graphite specimen. These low values clearly indicate the elimination of problems of bending stress in the specimen imposed by misalignment at the crosshead attachments, either initially or during loading.

Emphases in the design of the load train were placed on (1) large length-to-diameter ratios at each connection, (2) close sliding fits (less than 0.005 inch) of all mating connections, (3) the elimination of threaded connections, (4) the use of pin connections wherever possible and (5) increasing the size of components to permit precise machining of all mating surfaces. All members were machined true and concentric to within 0.0005 inch, and the entire load train was checked regularly to ensure overall alignment following assembly of the individual members. This process ensures concentricity and no kinks in the system.

The problems of unbalance within the load train and of external forces applied to the load train have been explored and corrected. The entire load train is statically balanced to less than 0.01 inchpound for normal operation.

One configuration of the tensile specimen is shown in Figure 3. This specimen provides a relatively large L/D ratio in the gripping area to ensure good alignment. All surfaces in the gripping area are cylindrical in order to make precision machining easier and repeatable from specimen to specimen. This specimen also has double breakdown radii from the gripping area to the gage section. This double breakdown allows a uniform transition of the stress pattern and reduces the frequency of radius (out of gage) fractures. This specimen provides a uniform gage section which gives a definable volume of material under stress and permits accurate measurements of strain. The flags for the measurement of axial strain are positioned one inch apart so that unit strain is recorded directly. The flag attachment for measurement of lateral strain is positioned between the flags for axial strain; see Figure 4.

A schematic of the precision tensile grip is shown in Figure 5. The design is much like the jaws of a lathe head or the chuck of a drill motor made with precision. Observe from the figure the long surface contact of the mating parts and the close fits to establish precise alignment with the specimen. As the load is applied, the wedges maintain alignment to fracture.

Figure 6 is a sketch of the 5500°F furnace used for tension showing the basic components. The furnace consists of a resistively heated graphite element insulated from a water-cooled shell by thermatomic carbon. The furnace and specimen are purged with helium to provide an inert atmosphere. Ports with visual openings are provided on opposite sides of the furnace as a means of allowing the strain analyzers to view the gage flags on the specimen. Specimen temperatures are determined by optical pyrometer readings taken through another small sight port containing a sapphire window. A calibration curve was established for the loss through the sapphire window, and since the furnace cavity acts essentially as a blackbody, true temperature readings are obtained. Power is supplied to the heating element by means of a 25 KVA variable transformer.

Strain measurement consists of measuring optically the elongation between two flags, or targets, which are mounted on the specimen and separated initially by a predetermined gage length. The travel of the targets is measured by sensing the displacement of the image of the edge of the targets and then electromechanically following the image displacement. The relative travel of the two targets provides the strain. Readout is continuous and automatic on a millivolt recorder. A schematic of the analyzer is shown in Figure 7.

A brief summary of the mechanical motions of the components involved in monitoring the strain is helpful in understanding the detailed performance. A tracking telescope follows the upper target and carries a second telescope mounted on its carriage. The second telescope is capable of independent motion to follow the lower target. The relative displacement between the upper and lower telescope, as strain occurs, defines the strain. The system usually is operated so that the tracking telescope follows the upper target and the strain is monitored by the relative displacement of the aperture rather than the telescope following the lower target. With this procedure the maximum range is the maximum displacement available for the lower aperture, of about 1/8 inch, and the sensitivity is limited by the optics and the noise level of the detector. Using both telescopes, the range is about 3/4 inch.

To provide optical references on the specimens, targets are affixed to the test specimen as mentioned. When the specimen is heated to temperature, the targets are self-luminous and are observed optically. The optics view past the luminous targets into a cooled cavity in the opposite furnace wall. The self-luminous targets are then visible against a dark background. To obtain data below 2000°F, a light beam is directed from behind the flags providing a shadow image for the detection system.

The image of the flowing target is focused through a rotating shutter (chopper) and onto a rectangular aperture. Small slits in the aperture pass a portion of the upper and lower edges of the light beam. A photocell receives the light thus transmitted, and an electronic circuit detects whether the energy passed by the two slits is equal. A servo drives the apertures to let a balanced quantity of light pass through the two slits and thus maintains an optical null.

To obtain lateral strain, a strain analyzer is supported horizontally on the tensile frame to view the diametrical or lateral strain of the specimen. A flag attachment, with the general configuration as shown in Figure 8, was developed to follow and transmit lateral motions of up to a few mils. The three-piece assembly consists of a ring and two rams bearing on the specimen.

Calibrations of the analyzers are performed in various ways including absolute correlations to precision micrometers, strain gage extensometers, and direct plots of stress-strain for reference materials such as steel, plexiglas, magnesium and aluminum. Precision is within ± 0.000020 inch.

Instrumentation includes primarily a stress-strain measurement system composed of a 1000-pound SR-4 Baldwin load cell, constant d.c. voltage power supply, two optical strain analyzers, and two X-Y recorders. Specimen temperature is monitored with an optical pyrometer. Stress (load) is measured by a commercial load cell. The cell receives a constant d.c. voltage input from the power supply and transmits a millivolt signal (directly proportional to load) to an X-Y recorder. Simultaneously, the optical strain analyzers measure both the axial and lateral strain and transmit a millivolt signal (proportional to strain) to the X-Y recorders. Thus, continuous plots of stress-axial strain and axial strain-lateral strain are recorded simultaneously.

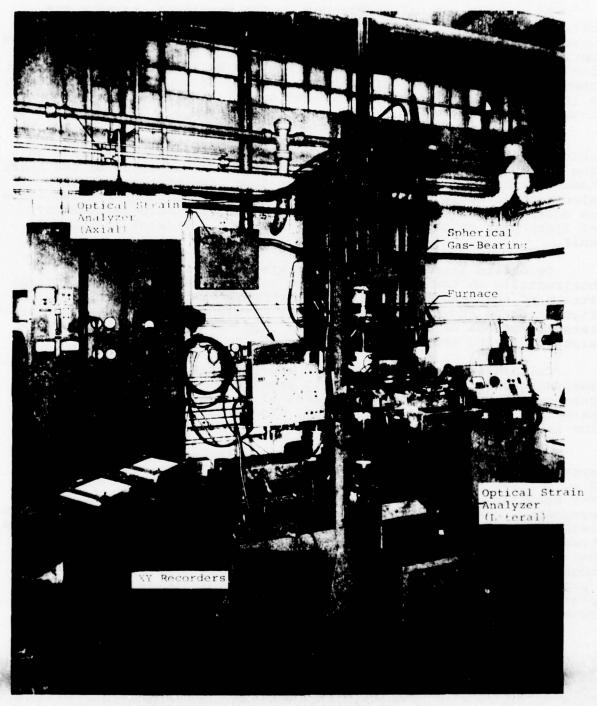


Figure 1. Photograph of a Tensile Stress-Strain Facility

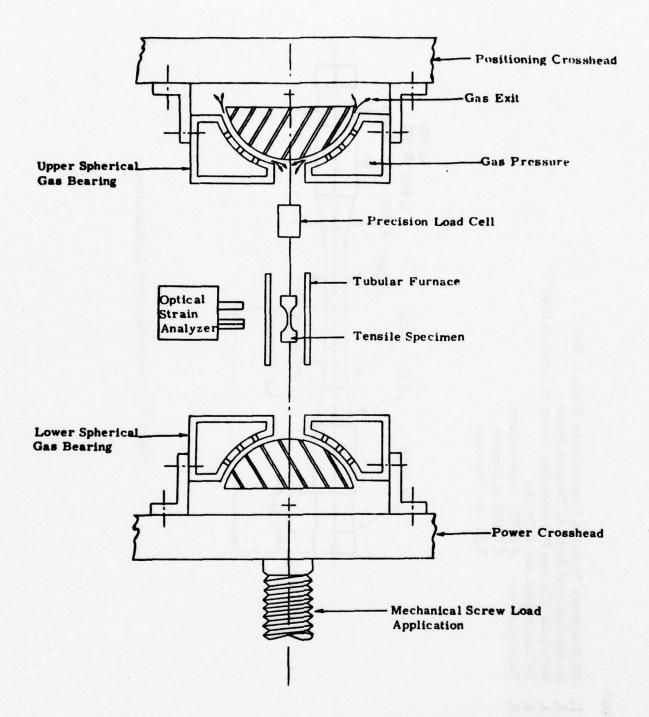


Figure 2. Schematic Arrangement of Gas-Bearing Universals, Specimen and Load Train

- All Diameters True and Concentric to Within 0,0005"
 - Do Not Undercut Radii At Tangent Points
- Both Ends Flat and Perpendicular to and to Within 0,0005"
- -. 0. 6. 4. C.

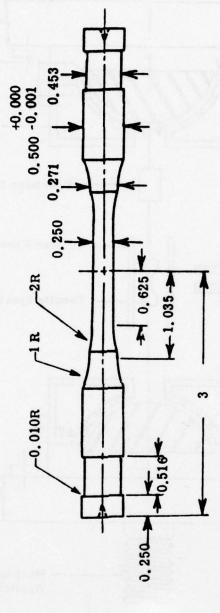


Figure 3. Tensile Specimen Configuration

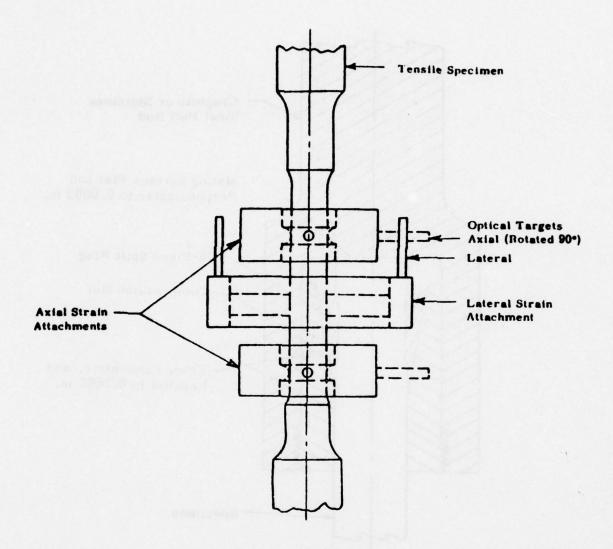


Figure 4. Location of the Flag Attachments on the Tensile Specimens

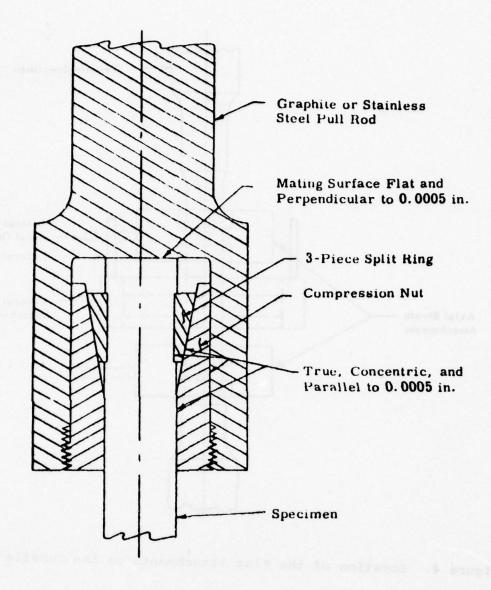


Figure 5. Precision Collet Grip for Tensile Specimen 2:1 Scale

THIS PAGE IS BEST QUALITY PRACTICABLE FROM COPY FURNISHED TO DDC

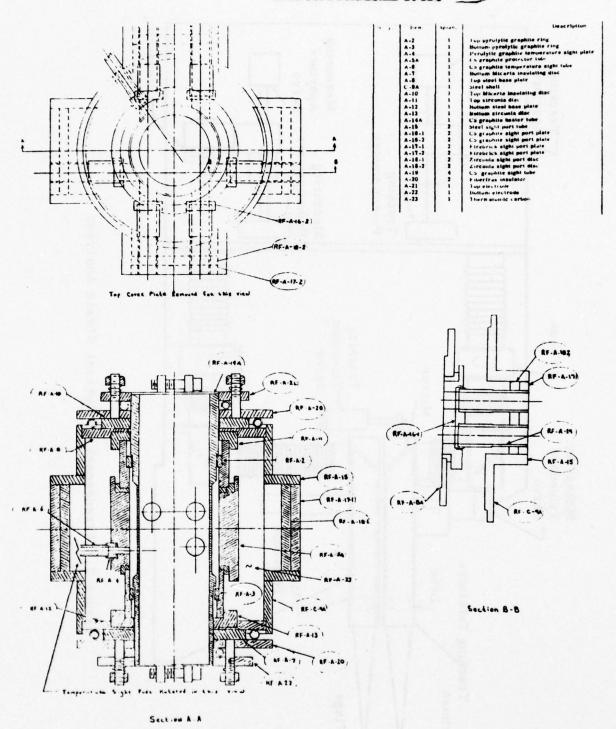


Figure 6. Small 5500°F Graphite Resistance Furnace

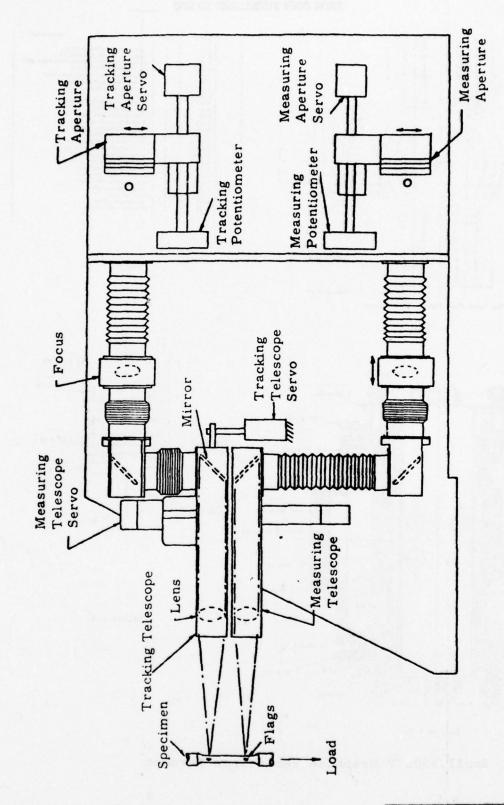


Figure 7. Arrangement of Optical Strain Analyzer

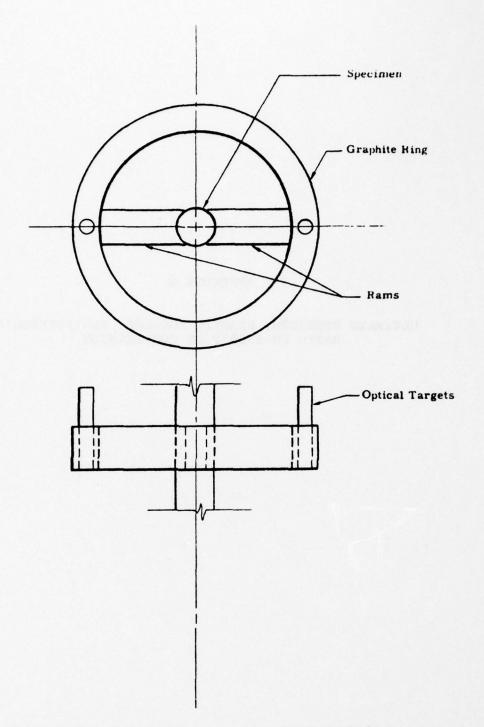


Figure 8. General Configuration of the Flag Attachment to Monitor Lateral Strain in Tension

APPENDIX B

ULTIMATE STRENGTH, ELASTIC MODULUS, AND POISSON'S RATIO TO 5500°F IN COMPRESSION

ULTIMATE STRENGTH, ELASTIC MODULUS, AND POISSON'S RATIO TO 5500°F IN COMPRESSION

The compressive apparatus is shown in the photograph in Figure 1 and in the schematic in Figure 2 and consists primarily of a load frame, gas bearings, load train, 50-ton screw jack, variable speed mechanical drive system, strain analyzers, 5500°F furnace, and associated instrumentation for the measurement of load and strain.

The load frame is similar to most standard frames. It was designed to carry a maximum load of 100,000 pounds and to support the furnace optical strain analyzers, and other related equipment.

Gas bearings are installed at each end of the load train to permit precise alignment of the loading train to the specimen. The upper bearing is spherical on a radius of 6.5 inches. This radius is the distance from the top of the specimen to the spherical bearing surface. The load train, not the specimen, shifts to maintain radial alignment. The lower bearing is flat and is about 6 inches in diameter. The lower bearing permits transverse alignment of the load train. The gas bearings are floated for only a small initial amount of load so that precise alignment of the load train can be attained.

The load train near the furnace consists of the specimen loaded on each side by graphite and water-cooled steel push rods. The graphite push rods are counter-bored to permit insertion of a pyrolytic graphite disc which serves as a heat dam and to align the specimen to the center-line of the load train. Extreme care is exercised in the preparation of all parts of the load train to ensure concentricity of the mating parts to less than 0.0005 inch.

The 50-ton jack is a power screw type. The mechanical drive system consists of a gear reducer driven by a Louis Allis Synchro-Spede Unit (300-3000 rpm). The gear reducer is connected to the Synchro-Spede Unit through a chain coupling and to the 50-ton jack by a single roller chain and sprocket system. Different load rates are obtained by adjustment of the variable speed setting on the Synchro-Spede and by changeout of sprockets on the gear reducer and screw jack.

Figure 3 shows details of the "dumbbell" specimen which maintains a 0.500 inch diameter over the 1.2 inch long gage section. The specimen provides sufficient room for the flag attachments that follow the axial and lateral strains and also minimizes the influence of end restraint.

The flag attachments for the measurement of axial strain are positioned one inch apart so that unit strain is recorded directly. The flag attachment for the measurement of lateral strain is positioned between the flags for axial strain; see Figure 4. The lateral flag attachment used in compression is shown in Figure 5. The 4-piece assembly consists of a ring, two rams bearing on the specimen, and a screw to adjust the contact pressure. The ring was designed to track lateral motions as great as 0.030 inch without breaking.

Figure 6 is a sketch of the 5500°F furnace used for compression showing the basic components. The furnace consists of a resistivity heated graphite element insulated from a water-cooled shell by thermatomic carbon. The furnace and specimen are purged with helium to provide an inert atmosphere. Ports with visual openings are provided on opposite sides of the furnace as a means of allowing the strain analyzers to view the gage flags on the specimen. Specimen temperatures are determined by optical pyrometer readings taken through another small sight port containing a sapphire window. A calibration curve was established for the loss through the sapphire window, and since the furnace cavity acts essentially as a blackbody, true temperature readings are obtained. Power is supplied to the heating element by means of a 25 KVA variable transformer.

Strain measurement consists of measuring optically the elongation between two flags, or targets, which are mounted on the specimen and separated initially by a predetermined gage length. The travel of the targets is measured by sensing the displacement of the image of the edge of the targets and then electromechanically following the image displacement. The relative travel of the two targets provides the strain. Readout is continuous and automatic on a millivolt recorder. A schematic of the analyzer is shown in Figure 7.

A brief summary of the mechanical motions of the components involved in monitoring the strain is helpful in understanding the detailed performance. A tracking telescope follows the upper target and carries a second telescope mounted on its carriage. The second telescope is capable of independent motion to follow the lower target. The relative displacement between the upper and lower telescope, as strain occurs, defines the strain. The system usually is operated so that the tracking telescope follows the

upper target and the strain is monitored by the relative displacement of the aperture rather than the telescope following the lower target. With this procedure the maximum range is the maximum displacement available for the lower aperture, or about 1/8 inch, and the sensitivity is limited by the optics and the noise level of the detector. Using both telescopes, the range is about 3/4 inch.

To provide optical references on the specimens, targets are affixed to the test specimen as mentioned. When the specimen is heated to temperature, the targets are self-luminous and are observed optically. The optics view past the luminous targets into a cooled cavity in the opposite furnace wall. The self-luminous targets are then visible against a dark background. To obtain data at below 2000°F, a light beam is directed from behind the flags providing a shadow image for the detection system.

The image of the glowing target is focused through a rotating shutter (chopper) and onto a rectangular aperture. Small slits in the aperture pass a portion of the upper and lower edges of the light beam. A photocell receives the light thus transmitted, and an electronic circuit detects whether the energy passed by the two slits is equal. A servo drives the apertures to let a balanced quantity of light pass through the two slits and thus maintains an optical null.

To obtain lateral strain, a strain analyzer is supported horizontally on the load frame to view the diametrical or lateral strain of the specimen.

Calibrations of the analyzers are performed in various ways including absolute correlations to precision micrometers, strain gage extensometers, and direct plots of stress-strain for reference materials such as steel, plexiglas, magnesium, and aluminum. Precision is ±0.000020 inch.

Instrumentation includes primarily a stress-strain measurement system composed of a 20,000-pound SR-4 Baldwin load cell, constant d.c. voltage power supply, two optical strain analyzers, and two X-Y recorders. Specimen temperature is monitored with an optical pyrometer. Stress(load) is measured by a commercial load cell. The cell receives a constant d.c. voltage input from the power supply and transmits a millivolt signal (directly proportional to load) to an X-Y recorder. Simultaneously, the optical strain analyzers measure both the axial and lateral strain and transmit a millivolt signal (proportional to strain) to the X-Y recorders. Thus, continuous plots of stress-axial strain and axial strain-lateral strain are recorded simultaneously.

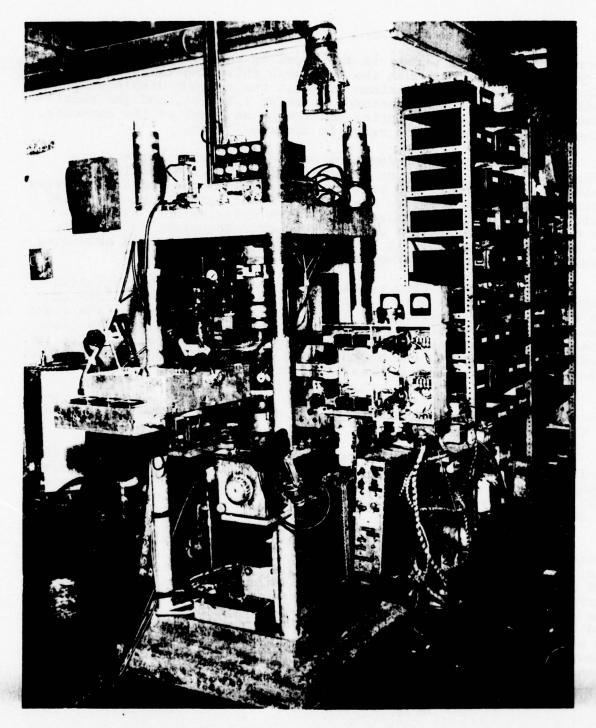


Figure 1. Picture of the Compressive Facility with Gas Bearings and Optical Strain Analyzer

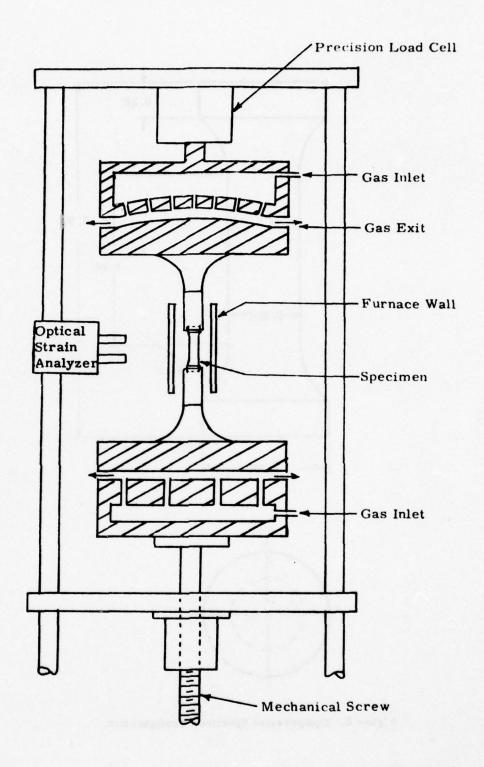


Figure 2. Schematic Arrangement of Gas-Bearing Universals, Specimen, and Load Train

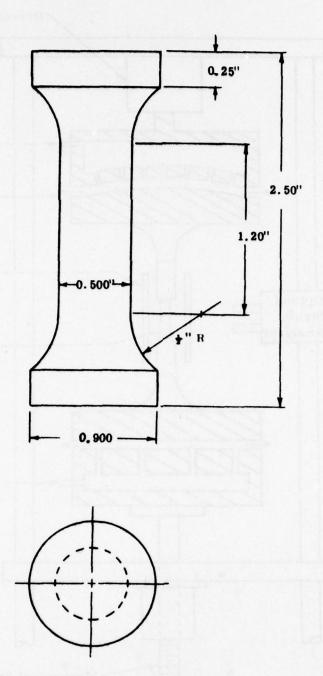


Figure 3. Compressive Specimen Configuration

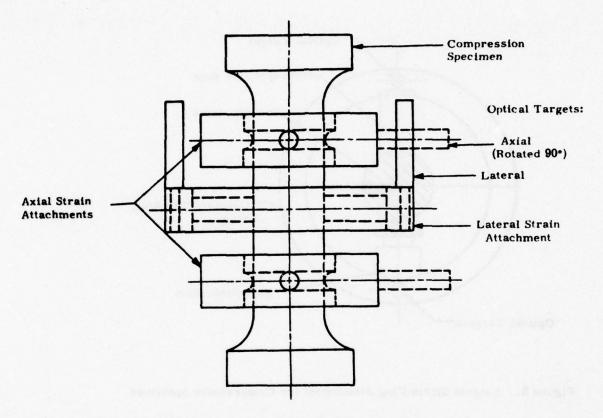


Figure 4. Location of the Flag Attachments on the Compressive Specimen

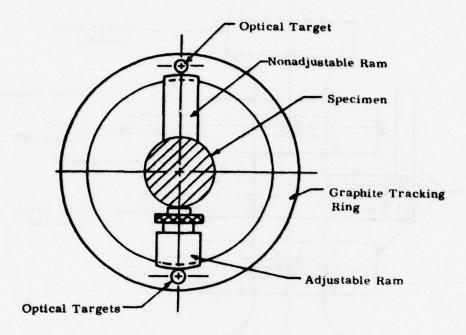


Figure 5. Lateral Strain Flag Attachment for Compressive Specimen

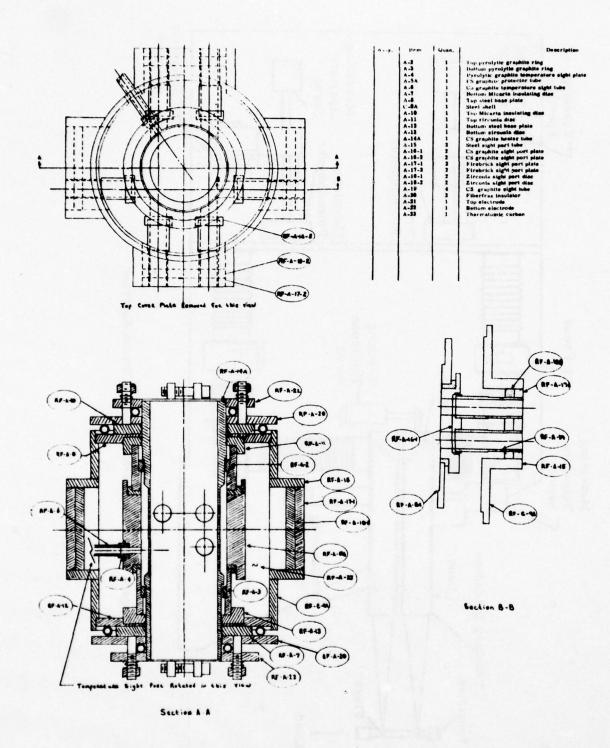


Figure 6. Small 5500°F Graphite Resistance Furnace

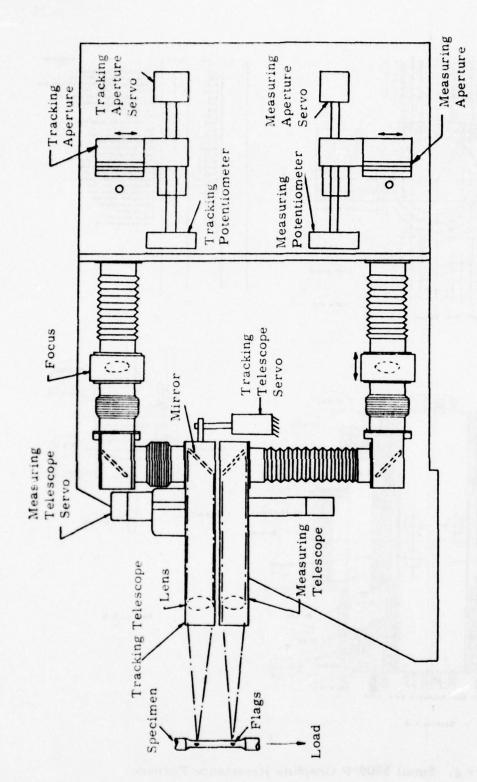


Figure 7. Arrangement of Optical Strain Analyzer

APPENDIX C

THERMAL EXPANSION EQUIPMENT

C-1 THERMAL EXPANSION TO 1800°F

C-2 THERMAL EXPANSION TO 5500°F

THERMAL EXPANSION TO 1800°F

Thermal expansion measurements are made utilizing quartz tube dilatometers of the Bureau of Standards design. The dial gages (B. C. Ames Co., Model 212, Shockless) are graduated in 0.0001-inch divisions with a total range of 0.500 inch. The manufacturer's stated mechanical accuracy for any given reading is ± 0.0001 inch at any point in the range. This accuracy has been checked with a precision micrometer.

Figure 1 shows a schematic drawing of a quartz tube dilatometer. The dilatometer head was designed to minimize any extraneous motions that would induce error in the monitored data. Water cooling was used to prevent temperature fluctuations and gradients that would induce erroneous motion in the dial gage. The parts were precision machined to allow for proper alignment and minimize spurious motions from excessive clearance. The core of a linear variable differential transformer is attached to the quartz rod, which rests on top of the quartz tube. By feeding the output of the LVDT into an oscillator-demodulator and employing an X-Y recorder, a continuous plot of expansion versus temperature may be obtained. Dial gage readings may also be taken concurrently.

For temperatures above room temperature, each dilatometer is heated by an individual heater. The temperature of the heater is maintained by a manual setting of a variable voltage transformer.

Cold specimen temperatures are obtained by use of a Dewar flask filled with dry ice and trichloroethylene. The flask surrounds the dilatometer tubes and the cold liquid level rises to a height above the specimens.

Liquid nitrogen is used in the Dewar flask for temperatures down to -300°F. A cooling coil has also been designed to provide better control of temperatures in the cryogenic range.

Thermocouples are placed at each end and the center of the specimens to monitor the temperature throughout. The specimens are nominally 1/2 inch diameter by 3 inches in length with the ends rounded on a 3 inch radius. Other diameters and cross-sectional configurations are employed where necessary due to configuration of supplied material.

To calibrate the dilatometers we employ a primary standard of fused silica purchased from NBS and designated as SRM 739. A secondary standard of fused silica developed in house is also used. From our calibrations and experience we have found no systematic error in this system. Based on the initial calibrations of this equipment a precision level has been determined. At 1300°F the standard deviation is no greater than ±0.025 x 10⁻³ in./in.

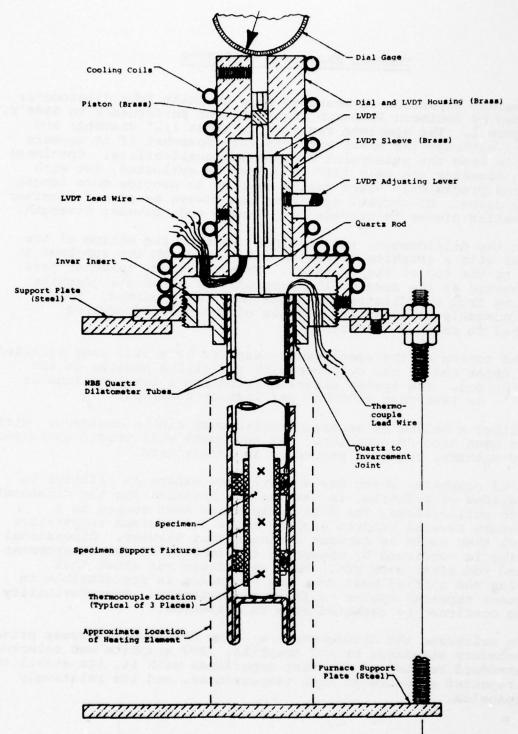


Figure 1. Assembly of Quartz Tube Dilatometer for Thermal Expansion Measurements

THERMAL EXPANSION TO 5500°F

Thermal expansion is measured in a graphite tube dilatometer developed by Southern Research Institute for performance to 5500°F, see Figure 1. The specimen required is about 1/2" diameter and 3" long, although the exact size can vary somewhat if it appears desirable from the standpoint of specimen availability. Specimens 3/4" in diameter and only 1/4" thick can be evaluated, but with a reduced precision. Discs can be stacked to provide more length in many cases. Of course, specimens can always be pinned together from smaller pieces to provide both length and columnar strength.

In the dilatometer, the specimen rests on the bottom of the cylinder with a graphite extension rod resting on the specimen to extend to the top of the cylinder. When required, tungsten pads are inserted at the ends of the specimens to eliminate graphite diffusion from the dilatometer parts into the specimen. This entire assembly is inserted into one of the 5000°F furnaces described in another brochure.

The motion of the specimen is measured by a dial gage attached to the upper end of the cylinder with the stylus bearing on the extension rod. The system accurately indicates total motions of 0.0001" - or less than 0.00004" per inch of specimen.

Either a helium or an argon environment can be employed. Nitrogen has been used on occasion. The equipment will permit operation at hard vacuums, but this procedure is rarely used.

A CS graphite, which has a fairly low expansion relative to other grades of graphite, is used as the material for the dilatometer. Prior to calibrations, the dilatometers are heat soaked to a temperature several hundred degrees above the maximum temperature to which they would be exposed during normal service. Dimensional stability is confirmed by measuring the lengths of the dilatometer tube and rod after each run. Past experience has shown that following the initial heat soak the expansion is reproducible in subsequent repeated cycles to lower temperatures. Reproducibility is also confirmed by repeated runs on standards.

To calibrate the dilatometers we have developed in-house primary and secondary standards of ATJ graphite. ATJ graphite was selected as a standard because of our vast experience with it, its stability after repeated exposure to high temperatures, and its relatively low expansion.

The true expansion of the primary standard was determined by a direct optical technique using a traveling Gaertner telescope. total error in the telescope readings, based on calibration data, was estimated to be 0.2×10^{-3} in./in. For the direct optical measurements, the 3.5 inch long specimen was heated in a graphite furnace, and the expansion was determined by sighting on "knife" edges machined on the ends of the specimen. Typically a total of 11 runs have been made in two different furnaces both in vacuum and helium environments. The two environments are used to check effects of refraction as reported in the literature. The same standard was then machined to the configuration of a regular dilatometer specimen and several runs were made in our precision quartz dilatometers. The optical expansion data were fitted to a quadratic equation over the temperature range from 2500°F to 5000°F using the method of least squares and statistically analyzed to determine the uncertainty (primarily the scatter). Below 2500°F, the quartz dilatometer data were fitted by hand since the uncertainty of this apparatus has been well established, and the imprecision is small ($<0.1 \times 10^{-3}$ in./in.). A typical plot of all data points with the curve fit is shown in Figure 2.

A check of the expansion of the standard was obtained by making runs on round robin specimens of various graphites and synthetic sapphire which had been previously evaluated by others, including the National Bureau of Standards. Our data on these specimens agreed within a 2.5 percent random difference with the data reported by the other laboratories.

After establishing the expansion of the ATJ standard, several graphite dilatometers were then calibrated by making runs on this standard. These dilatometers were used to establish the expansion of secondary standards (also ATJ graphite) which are used to calibrate new dilatometers and to make periodic checks on dilatometers currently in service. This use of secondary standards thus minimizes the wear and tear on the primary standard and prolongs its life.

Table 1 lists the uncertainties in the dilatometer measurements in 10^{-3} in./in. Observe that most of the uncertainty is in the expansion of the standard and includes both random and systematic uncertainties. Other sources of uncertainty, resulting from such factors as dial gage and temperature measurement, are small amounting to less than 0.2×10^{-3} in./in. at any temperature. The precision in the dilatometer measurements is quite good and amounts to about 0.1×10^{-3} in./in. From Table 1, it can be seen that the maximum total uncertainty, which occurs at a temperature of 4500° F, is $\pm 0.45 \times 10^{-3}$ in./in. For a low expansion graphite, such as ATJ, this amounts to an uncertainty of ± 4.5 percent at 4500° F (see Figure 2). For graphites having higher expansions, the percentage uncertainty would be lower.

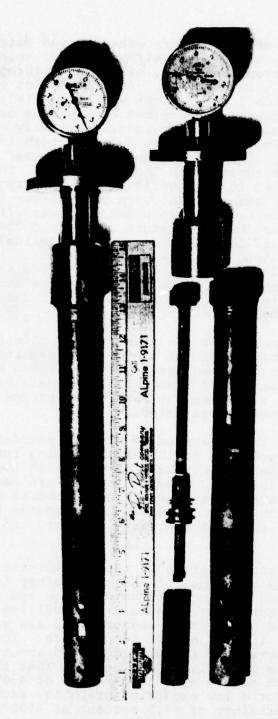


Figure 1. Picture of the Graphite Dilatometer Tubes for Measuring Thermal Expansion to 5500°F

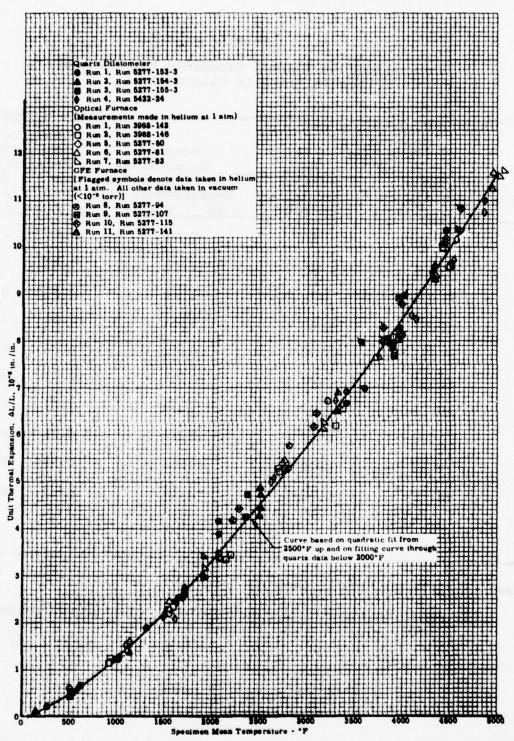


Figure 2. The Thermal Expansion of ATJ Graphite (wg) Standard No. 5 by In-House Optical Calibration

Table 1
Uncertainty in Thermal Expansion Measurements
Made in Graphite Dilatometers

Temperature °F	Uncertai Expansic Standa in 10 ⁻³	on of ard	Random Uncertainty	Total Uncertainty in Dilatometer Measurements				
	Random Uncertainty (See Note 1)	Systematic Uncertainty (See Note 2)	in Dilatometer Measurements in 10 ⁻³ in./in.	from all in 10 ⁻³				
500	±0.04	0	±0.03	0.05	0.05			
1000	±0.04	0	±0.03	0.05	0.05			
1500	±0.05	0	±0.04	0.07	0.07			
2000	±0.17	+0.03	±0.05	0.21	0.18			
2500	±0.11	+0.20	±0.07	0.33	0.13			
3000	±0.12	+0.21	±0.08	0.35	0.14			
3500	±0.19	-0.02	±0.10	0.21	0.23			
4000	±0.14	-0.09	±0.12	0.18	0.27			
4500	±0.14	±0.25	±0.14	0.45	0.45			
5000	±0.19	-0.12	±0.16	0.25	0.37			

Notes: 1. 95% confidence limits.

 Represents deviation between average measured value and least squares curve through all data.

APPENDIX D

RAW DATA FOR MECHANICAL EVALUATIONS (STRESS-STRAIN CURVES)

	6	
2	4	
ŭ.	9:	
CHAR	90	
	200	
0	900	
CORD	1	
-	37 4.4	
	1	
15.71	100	

	-	-	=	1	_	1	1	-	-	77	T	2 1 1	-		T	++-	1	H		11	1				-	
X		-									1		1	3.2700)050	-1	111	1:		1	11		!!			13	
S					-				20	11	-		+	-0	1-		+-	-	1	11			+		-	-
-	4					4.	100	50107	2		1		1	76	1		1:		1::	1		11	i.			,
1	R	16.	3			1	0	10	2		1		I	N	1	>	1					-:			1	- :
355 3 Tech.			1	- dela		4	•	4	10		1		434		1	with	1:	1		1 1	::	::	:			::
14	Temperature:		1			00	11m/ 1"=	1	0		-		-	0			1			11		: 1.			1	: ;
	per	0	'n	110		õ,			0				0	8	0.0055	9						::		1	1:	
2	Ten	1	4	1	ë	6	1	1	_		1		Tu= 14600		0	E4 = 0.0043		-				11.	1	•	1:	
ö	10		`		ot;	:0	1	12	ctio		1		11	- 11	1	4	1					1	i		1	
7	1	1		ii.	Dire	Ra			Š				6	_ 4	1	Ą			11		,	::	1		1	
Pro	10.9.75		.0	- C	2	CELL			Gag	Ш	-				L		1								-	
SRI Run & Proj. No: 72	1	.:	Specimen No.:	Lording Di. ections	Leteral Strain Direction:	Stress Strein Rate: 10 000 Psylmin	ä	ä	Specimen Gage Section 0.06 010,250		1		-	1	1	111		+ 1	1				-	Hi	1	
2	Date	Katerial	eir	1	3:0	839	X Sca'e:	Sca.	ecir		1		-		1		+		-		-	-		T	1-	-
SRI	Da	N.a.	Sp	2	تز	ů.	×	>	Sp				1	-				11								
					-			-			+		+		+		+	+	-		-	-			+	-
				11					11.	111		1		L:	1	Hi			1			1.	Η.		1	
	-	i.,			-	1		-			+		+		+		+						T.	1	+	
			1			1							1				1	* !								
	-		+								-	-	-		+		1		-				-	-	+	
								1			1					Ш						11	1		1	- :
											1	1	T					11		1					1	-
				1						-1-		-	1		1	113	1::		-1	-			1	+	1	
									11	111	T			1	-	1						7.		1	1.	
1		1										1	1	1		1		11		11		H	-	H	1	-
				:				1		HI		17:	14		1		1	11	1	-	. :	1::	+	#	1.	
		1:					11.				1	Ш	1			1	1:	-11		1.				Н	1_	
							* 1			1	1			11.	Ti		1							#		-
							: :			1 4	+		+		+	-++	+	1	-			1	#		1	
				-		-:-				##	-		1	-	1	Ш			1					Ŧ	100	
-			-		-			-			+		+		+		+-		-	X			-	+ +	P	
				11			1 1	1						1	1	- ; -	111	1		1				-:	1	
-						-			+	101	1				+		1	1 ,			1	-			Imi	
											1		: 1	11:	1	11:	1					1			1	
-			-		-		7 1	-			+		+	-	+	10.10	+	-		-			1		-	
- 1			4				+-!	::	1	11	-	1	1	1::	1		13	3		1:	1:			1	1	
		-		-						7-11	1		T		1	111						1:		11	1	
			1		. 1	1		1:			1		1			111	11							1	::	

THIS PAGE IS BEST QUALITY PRACTICABLE FROM COPY FURNISHED TO DDC

0.06000.250 E = 14000 = 3.//409 psc 1"= 601.05 Stress | Sect 8. 10. 19,000 25 //mir 100' ="1 Tech. Date: 10-9-75 Temportt re. 70% Materi-: 7.6. Specifica 194: 17-717-7-6A D.0043 "I'm Ty = 14000 pst 0.0045 SRI Run & Proj. No:73 Lateral Stril Directors Specimen Gage Section , Loading Di ne'l' : שלי Materi-': X Scale: Y Scale: Press D. 2 . Tast Heaults for Specimen M-212-T-6A rocs 101 105 HH

No. XY-1001 -SP6

GRECORDING CHARTS]
HARPHIL CONTROLS CHARTS]
BUFFALC NEW TOLK
FRANCE OF USA

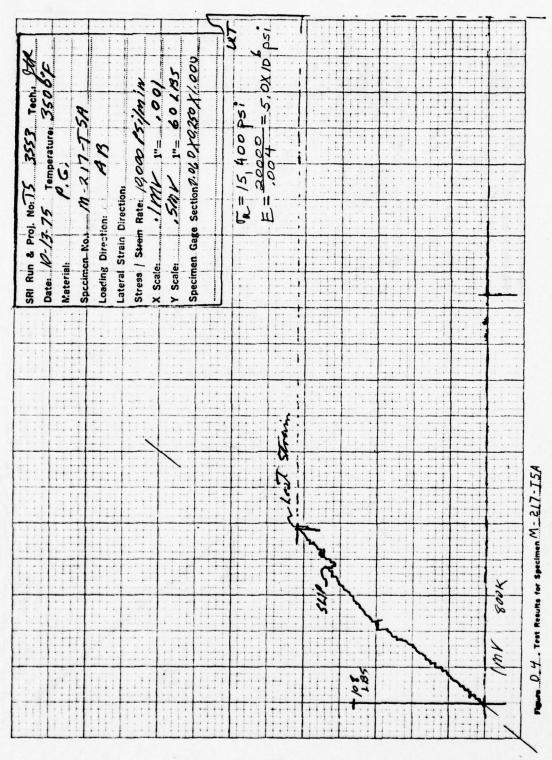
A-87

Figure D. 3 . Test Heaults for Specimen M-217-TIA

A-88

:

BARCORO.AG CHARTS]
HARM CONHOLS CORPORATION
HEFFALO NEW YORK
HERMICO IN USA



GRECORDING CHARTS

BARRIO CHARTS

BARRIO NO COR

BARRIO A SA

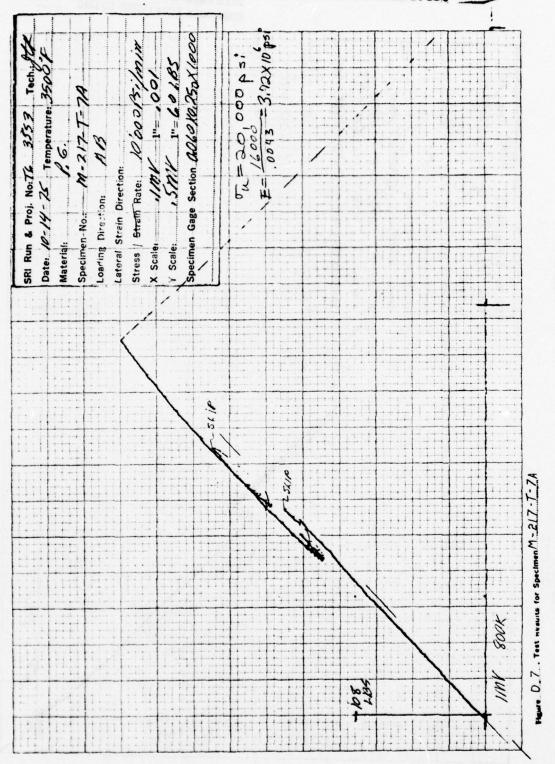
							Date:	Date: 10-14-75 Temperature 3500	Temperatura	3500	Χı
							Material:		6	9.6.	
							Specimen No.		11-217-34	34	
							Loading	Loading Direction:	AB		
The second second				-			Lateral	Lateral Strain Direction:	п.	A contract of the contract of	
			7 1 1				Stress	Stress Shein Rate: 10000	lociol	Bilonin	
		4	1			-	X Scale:	MIN!	1.1	100	
		7	/	`			Y Scale:		1	1"= 401.85	
			,			-	Specime	Specimen Gage Section 2060 X0,350 X 1,005	10000x	1.X026.0	206
		1								_	
				,							
		1		/							
		34,	12	1				of 18,400 ps	8,400	150	
	<i>J</i>		Sul		+			06	000	9	•
i		/			,			E	0/X+4.4 = 4.44XID	0/XLL	150
	3.7	1							<u> </u>		
		\	1								
	\ 					7					
	\										
30+	<u>\</u>					1					
597	\										
	\						1				
							1				
\\\\\\\\\\\\\\\\\\\\\\\\\\\\\\\\\\\\\\											
The second secon		+									
7											
*					+	-	1	1	ľ	•	
8 1111/	Sook				1						
			1.		•				-		

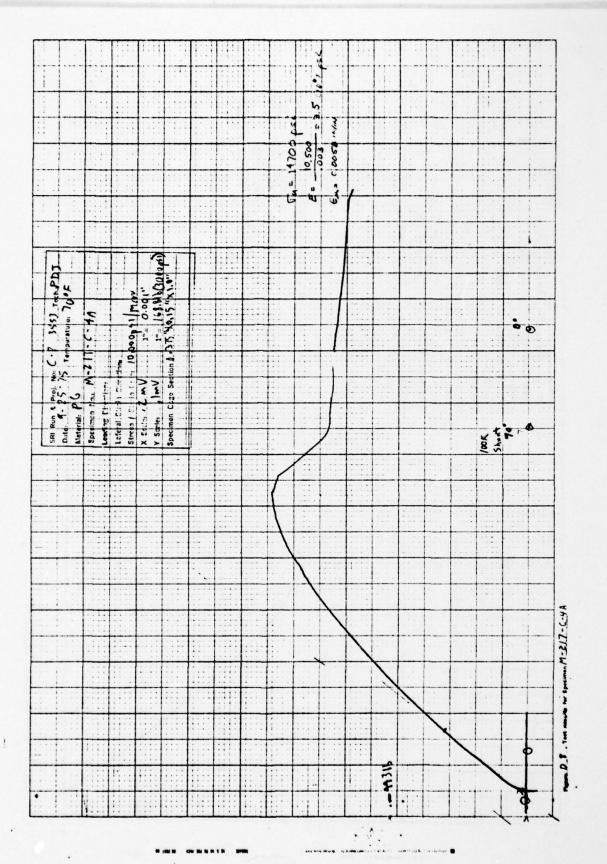
SRECHONG CHARTS)
CRANT CONTROL OF ARTS
RESEARCH NO NEW ACTION

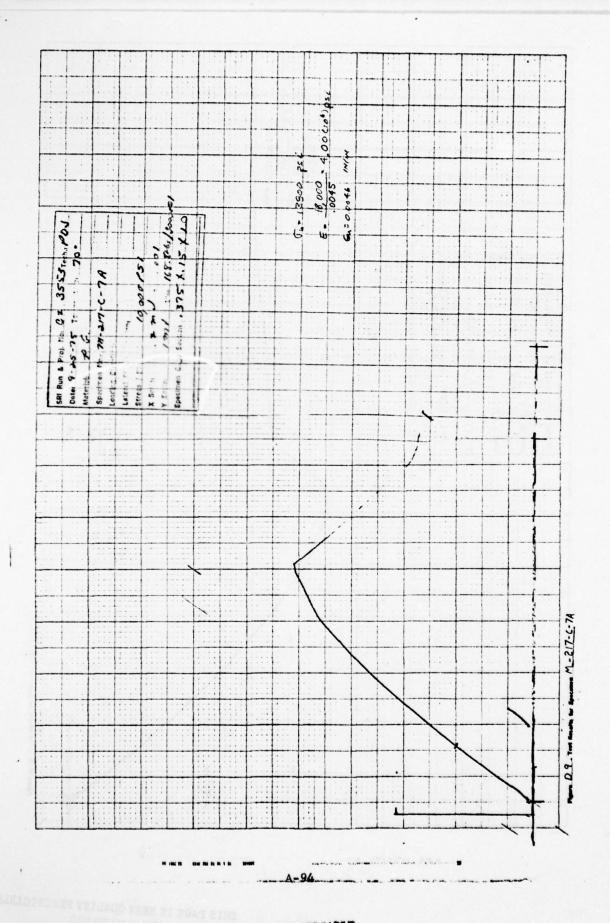
NO. XY-1001 -SP6

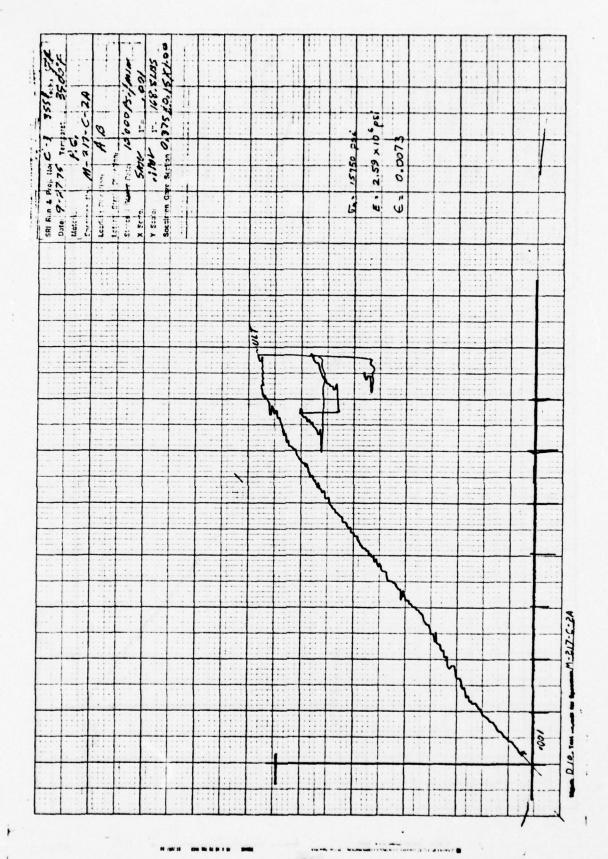
						3 QI							
11/1		1	182	Specimen Gage Section Q.O.L.O.Y.C.250,X.1.0.D.D	psi	-4.80x10 ps							
SRI Run & Proj. No.74 3553 Tech Date: 10-13-75 Temperature: 3500 Material:	2.8	Etress Street Rate: 10,000 (5) min. X Scele:	Saw 1"= 60 185	1380	1	10	5						
SRI Run & Proj. No.74 3553 Tech.: Date: 10-13-75 Temperature: 3500 Material:	217-1	00.	7.1	100	Tu= 16,600	24000	5400						
Temper 3		, jo	1	on 0,0	13	n)	13						
. No.		Ctres Stein Direction: Ctres Steff Rate: // X Scele://///	.50	e Secti			1						
10-13	Specimen No.	Strin		C98					<u> </u>				
SRI Run Date: 10 Material:	الاجوالية مدرية	Stress / S X-Scele:	Y Scale:	pecim	1.1.1.				1::				
ν <u>σ</u> =						/							<u> </u>
					/								
			<										
				1									
					1								
						Be							
						7	2						
						2018	1						
								1					1
									1				NOO8
						1::				1			
											1		1111
									ts		1111	1	<u> </u>
									1987				1

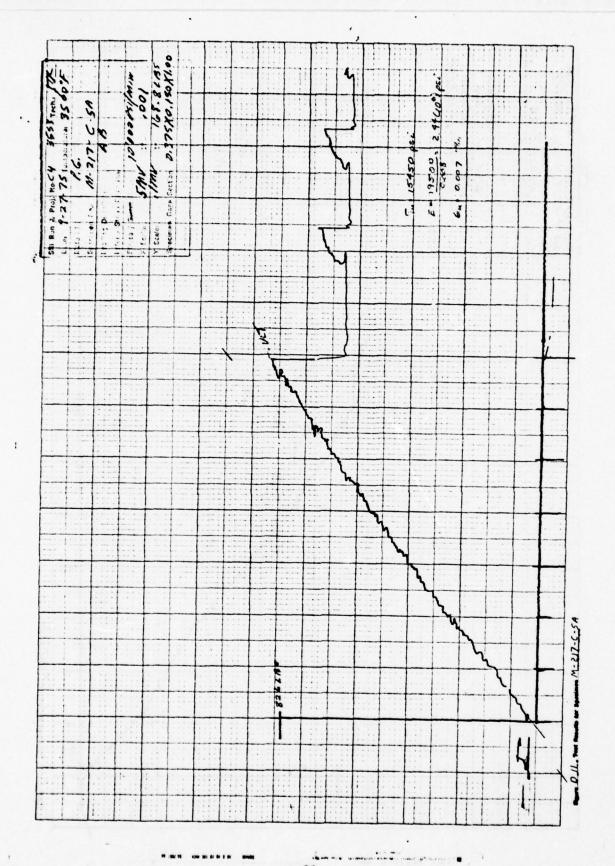
GRECORDING CHARTS	HOFFACT NEW YORK

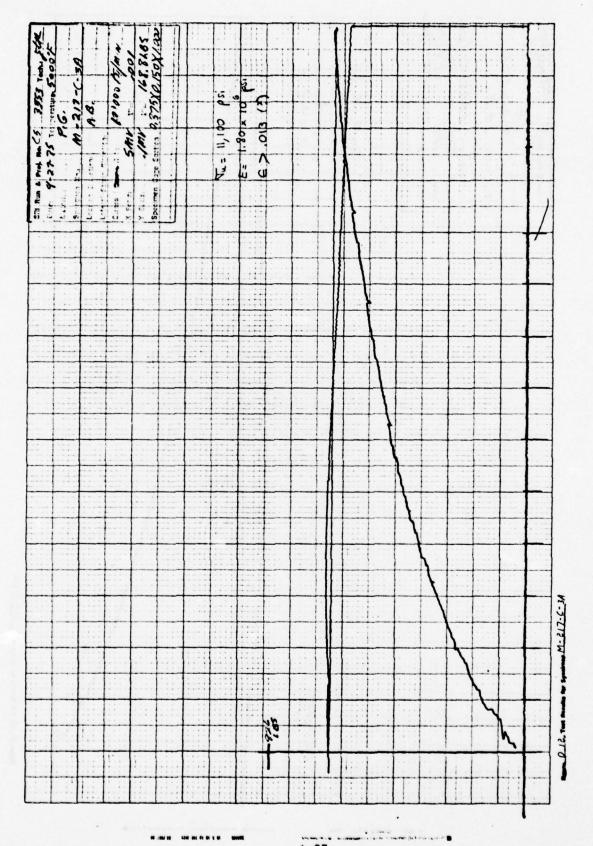


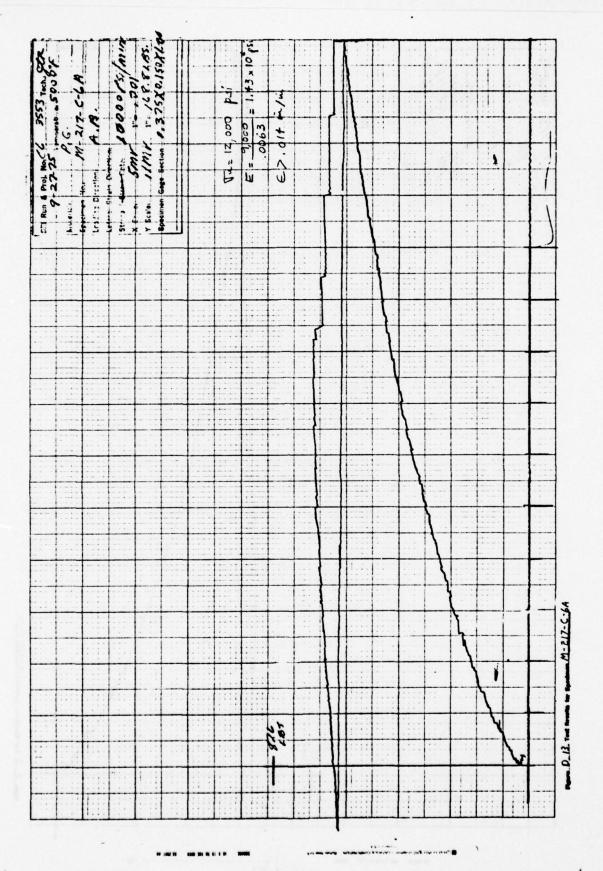


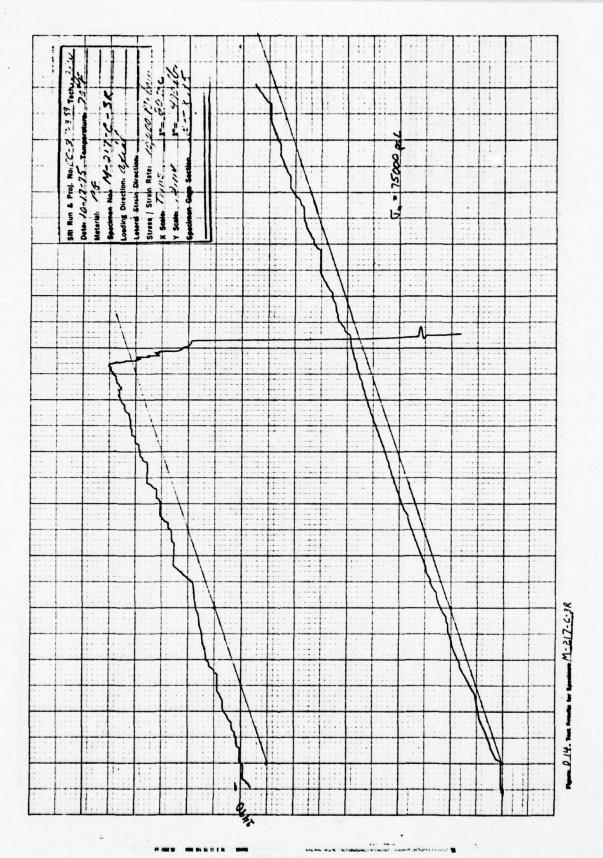


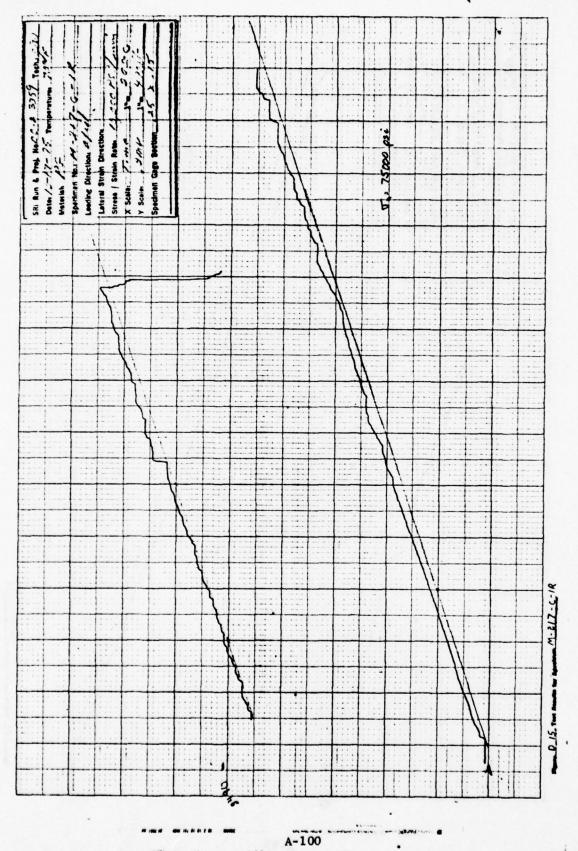


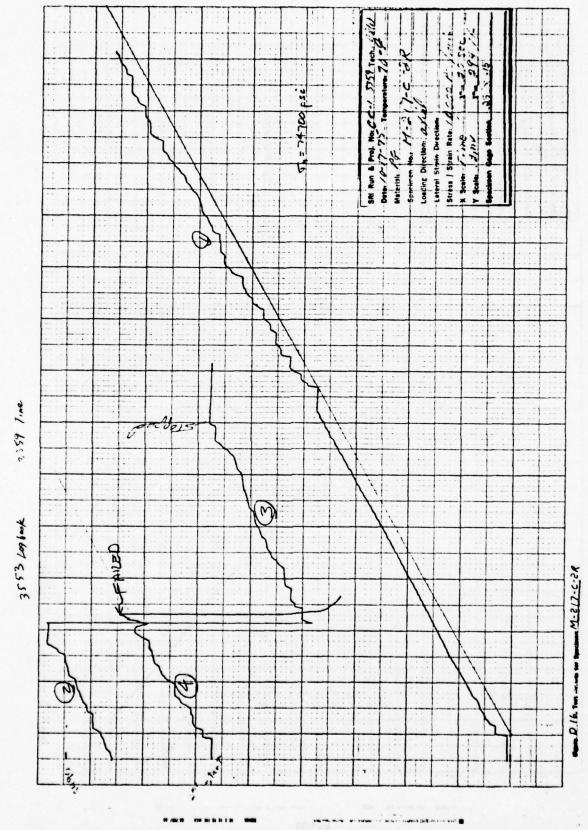


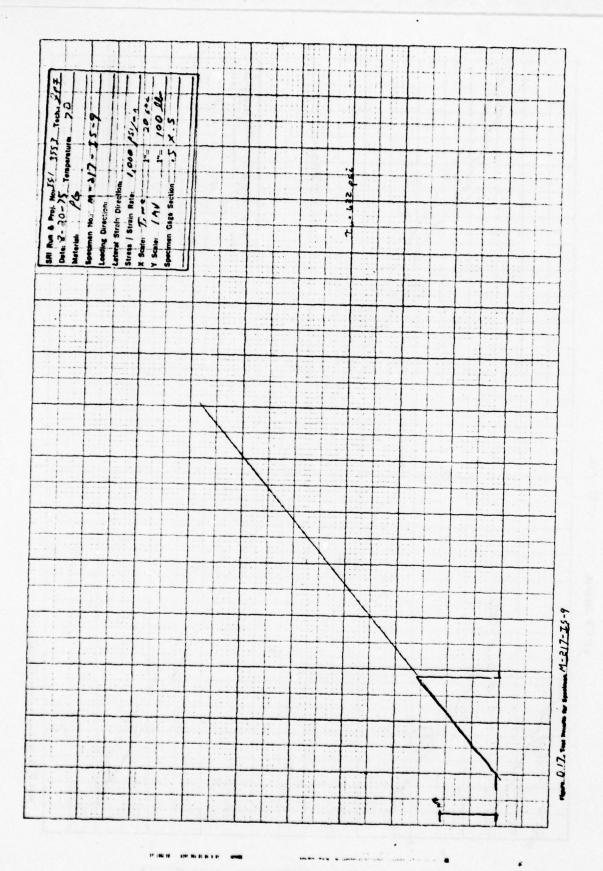


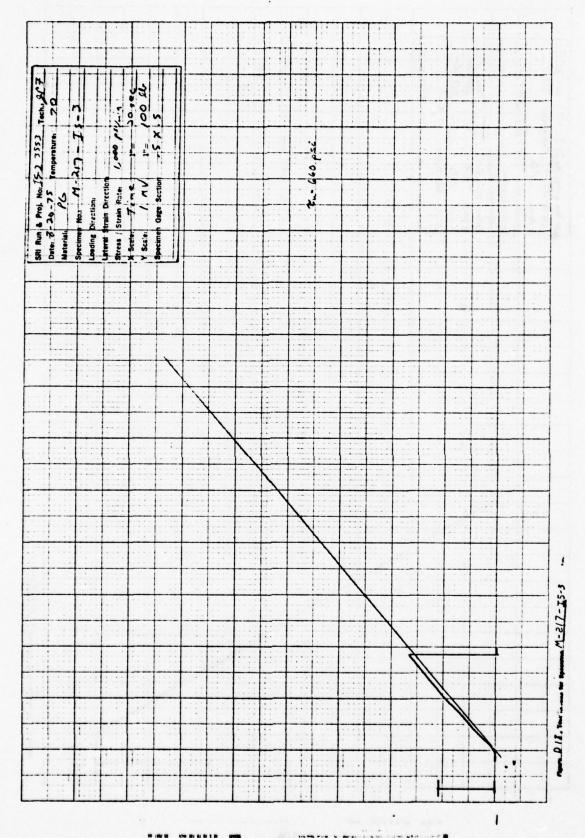


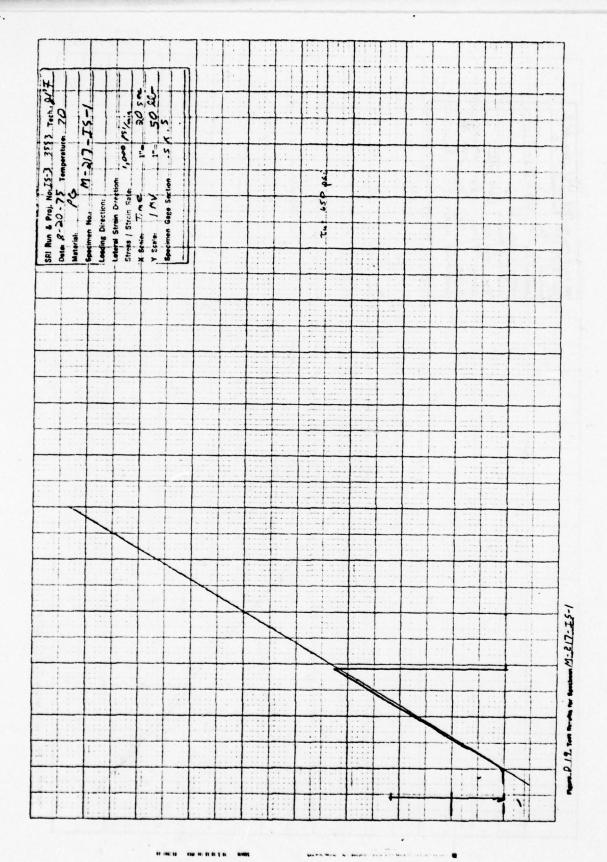


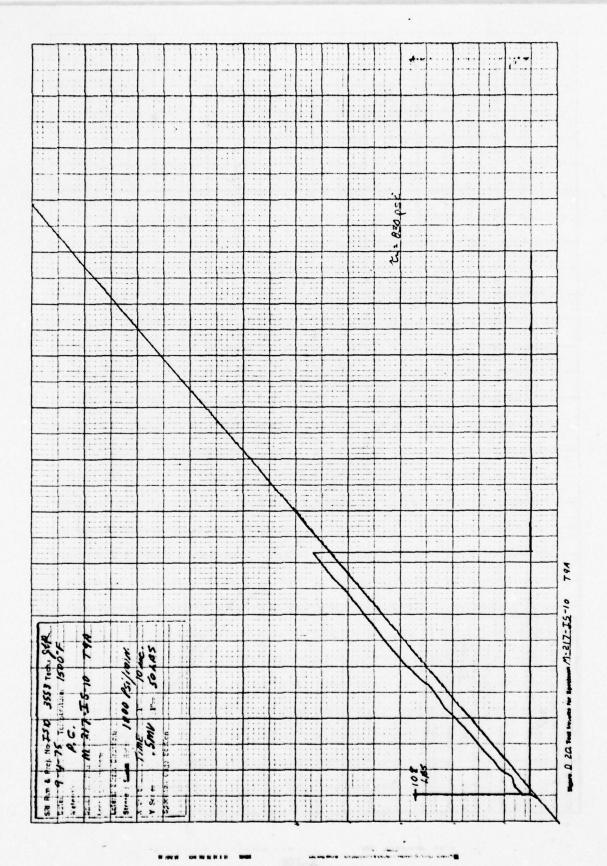




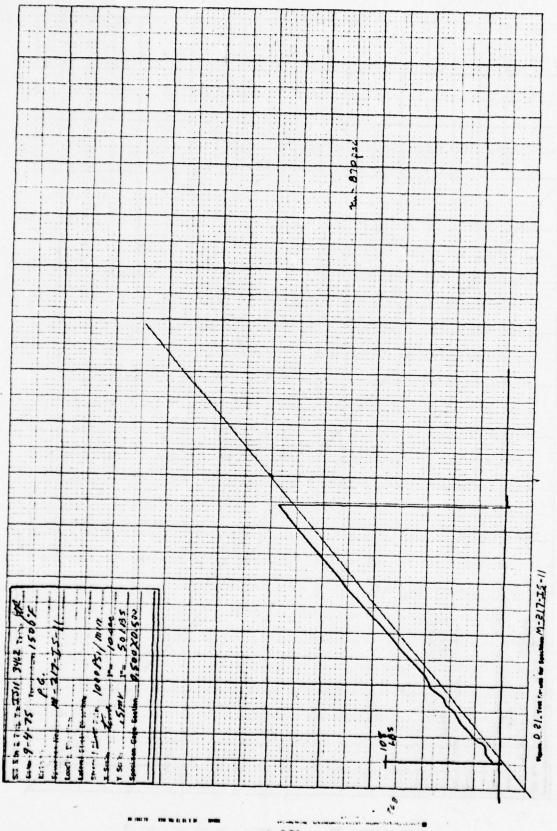


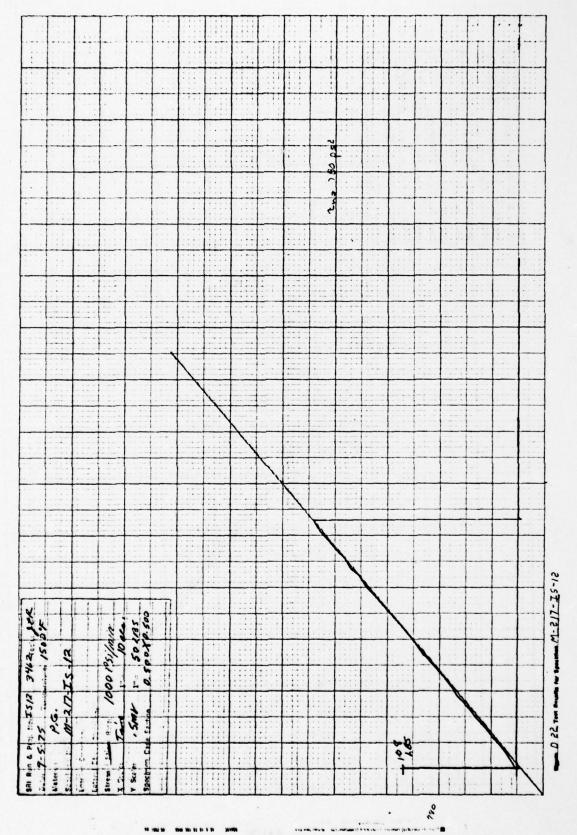


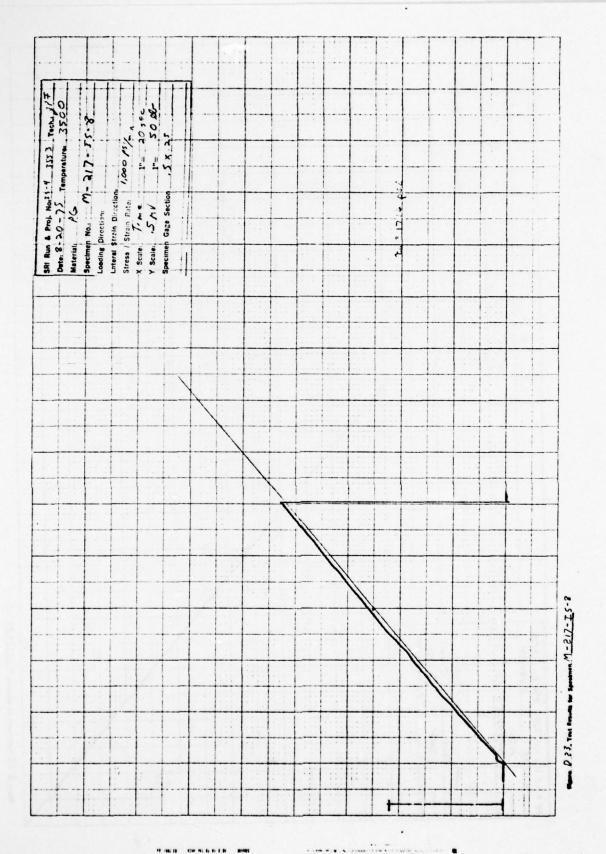


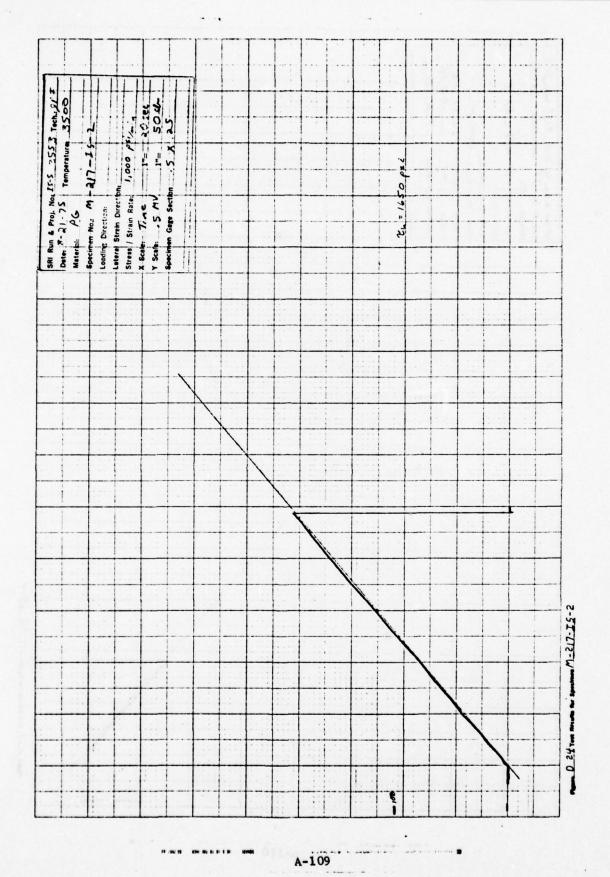


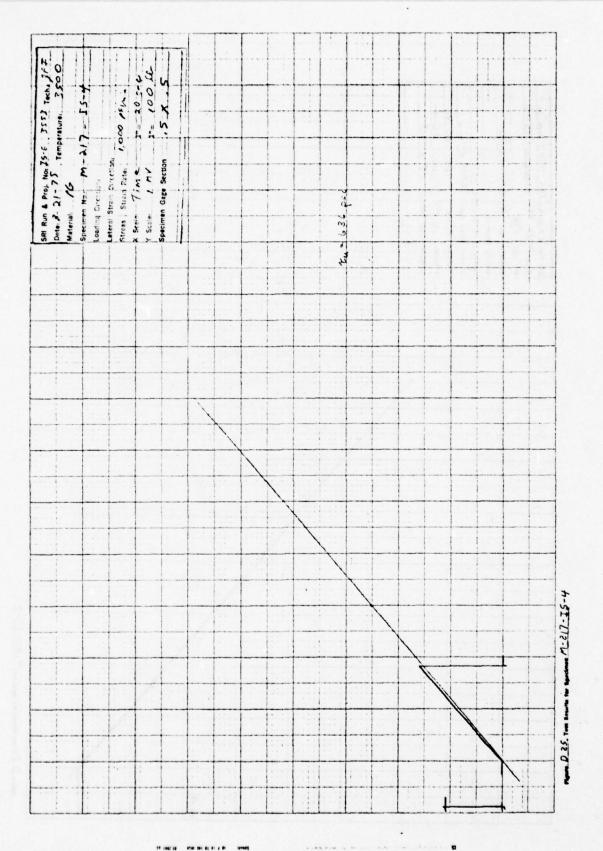
THIS PAGE IS BEST QUALITY PRACTICABLE
FROM COPY FURNISHED TO DDC

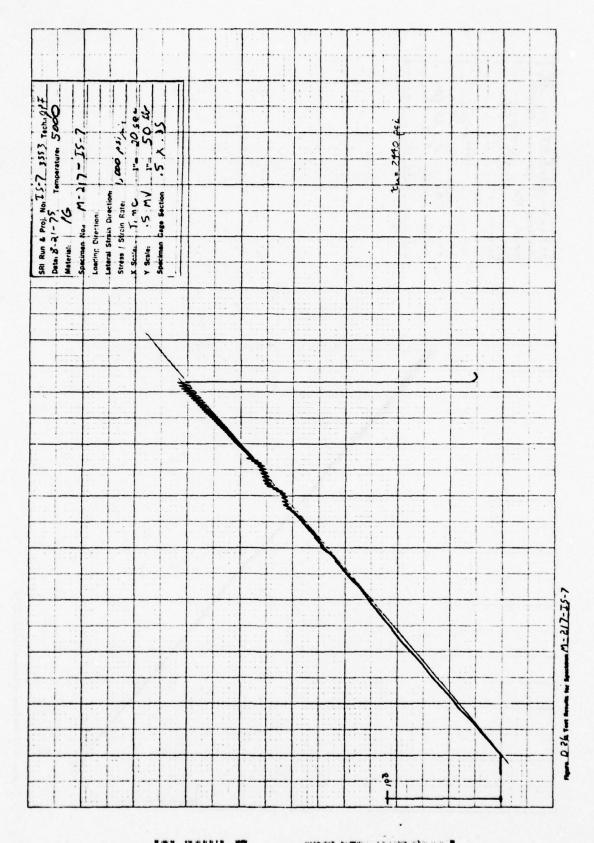


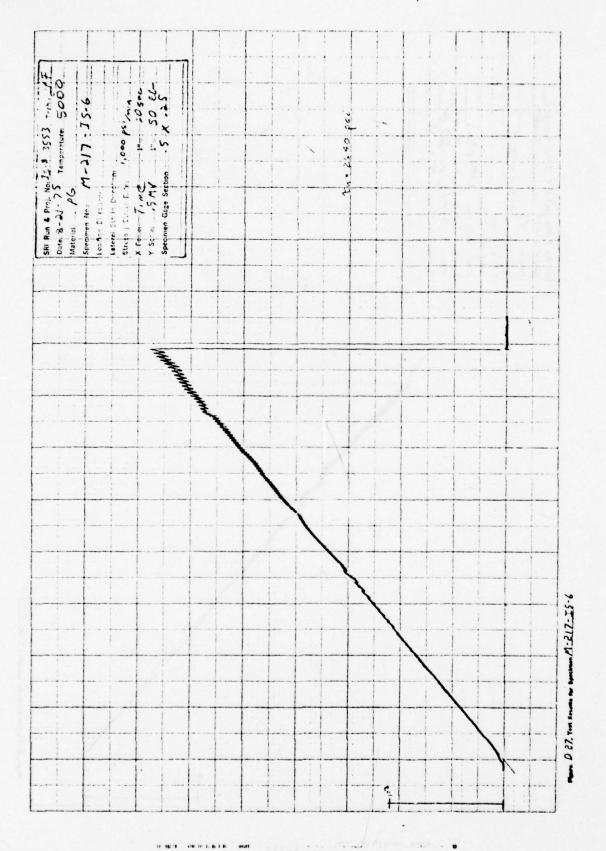


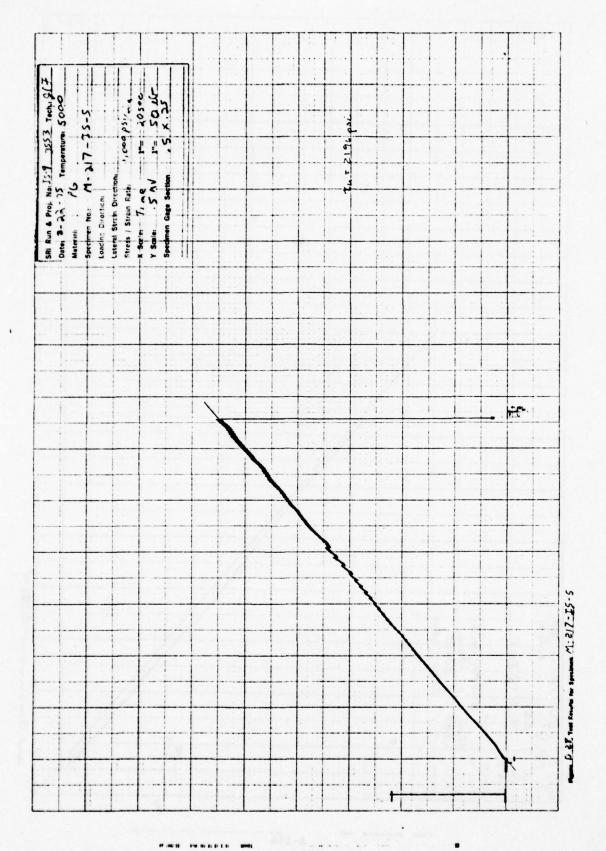


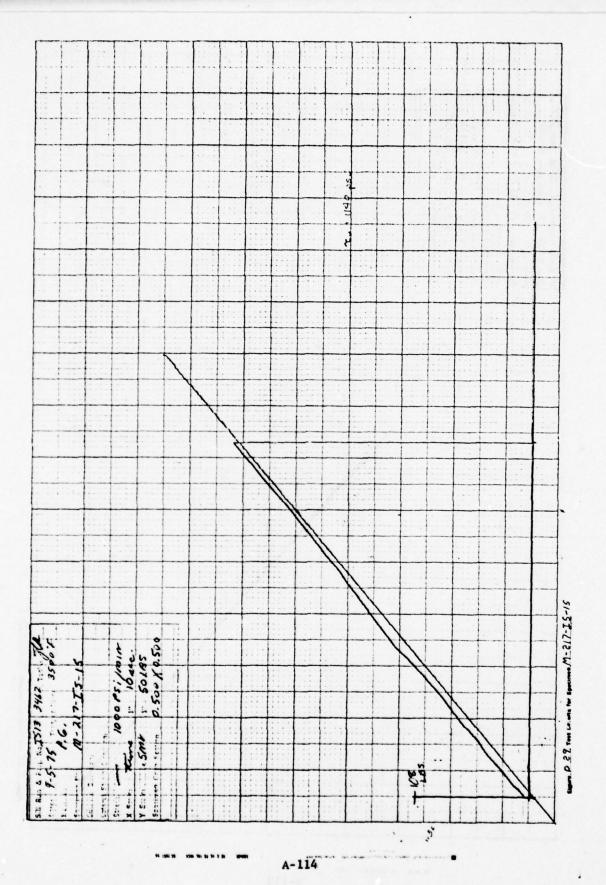




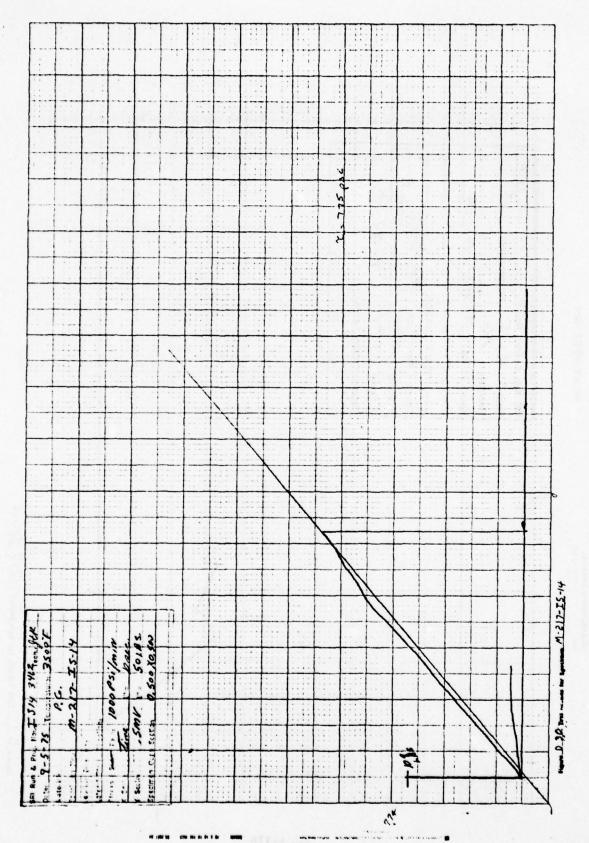




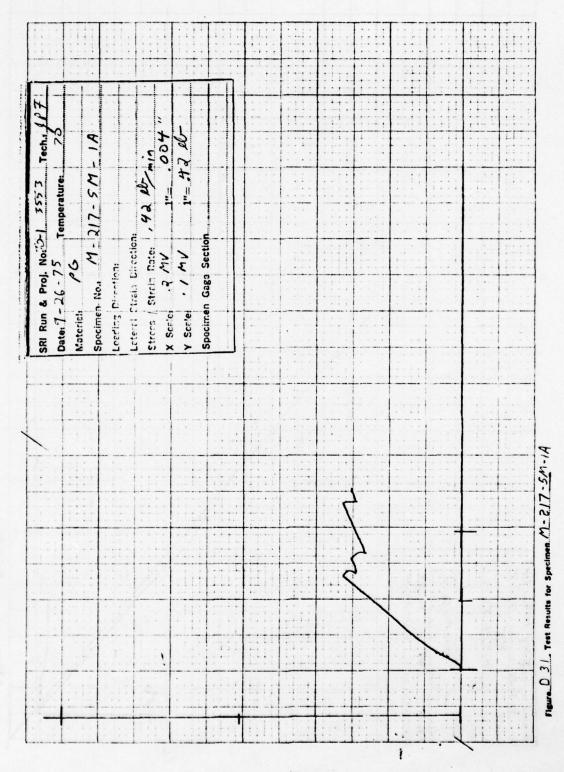




THIS PAGE IS BEST QUALITY PRACTICARES



A-115



A-116

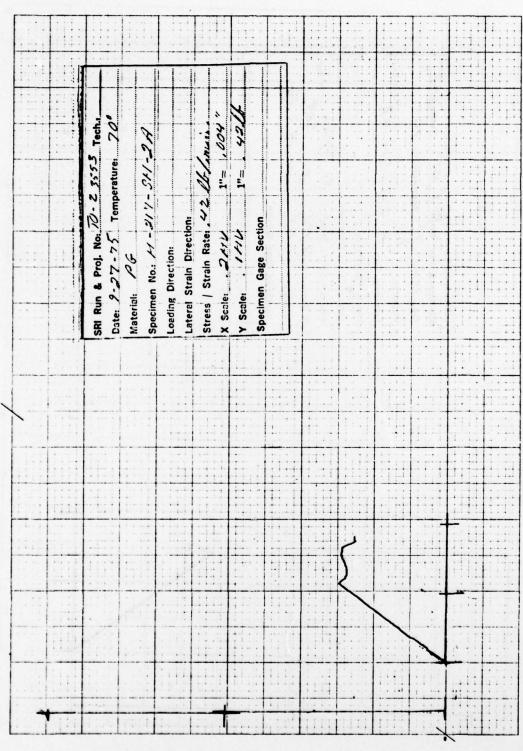


Figure D 32, Test Results for Specimen M-217-5M-2A

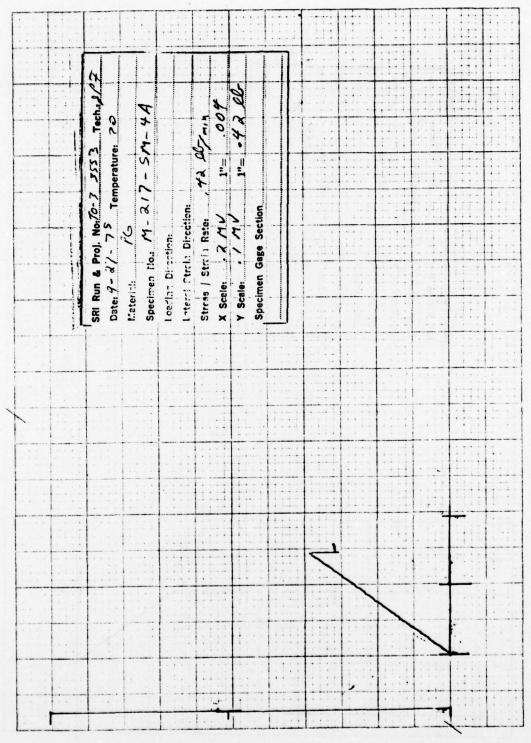
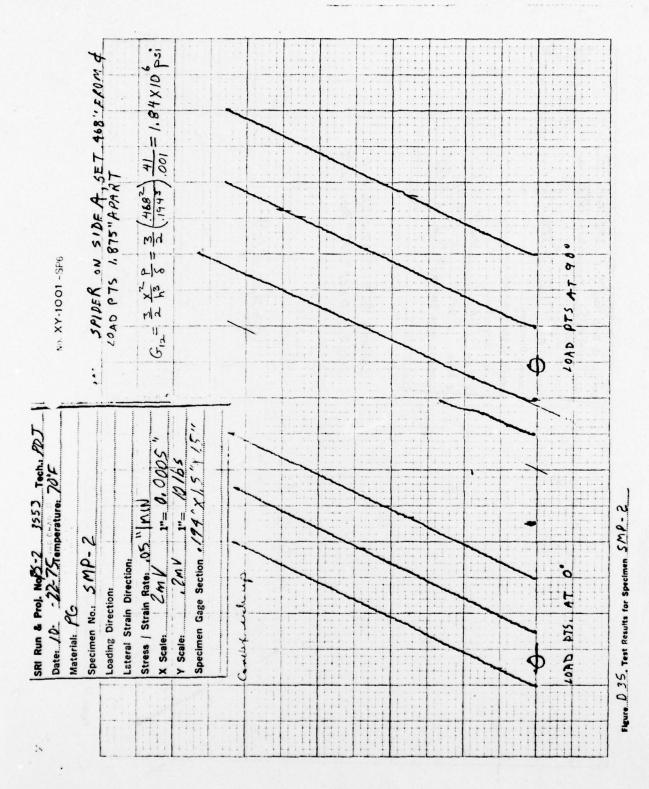
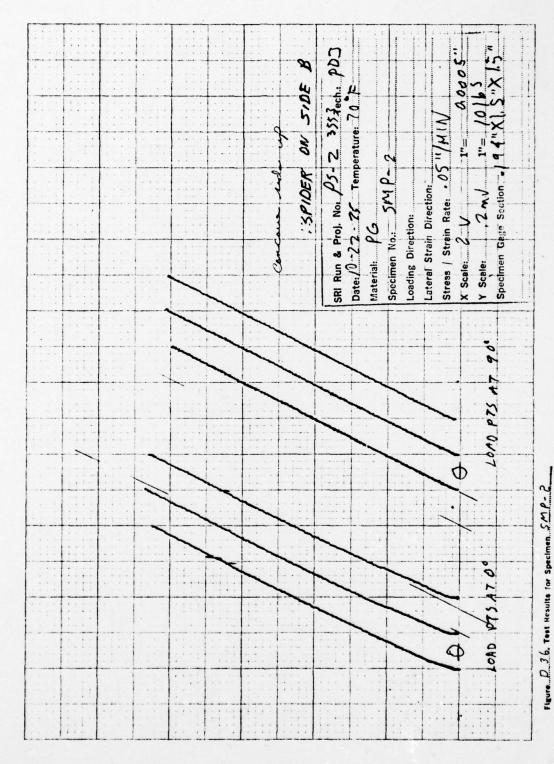


Figure D.33. Test Results for Specimen M-217-5M-44

SRI Run & Proj. Nov PS-1 355.57rech.PDJ Date:													
Baym of Leaving 188	.ch. 20J	7-6		/ 00				m leith					
Baylon on Leving 18 8 8 9 9 8 9 9 9 9 9 9 9 9 9 9 9 9 9	5- / 3553T emperature. 7	17-SM(1			1"= 2 'x 2		-	1 - 101 = 3		(90)			
Baylon on Leving 18 8 8 9 9 8 9 9 9 9 9 9 9 9 9 9 9 9 9	& Proj. No. P	n No. M-2	Direction: Strain Direction	Strain Rate:	1. 2 m V	39	MING PING	ER DISTANCE			7		
	SRI Run Date:7	Material	Loading	Stress	Y Scale		607	Olas :					
									•	1			##
										3 6	2		
										and an kind			
the same of the sa										Dilysin on these			

Figure D 34. Test Results for Specimen M-217-SMCP)-1





A-121

APPENDIX B

PRELIMINARY MATERIAL SPECIFICATION

FOR AB PLANE PG.

FREE STANDING SHAPES

MATERIAL SPECIFICATION - PRELIMINARY MS426-01

1.0 SCOPE

- 1.1 Type. This specification covers Pyrolytic Graphite, Free Standing Shapes, to be used in rocket motor applications (see 6.3).
- 1.2 <u>Description</u>. The material is a chemical vapor deposited form of high purity graphite. This material shall be produced by the chemical vapor deposition of carbon in a high temperature furnace.

2.0 APPLICABLE DOCUMENTS

2.1 The following documents, of the issue in effect on date of invitation bids or request for proposal, form a part of this specification to the extent specified herein.

Military Specifications

MIL-T6866	Inspection,	Penetrant
TBD	Inspection,	C-Scan Ultrasonic
MIL-STD-453	Inspection.	Radiographic

Military Standards

MIL-STD-129	Marking	for	Shipment	and	Storage

2.2 Other Publications. The following documents form a part of this specification to the extent specified herein. Unless otherwise indicated, the issue in effect of invitation for bids or request for proposal, shall apply.

Publications:

American Society for Testing and Materials

ASTM D790-66	Flexural Properties of Plastics
ASTM D792-60T	Density and specific Gravity of Plastics
ASTM D695-63T	Compressive Properties of Plastics
ASTM D2344-65T	Apparent Horizontal Shear Strength of Reinforced Plastics by Short Beam Method

(Application for copies should be addressed to the American Society for Testing and Materials, 1916 Race Street, Philadelphia, PA 19103)

3.0 REQUIREMENTS

3.1 Material Type. The material shall be a pyrolytic graphite which can be classified as continuously nucleated (see Para. 3.2.2).

3.2 Material Properties.

- 3.2.1 <u>Basic Process</u> Parts shall be formed by pyrolytic deposition of appropriate carbon bearing gases on the internal form of a high quality graphite mandrel at temperatures in excess of 2000°C.
- 3.2.2 Microstructure The microstructural characteristics of the continuously nucleated CVD pyrolytic graphite shall exhibit visual homogeneity of nucleation sites and shape across the total thickness of the part as recorded by photomicrographs at approximately 50X under polarized light. A similar level of homogeneity must be evident at both ends of the part as determined per Para. 4.4.7.
- 3.2.3 <u>X-Ray Properties</u> The X-Ray characteristics of the pyrolytic graphite are specified by paragraphs 3.2.3.1 through 3.2.3.3. Paragraph 4.4.8 specifies the methods of making the measurements.
 - 3.2.3.1 <u>d-Spacing</u> The interlayer spacing (d-spacing) of parts formed by CVD shall be 3.40 \pm 0.02 Å.
 - 3.2.3.2 Crystallite Size, L_c The crystallite size shall be 185 \pm 35Å.
 - 3.2.3.3 <u>Preferred Orientation</u> The preferred orientation shall be $60 \pm 5^{\circ}$.
- 3.2.4 Physical Properties The physical properties of the CVD pyrolytic graphite shall be as specified in Table I.

TABLE I. PHYSICAL PROPERTIES

Property	MIN/MAX
Density - gm/cc @ 75 ± 5°F	2.185/2.205
Flexural Strength, "a" direction psi @ 75 ± 5°F	> 15000
Compression Strength, "a" direction psi @ 75 ± 5°F	> 10000
Short Beam Shear, "a" direction psi @ 75 ± 5°F	> 750

3.2.5 Nodule Size and Frequency

- 3.2.5.1 The diameter of any nodule or cluster of nodules on the surface shall not exceed 50% of the material thickness.
- 3.2.5.2 Nodule distribution shall be such that not more than two nodules of acceptable size shall be closer than 1.0 inch apart.

3.2.6 Delaminations

- 3.2.6.1 Delaminations as determined from radiographic analysis or visual inspection of machined edges are cause for rejection in parts with a maximum t/r of 0.07.
- 3.2.6.2 Delaminations in parts with a t/r greater than 0.07 are only acceptable as defined in paragraphs 3.2.6.2.1 through 3.2.6.2.3.
 - 3.2.6.2.1 Maximum Material Separation The maximum material separation as determined from radiographic films with low magnification (TBD) for an acceptable delamination is (TBD) inches.
 - 3.2.6.2.2 <u>Delamination Pattern</u> An acceptable delamination shall be parallel to the outside contour of the part except (TBD). (see Figure 1)
 - 3.2.6.2.3 Continuous Delaminations Any delamination that can be traced for more than (TBD) percent of the length (both sides) of a part on the radiographic film in any of the four views required shall be cause for rejection.
- 3.2.7 <u>Deposition Symmetry</u> The material thickness at any station along the length of an "as-deposited" part shall not vary more than (TBD) inches from the minimum material thickness to the maximum material thickness.

- 3.2.8 <u>Dimensions and Finish</u> Unless otherwise specified in the contract or purchase order, dimensions and finish shall be as specified on the Design Drawing.
- 3.2.9 Workmanship The pyrolytic graphite forms procured under this specification shall be uniform in quality and condition, free from surface defects such as porosity, pits, cracks, and chips and internal defects such as voids, cracks and inclusions.

3.3 Process History

3.3.1 The vendor shall record and have available for each piece submitted a complete process history.

4.0 QUALITY ASSURANCE PROVISIONS

- 4.1 <u>Inspection</u> The vendor shall be responsible for the performance of all inspection requirements as specified in para. 4.3. The vendor shall also maintain complete inspection records of all examinations and tests as specified on each piece submitted for acceptance.
- 4.2 A lot shall consist of the material fabricated in one furnace run.
- 4.3 Sampling Each part fabricated shall have sufficient length to allow for the removal of a test ring (TBD) inch long from each end. One portion of each ring shall be tested by the vendor to the requirements of this specification. The other portion of each ring will be shipped with the part for verification testing at Atlantic Research. The tests outlined in Paragraphs 4.4.1, 4.4.2, 4.4.3, 4.4.6 and 4.4.8 shall be performed on the test ring.
- 4.4 Acceptance Test The following destructive and non-destructive tests shall be performed on each piece. Failure of the material to conform to any requirement of this specification shall be cause for rejection.
 - 4.4.1 <u>Visual Examination</u> Each part shall be visually inspected for defects such as porosity, pits, cracks and chips. Porosity, pits, cracks, and chips are cause for rejection.

- 4.4.2 Deposition Symmetry- The deposition symmetry as required in Paragraph 3.2.7 of the specification shall be determined from radiographs of the "as-deposited" shape. Two radiographs at a 90° interval shall be submitted with each part for verification to the requirements of Paragraph 3.2.7.
- 4.4.3 Specific Gravity The specific gravity shall be determined in accordance with ASTM D-792-60T using deionized water as the immersion fluid. Each piece tested for specific gravity shall be free of cracks and delaminations as determined by visual inspection and/or dye penetrant inspection.
- 4.4.4 Flexural Strength (TBD)
- 4.4.5 Compression Strength (TBD)
- 4.4.6 Short Beam Shear Strength (TBD)
- 4.4.7 Structure Photomicrographs shall be made on each piece of material submitted for acceptance. Sample location shall be from the trim rings unless otherwise specified on the engineering drawing. These photomicrographs shall be approximately 50% under polarized light.
- 4.4.8 X-Ray Characterization
 - 4.4.8.1 d-Spacing Measurement (Rotation of 20 Angle) Values of d-spacing shall be obtained using a Phillip's Model 120 X-ray diffractometer equipped with a scintillation detector. Since sample alignment for this type of measurement is critical, each sample will be removed from the sample holder and the analysis repeated a minimum of three times. Samples will be examined at the 29 angle of the 002 carbon planes by rotating the X-ray goniometer through the angle 25.88 to 26.60° 20. The 002 peak maximum will be used as the average angular value. The results of this measurement will be applied to the basic Bragg equation, $n\lambda = 2d \sin \theta$, to obtain d-spacing values where n is unity, \(\lambda\) is the wavelength of radiation being used (CuK₂ = 1.540Å) and θ is the Bragg angle for the 002 reflexion. Results shall be reported in angstroms (A).

4.4.8.2 Crystallite Size - Apparent crystallite size shall be calculated by using the equation $L_c = \frac{0.89\lambda}{\beta \cos \theta}$ where λ is the wavelength of the radiation being used, CuKa = 1.540A, B is half-height (002) line width and θ is the Bragg angle for the 002 Reflexion. B shall be determined by measuring the width of the carbon peak at one-half its peak height and correcting for instrumental line broadening by substitution into the equation

 $\beta = \sqrt{\left(\beta_{OBS}^{2}\right) - \left(F^{2}\right)}$ The factor, F, is the instrumental line broadening factor and β_{ORS} is the measured peak width. Results shall be reported in angstroms (A).

- 4.4.8.3 Preferred Orientation Measurements (Rotation of \$ Angle) - Samples shall be prepared for preferred orientation measurements by honing rods (across the a-b planes), 50 mils or less in diameter by one inch long out of the material to be examined. The sample will then be rotated in the X-ray beam through the ? direction at 1/3 rpm while the 20 angle is held constant at the 002 carbon plane maximum. The data resulting from this measurement shall be a set of peaks generated each time the 002 plane passes through the correct orientation with the X-ray beam. Preferred orientation data will be reported as degrees \$ at one-half peak height at the 002 plane maximum.
- 4.4.9 Radiographic Inspection All parts shall be radiographically inspected. Four radiographs shall be taken at 45° intervals perpendicular to the longitudinal axis of the part. Any internal cracks, inclusions of voids are cause for rejection of part. Delaminations are acceptable only as defined in Paragraph 3.2.6 of this specification.
- 4.4.10 Process History The vendor shall record and have available for each piece offered for acceptance the following process information.

- 4.4.10.1 Deposition temperature, pressure, flow rate and gas composition taken at least every 15 minutes.
- 4.4.10.2 Any interruptions in the deposition cycle.

4.4.11 Packaging and Marking

- 4.4.11.1 Each part and its associated trim rings shall be marked in accordance with the applicable engineering drawing. Each part shall be indexed at 0° and 90° by a solvent solution ink. Inspection reports shall reference these indices for location of defects.
- 4.4.11.2 Each part and its associated trim rings shall be packaged in conformance to Section 5.0.

5.0 PREPARATION FOR DELIVERY

- 5.1 Packaging and Packing
 - 5.1.1 <u>Level C</u> Unless otherwise specified by the procuring activity, the packaging and packing shall be in accordance with the best accepted commercial practice.
- 5.2 Marking Marking shall be in accordance with MIL-STD-129, and shall include, but not be limited to the following:
 - a. Title, number, and revision letter of this specification.
 - b. Manufacturer's grade and designation.
 - c. Manufacturer's name.
 - d. Lot number
 - e. Part serial number.

6.0 NOTES

- 6.1 <u>Intended</u> Use The material covered by this specification is intended for use in rocket motor applications.
- 6.2 Ordering Data Procurement documents shall specify but not be limited to the following information:
 - a. Title, number, and date of this specification.
 - b. Type, grade, and class required, if applicable.
 - c. Lot size (see 4.3).
 - d. Sampling requirements, if not specified (see 4.4).
 - e. Size of container.

- f. Place of delivery
- g. Responsibility for inspection (see 4.1).
- h. Disposition of test data.
- 6.3 <u>Definitions</u> To insure uniformity of interpretations the following items are defined.
 - 6.3.1 Nodules A single grain growth significantly larger in size than the surrounding matrix, appearing as a blister on the deposited surface.
 - 6.3.2 <u>Delaminations</u> A material separation parallel to the plane of deposition that is discernible at low magnification from radiographic film.
 - 6.3.3 t/r Ratio The t/r ratio is the ratio of material thickness at a point to the radius of curvature at that point.
 - 6.3.4 Cracks Any material separationother than a delamination.
 - 6.3.5 Clusters Two or more nodules in contact.
 - 6.3.6 "As-Deposited" The "as-deposited" condition refers to the condition of the part after it has been removed from the furnace and the mandrel has been removed from the part but prior to any internal machining.
 - 6.3.7 Station Station as used in this specification refers to any axial location in inches measured from (TBD).
 - 6.3.8 "a" Direction The direction parallel to the plane of deposition. Also known as the a-b direction.
 - **6.3.9** "c" Direction The direction perpendicular to the plane of deposition.
 - 6.3.10 <u>Document Precedence</u> In case of discrepancy between Engineering Drawing and this specification, the requirements of the drawing shall prevail.